U.PORTO

FEUP FACULDADE DE ENGENHARIA UNIVERSIDADE DO PORTO

Experimental and Numerical Study of Laser Beam Welding of PBT-GF3 Components

Author:

Luiz Rafael Resende da Silva

Supervisors:

Eduardo André de Sousa Marques

Co-Supervisors:

Lucas Filipe Martins da Silva

Ricardo João Camilo Carbas

Thesis submitted for the degree of Doctor of Philosophy

Doctoral Program of Mechanical Engineering (PRODEM)

Faculty of Engineering of the University of Porto

DEMec, Faculdade de Engenharia da Universidade do Porto, Rua Dr. Roberto Frias, 4200-465 Porto, Portugal

Porto, 2025

© Luiz Rafael Resende da Silva

Departamento de Engenharia Mecânica
Faculdade de Engenharia da Universidade do Porto

Rua Dr. Roberto Frias, s/n
4200-465 Porto
Portugal

Acknowledgements

I would like to thank my co-supervisor Lucas da Silva, for the opportunity to integrate in your research group and for the support of your experts in this doctoral thesis.

A special thank you to my supervisors Eduardo Marques, Ricardo Carbas for the guidance, the knowledge shared, the long hours of work and constant availability and help along this project. Additionally, to all the members of the Advanced Joining Processes (AJP) unit.

Additionally, I extend my thanks to all members of the Advanced Joining Processes (AJP) unit, who have also kindly provided support to my work.

I would also like to thank my educational institution, the Instituto Federal de Educação, Ciência e Tecnologia do Espírito Santo (IFES), where I am currently working and which has given me the support and backing to climb this new and inherent step in my life.

I would like to say a special thank you to my wife Cleudiana Assis do Santo and my daughter Emanuella Resende do Santo, who have supported me with their strength, love and consolation in moments of tiredness, my cosiness throughout this journey.

And finally, I could never forget to thank my Father God for everything he has provided me with throughout this journey.

Abstract

The constant advancements in joining processes, in sectors such as the automotive, medical and aeronautical industries, has given rise to products with excellent mechanical performance, good durability and high production rates. Numerous joining processes exist, which can be classified into several main categories. These include purely mechanical methods, such as mechanical joining; intrinsic methods that involve the addition or fusion of a material, such as adhesive bonding and welding joining. Additionally, there are hybrid processes that integrate two or more of these techniques.

The analysis presented in this thesis focuses on the automotive industry, with a specific emphasis on the joining of housings for electronic protection, made from PBT-GF30. To optimize productivity, the proposed method of study is autogenous laser welding, as the material to be utilized is a glass fibre-reinforced thermoplastic polymer. This process has been selected due to its increasing adoption in the industrial market, which facilitates productivity in terms of time and automation. It enables the formation of monolithic joints with superior sealing properties and visual quality, while also being applicable to complex joint configurations.

Resumo

Os constantes avanços nos processos de ligação, em setores como a indústria automóvel, médica e aeronáutica, têm dado origem a produtos com excelente desempenho mecânico, boa durabilidade e altas taxas de produção. Existem numerosos processos de ligação, que podem ser classificados em várias categorias. Estas incluem métodos puramente mecânicos, como a ligação mecânica por conformação e outros métodos que envolvem a adição ou fusão de um material, como a ligação adesiva e a soldagem. Além disso, existem processos híbridos que integram duas ou mais dessas técnicas.

A análise apresentada neste estudo foca-se na indústria automóvel, com uma ênfase específica na união de caixas de proteção eletrónica produzidas a partir de PBT-GF30. O método proposto para o estudo é a soldadura a laser autógena, uma vez que o material a ser utilizado é um polímero termoplástico reforçado com fibra de vidro. Este processo foi selecionado devido à sua crescente implementação no mercado industrial, sendo compatível com a alta produtividade em termos de tempo e automação. Permite a formação de juntas monolíticas com propriedades de vedação e qualidade visual superiores, sendo também aplicável a configurações de juntas complexas.

Contents

1 INTRODUCTION 1
2 ENGINEERING POLYMERS 11
2.1 MATERIALS USED IN ELETRONIC HOUSINGS 13
3 POLYMER JOINING PROCESSES 14
3.1 LASER WELDING 15
3.2 ADHESIVE BONDING 20
4 EXPERIMENTAL METHODS 31
4.1 CHARACTERIZATION OF THE BASE MATERIAL 31
4.1.1 THERMAL TREATMENT OF PBT-GF30 31
4.1.2 OPTICAL PROPERTIES 32
4.1.3 THERMAL PROPERTIES 33
4.1.4 MORPHOLOGICAL ANALYSIS 33
4.1.5 TENSILE TEST 33
4.1.6 HARDNESS TESTING 34
4.1.7 FRACTURE TOUGHNESS TESTING 34
4.2 CHARACTERIZATION OF THE ADHESIVE 36
4.2.1 THICK ADHEREND SHEAR TEST 36
4.2.2 TENSILE TESTING 38
4.3 JOINT LEVEL TESTING 38
4.3.1 WELDED FILLET LAP JOINTS 38
4.3.2 BONDED SINGLE LAP JOINTS 40
4.3.3 COMPONENT LEVEL JOINT 42
5 NUMERICAL MODELLING 45
5.1 LAP JOINTS 48
5.2.1 WELDED FILLET LAP JOINTS 48
5.2.2 ADHESIVELY BONDED LAP JOINTS 50
5.2 COMPONENT LEVEL JOINT 54
6 CONCLUSIONS 56
7 FUTURE WORKS 59

List of Figures

Figure 1 - Scheme of tasks *of this PhD* thesis....3
Figure 2 – Scheme *depicting the planning* of the tasks and papers *associated to this thesis*....5
Figure 3 - Main polymer....14
Figure 4 - Different polymer laser welding techniques. a) Laser welding in pair of absorbent materials, b) laser welding in different materials, absorbing with transparent material and c) laser welding in pair of transparent materials with absorption coating. 16
Figure 5 - Correlation between a) welding depth and welding width with b) welding speed adapted from [89]. 17
Figure 6 - Laser *absorption coefficient* vx wt. % Black carbon level. a) PA6, b) PA6GF c) and PC adapted from [100] 19
Figure 7 - Examples of specimens used for testing the performance of adhesive joints: single lap shear joint (SLJ), tube butt joint and tube lap shear joint adapted from [107] 22
Figure 8 - a) Application diagram of T-ZnO at the substrate-adhesive interface. b) Comparison of the joint peeling strength without and with the T-ZnO filling. Adapted from [113]....23
Figure 9 - Load vs. displacement of experimental DCB testing and FEM model. Adapted from [116]....24
Figure 10 - a) Average of Load - Pm for each adhesive thickness - tA, b) Energy release rate for mode I - GI, and mode II - GII to each tA by the compliance-based beam method (CBBM) adapted from [120] 25
Figure 11 - Maximum shear stress sustained by PTFE-PTFE and PVT-PVT joined with different adhesives adapted from [122]....26
Figure 12 - Representative stress–strain curves of the TEPs-modified adhesive as a function of moisture adapted [125]....27
Figure 13 - Comparison of the error between the experimental and numerical results, adapted from [128]....28
Figure 14 - The static failure characteristic of fillets in SLJ adapted from [128]....28
Figure 15 - Compliance as a function of load cycles: Comparison between the numerical data and the experimental results adapted from [129]....29
Figure 16 - Detail of the mould used for heat treatment....32
Figure 17 - Geometry of the dog-bone tensile test specimens. (A) PBTGF30 in as supplied state. (B) PBT GF 30 heat treated state....34
Figure 18 - Machined tensile testing specimens. a) PBT-GF30 in as supplied state. b) PBT-GF30 heat treated state at 257°C....34
Figure 19 a) Compact tension sample dimensions (in mm). b) Manufactured sample of compact test....35

Figure 20 - Representation of the a) pre and b) post crack specimen.....35
Figure 21 - Spot laser welding machine.....38
Figure 22 - Step-by-step procedures used for the determining the advance on the spot weld bead.....39
Figure 23 - Scheme of sample inclination angle, showing the laser beam and the laser incidence positions on the samples.....39
Figure 24 - Scheme of the procedures used for the analysis of the welded region with optical microscopy.....40
Figure 25 – a) Adhesive joint geometry with low thickness (0.06 mm). b) Adhesive joint geometry with reference thickness (1 mm).....41
Figure 26 –a) Rubber frame configuration. b) Adhesive joint configuration with low thickness. c) Adhesive joint configuration with reference thickness.....42
Figure 27 - Actual component of the electrical circuit protective enclosure, illustrating the section tha.....42
Figure 28 - a) Representation of the cross-sectional view of the actual joint samples, including both the female and male components. b) Mould for fixing parts for joining by spot laser beam welding.....43
Figure *29* - Real joint test fixing configuration.....43
Figure 30 - Representative configuration of the boundary conditions for the tensile simulation (both as supplied and heat-treated conditions).....47
Figure 31 - Compact test model configuration. a) Boundary conditions and b) Mesh details.....48
Figure 32 - Configuration of the model, showing the overlapped region and the boundary conditions (US joint configuration shown) 49
Figure 33 - Material partitions showing weld and base material in the a) US model, b) MS model and c) DS model.....49
Figure 34 – Stress-strain curves of PBT-GF30 treated at different temperatures, showing plastic behaviour.....50
Figure 35 - Hyperelastic constitutive laws maps.....51
Figure 36 - Damage scheme of the triangular cohesive zone model in single lap joint.....52
Figure 37 - Traction separation law.....52
Figure 38 - Representation of joints. a) Division of the joint part and the adhesive layer to 1 mm thickness. b) Boundary condition for the 1 mm thickness. c) Division of the joint part and the adhesive layer to 0.05 mm thickness. d) Boundary condition for the 0.05 mm thickness.....53
Figure 39 - Meshing details of the adhesive joints.....54
Figure 40 - Representation of layer divisions of the property's gradient – Real joint setting.....55
Figure 41 - Schematic representation of the joint model. a) Boundary conditions and b) Mesh size division.....56

List of Tables

Table 1 – Main applications of engineering polymers.....11
Table 2 - Main polymers and polymer-based composites used for engineering purposes and their main characteristics.....12
Table 3 - Staging temperatures and stage durations used for heat treatment.32
Table 4 Parameters of the compact test specimens for all PBT-GF30 conditions tested.....36
Table 5 - Simulation parameters applied in ductile damage to validate the model in tensile test of PBT-GF30.....46
Table 6 - Simulation parameters applied in traction separation Law with Maxps and XFEM, to be validated against the experimental compact test results.....48
Table 7 – Basic properties of PBT-GF30.....50
Table 8 – Mechanical properties of PBT-GF30 necessary for the implementation of a ductile damage model.....50
Table 9 - Properties of the substrate and adhesive layers.....54
Table 10 - Gradient expressed as a percentage representing the mechanical properties in the weld zone. 55

List of Acronyms

PBT GF30 - (Polybutyleneterephthalate with Glass fiber 30% Reinforced

SLJ - Single Lap Joint

PA6 GF - Polyamide 6 Glass Reinforced

FEM - Finite Element Method

CB - Carbon Black

PC - Polycarbonate

CNT - Carbon Nano Tubes

PET- Polyethylene Terephthalate

NaOH - Sodium hydroxide

ZnO - Zinc Oxide

T-ZnO – Zinc Oxide Tetrapodal

DCB - Double Cantilever Beam

ENF - End-Notched Flexure

CBBM - Compliance Based Beam Method

SBCM – Surface Based Cohesive Model

VCCT – Virtual Crack Closure Technique

XFEM – Extended Finite Element Method

PTFE – Polytetrafluoroethylene

PVT- Polyvinyl Toluene

DOPA – 3,4-Dihydroxyphenylalenine

IO_4 – Periodate

CNA – Cyanoacrylate

NAC - N-acetyl-l-cysteine

MCNT – Multiwalled Carbon Nnanotubes

TEP – Thermally Expandable Particles

MSLJ – Monolithic Single Lap Joint

LDB – Laminated Double in Bending

CZM – Cohesive Zone Mode

UMAT – User Material subroutine

BASF - Badische Anilin & Soda Fabrik

FTIR - Fourier-Transform Infrared Spectroscopy

DSC - Differential Scanning Calorimetry

ASTM - American Society for Testing and Materials

BS - British Standards

CT – Compact Test

TAST - Thick Adherend Shear Test

ISO - International Organization for Standardization

Nd:Yag - Neodymium-doped yttrium aluminum garnet; Nd:$Y_3Al_5O_{12}$

US - Upper Specimen

DS - Down Specimen

MS Middle Specimen

ABS - Acrylonitrile Butadiene Styrene

2D – Two Dimensions

CPS4R type - Four-node plane stress element

FEA - Finite Element Analysis

List of Notations

D - Damage

σ_{y0} – Maximum stress

$\bar{\varepsilon}_0^{pl}$ - Equivalent plastic strain

G_f – Fracture energy

L - Effective element length

$\bar{\varepsilon}_f^{pl}$ - Equivalent plastic strain at failure

u_f^{pl} - Displacement to failure

U – Potential energy

I – Invariant

$T_{I,c}$, - Normal principal stress

$T_{II,c}$ - Shear stress (mode II)

$T_{III,c}$ - Shear stress (mode III)

1 INTRODUCTION

1.1 BACKGROUND AND MOTIVATION

In the wide range of technological processes employed in manufacturing activities, joining processes are among the most important and indispensable, since they significantly contribute to the aesthetics, the ease of assembly and the mechanical performance of the final product. Joining processes are thus encountered in practically all industrial fields, ranging from the automotive industry to aircraft construction, while also including applications such as the manufacture of renewable energy systems, packaging and even the manufacture of biomedical components.

Industrial entities currently have wide range of joining processes at their disposal, each with its own advantages and disadvantages. Given this large variety of joining solutions and its vastly different characteristics, it is evident that each specific application or product can benefit from a specific and well optimized process. One important application is the case of products composed of fibre reinforced, thermoplastic polymer matrixes, materials which are gaining importance in applications that demand high stiffness, low weight and good thermal properties but also require easy moldability of complex parts. In this application, the most commonly used joining processes include adhesive bonding, laser welding and friction stir welding. These processes are all compatible with thermoplastic composites and provide sufficient mechanical strength to the joint, but also enable the automation of the processes. If properly optimized, the resulting joints can also redistribute the stresses acting on the joint. Still, although these processes are already industrially implemented, there is still much to be learned regarding their mechanics and their key process parameters, knowledge which is essential for optimizing the joint performance, durability and the manufacture process. Thus, a clear research opportunity was identified in this field, focusing on the development of suitable joining methods for application on thermoplastic polymers reinforced with fibre.

1.2 OBJECTIVES

This project has four main objectives. The first is to characterize PBT GF30 (Polybutylene Terephthalate reinforced with 30% glass fibre) in terms of its mechanical properties (such as thermal, optical, and morphological properties). This characterization aims to assess the material's applicability in the laser welding process of single-fillet lap joints,

alongside the characterization of the properties and parameters necessary for the development of numerical models for the simulation of these joints.

The second objective is to investigate the optimal parameters for laser welding, such as power, pulse duration, and beam diameter, with the goal of optimizing the joint strength of laser-welded joints using PBT GF30, targeting their employment in electronic components within the automotive industry. This will be conducted in parallel with a numerical analysis to evaluate the behaviour of the joint in terms of strength and fracture performance.

The third objective is to conduct a comparative study of joining processes by optimizing an adhesive joint to achieve joint strength comparable to that of the single-lap joint used in laser welding. Specifically, the study will determine the required adhesive length to achieve equivalent strength to that of the laser-welded joint. Additionally, a computational numerical model will be developed to full analyse the behaviour of adhesive joints.

Finally, the fourth objective focuses on exploring the performance of laser welding in an industrial automotive case study, specifically the joining of an electrical component enclosure that requires sealing. This includes analysing the joint strength through experimental testing and developing a computational numerical model to assess the joint strength response of the component.

1.3 RESEARCH METHODOLOGY

This section details the main research activities of this thesis, divided into five main tasks. In this work, a reference joint will be manufactured by laser beam welding. This joint is proposed to join a two-part housing for electronic components. Afterward, a new joint with the same geometric parameters will be manufactured using adhesive bonding. The performance of the two joints will be compared based on various parameters. In parallel, a numerical model will be developed to simulate both joints. Subsequently, the research will continue onwards to test the optimized laser welding process in a real-world case, developing a supporting numerical model to validate the specific joint. An overview of the tasks can be found in Figure 1.

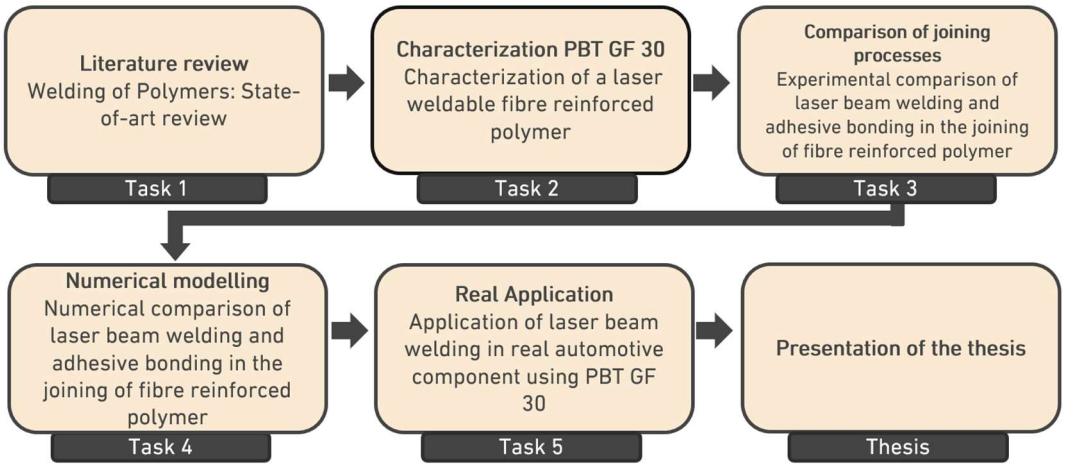


Figure 1 - Scheme of tasks of this PhD thesis.

TASK 1: WELDING OF POLYMERS: STATE-OF-ART REVIEW

This task consists of a comprehensive review of the published results to illuminate the road of the research. In this part, numerical and experimental results available in literature will be reviewed. This task will cover the main engineering polymers applied in joining process, a general analysis of joining processes specifying the most researched areas used like automotive, aerospace, biomedical and other. And lastly, a more detailed study of the joining processes, experimental and numerical, approaching the mechanical joining, adhesive joint, friction stir welding, laser welding and hybrid joining process.

TASK 2: CHARACTERIZATION OF A LASER WELDABLE FIBRE REINFORCED POLYMER

The second task involves characterizing the substrate material used in the joint. The chosen material, a polybutylene terephthalate reinforced with 30% glass fibre by weight (PBT GF30), was provided by the automotive industry as part of an external research demand. Given the plan to use laser welding and adhesive bonding processes, this task focuses on characterizing the substrate material in its as-received state, as well as after being treated at various temperatures, including near its melting point. The characterization approach encompasses mechanical, thermal, optical, and morphological properties. Finally, mechanical characterization is also performed using numerical modelling and validated to propose a numerical joint model.

TASK 3: EXPERIMENTAL COMPARISON OF THE PERFORMANCE OF LASER WELDING AND ADHESIVE BONDING IN THE JOINING OF FIBRE REINFORCED POLYMER

Task 3 is divided into two parts. First, a study was conducted on the parameterization of laser welding for PBT GF30, aimed at identifying parameters that yield improved joint efficiency through fillet welding, including optimal positioning and incidence angle. The analysis will focus on several factors: laser power, pulse duration, pulse frequency, laser beam diameter, and the movement rate of the specimen. With the optimization of these parameters, an adhesive joint will be created using a silicone adhesive, selected for its high sealing capabilities, vibration absorption properties, and market accessibility. In this adhesive joint, the geometric parameters were studied to closely match the joints produced by laser welding, enabling a comparative analysis of the results. Additionally, the study was assessed the adhesive thickness of the joint to propose a hybrid joint combining both joining techniques to achieve the joint with highest performance.

TASK 4: NUMERICAL COMPARISON OF LASER BEAM WELDING AND ADHESIVE BONDING IN THE JOINING OF FIBRE REINFORCED POLYMERS

A numerical study was conducted to validate the laser welding and adhesive bonding processes through the development of individual models based on experimental data. Subsequently, the numerical model of laser-welded joints in a simple overlap fillet configuration was enhanced by incorporating information obtained through morphological characterization using Raman Spectroscopy, which optimized the joint validation. This enhanced model with Raman spectroscopy technique will be suitable for application in a real automotive component, ensuring compliance with specific requirements.

TASK 5: APPLICATION OF LASER BEAM WELDING IN REAL AUTOMOTIVE COMPONENT COMPOSED OF A FIBRE REINFORCED POLYMER

After a comprehensive analysis and comparison of the individual laser welding and adhesive bonding processes, both experimentally and numerically, it was determined that the application of the laser welding process is more advantageous for the joint performance. Therefore, the final task is to propose the most suitable contact and fit positions for the real joint, applying the optimized welding process parameters and the adjusted numerical model, along with the Raman spectroscopy technique, aiming to revalidate the joint's complexity.

1.4 OUTLINE OF THE THESIS

This thesis consists of six peer reviewed papers and a summary. The correspondence between these papers and the general project tasks is presented in Figure 2.

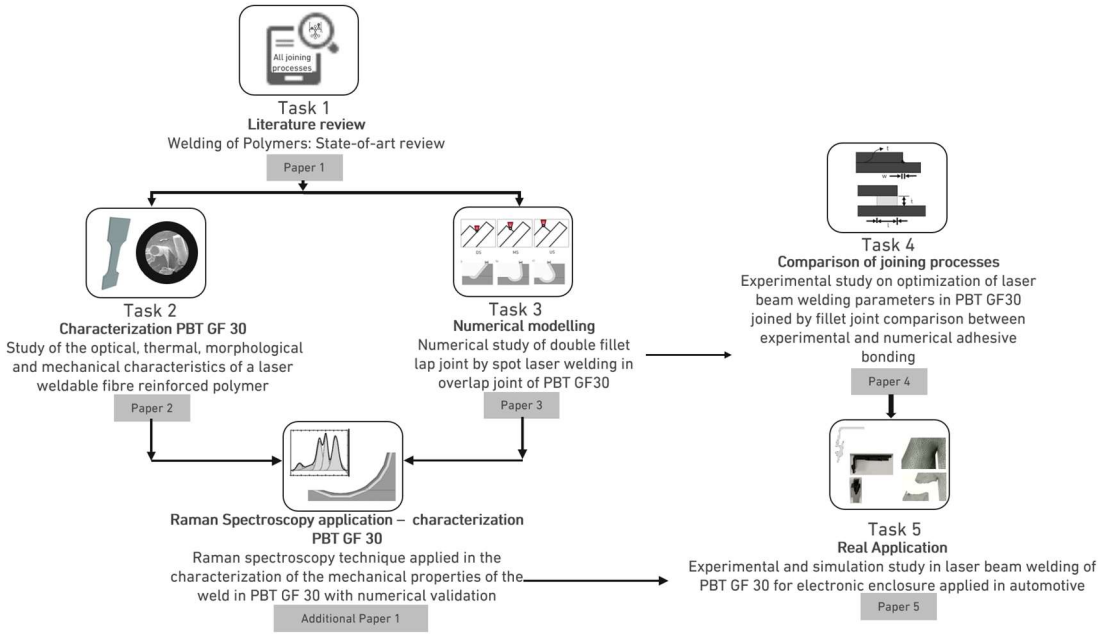


Figure 2 – Scheme depicting the planning of the tasks and papers associated to this thesis.

The thesis is comprised of a summary, 5 main papers and 1 additional paper. The summary is divided into seven main parts. This introductory chapter contains a brief description of the problem under study, as well as the background and motivation of this work and its objectives. Additionally, it contains a brief summary of each paper presented. Chapter 2 provides an overview of the application of polymers in industrial sectors, with a specific focus on the use of polymeric materials in electronic enclosures for automobiles. Chapter 3 discusses the joining processes for polymers, emphasizing laser welding and adhesive bonding, which were both used in this work. For both processes, the materials used in electronic enclosures within the automotive industry are specified. Contextually, Chapters 2 and 3 serve as a brief literature review of the thesis, highlighting laser welding and adhesive bonding. Chapter 4 details the experimental procedures used to characterize PBT GF30 and the material under study. It also outlines the analysis and procedure for laser welding of this specific material, compares the application of adhesive joints with laser welding, and ultimately discusses the application of laser welding in a real joint. Chapter 5 presents a concise description of the numerical models used in this thesis. Chapter 6 summarizes the main conclusions drawn from the research topics, while Chapter 7 offers suggestions for future work in these areas. The

appendices include the 5 main papers produced in the context of this thesis and one additional paper, representing the research conducted in detail and providing the most relevant results.

Paper 1: **Polymer Joining Techniques State of the Art Review**

Task 1

L. R. R. Silva, E. A. S. Marques, L. F. M da Silva.
Published in "*Welding in the World*"

Abstract: Modern products and structures require efficient material joining processes for their construction, able to combine similar or dissimilar materials, which almost always includes high-performance polymers. To design such joints, it is necessary to first understand the techniques currently used in this technological field and how they can be improved using advanced technological joining processes. In this manuscript, a review of several polymer-joining techniques is made, highlighting the recent technological advances in this field. The search for improved mechanical performance and lower costs has led to the development of new, high-performance engineering polymers, which require highly specific joining processes. These can include adhesive bonding, mechanical joining, welding or a combination of different processes, a technique known as hybrid joining. Several experimental works available in the literature have proven the validity of these techniques, although optimization processes are necessary to attain maximum performance. Additionally, extensive numerical with different methods and models has been carried out to better understand the processes and support parametric analysis. The intent of this work is to review studies on the most important polymer bonding techniques, the numerical models applied to simulate these techniques, the use of hybrid joints and describe promising techniques that are being developed and proposed for future use.

Paper 2: **Study of the optical, thermal, morphological and mechanical characteristics of a laser weldable fiber reinforced polymer**

Task 2

L. R. R. Silva, E. A. S. Marques, R. J. C. Carbas, A. Akhavan-Safar, L. F. M. da Silva.
Published in "*Polymer composites*"

Abstract: In recent years, varied industrial users such as the automotive and electronic manufacturers, have greatly expanded the application of technical polymers, exploring the lower weight, improved moldability of complex parts and good mechanical performance that these materials can provide, especially when reinforced with fibres. Among these materials, polybutylene terephthalate reinforced with 30% glass fibre, designated as PBT GF30, is highly interesting, since it combines excellent mechanical properties with watertightness, allowing PBT GF30 to be used in the encapsulation of sensitive electronic elements. However, to maintain access, PBT GF30 products always require the use of joints, which are often created using laser welding. This work presents a detailed characterization of the thermal, optical, mechanical, and morphological characteristics of PBT-GF30 suitable for laser welding, supported by a numerical analysis. This process allowed to determine the influence of thermal energy on the behaviour of the material and thus fully understand the mechanical response of the material after laser welding. Testing of the PBT GF30 in the as received state confirmed a fusion temperature of 225°C and large energy absorption for wavelengths around 1000 nm. Exposure to large temperatures leads to increased fibre exposure and matrix degradation, with a deleterious effect on the mechanical properties. When treated at the highest temperature under consideration, the material exhibited a reduction of 66% in its ultimate tensile stress, 67% in the yield at failure, 45% in the Young's modulus and 44% in the stress intensity factor. Hardness was less affected by the temperature increase. From the numerical model for the tensile and the compact tension tests, it was possible to find a good degree of convergence. This material was generally found suitable for laser welding processes and the determined useful to support the modelling the behaviour of laser welded joints.

Paper 3: **Numerical study of double fillet lap joint by spot laser welding in overlap joint of PBT-GF30**

Task 3

L. R. R. Silva, E A. S. Marques, R. J. C. Carbas, L. F. M. da Silva.
Submitted to " *Journal of Applied and Computational Mechanics*"

Abstract: This study presents a numerical investigation of elastoplastic damage in laser-welded double fillet lap joints fabricated from PBT GF30. Experimental testing was conducted on joints with varying laser beam diameters and incidence positions to determine the optimal welding parameters. The results revealed that a 1.5 mm diameter beam incident on the upper surface (US) of the joint yielded the highest joint strength of 51.8 ± 1.6 N. To accurately simulate the mechanical behaviour of these joints, a numerical model incorporating elastoplastic and ductile damage models was developed. The model demonstrated good agreement with the experimental force-displacement curves, especially for the US position, where the error was just 1.08%. This level of precision highlights the model's ability to capture the complex deformation and failure mechanisms inherent to laser-welded joints. The successful validation of this numerical model provides a powerful tool for future design and optimization of laser-welded joints in PBT GF30. By accurately predicting joint strength and failure modes, engineers can tailor welding parameters to achieve desired mechanical performance and minimize the risk of premature failure.

Paper 4: **Experimental and numerical study for the optimization of process parameters in laser welded and adhesively bonded PBT GF30 fillet joints**

Task 4

L. R. R. Silva, C. S. P. Borges, E. A. S. Marques, R. J. C. Carbas, A. Akhavan-Safar, L. F. M. da Silva.
Published in "*Proceedings in Engineering Mechanics*"

Abstract: With the advancement of technological processes and the application of fibre-reinforced polymer matrices in elements of vehicles, there has been a demand for the optimization of productivity, enhancing automation, reduction in process time and increasing

the quality of part joining, allowing to manufacture high performance protective enclosures for electrical circuits. In this context, the laser welding process has gained importance especially when the polymer matrix is thermoplastic. On the other hand, adhesive bonding also has a wide application in this market, although it often harder to automate and requires a longer time for the curing of the process, which can reduce productivity. This work aims to study and optimize the laser welding parameters in overlapped joints of PBT GF30, joined by fillets at the ends performed through manual laser spot welding, to experimentally compare with joints with similar geometries joined by adhesive joints, validated by numerical models for the experimental conditions. The model identified the most effective parameters and was found to replicate the experimental results with a high degree of accuracy.

Paper 5: **Experimental and numerical study of laser beam welding of PBT-G30 for electronic housings in automotive applications**

Task 5

L. R. R. Silva, E. A. S. Marques, R. J. C. Carbas, L. F. M. da Silva. Experimental and numerical study of laser beam welding of PBT-G30 for electronic housings in automotive applications.

Abstract: This study investigates the application of laser spot welding to join protective housing components in the automotive electronics industry. The PBT GF 30 components were joined using two primary configurations: a purely overlapping joint and a top-overlap joint, both autogenous (i.e., without filler material). To complement the experimental analysis, a numerical model, previously validated for a simpler joint configuration, was adapted and applied to these more complex joint configurations. The results demonstrated that butt-overlap joints exhibited significantly higher strength (85% increase) than purely overlapping joints. This enhancement is attributed to the combined effect of normal and shear stresses in the top-overlap configuration, whereas purely overlapping joints rely solely on shear stress. The validated numerical model accurately predicted the experimental results, including displacement and force values. While minor deviations were observed, the numerical model's predictions converged within the average experimental values and standard deviation, demonstrating that such model can be used to precisely design laser welded joints for similar applications.

Additional Paper 1: **Raman microspectroscopy applied in the characterization of the properties of laser welded PBT GF 30 with numerical validation**

Extra task

L. R. R. Silva, E. A. S. Marques, Ricardo J. C. Carbas, A. Q. Barbosa, Alexandra G., L. F. M. da Silva

Abstract: Automotive electronics demand compact, robust sealing solutions. Laser welding of fiber-reinforced polymer matrixes offers a promising approach to solve this challenge. This research aims to optimize a numerical model of a laser-welded joint, based on the Raman microspectroscopy characterisation of the properties of a glass fibre reinforced polymer. The study was developed considering autogenous overlapped joints, of the fillet type at the ends, with Polybutyleneterephthalate with a 30% glass fibre reinforced (PBT GF30) as the substrate material, welded by the laser welding process. The spectra of melted and solidified PBT GF30 material at three different temperatures was compared. This data was used to construct a numerical model with variable mechanical properties along the transverse region, using optical microscopy for geometry. The performance was compared with the results of the tensile test of the joints showing good convergence with the failure process of the joint.

2 ENGINEERING POLYMERS

The number of commercially available high-performance polymer formulations is quite large, encompassing a wide range of mechanical, physical and chemical properties. However, such variety in requirements can create significant difficulties in the material selection processes [1]. The main features of polymers are:

- High strength to weight ratio;
- High moldability;
- Low transformation energy;
- Good optical properties;
- High durability;
- Bio-degradable and recyclable;

Polymer-joining techniques now find extensive use in both structural and non-structural applications, for example thermal systems and coatings [2, 3]. Special polymeric-joining techniques are also available for applications where low chemical reactivity is required, as is the case of biomedical components manufactured with biocompatible materials [4].

Engineering polymers are now used in a wide range of industries, including bioengineering applications, the aerospace and automotive sectors, packaging of consumer products and electronics, among others. In all these cases, effective joining processes are essential to create a complete final product. Table 1 summarises the common applications of engineering polymers and provides references on joining materials for each specific application.

Table 1 – Main applications of engineering polymers.

Main areas	Specific application	References
Aerospace	Airframe structures	[5-11]
Automotive	Headlights, panels, chassis	[5-7, 9, 10, 12-18]
Biomedicine	Prosthetics	[4, 7, 8, 10, 19-25]
Packaging and food sustainability	Food and drug packaging	[5-10, 26]
Clothing and protection	Clothing coating, ballistic protection	[2, 5, 8-10, 27]
Others	Electronics, Concrete reinforcement, Marine	[6-8, 10, 28-34]

Due to the wide diversity chemical formulations of polymers, there is a large number of engineering polymers currently available in the market and which find extensive use. Before the discussion of the most important polymer joining techniques is made, it is important to understand the key engineering polymers that are the target of research on joining methods, their uses and main characteristics. Table 2 lists some of the main engineering polymers and some of their composites and provides examples of research works on joining these materials.

Table 2 - Main polymers and polymer-based composites used for engineering purposes and their main characteristics

Polymers and polymeric composites	**Key characteristics**	**References**
Epoxy	Resin used as a cohesive material in adhesive, great impact resistance, stiffness and durability	[5, 7, 9, 10, 19, 25, 28, 30, 34-41]
Carbon reinforced epoxy	Material used to ensure cohesion of fibre reinforced composite	[5, 7, 9, 10, 16-18, 32, 42]
Polyurethane	Material used as thermal insulator and flexible sealant	[5, 7, 9, 10, 39, 42]
Polyethylene	Material used as component of artificial mobile protheses and other biomedical application	[4, 7, 43]
Acrylic	Provides excellent fatigue endurance, impact resistance, and superior toughness when compared to other systems polymers.	[9, 10, 30]
Polyamide 6	Typical material used in the automotive sector for moulded components	[2-5, 7, 9, 10, 44]
Polyamide 6 Glass Reinforced – PA6 GF	Typical material used in the automotive sector for high strength and durable moulded components	[2, 5, 8-10, 27, 45]
Others	Electronics, concrete reinforcement	[6-8, 10, 28-34]

To join polymers, the most cited processes are mechanical and chemical joining methods. For example, polymers are connected using fasteners, relying on a physical load transfer, while welding joins the material efficiently at the chemical level. In addition, it is also possible to achieve a strong joint with a combination of physical and chemical connections. Another example is the case of adhesive bonding, where chemical forces and mechanical interlocking processes are responsible for transferring the load [38, 46, 47]. There are, of course, many other processes suitable for joining polymers and polymeric matrix composites. However, this short review focuses mostly on adhesive bonding, mechanical joining, laser welding, and friction stir welding, correlating experimental and numerical work to explore the advantages and disadvantages of these four joining processes.

2.1 MATERIALS USED IN ELETRONIC HOUSINGS

The automotive sector employs a diverse range of materials, encompassing metals for transmission components, plastics for bodywork, and ceramics for brake pads, ignition valves, and sensors [48, 49]. However, the industry's landscape is rapidly evolving due to technological advancements, with polymers and composites steadily gaining market share for the automotive industry [50, 51]. Polymeric composites are increasingly favoured for electronic circuit enclosures due to their advantageous combination of mechanical strength, low density, thermal and electrical insulation, and high conformability. As highlighted by Zimmermann et al. [52], reinforced polymers are becoming the material of choice for cases and enclosures designed to protect electronic circuits, as they meet the essential requirements of this application. One key material for this application is polybutylene terephthalate (PBT). Borges et al. [53]characterized PBT-G30, which is reinforced with glass fibres and thus exhibits elevated mechanical strength, favourable thermal and electrical properties, high moldability, and compatibility with water absorption. These properties make PBT a strong contender for manufacturing electronic circuit protection enclosures. Furthermore, a study by Cousins et al. [54] underscores PBT's superior chemical resistance to solvents, fuels, lubricants, and brake fluids, as well as its enhanced tribological characteristics against abrasion. These findings, coupled with PBT's suitability for electrical and electronic components, further solidify its position as a preferred material for electronic circuit enclosures.

3 POLYMER JOINING PROCESSES

Modern society is highly reliant on diverse tools, components and equipment that are only possible due to use of advanced engineering polymers and composites with polymeric matrices. Automobiles, cell phones computers and medical devices are all prime examples of these objects, which must be manufactured in economically in large scale. Due to complex design of these products, joining technologies play a key role in their construction and the importance of joining polymeric materials has thus increased significantly [2, 3].

Technical, or engineering polymers have evolved greatly since they were first synthesised in the early twentieth century and, following many decades of evolution, they now present greatly improved properties, achieved with new chemical synthesis and doping methods, forming novel copolymers or composites that meet rigorous industrial technological demands. Such advances have led to drastically improved mechanical, thermal, optical and chemical properties, as well as important manufacturing cost reductions [55-58].

A general analysis, shows that the number of joining processes suitable for use with polymers is very large and is in constant evolution, providing new alternatives that overcome the limitations of classical joining methods [46, 59-61]. Although the number of techniques available is extensive, methods for joining polymers can all be classified into three main groups. These are adhesive bonding, mechanical joining and welding, as shown in Figure 3.

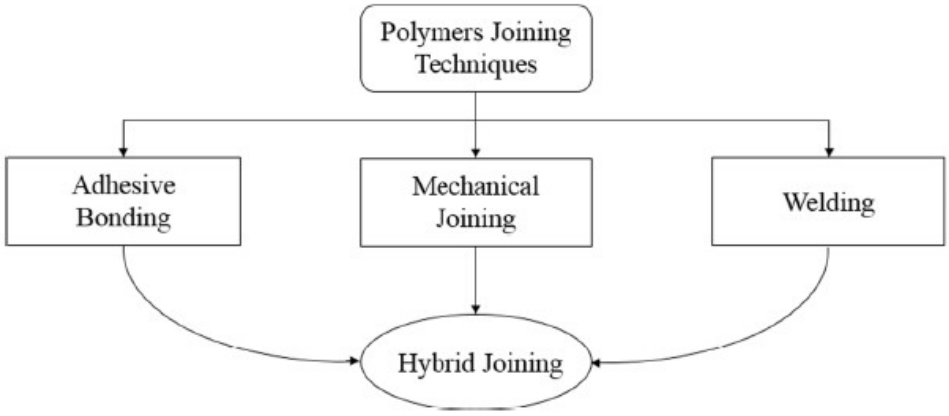


Figure 3 - Main polymer joining processes

In addition, hybrid joining methods, combining these different techniques in a single joint are also a valid solution. One other important consideration to be made when analysing polymer-joining techniques is making the distinction between their suitability for use with thermoplastic or thermoset polymers and the strict limitations in the applicability to complex geometries, restricting the joint configurations and contours [62-64].

3.1 LASER WELDING

Laser welding techniques, although relatively recent, have grown in their capabilities in the last few decades [8, 65-68]. For example, extensive research has enabled this technique to effectively join dissimilar metals, metals with low weldability [69-72] and polymers to metals [73-78]. Technological advances in this technique have even enabled to weld ceramic materials [79-81] mainly because it allows for a large thermal input to be applied in a small region. This technique has also greatly increased in importance for the joining of thermoplastic materials [82-88] and still possesses a good future growth potential. This opens applications such in the biomedical sector as well as the automotive and aerospace industries, allowing to create high performing, defect free joints with good aesthetic qualities.

The laser joining technique consists in joining two materials using a laser beam that, when aimed at the welded area, releases a large amount of energy. The laser energy is transformed into a wave of thermal energy, fusing the heated region in a localized manner. After cooling, the material solidifies, establishing a strong joint. The technique can be carried out in three different ways, Figure 4-a represents the optimal technique for materials that have high light absorption. The joint is created in the surface of the material with small thickness, since the laser energy transformed into thermal energy only on the surface of the material. Figure *4*-b shows a case where one of the materials to be joined has high light transmittance (transparent) and the other material has high absorbance characteristics. The laser beam passes through the first material and is stopped in the second material, in which the beam is converted into thermal energy, heating the interface of the materials and uniting them. For the third case, a pair of materials that have low absorbance is used. For this case, the absorbance of the light is attained by introducing a third material that is placed at the interface of the two transparent materials. This usually takes the form of an absorbing coating, in which the transformation from wave energy to thermal energy takes place, Figure 4-c.

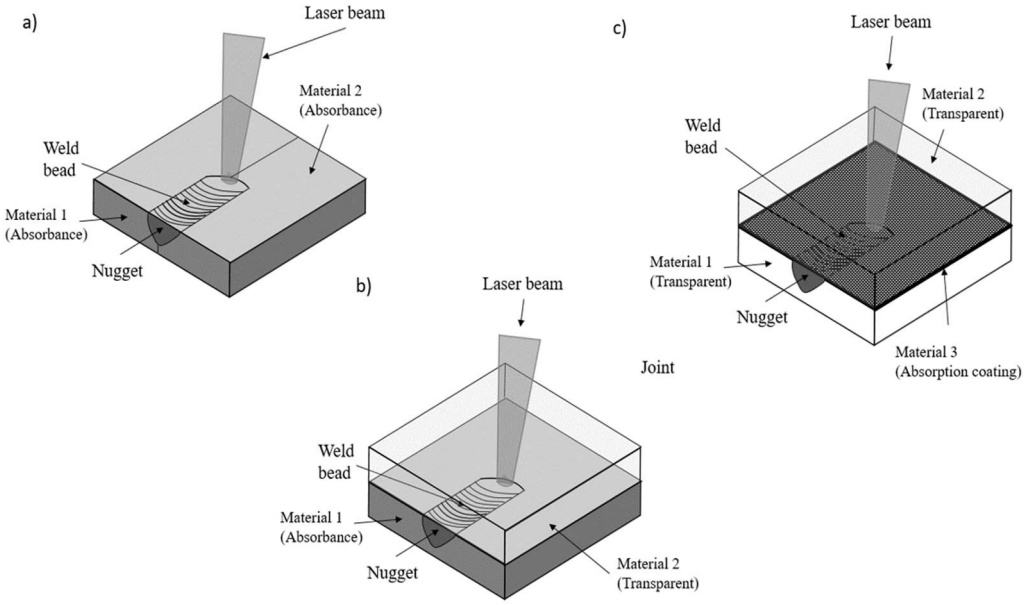


Figure 4 - Different polymer laser welding techniques. a) Laser welding in pair of absorbent materials, b) laser welding in different materials, absorbing with transparent material and c) laser welding in pair of transparent materials with absorption coating.

The laser welding technique is governed by many different parameters, all of which have great importance on the results. These parameters include the wavelength of the laser radiation, the incident power, the pulse length and shape and the pulse frequency and the welding speed, among many others. Thus, a few authors have produced studies devoted to studying the effect of some of these parameters on joint performance. Hubeatir et al. [89] have carried out a study to analyse the influence of the advance speed in a PMMA polymer, analysing the width and depth of the weld bead. It was found that the width and depth of the weld is inversely proportional to the advance speed, as illustrated in the graph adapted in Figure *5*-a and Figure *5*-b.

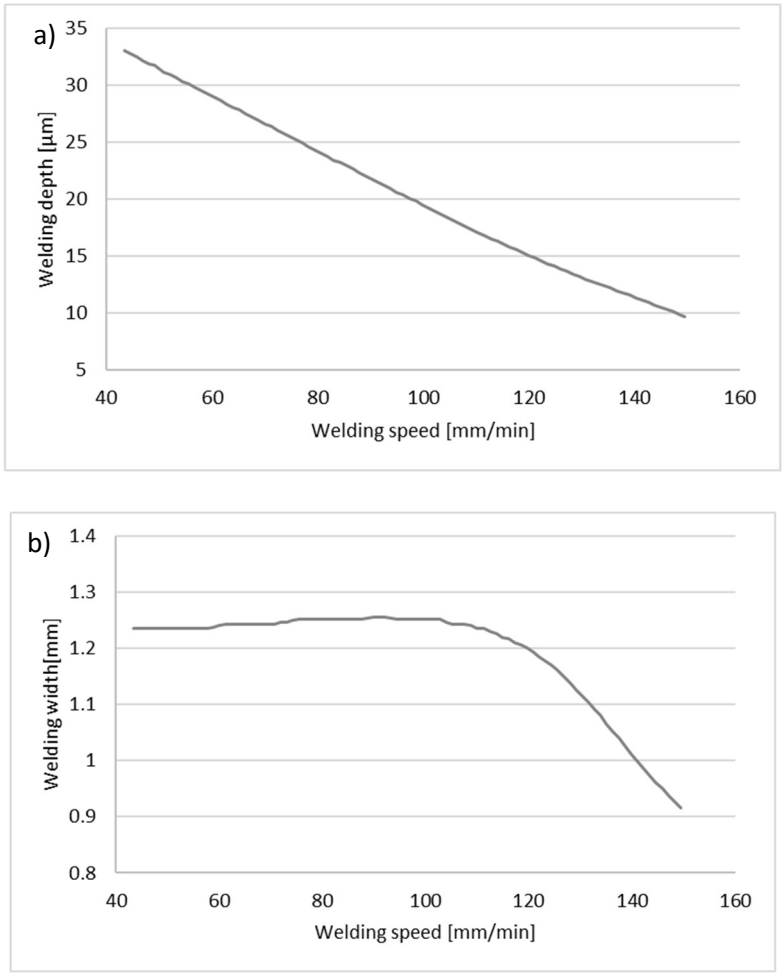


Figure 5 - Correlation between a) welding depth and welding width with b) welding speed adapted from [89].

Taha et al. [90] performed a study based on mathematical modelling, using heat transfer equations, aiming to quantify the width and depth of the laser weld bead in a polyethylene. It is concluded that a higher advance speed corresponds to a smaller width and depth of the bead, although it is noted that the discrepancy between the numerical prediction and the experimental data is greater for low speeds.

Acherjee et al. and Casalino et al. have used FEM, [91, 92] to reach similar conclusion. Through the results obtained, it is seen that the greater the energy applied during the welding process, the greater the width of the weld bead. The results of Acherjee et al. [91] also corroborate the fact that the greater the amount of black carbon added on the surface of the materials, the greater the energy absorption in the material, conferring a greater width and depth to the weld bead. By comparing the laser power instead of the advance speed, Ruotsalainen [93]

studied the welding process of a polyamide, using a 1940 nm wavelength laser. The results show that greater laser power leads to a greater width and depth of the weld bead.

An important consideration in the laser welding process is the effect of the strong energy pulse on the properties of the welded material. Infrared thermography is a well-used method to indirectly characterize and quantify the properties of materials through a temperature gradient. In order to validate studies of the melt pool irradiation process and temperature gradient, several studies [94-97] show experimental and numerical convergence of these results. To quantify and qualify the thermally affected zone of a semi-transparent polyamide 6, using computational methods, Schmailz et al. [98] used a pyrometer integrated with a laser welding process, in which the temperature gradient is correlated with the thermally affected zone. This study confirms that the higher the laser power, the higher the localized temperature. It is also observed that the greater the amount of black carbon resin applied at the polymer interface to increase light absorption, the higher the temperature. These higher temperatures lead to larger heat affected zones. Using the same infrared thermography technology implemented in previous works [96-98] as well as the analysis of the width of the weld bead and the welding power performed by Hubeatir et al. [89], Schmitt et al. [99] have shown that it is possible to combine these techniques to characterize dimensional defects of the weld bead such as residual gap, weld geometry, internal pores and leaks.

Another key area of research associated with laser welding of polymers is the addition of particles and materials that can change how the materials to be joined react to the laser light [91, 98], Chen et al. [100] carried out an experimental study demonstrating and effect of the addition of carbon black to thermoplastics, for cases of welding in transparent materials. The results of this work are summarized in Figure *6*-a, Figure *6*-b and Figure *6*-c. It is observed that the larger the content of carbon black added, the greater is the absorption of the laser energy, optimizing the bonding process at the polymer interface. This was found to be true for welding Polyamide 6 to PA 6, glass fibre reinforced polyamide 6 to PA 6 GF and polycarbonate.

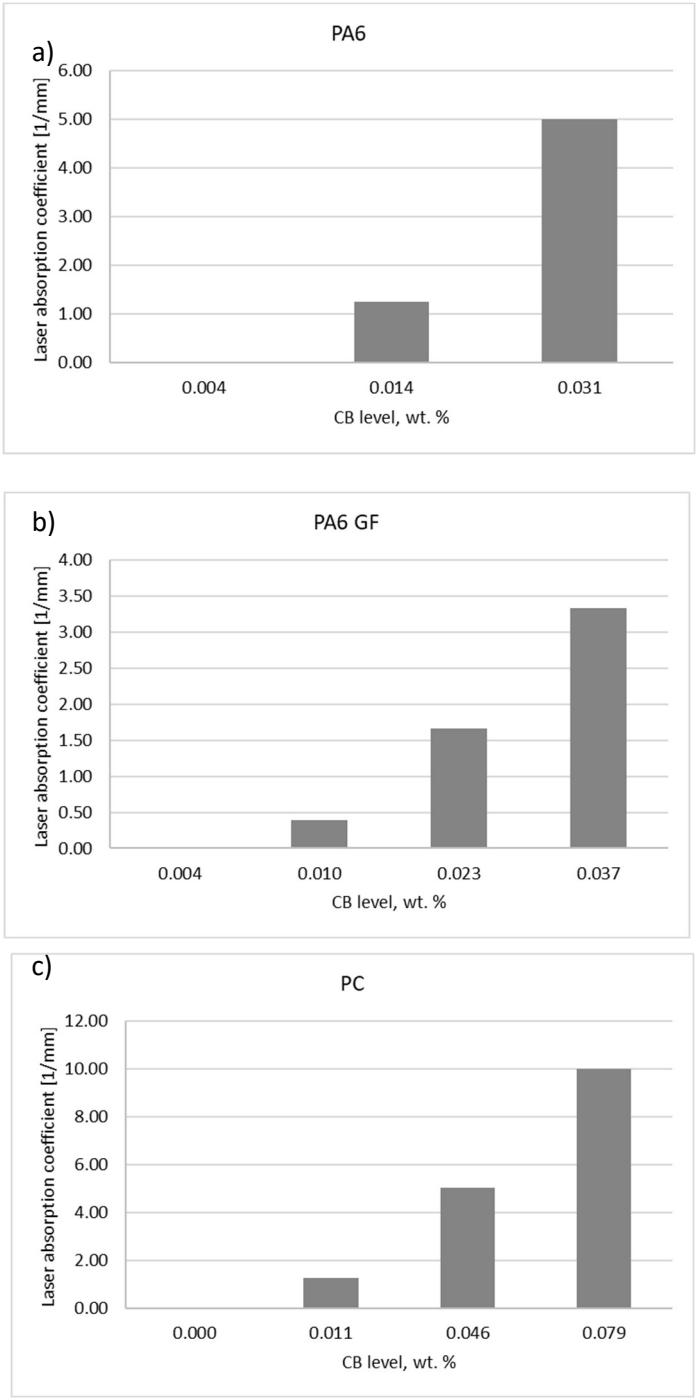


Figure 6 - Laser absorption coefficient vx wt. % Black carbon level. a) PA6, b) PA6GF c) and PC adapted from [100].

Rodríguez-Vidal et al. [101] shows that, due to the low energy absorption in ABS for a 880 nm wavelength diode laser energy absorption in the material can be increased with the application of carbon nanotubes (CNT) in the matrix, which is in agreement with some of the conclusions reached by Chen et al. [100]. This work compares the resistance voltage in relation to the percentage of nanotubes added. It is shown that with 0.01 wt.% CNT added, the joining process takes place at 880 nm, however, when placed 0.05 wt.% CNT in addition to the joining

process, the weld is more resistant because it has better energy absorption to melt the material. Gisario et al. [102] further studied the addition of black carbon at the interface of materials to be laser welded with high transparency. This work considers polyethylene terephthalate (PET) materials in neat state and with 5 wt.%, 10 wt.% and 15 wt.% of carbon black. Through these fractions, using a 940 nm wavelength laser, it was found that the greater the addition of black carbon, for a weldability map varying the power and the advance speed, the greater the effective welding area, the smaller the area of degradation was obtained.

As the literature shows, laser welding of polymers is seen as a very powerful and advantageous technology which is rapidly becoming ubiquitous as laser welding equipment gradually reduce in price. Research wise, it seen that most of the research is devoted to optimizing the wide range of welding parameters that govern this technique, as well as understanding how the highly concentrated incident energy affects the mechanical performance of the base polymeric materials. It is also seen that many of the research works study methodologies to control the transmission and absorption of the laser light, using transparent polymers or introducing additives that allow to precisely control the location of maximum energy transfer and thus, the location of the weld itself.

3.2 ADHESIVE BONDING

Even though its use for engineering purposes is relatively recent, adhesive bonding is an ancient technique, first used when the early civilizations started to explore the adhesive properties of several natural materials, such as lignin, a natural adhesive extracted from wood fibres, which was used to produce tools and other primitive instruments. Although the mechanical performance of these early adhesives is very limited, subsequent technological advances gradually led to more powerful adhesives. Obtained through chemical synthesis these structural adhesives can support much larger, structural mechanical loads. The industrial sectors that spearheaded the application of this technique were the automotive and aerospace industries [6, 7, 103], which have mastered this technique to produce highly complex multi-material vehicle structures where adhesives join metals, polymers and composites.

If used properly, adhesive bonding can enable the design of high-performance structures and research in this field has significantly increased, with many works devoted to experimental and numerical methodologies to predict joint performance and validate its application in industrial applications. Many key works [5, 6, 9, 10, 42-44, 104] analyse variables such as stress field and its geometrical dependence, the stress intensity factor for the fracture process and the

correlation between adhesive joint performance and the adhesive and substrate behaviour, encompassing thermal, mechanical and chemical parameters.

This technique is suitable for bonding many different materials [19, 21, 22, 28, 32, 34, 36, 40, 41, 105], but its true power lies in its unrivalled capability to join dissimilar materials. In many of these applications, one of the two materials to be bonded is often a polymer or a fibre-reinforced polymer composite.

At its most basic form, the adhesive bonding technique consists in joining two materials (the substrates) to form the joint, using a fixing material called the adhesive. The adhesive is usually applied between the two substrates in an uncured liquid form or paste form and is later polymerised into a solid final product. It can also be applied in solid form, melted to create the joint and then cooled down to create a solid connection. Both methods may use pressure to create a better quality, defect-free connection. There are many different types of joint geometries available to assess the strength of an adhesive connection or the strength of the adhesive itself. Figure 7 illustrates examples of some of the most commonly used geometries.

Although highly advantageous for many applications, adhesive bonding of polymeric substrates is notoriously complex, as the surface energy of polymers is quite low. As modern adhesives are also mostly polymeric in nature, they exhibit a low level of surface energy and this almost inevitably leads to low adhesion at the adhesive-polymer interface [7]. It is thus necessary to avoid this issue with the application of suitable surface treatments. These treatments can be passive or active in nature. While the first just modify the morphology of the substrate's surface, active treatments effectively change the chemistry of the substrate, greatly enhancing its surface energy. The work of Ebnesejad et al. [106] details types of surface preparation techniques for polymer adhesive joints.

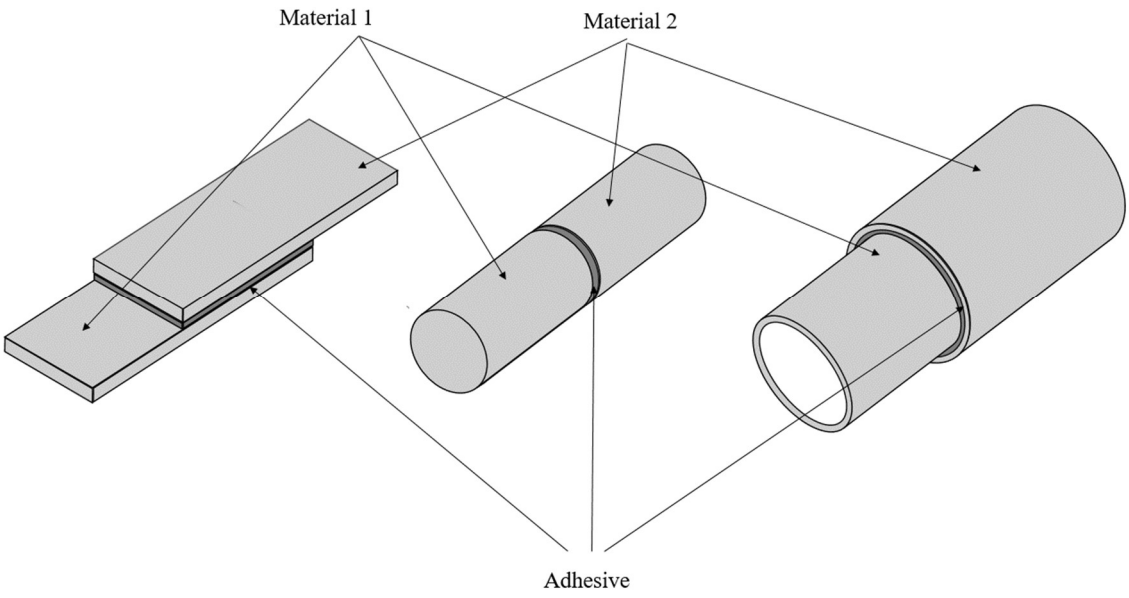


Figure 7 - Examples of specimens used for testing the performance of adhesive joints: single lap shear joint (SLJ), tube butt joint and tube lap shear joint adapted from [107].

Molitor et al. [108] and Sabreen et al. [109] studied the effect of different types of surface treatments for bonding titanium and polymers. The prevalence of treatments that oxidize the surface of the material is observed, with most effective using corona discharge, plasma, flames and laser energy. Zhang et al. [110] report that the effectiveness of the surface treatment for bonding polymers based on corona discharge is proportional to the exposure time. It is also specified that the resting time after the discharge is made on the corona surface is inversely proportional to the effectiveness of the joint strength. Necasova et al. [111] studied the joining of polyurethane with wood for different types of surface treatments. This included plasma, chemical etching (NaOH based) and sandblasting as well as the addition of a of the primer coating to support these treatments. In this work it is reported that regardless of the treatments, the addition of the primer coating enhances the joint resistance. It is also observed that the physical based treatment provides better results than the chemical treatments. Bukhari et al. [112] pointed out that physical-chemical interactions directly interfere in the effectiveness of adhesive joints, specifying the mechanical locking models and their failure modes, the theory of adhesion explaining the theories of adsorption, diffusion, electronic and electrostatic force, chemical bonding and weak forces, wettability, and surface energy. For cases where even after the surface treatment the surface energy of polymeric substrates is still too low to allow bonding with adhesives, Jin et al [113] propose the use of "tetrapodal ZnO linkers". This technique introduces fixing particles on the surfaces of the two materials, generating an interlock between

the two surfaces. The working principle of this technique is illustrated in Figure *8*-a. Experimental testing has shown this to be a very effective solution to increase the peel strength of bonded joints with polymeric substrates (Figure *8*-b).

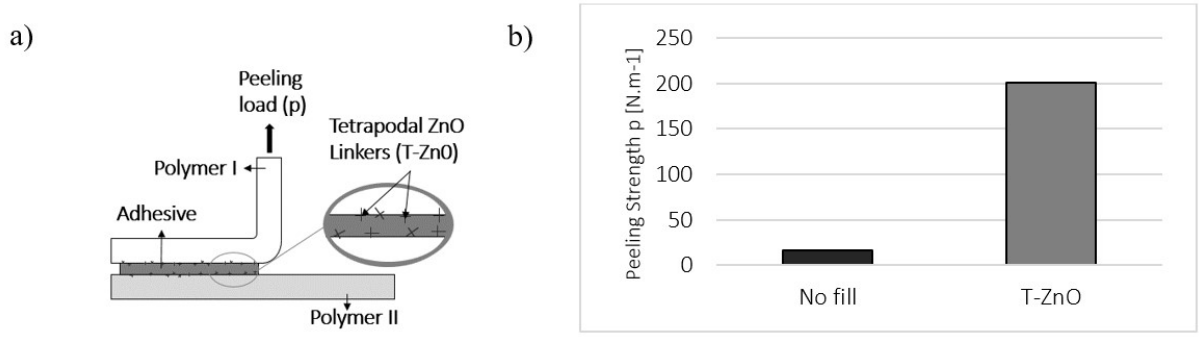


Figure 8 - a) Application diagram of T-ZnO at the substrate-adhesive interface. b) Comparison of the joint peeling strength without and with the T-ZnO filling. Adapted from [113].

Irrespective of the type of substrate being bonded, be it metallic, composite or polymeric in nature, proper adhesive joint design is crucial to ensure maximum adhesive joint performance. To aid in this design phase, modelling is often employed, allowing to precisely determine the geometry and the materials which can most efficiently withstand the service loads and conditions. The first approaches for predicting adhesive joint behaviour were based on analytical models, which although limited in scope are quite powerful and fast to use as described by da Silva et al. in a detailed review of these methods [114]. Presently, numerical modelling has become the favoured design methodology for predicting the performance of bonded joints, as it allows for the analysis of highly complex models. Numerical modelling can employ continuum mechanics and simpler stress analysis or it can make use of cohesive zone modelling, which combine continuum mechanics with fracture mechanics, reproducing the onset of damage and its propagation through the adhesive joint [115].

Many research works generate models for the mechanical response of simple specimens used to characterize an adhesive, with the objective of using this data for more complex joint models at a later stage. For example, Braga et al.[116] characterized the behaviour of double cantilever beam (DCB) specimens bonded with an epoxy adhesive using cohesive zone modelling. The results were found to agree with those experimentally obtained, employing a 2D model constructed with a combination in stress plane and cohesive elements, as shown in Figure *9*.

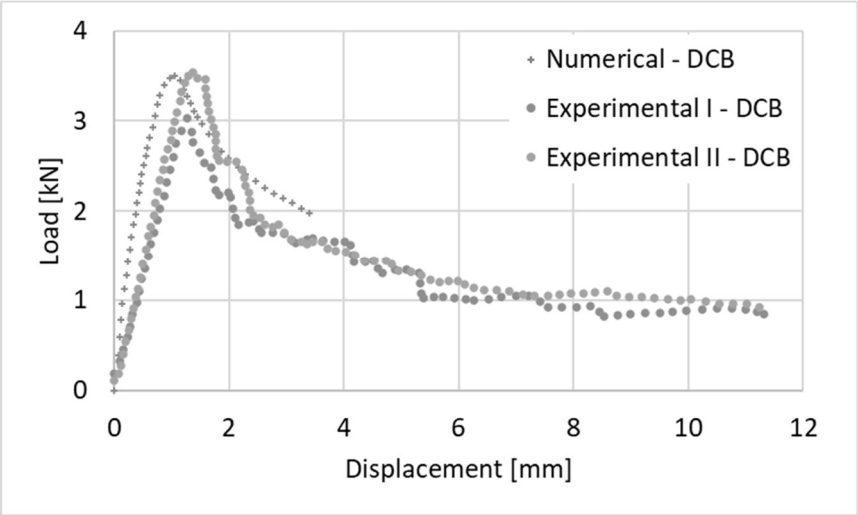


Figure 9 - Load vs. displacement of experimental DCB testing and FEM model. Adapted from [116].

Numerical modelling is also suitable for precisely determining the influence of geometrical parameters on the behaviour of bonded joints. The work of Adams et al. pioneered this approach by studying different effects such as the influence of the spew fillet in the ends of the adhesive layer and the adhesive layer thickness [117, 118]. da Silva et al followed with a detailed experimental study devoted solely to the analysis of the adhesive layer thickness in SLJs [119], stating that the lap shear strength increases as the bond line gets thinner and the adhesive gets tougher. More recently, the work of Silva et al. [16], numerically modelled the behaviour of scarf joints, using three different adhesives formulations and varying the scarf angle. These models employ the cohesive zone model formulation, using three different cohesive zone law shapes. The triangular, trapezoidal and linear-exponential formulation are used, and it is found that for each adhesive formulation there is a specific cohesive law shape that better fits the experimental results. Oliveira et al. [120] carried out several experiments in SLJs, bonded with five different adhesive layer thickness and also determined the corresponding fracture toughness in mode I or mode II using DCB and ENF testing of the adhesive. The results of this work are summarized in Figure *10*-a and Figure *10*-b.

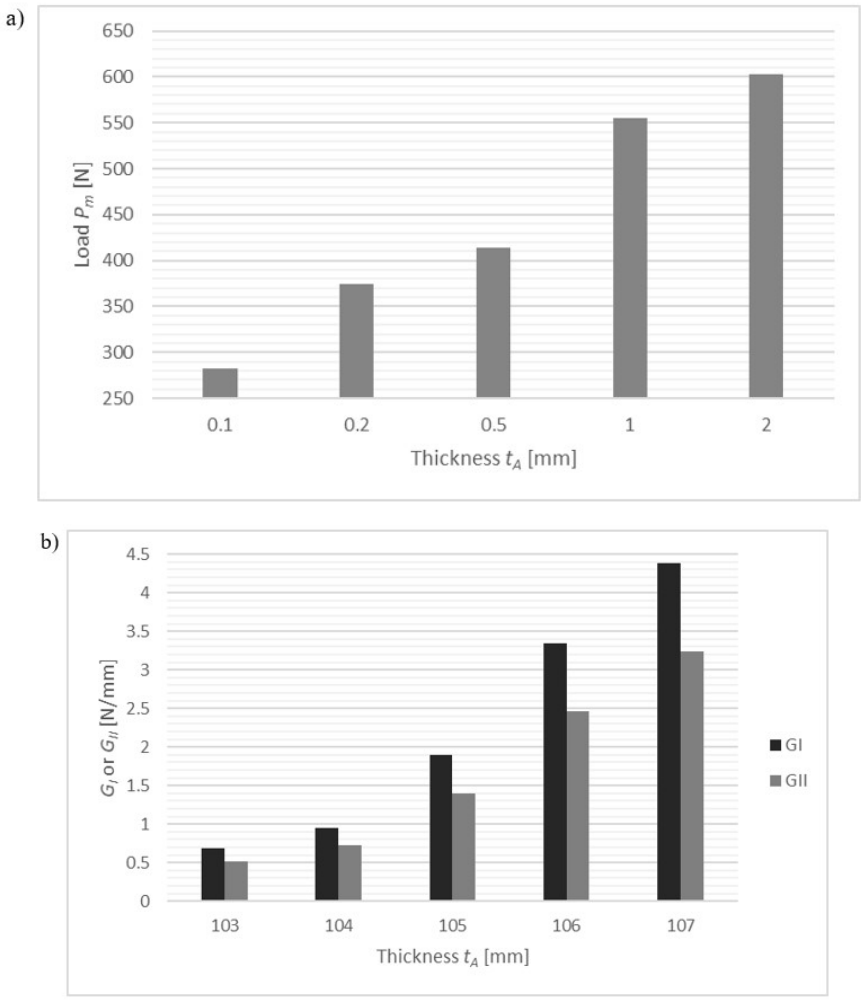


Figure 10 - a) Average of Load - Pm for each adhesive thickness - tA, b) Energy release rate for mode I - G_I, and mode II - G_{II} to each tA by the compliance-based beam method (CBBM) adapted from [120]

The results show that for this specific joint configuration, a greater load capacity is obtained for larger adhesive thicknesses. As for the G_I and G_{II}, a linear increase was found with the increase of the studied thicknesses up to the value of 1 mm. In search for a deeper understanding of the influence of the thickness of the adhesive in the performance of a bonded joint, Sadeghi et al. [121] proposed different numerical methods to characterize the behaviour of bonded joints with adhesive layer thicknesses of 0.2 and 0.9. The analysis is performed in a SLJs, using an epoxy adhesive and steel as an adherent material. The models under comparison are cohesive zone modelling, surface-based cohesive model (SBCM), the virtual crack closure technique (VCCT) and the extended finite element method (XFEM). In general, the results show that all techniques can obtain reasonable correlation between the experimental and the numerical results and can capture well the effect of adhesive layer thickness. However, there

are varied specificities for each of these methods which requires a critical analysis of their capabilities and limitations in the selection of the most suitable method for each case.

One of the main factors influencing the performance of bonded joints is the interaction between the mechanical behaviour of the substrate and the adhesive and this especially true when polymeric substrates are used. Pérez et al. [122]carried out a study on two pairs of polymeric substrates (PTFE and PVT), bonded with five different types of adhesives. One of the adhesives is biomimetic, based on 3,4-dihydroxyphenylalanine (DOPA) found in shellfish, the second is based on the same biomimetic adhesive but with the addition of a periodate (IO4), used to increase the adhesion of the adhesive (DOPA + IO4). Finally, three other synthetic artificial adhesives were considered, and these are polyvinyl acetate (PVA), cyanoacrylate (CNA) and epoxy. The results are shown in Figure *11*.

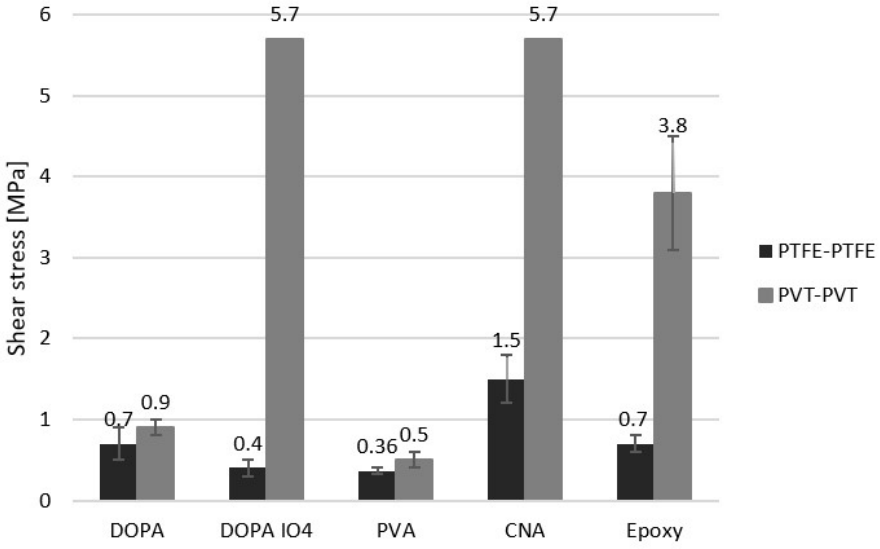


Figure 11 - Maximum shear stress sustained by PTFE-PTFE and PVT-PVT joined with different adhesives adapted from [122]

For the DOPA-IO4 and CNA adhesives applied to the PVT substrate maximum load was of 5.7 MPa because the failure was always cohesive in the substrate. For the PTFE substrate, the best performing adhesive is the CNA, due to the higher number of cross-links it creates. When bonding PVT, besides the crosslinking relationship of the NAC, there is also a higher interrelation between the forces of the molecules at the interface, simultaneously increasing the adhesion and cohesion. This adhesive and cohesive effect is also pronounced for the other adhesives in PVT. In conclusion, the interface strength is highly dependent on the adhesion and cohesion levels. In another configuration, Hsiao et al [123] studied the application of multiwalled carbon nanotubes - MCNT in the adhesive. This was carried out to reinforce an

epoxy adhesive shear strength in SLJs using graphite composite substrates. The study was done with the addition of 1 and 5% of MCNT, compared with the performance of neat epoxies. The increase in shear stress in response to the addition of 1 and 5%, when compared to the adhesive without MCNT, is 31.2 and 45.6% respectively, showing this to be an effective method to increase joint strength.

In the automotive industry, adhesives are finding greater and greater use for the construction of vehicle bodies. In this specific application, the impact behaviour of the adhesive and the joints it forms is crucial to ensure occupant safety in the event of a collision[16, 18, 124] An example of a work in field is the study made by Machado et al [17] which models the quasi-static and impact behaviour of single lap joints with composite and aluminium substrates, bonded with a high performance crash resistant adhesive. The proposed cohesive zone model for impact uses material data which has been determined at high strain rates and good agreement is reached between experimental and numerical results.

The behaviour of adhesively bonded joints under harsh environmental conditions has been the target of several studies. [125, 126]. As stated by Borges et al. [127] this is a critical subject for the design of bonded polymeric components, as these materials absorb water which can migrate into the adhesive-substrate interface and dimmish joint strength and cause adhesive failure. Banea el al.[125] conducted a study to characterize mechanical properties such as the Young's modulus and failure stress in adhesives subjected to ageing by moisture uptake and reinforced with thermally expandable particles (TEPs). The results are summarized in Figure *12*.

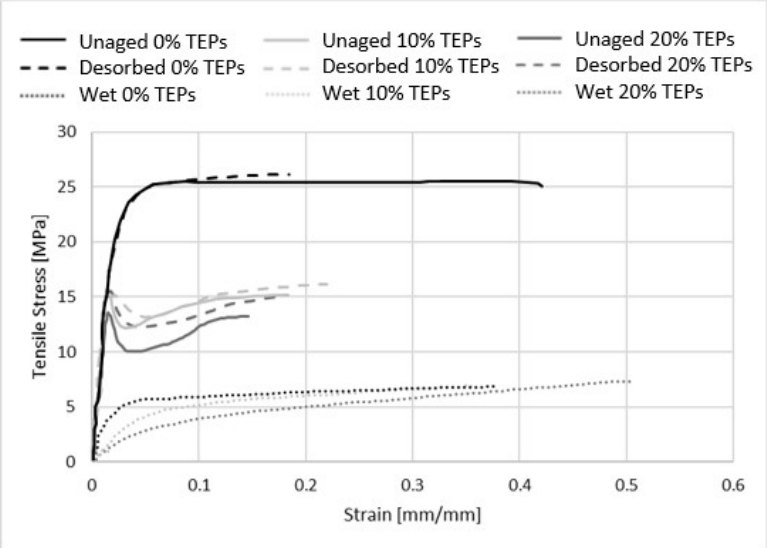


Figure 12 - Representative stress–strain curves of the TEPs-modified adhesive as a function of moisture adapted [125].

It is observed that the modulus of elasticity is affected by the increased TEP content only in aged materials. Fatigue testing was also carried, and reduction of the fatigue life was also found with an increase in TEP content. Sugiman et al, [128] has used numerical modelling to analyse the behaviour of monolithic single lap joint (MSLJ) and laminated double in bending (LDB) joints, bonded with a film adhesive and tested under natural and aged conditions (one year and two years). Their methodology allows the models to consider the degradation of the material properties due to ageing. Figure *13* illustrate the relationship of the maximum error between the experimental and the FEM study.

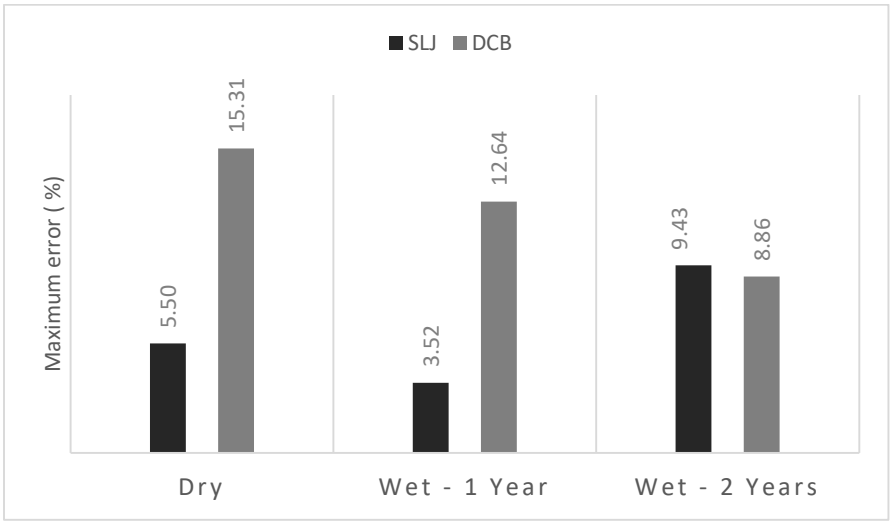


Figure 13 - Comparison of the error between the experimental and numerical results, adapted from [128].

The numerical model can precisely reproduce the experimental fracture process for the LDB test. Showing that it occurs in in the adhesive fillet formed at the ends of the overlap and at an of 45º relative to the load direction, as shown in Figure *14*.

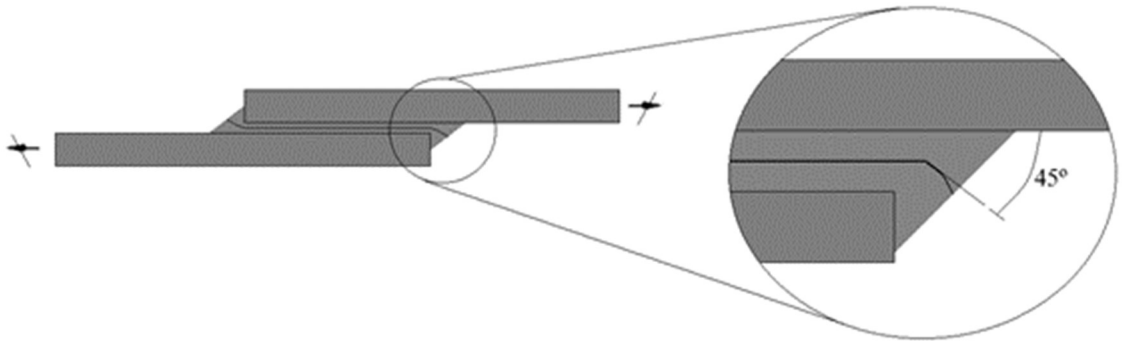


Figure 14 - The static failure characteristic of fillets in SLJ adapted from [128].

Although adhesively bonded structures perform better under fatigue loads than other joining methods, such as fastening and welding, adhesive joints are still susceptible to fatigue

failure and this has been the target of many studies, both experimental and numerical. The work of Rocha et al. [129] is an example of how numerical modelling can be employed to predict the fatigue behaviour of and adhesively bonded joints. In this case, a fatigue crack growth analysis is carried out with a model based on cohesive zone mode (CZM), with triangular cohesive laws. DCB and ENF joints (mode I and mode II) were simulated with Abaqus using a User material subroutine (UMAT) to reproduce the fatigue behaviour of the adhesive. A Paris law-based approach was employed using experimentally obtained adhesive fatigue crack data growth data. The accuracy of the model can be assessed by comparing the predicted number of cycles to failure and by comparing experimental and numerical compliance curves as shown in Figure *15*.

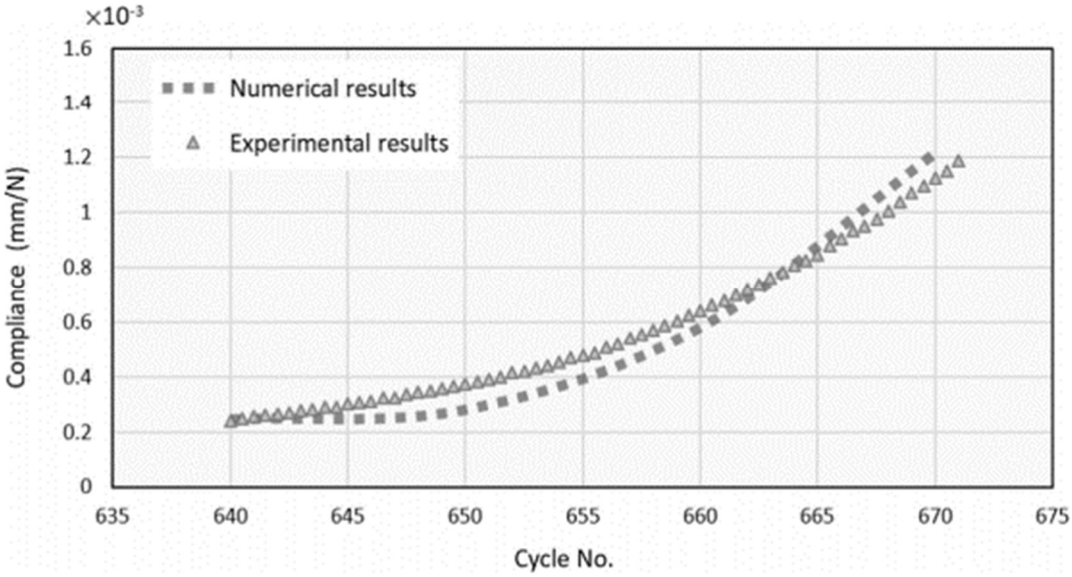


Figure 15 - Compliance as a function of load cycles: Comparison between the numerical data and the experimental results adapted from [129].

Other works [30, 130, 131] have studied the fatigue crack growth in adhesives in order to generate a Paris law. These works have included several different structural adhesives and indicate that greater load amplitudes lead to a faster crack propagation, shortening the service life.

As a summary of this section, it can be stated that adhesive joining is a very powerful technique, suitable to join a wide range of materials, including polymers. However, the specific case of polymer joining requires special attention to be devoted to the surface preparation and many researchers have demonstrated the effectiveness of several surface treatment techniques. It has also been shown that proper geometrical design of a joint can be supported with finite element modelling. Lastly, the degradation of the performance of adhesives under service

conditions, such as high humidity environments and fatigue loads, must also be taken into account in the design phase.

4 EXPERIMENTAL METHODS

In the initial phase of the work, experimental testing was carried out with the objective to characterise the materials to be used throughout the project and determine the base-line mechanical performance of joints made by laser welding and adhesive bonding. In this phase, the characterization of the 'as supplied' properties of PBT-GF30 as substrate were completed as well as those resulting from exposure to the heat generated during laser welding (thermal treatments were performed at three high temperatures). Mechanical, thermal, optical and morphological properties were the target of this study. An analysis of specific process parameters was also carried out for the laser welding method. This study was carried out manually, through a spot-welding procedure using individual laser pulses. This enabled a more precise control of parameters such as power, pulse time (in a rectangular pulse shape), diameter of the laser pulse, region of incidence of the laser in the joint and inclination of the laser in the joint.

Once the spot laser welding process was deemed as optimized, a reference adhesively bonded joint was made, with dimensions and performance close to that of the joint achieved using a laser process, allowing to compare processes. The adhesive used to create the adhesive joint is silicone-based and most of its mechanical properties were already determined in previous works of the research group.

4.1 CHARACTERIZATION OF THE BASE MATERIAL

The PBT-GF30 thermoplastic used in this work is a commercial product, supplied by BASF (Ludwigshafen, Germany), also characterized as BASF ULTRADUR B4520. It is an injection moulding grade material, reinforced with 30% of glass fibres in weight [132]. Its Poisson coefficient is 0.45, its expansion coefficient is 2.4x10-5 K^{-1}. It has a thermal conductivity of 0.288 W/m.K, thermal capacity of 1600 J/kg.K and its melting temperature is of 225°C, according to Jasen [133]. According to Koppl [134] the energy absorption capability under impact is 65 kJ/m^2. The density has been determined to be 1525 kg/m^3 by several authors [132, 133, 135-137].

4.1.1 THERMAL TREATMENT OF PBT-GF30

To accurately determine the mechanical properties of the PBT-GF30 material that is located in the weld bead and the heat affected zone during a laser welding process, an experimental procedure was devised where the material is submitted to precisely controlled

heat treatments in a closed chamber. The PBT-GF30 material was supplied in pre-cut sheets of 80 x 80 x 2 mm. To ensure that the PBT-GF30 sheets do not deform during the heat treatment, these were placed inside a steel mould, pressed with a load of 8 kg. A 2 mm thick nylon plate was used to control both the shape and the thickness of the samples, as shown in Figure 16.

Three different heat treatment temperatures were considered, as shown in Table 3, with the oven being controlled to ensure that that material is staged at its target temperature for a period of 10 minutes. The staging temperature was directly controlled with a K-type thermocouple inserted into the mould and in contact with the PBT-GF30 material. After the heat treatment stage was completed, the material was naturally cooled down to room temperature.

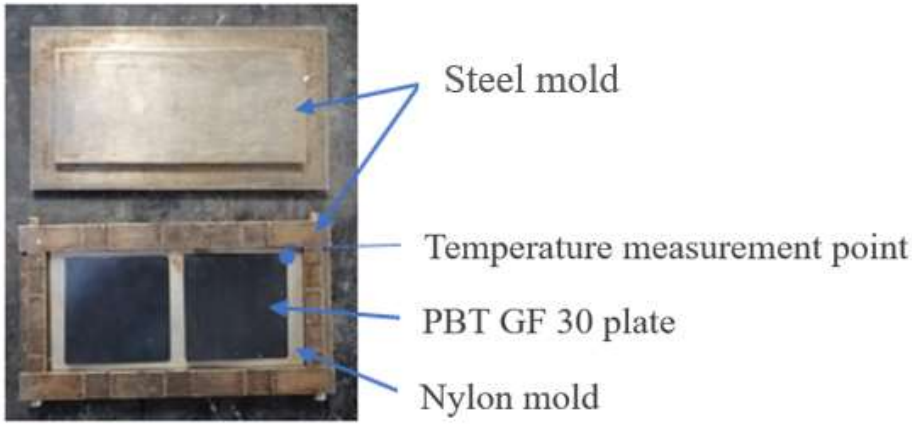


Figure 16 - Detail of the mould used for heat treatment.

The heat treatment temperatures under analysis include the melting temperature of the material (225°C) [133], the end point of melting transition of the DSC curve, (237°C) and finally a temperature of 257°C, slightly before the expected temperature of thermal degradation of the material.

Table 3 - Staging temperatures and stage durations used for heat treatment.

Staging temperature	Stage duration
225°C	60 min
237°C	70 min
257°C	95 min

4.1.2 OPTICAL PROPERTIES

To characterize the response of PBT-GF30 to laser radiation, FTIR spectroscopy was performed, allowing to determine the material's transmissivity and absorbance, in a range of 500 nm to 1100 nm, which includes wavelengths typical of laser equipment suitable for joining

thermoplastics such as PBT-GF30. The analysed specimen has the dimensions of 10 x 20 x 1 mm and is of a dark, almost black colour, a characteristic favourable to the absorption of light in these wavelengths. With reference to the work performed by Frick [138], after performing the test for characterization of transmittance, the Beer-Lambert's law was used to calculate the absorbance of the material at a wavelength of 1064 nm.

4.1.3 THERMAL PROPERTIES

Based on the work performed by Khosravi [139] to characterize the thermal properties of the adhesive, such as the level of polymerization in the material, the melting point and temperature of degradation, DSC testing of PBT-GF30 was performed. The test was carried out in a NETZSCH DSC 214 Polyma DSC21400-0655-L device in the range of -20°C to 300°C, with a heating ramp of 10K/min, in an N_2 medium.

4.1.4 MORPHOLOGICAL ANALYSIS

Based on work described in the literature [134, 136, 140], the morphology of PBT-GF30 was generally characterized by the matrix of polybutylene terephthalate with undirected glass fibres, with diameters of 10-12 μm. The PBT-GF30 used in this work (both in the supplied state and the heat-treated state) was morphologically characterized via optical microscopy. Concurrently, a macro analysis of the surface of the materials under study was also carried out, comparing their key characteristics.

4.1.5 TENSILE TEST

The mechanical properties of PBT GF 30PBT-GF30 were characterized using three different methodologies, allowing to determine the tensile strength, hardness and fracture toughness of the material in the received and the heat-treated states. Tensile testing was carried out in an INSTRON® (Norwood, Massachusetts, EUA) 3367 universal testing machine, using an extensometer for the strain measurement. The properties directly obtained in this test were the maximum stress and the maximum deformation of the material. The modulus of elasticity was calculated from the stress-strain curves, following the ASTM D638 -14 [141] standard.

The tensile specimen dimensions were based on the BS 2782 [142] standard. The specimens for PBT-GF30 in the as received state had different dimensions from those subjected to a heat treatment process. This was mainly due to the dimensional constraints of the mould and the ovens used for heat treatment, which forced a reduction in size. Figure 17-a shows the

dimensions of the tensile specimens of PBT-GF30 in the as received state and Figure 17-b shows the dimensions of the tensile test specimens that were subjected to heat-treatment.

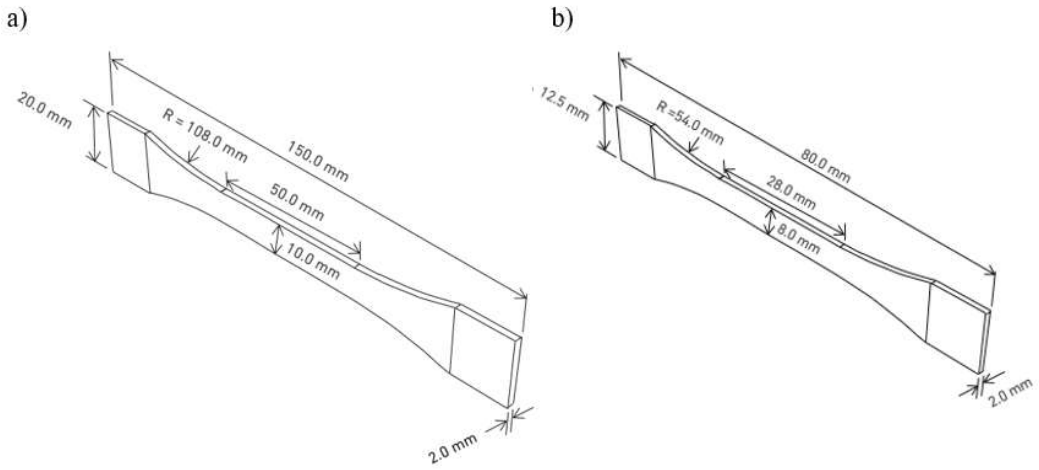


Figure 17 - Geometry of the dog-bone tensile test specimens. (A) PBTGF30 in as supplied state. (B) PBT GF 30 heat treated state.

The PBT-GF30 samples in the as received condition were supplied as pre-moulded plates which, after machining, led to a tensile test specimen length that was below the recommendation of the BS 2782 standards, as shown in Figure 18-a and Figure 18-b. However, no interference was expected to occur with the results, since the specimens were clamped in the universal testing in the same position and the strain was measured in the central region of the specimen using a 25 mm extensometer. Three specimens were tested for each condition of PBT-GF30.

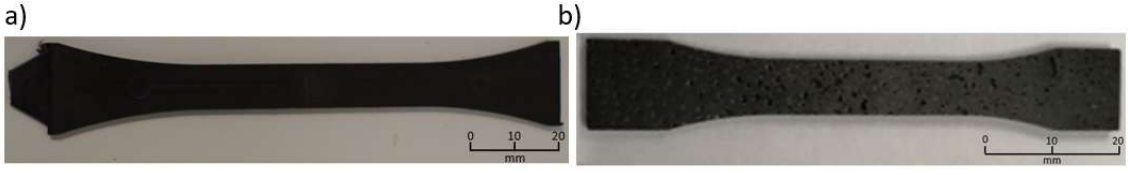


Figure 18 - Machined tensile testing specimens. a) PBT-GF30 in as supplied state. b) PBT-GF30 heat treated state at 257°C.

4.1.6 HARDNESS TESTING

The second test characterized the hardness of the PBT-GF30 using a Shore D type durometer, model SAUTER (Balingen, Germany) HBO 100-0. The hardness was measured for material in the as supplied state and following the three different heat-treatment temperatures. A total of 10 indentations were made for each of these four states.

4.1.7 FRACTURE TOUGHNESS TESTING

The compact test (CT) configuration, as described on ASTM D5045 – 14 [143] was considered for the determination of the fracture toughness of the PBT-GF30 material. However, considering that the sample thicknesses of 2 mm used were not within the requirement of the standard for characterization in the plane state of deformation, the standard was used to determine the stress intensity factor for the PBT-GF30 material in the supplied and the heat-treated state. Figure 19-a shows the dimensions of the CT specimen used, while Figure 19-b presents an image of a representative specimen after the notch was machined by a 2 mm cutting disc, with a 60° tip angle and a radius of 0.1 mm. A paper scale was bonded to the specimen to serve as a reference of the measurement of crack propagation.

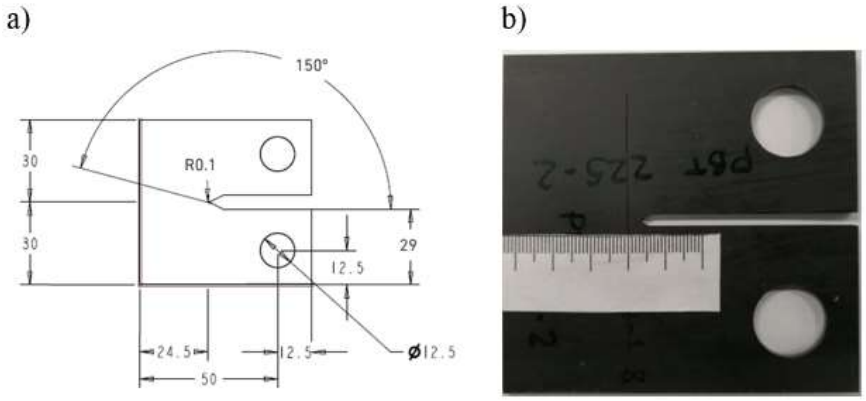


Figure 19 a) Compact tension sample dimensions (in mm). b) Manufactured sample of compact test.

For crack nucleation, the tapping method was used, using a shaving blade, as cited in [144]. Figure 20-a illustrates the notch in the CT specimen caused by the shaving blade and Figure 20-b shows the notch with the nucleated crack.

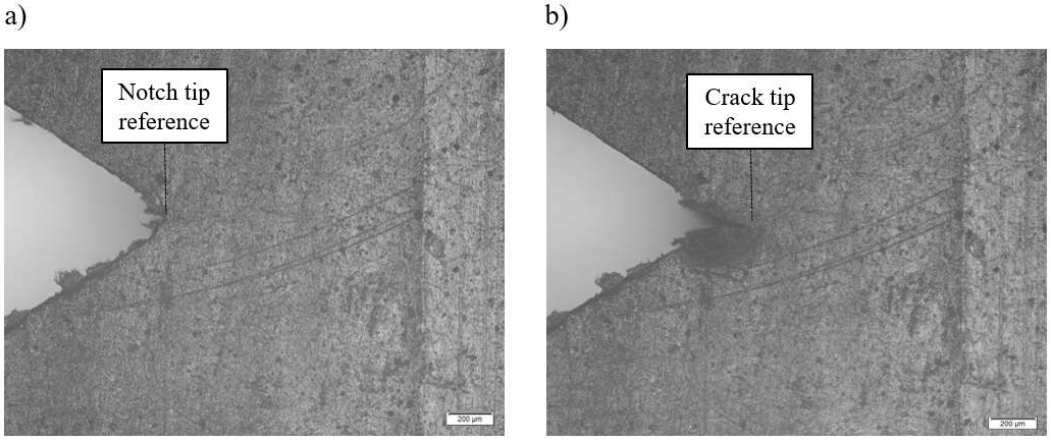


Figure 20 - Representation of the a) pre and b) post crack specimen.

Figure 20 shows the initial notch sizes, the crack nucleation length resulting from the tapping method, the effective length and the thickness of the specimens and the results of the

function f(x) used for calibration by the standard, considering the sum of the notch and the nucleated crack size and the effective length of the specimens.

Table 4 Parameters of the compact test specimens for all PBT-GF30 conditions tested.

Specimens	Load (N)	Total crack (mm)	Notch size (mm)	Nucleated crack (mm)	Width (mm)	Thickness (mm)	T/W	f(x)
As received	260.00	24.85	23.3	1.55	52.6	2	0.47	8.8933
	265.65	24.5	23.4	1.1	52.6	2	0.47	8.7231
	298.86	25.7	24	1.7	52.5	2	0.49	9.3557
Treated at 225°C	206.00	26	24	2	51.9	2.2	0.50	9.6878
	179.65	26.19	24.8	1.39	51.9	2.2	0.50	9.7982
	194.00	28.72	24.5	4.22	52.2	2.15	0.55	11.3718
Treated at 237°C	162.00	25.78	24	1.78	51	2	0.51	9.8246
	156.30	26.6	23.3	3.3	52.2	2.1	0.51	9.9510
	178.62	24.2	23	1.2	51.5	2.1	0.47	8.8279
Treated at 257°C	122.86	28.9	23.4	5.5	52.7	1.9	0.55	11.3015
	100.80	28.3	23.3	5	52.1	2	0.54	11.1029
	137.00	28.15	23.5	4.65	52	2	0.54	11.0341

In order to measure crack propagation, a digital camera was used to capture images every 5 seconds during the CT test. These images were synchronized with the universal testing machine data, allowing them to be correlated with the force and displacement curves.

4.2 CHARACTERIZATION OF THE ADHESIVE

The adhesive used in the adhesive joints for the purpose of comparing the joining processes was a silicone adhesive, supplied as a flowable two-part addition curing silicone rubber, which is commercially available. The main characteristics of this adhesive after curing are medium hardness, ability to bond a wide variety of substrates, heat resistance and long-term stability. The manufacturer suggests an adhesive/catalyst ratio of 10:1 and a cure at room temperature for two weeks. In this work, these values were adjusted to match those used in the productive process at the company of interest. The adhesive/catalyst ratio used was 1:1, the mixture was achieved using a centrifugal mixer and curing took place at 120 ◦C for 25 minutes.

4.2.1 THICK ADHEREND SHEAR TEST

The thick adherend shear test (TAST) was used in order to measure the shear properties of the adhesives according to standard ISO 11003-2:1993 [145]. The machine used to test was the same machine used to tensile test and fracture toughness test of the PBT-GF30.

4.2.2 TENSILE TESTING

The tensile test used to characterize the silicone adhesive followed the BS 5214 standard[146]. The universal tensile testing machine was also used to carry out this test.

4.3 JOINT LEVEL TESTING

Following the completion of the of the PBT-GF30 and the adhesive characterization, an experimental study of the laser welding process was started, using laser welding equipment available in the laboratories of the Advanced Joining Processes Unit. The initial part of this study focused on the process of joining overlapped joints with a fillet, created using a manually controlled laser spot-welding process. This activity aimed to characterize the process and define the static parameters of the laser welding equipment. Concurrently, the design of a special feed table was also initiated, in order to allow for a more detailed parameterization of the pulse frequency and advance rate.

The comparison process between laser-welded joints and adhesively bonded joints was also started at this stage, using a commercially available two-part silicone elastomer adhesive cured by addition. Parameters such as the overlap length and the adhesive layer thickness were studied and adjusted in order to achieve a comparable performance to laser welding.

4.3.1 WELDED FILLET LAP JOINTS

For the initial characterisation and parameterisation of the laser welding procedure, a study of the machine's static parameters was initiated, determining input settings such as a pick power, pulse time and laser beam diameter. The inclination of the sample and the influence of the laser incidence position were also studied.

The machine used in the process to make the welded joint was a SISMA LM-D 180, with a Nd:Yag 1064 nm laser, and a maximum laser power of 80 W, shown in Figure 21.



Figure 21 - Spot laser welding machine.

In accordance with the recommendations of the laser welding equipment, the baseline configuration for laser welding was a lens-to-incidence-point distance of 70 mm, maintaining the microscope focus at this distance. A peak power of 36 W, a rectangular pulse time of 1.5 ms, was also initially applied, manually ensuring that the point-to-point frequency remained below 1 Hz, as shown in Figure 22. The forward movement was executed based on the diameter measured by the machine's laser microscope itself.

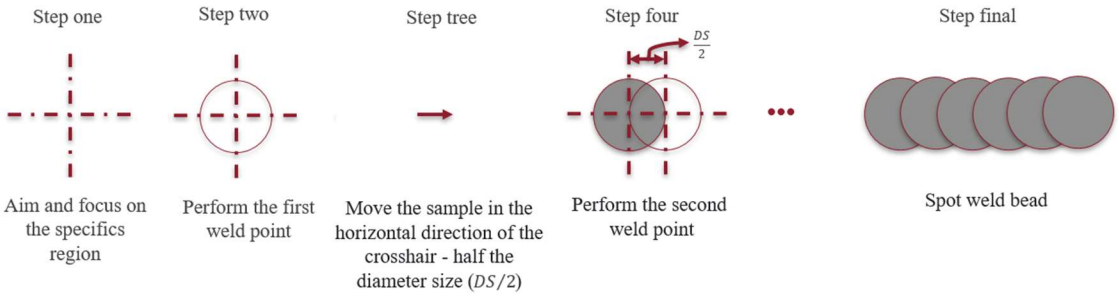


Figure 22 - Step-by-step procedures used for the determining the advance on the spot weld bead.

Taking as a basis the study made by Berger (2015) [187], the samples were initially fixed at 45° relative to the laser direction. Considering that the laser pulse is very short and localized and that its action, which can occur through heat conduction across the material, may vary significantly depending on the weld location and its melting mode, in other words, conduction-limited welding or keyhole—a study was conducted on the position of laser beam incidence. Three different laser incidence positions were considered for analysis. The first position was on the upper edge of the overlapped plate (US), the second position was in the middle of the thickness of the upper plate (MS), and the third position was at the interface between the two plates (DS), welding both sides of the joint without adding material, as shown in Figure 23. The eyepiece of the laser welding machine has a crosshair which is superimposed on the sample and allows for precise aiming of the laser incidence point.

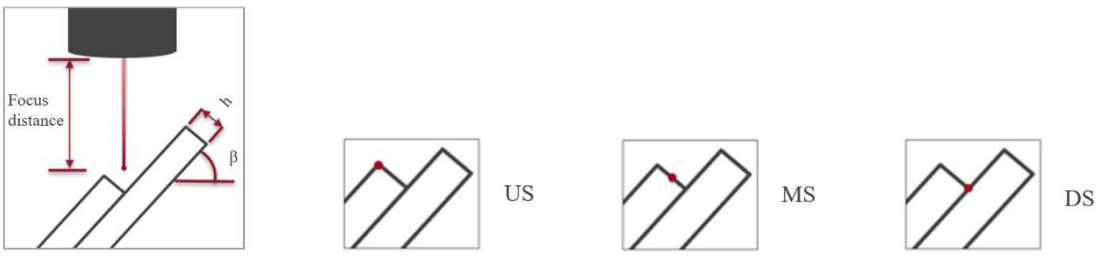


Figure 23 - Scheme of sample inclination angle, showing the laser beam and the laser incidence positions on the samples.

In this approach, the beam diameter was also varied, changing the way the laser energy is distributed over the weld. Four different values were selected 0.5, 1.0, 1.5 and 2.0 mm.

4.3.1.1 MACROSCOPIC ANALYSIS OF THE WELDED REGIONS

An initial macroscopy analysis of the laser welded regions was carried out using a NIKON D5300 digital camera adapted to the eyepiece of the laser welding machine. Individual pictures were taken of the laser welding points, representative each position of laser incidence (US, MS and DS) and each beam diameter under consideration (0.5, 1.0, 1.5 and 2.0 mm).

A microscopic analysis was carried out to characterize a transverse section of the welded region, allowing to determine the depth and penetration of the weld, defects such as underbite, the geometric profile of the surface and the actual spacing between the plates.

For this analysis, laser welding was performed experimentally on 10x15x2 mm samples of PBT-GF30 material. Since the welding profile is small and may fracture with the large loads encountered during the grinding and polishing process, a notch was made in the surface of each rectangle, where on one side of the notch the material would be welded according to the pre-established parameters and on the other side of the notch the plates were joined with a supporting adhesive, increasing the resistance of the joint and allowing for easier sanding of the cross section, as shown in Figure 24. The sanding process was carried out was done with emery paper of 220, 320, 800, 1200 and 4000 grain sizes and in water. After the grinding process was complete, the specimens were dried and analysed with an optical microscope (Carl Zeiss El-Einsatz HAL 100).

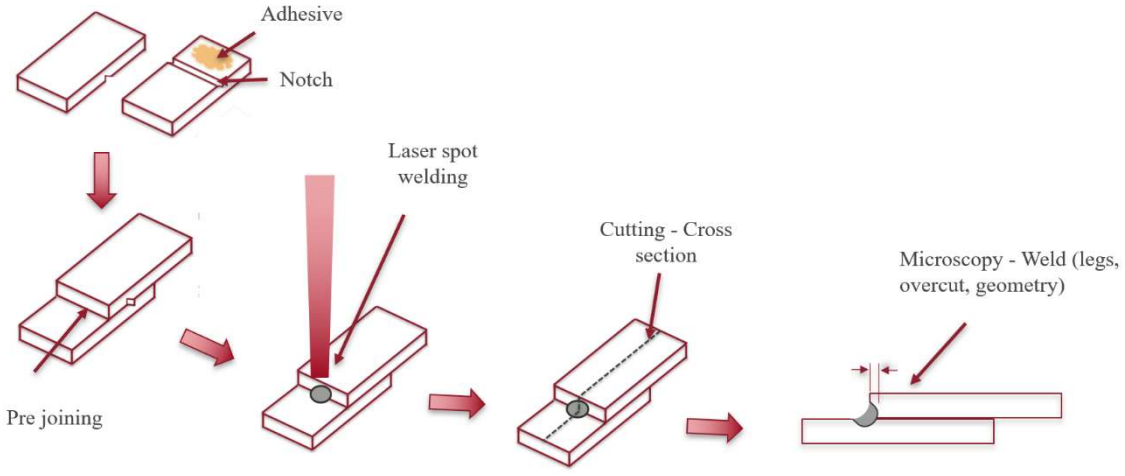


Figure 24 - Scheme of the procedures used for the analysis of the welded region with optical microscopy.

4.3.2 BONDED SINGLE LAP JOINTS

In order to allow for a comparison between the two different joining processes, two configurations of adhesive joints were designed this purpose. The first configuration, as shown in Figure 25-a, includes a free space between the plates of the substrate and has an adhesive

layer thickness of 0.05 mm, a value which is consistent with the minimal gap introduced during compared with the thickness used in the laser welding.

The second configuration, shown in Figure 25-b, used a thickness of 1 mm, which is often reported to be the optimal thickness for obtaining maximum performance with a silicone adhesive [147]. For both configurations, the overlap length can be adjusted to ensure mechanical performance which is consistent with that of the laser welded joint.

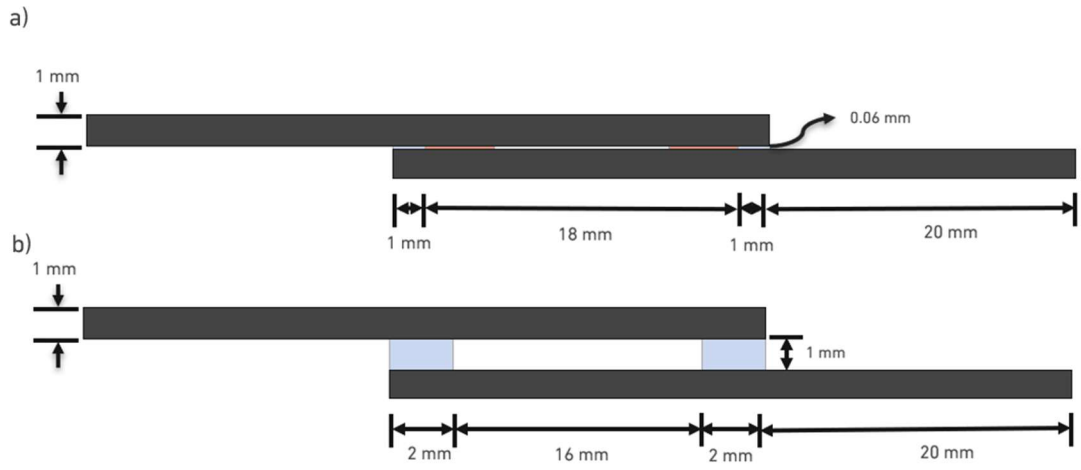


Figure 25 – a) Adhesive joint geometry with low thickness (0.06 mm). b) Adhesive joint geometry with reference thickness (1 mm).

The adhesive joints were manufactured with the assistance of rubber frames which included rectangular notches of 10 x 60 mm that allowed to manufacture three joints in each desired condition, as shown in Figure 26-a. To maintain parallelism, the rubber frames were assembled between thick aluminium plates. The curing process was assisted by a hot plate press, set to a pressure of 300 bar and a temperature of 120ºC for 25 minutes. After the curing process was completed, the specimens were allowed to cool down naturally until room temperature was reached. To control the spacing between the plates, a 0.06 mm Kapton tape was used for the first configuration (Figure 26-b), whereas a 1 mm thick rubber tape was used (Figure 26-c) for the thicker joints. For both configurations, 1 mm stainless steel tapes were used as spacers to compensate for joint thickness.

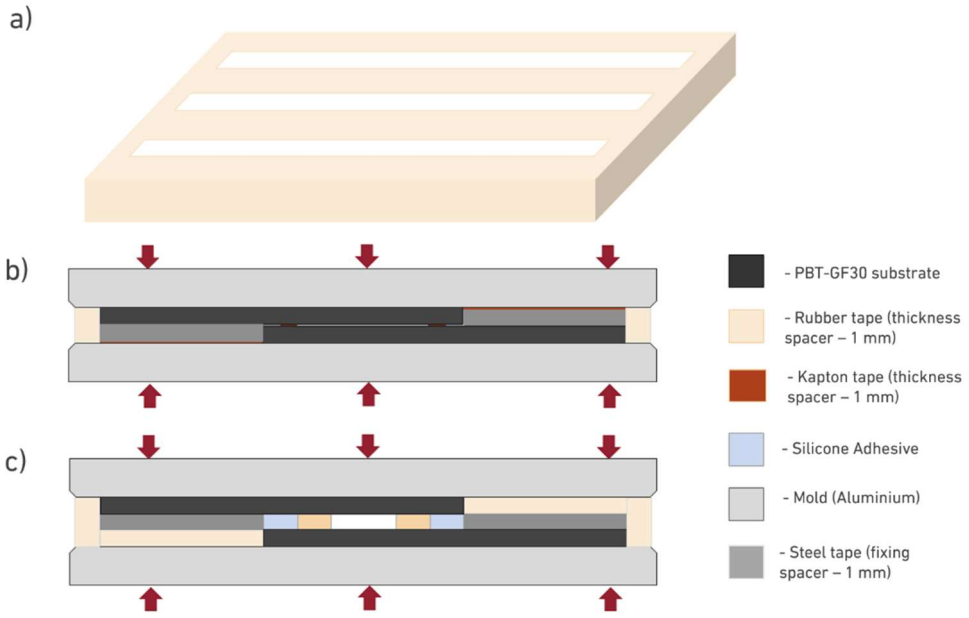


Figure 26 –a) Rubber frame configuration. b) Adhesive joint configuration with low thickness. c) Adhesive joint configuration with reference thickness.

4.3.3 COMPONENT LEVEL JOINT

In response to the specific requirements of a company that manufactures protective enclosures for automotive electrical circuits (Figure 27), tensile tests were performed joints consistent with those used in practical applications. This testing was carried out after optimizing the production process and conducting comparative tests on parallel joints, constructed from the same material as those found in this component.



Figure 27 - Actual component of the electrical circuit protective enclosure, illustrating the section that is used for testing

To optimize the testing process and accurately simulate potential failures in the actual component, a pair of test specimens were sectioned, preserving the original joint configuration.

This approach enabled the clamping of components during the welding process. Figure 28-a depicts the sectioned upper and lower elements of the protective enclosure. Figure 28-b illustrates the fixture apparatus utilized for the laser welding process.

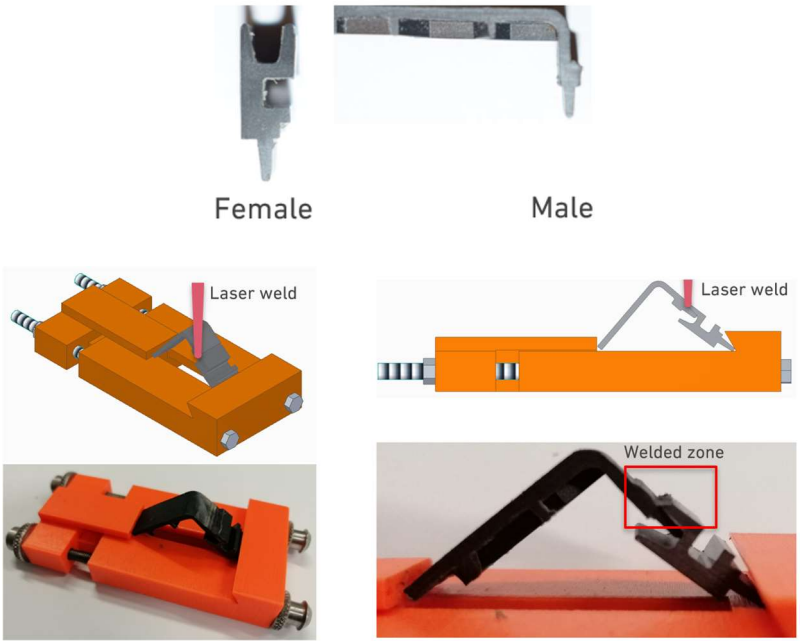


Figure 28 - a) Representation of the cross-sectional view of the actual joint samples, including both the female and male components. b) Mould for fixing parts for joining by spot laser beam welding.

To conduct the tensile joint testing, one component was bonded to a rectangular ABS block using structural adhesive. This allowed for secure clamping in the testing machine. A fixture mold was then clamped to the other component, also using structural adhesive. The alignment of the block and mold was ensured to be perpendicular, as illustrated in Figure 29.

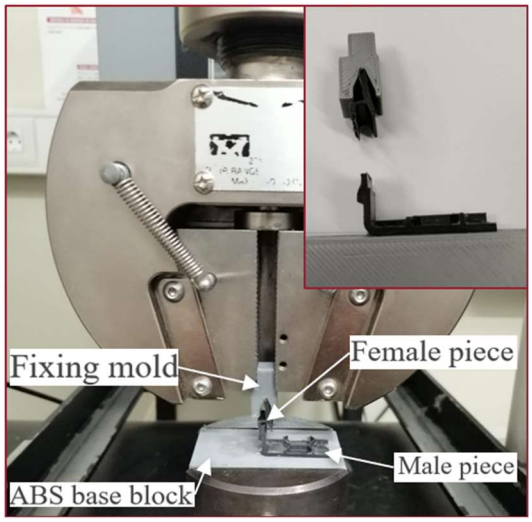


Figure 29 - Real joint test fixing configuration.

For the tensile testing, a universal testing machine, INSTRON® 3367, was used. The tensile specimens were tested at a displacement rate of 1 mm/min, consistent with the tensile tests mentioned in previous chapters. For displacement measurement, digital image correlation (DIC) method was used, following the studies conducted by Borges et al. (2020) [148], using the GOM Correlate Pro software the displacement was recorded.

To gain a deeper understanding of the welded region and to examine how material properties vary with thermal gradient - particularly in relation to mechanical properties - an analysis was conducted using a micro-Raman spectrometer. This test qualitatively compares the region along the autogenous weld performed on the thermally affected PBT-GF30 and identifies the phase boundary regions. In addition to demonstrating the differences in material properties in the welded region, this analysis provides data to optimize the simulation of the actual joint.

5 NUMERICAL MODELLING

The numerical models created in this work rely on material models which are based on mechanical characterization test data, including the temperature dependent properties of the PBT-GF30 substrate and mechanical properties of the silicone adhesive used in the adhesive joints. In general, they are optimized elastoplastic models with damage models, either by ductile damage or cohesive damage. Joint models are initially validated against experimental testing data and then expanded for more complex joint geometries.

4.4 PROPERTY VALIDATION

To first validate the mechanical properties determined experimentally, a numerical model was developed, based on the mechanical characterization of PBT-GF30, utilizing an elastoplastic behaviour with ductile damage. For the silicone adhesive, the numerical model employed a hyperplastic behaviour with cohesive damage. Given that the models demonstrated compatibility with the experimental results, the necessary properties and parameters were extracted to simulate hybrid joints (both welded and adhesive joints).

4.1.8 MODEL FOR THE TENSILE BEHAVIOUR OF PBT-GF30

For the tensile test, a ductile damage model was used [149, 150], since it enables a better reproduction of the crack path that occurs in this sort of material. In such case, the polymeric matrix (a ductile material) interacts with the high stiffness glass fibre. Taking into consideration that the bond between the surface of the two materials is often of a low energy nature [151], many authors in the literature [150, 152, 153] cite that the application of the ductile damage model is effective, more closely reproducing the fracture process.

In this model, the damage, D, occurs once the maximum stress σ_{y0} is attained. This value is determined using experimental data, based on the peak stress of the elastoplastic behaviour. Once damage is triggered, the material degradation is progressive, based on the relationship (1-D)E from the equivalent plastic strain $\bar{\varepsilon}_0^{pl}$ [153-155]. The damage calculation is based on the dissipation of fracture energy G_f (Equation 1), calculated by the integral of the product of the effective stress by the effective element length L within the range from plastic deformation to the maximum deformation $\bar{\varepsilon}_f^{pl}$. Considering that even at the maximum stress the damage is null, and that the maximum deformation is the required variable, the base change is made for the displacement of the element until failure occurs.

$$G_f = \int_{\bar{\varepsilon}_0^{pl}}^{\bar{\varepsilon}_f^{pl}} L\sigma_y d\bar{\varepsilon}^{pl} = \int_0^{L\bar{\varepsilon}_f^{pl}} \sigma_y d\bar{u}^{pl} \quad (1)$$

With the change of basis, simplifying the curve by the linear decrease model, without strain hardening rate, the displacement to failure u_f^{pl} is calculated by correlating the maximum strain imposed on the unit length of the characteristic element, according to Equation 2.

$$u_f^{pl} = L\bar{\varepsilon}_f^{pl} \quad (2)$$

The material behaviour was established as elastoplastic. The mechanical properties used in the model were based on the properties determined in the experimental tests and on literature references. The Poisson's coefficient was set at 0.42 for the conditions of the treated PBT-GF30, reflecting the degradation of the material. Based on the tensile test, carried out at a single test speed, the triaxiality was assumed to be 0.33 and the strain rate as null. The damage evolution was based on displacement type, linear smoothing, with maximum degradation. The simulation conditions used to validate the model are represented in Table 5

Table 5 - Simulation parameters applied in ductile damage to validate the model in tensile test of PBT-GF30.

Ductile damage model			
Elastic plastic isotropic			
Material	Young's modulus (MPa)	Poisson ratio	Displacement at failure
As received	8885	0.45	0.1
Treated at 225°C	5317	0.42	0.1
Treated at 237°C	5183	0.42	0.07
Treated at 257°C	4826	0.42	0.07

The boundary conditions correspond to a clamped condition on one side of the specimen and the application of a displacement to the other side, as shown in Figure 30 for both tensile test specimens. The mesh size was set to 1 mm for both conditions. Aiming to reach complete failure, the maximum degradation was set as 0.99 and element exclusion was triggered.

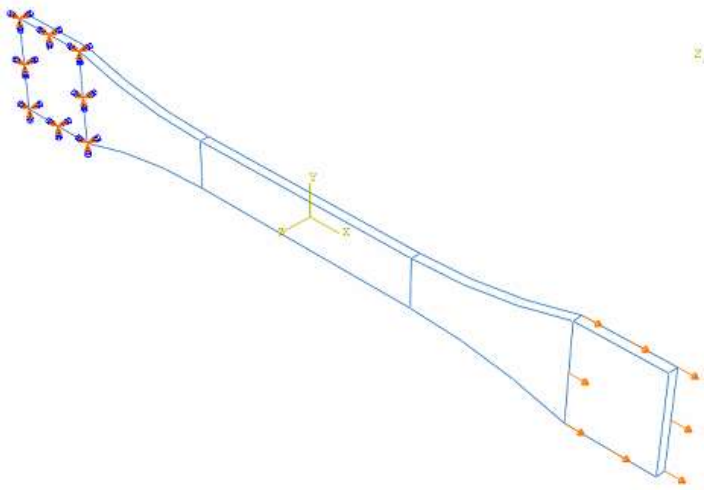


Figure 30 - Representative configuration of the boundary conditions for the tensile simulation (both as supplied and heat-treated conditions).

5.1.1 Model for the fracture behaviour of PBT-GF30

For the validation of the compact test a 2D model was used, employing cohesive elements based on a traction separation law. According to the literature [156], this methodology allows for accurate simulation of the fracture propagation in reinforced polymers. Furthermore, the thickness of the specimen under study is very small, leading to the application of max plane stress damage (Maxps). The cohesive model is also characterized by a penalty in the material stiffness, with reference to the maximum stress and displacement at damage initiation.

For the simulation of the nucleated crack, the extended finite element method (XFEM) was used. Martínez (2017) [40] cites that such procedure dispenses with mesh refinement, even for complex geometries, promoting crack propagation instead of momentary stress concentration. Another advantageous factor for the use of this model, besides the damage evolution parameters, is the need to consider only the maximum principal stress.

The material behaviour was established as purely elastic. The mechanical properties such as modulus of elasticity and Poisson's ratio were the same used in the numerical model for the tensile test simulation. The damage evolution was based on displacement type, linear smoothing, with maximum degradation. The simulation conditions necessary to validate the model are shown in Table 6.

Table 6 - Simulation parameters applied in traction separation Law with Maxps and XFEM, to be validated against the experimental compact test results.

	Material - PBT-GF30			
	As received	Treated at 225°C	Treated at 237°C	Treated at 257°C
Max principal stress (MPa)	67	40	39	37.7
Displacement at failure	0.33	0.33	0.33	0.12
XFEM - crack size (mm)	1	1	1	1

Specimen measurements are based on those shown in Figure 31. Boundary conditions have the model pinned by one of its holes, while the other hole is forced to displace vertically, as per Figure 31-a. The mesh was refined in the crack zone to a 0.5 mm size, with a maximum size of 2 mm away from the crack. The elements used a quad-dominated (free - medial axis) mesh control as per Figure 31-b.

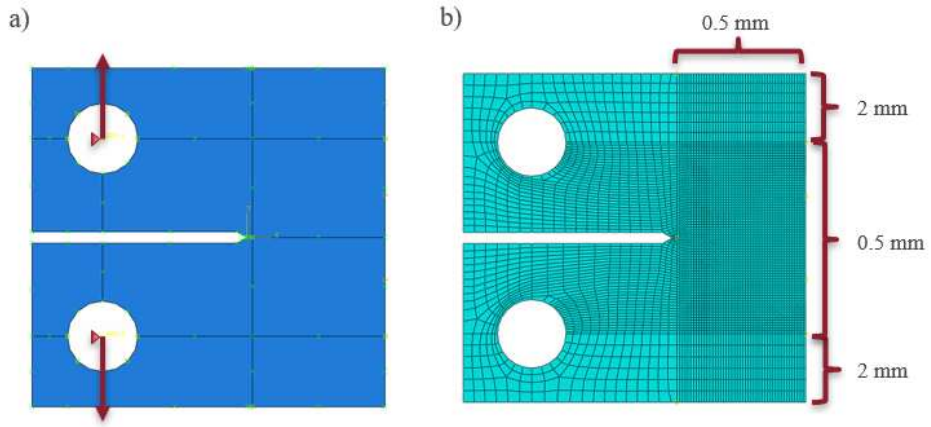


Figure 31 - Compact test model configuration. a) Boundary conditions and b) Mesh details.

5.1 LAP JOINTS

Numerical models were developed to simulate laser-welded and adhesive joints using different methodologies. The aim was to enhance the accuracy and reliability of validation results by carefully considering the specific material properties and process parameters involved in each joint type.

5.2.1 WELDED FILLET LAP JOINTS

A detailed two-dimensional model was created using a dynamic explicit analysis, considering elastoplastic behaviour with ductile damage. The analysis step was configured with a time period of 0.2 seconds, with the aid of non-linear geometrical considerations. The

integration was based on a scaling time factor of 1 s, a mass scaling factor of 10000 and target time increment of 10-10 s.

5.2.1.1 Geometry model

The geometry was based on the measurements of the length, width and height of 40 mm, 10 mm and 1 mm respectively. The plates were overlapped by 20 mm. The separation between the samples was given 5.35 µm. For the interaction between the plates, a friction coefficient of 0.2 was set [157].

Figure 32 illustrates representatively the configuration of the model, showing the overlapped region and the boundary conditions. These include an encastre on the left side of the joint and a 0.2 mm displacement on the left side, with only a single degree of freedom in the *x* direction.

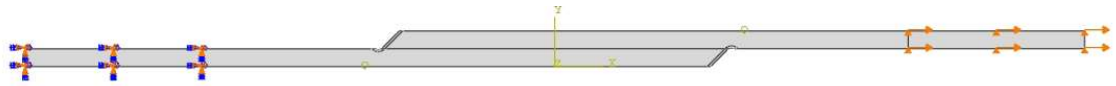


Figure 32 - Configuration of the model, showing the overlapped region and the boundary conditions (US joint configuration shown)

In Figure 33-a, Figure 33-b and Figure 33-c the partitions for the fillet region (weld) and the base material for the US, MS and DS positions, respectively, are illustrated.

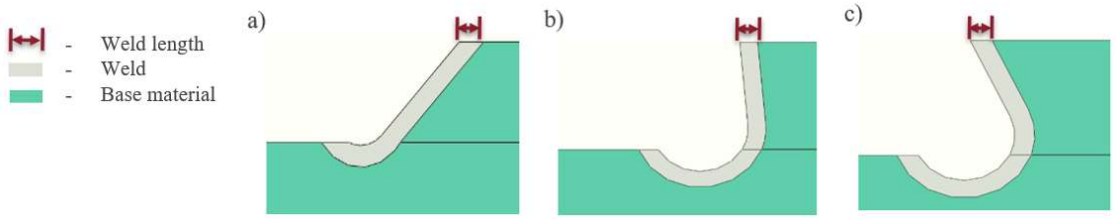


Figure 33 - Material partitions showing weld and base material in the a) US model, b) MS model and c) DS model.

A mesh size of 0.01 mm was used in the weld region and 0.1 mm in the base material. Reduced integration plane stress elements were used, of the CPS4R type.

5.2.1.2 Material properties

The physical and mechanical properties of the PBT-GF30 material used in the simulation were based on those presented in section 4.2.1 and summarised in Table 7, where basic properties of the material such as density, modulus of elasticity and Poisson's ratio are

presented. For the elastoplastic simulation, along with damage parameters, Table 8 indicates the failure strains, triaxialities, strain rates and displacements until failure necessary for implementing ductile damage. Finally, Figure 34 illustrating the stress-strain curves in the plastic regions of the materials, detailing the characteristics of PBT-GF30 in the as received state and the treated at 225ºC, 237ºC and 257ºC states.

Table 7 – Basic properties of PBT-GF30.

Material	Density [g/cm^3]	Young's Modulus [MPa]	Poisson Ratio
As Received	1.31	8398	0.45
Treated at 225°C	1.31	5317	0.42
Treated at 237°C	1.31	5183	0.42
Treated at 257°C	1.31	4826	0.42

Table 8 – Mechanical properties of PBT-GF30 necessary for the implementation of a ductile damage model.

Material	Fracture Strain [mm/mm]	Stress Triaxiality	Strain rate [s-1]	Displacement at Failure [mm]
As Received	0.011492123	-0.33	0	0.001
Treated at 225°C	0.006559261	-0.33	0	0.001
Treated at 237°C	0.003570756	-0.33	0	0.0007
Treated at 257°C	0.000821712	-0.33	0	0.0007

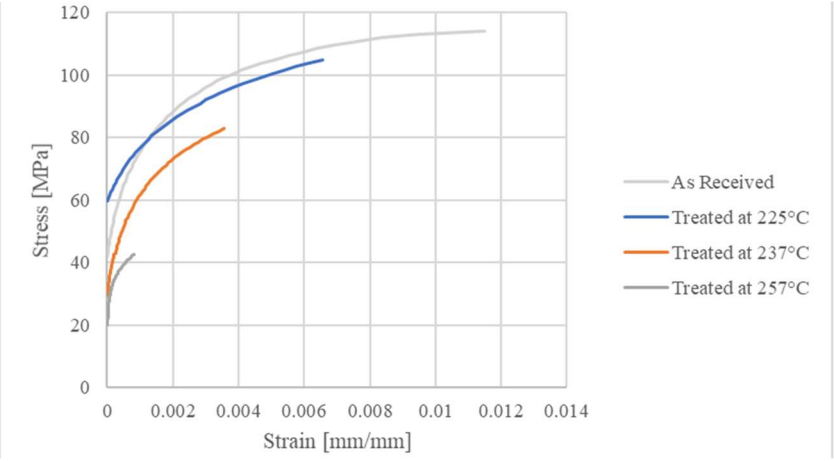


Figure 34 – Stress-strain curves of PBT-GF30 treated at different temperatures, showing plastic behaviour.

5.2.2 ADHESIVELY BONDED LAP JOINTS

The numerical simulation of the adhesive joints aims to validate the model from the determined mechanical properties of the adhesive and substrate. The simulation was

development in two-dimensional but was created using a hyperlelastic behaviour with cohesive damage.

5.2.2.1 Hyperelastic model

To simulate the silicone, hyperelastic behavior was used as a base, and this requires the analysis and validation of the constitutive laws applied to the finite element analysis (FEA) conducted in Abaqus. The constitutive laws available, as presented by Simon et al. (2022) [158], Dias et al. (2014) [159] and proposed by Abaqus, are represented in Figure *35*.

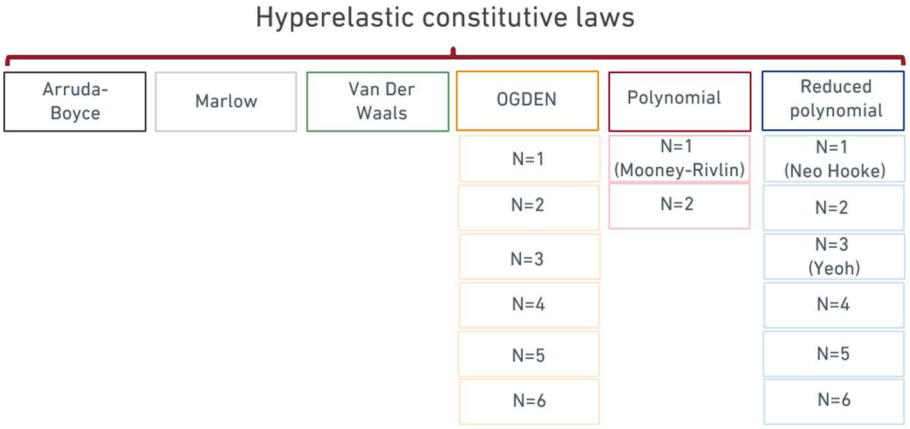


Figure 35 - Hyperelastic constitutive laws maps.

As stated by Mavrodontis (2017) [160], the general equation of a hyperelastic element is based in equation (5), which defined the strain potential energy (U). The first term is dependent on the invariant (I), which is defined according to equation (6). The second is a volumetric term.

$$U = \sum_{i+j=1}^{N} C_{ij}\,(\bar{I}_1 - 3)^i(\bar{I}_2 - 3)^j + \sum_{i=1}^{N} \frac{1}{D_i}(J_{el} - 1)^{2i} \tag{5}$$

$$\bar{I}_1 = \lambda_1^2 + \lambda_2^2 + \lambda_3^2 \quad \text{and} \quad \bar{I}_2 = \lambda_1^{-2} + \lambda_2^{-2} + \lambda_3^{-2} \tag{6}$$

In each constitutive law presented in Figure 35, depending on the type of experiment chosen - uniaxial, planar, equiaxial, or volumetric - there is a corresponding modelling for the invariant term, as indicated in Equation 4. However, having the bulk tensile test as a reference, the principal strains can be given by equation (7).

$$\lambda_1 = \varepsilon_u + 1 \quad \text{and} \quad \lambda_2 = \lambda_3 = \frac{1}{\sqrt{\varepsilon_u + 1}} \tag{7}$$

where ε_u is the principal nominal strain.

5.2.2.2 Cohesive zone modelling (CZM)

Cohesive zone models (CZM) are often used to simulate adhesive joints, since it can predict the adhesive damage and failure of joints. The CZM used has a triangular shape, i.e., the traction increases its value until a maximum is reached, this maximum corresponds to the strength of the material. Afterwards, the material starts exhibiting damage, until the traction reaches zero and the adhesive fails, as shown in Figure 36.

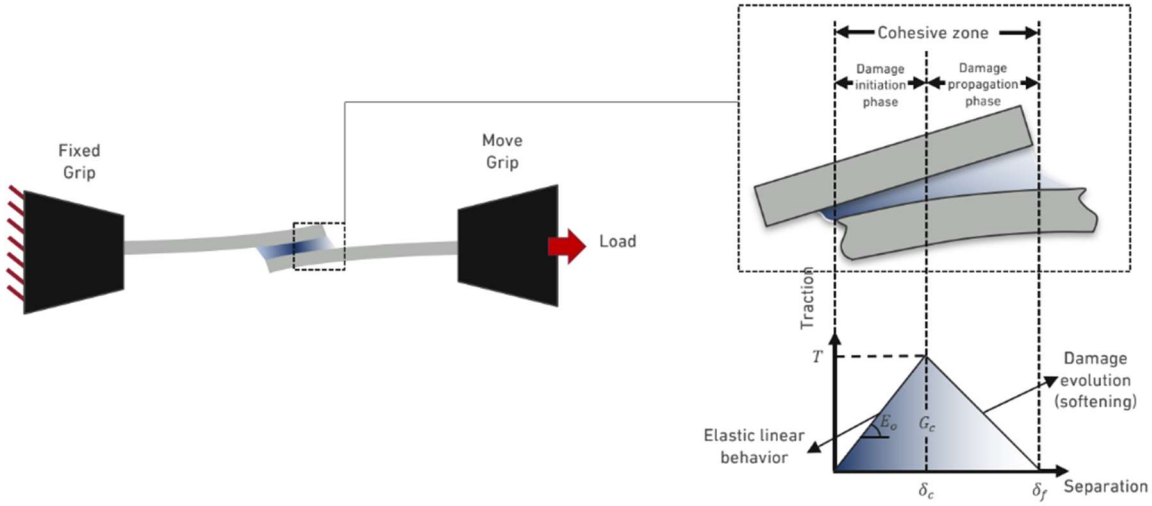


Figure 36 - Damage scheme of the triangular cohesive zone model in single lap joint.

As presented in Figure 36, the damage occurring after the elastic domain was modelled using a quadratic normal stress model, effectively addressing the two proposed experimental approaches. This model encompasses the two principal directions: normal and shear, as illustrated in Figure 37.

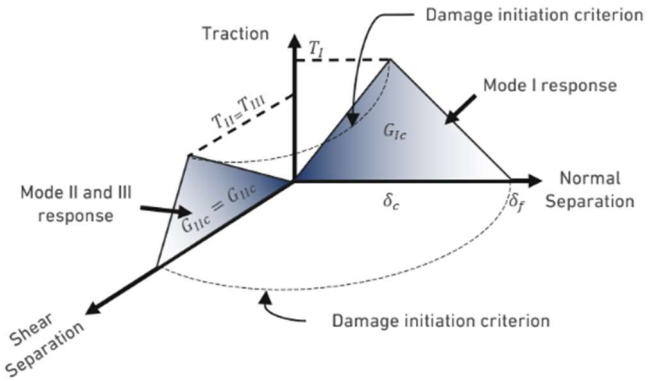


Figure 37 - Traction separation law.

Based on the normal principal stress, $T_{I,c}$, and the shear stresses $T_{II,c}$ and $T_{III,c}$ the damage can be established by equation (6) [161] .

$$\left(\frac{T_I}{T_{I,c}}\right)^2 = \left(\frac{T_{II}}{T_{II,c}}\right)^2 = \left(\frac{T_{III}}{T_{III,c}}\right)^2 = 1 \quad (8)$$

It should be noted that mode II and III are analogous and, therefore $T_{II,c} = T_{III,c}$.

5.2.2.3 Model geometry and construction.

The geometry of the joints simulated are shown in Figure 38-b and Figure 38-d, where an out of plane dimension of 10 mm was considered. The adhesive overlap was divided in three sections: the regions in contact with the substrate, modelled using hyperelastic elements, and the central region, where the failure occurs, where CZM is used, Figure 38-a and Figure 38-b.

Regarding the boundary conditions (Figure 38-c and Figure 38-d), one of the edges of the SLJ is fixed and a 10 mm displacement is imposed to the opposite edge.

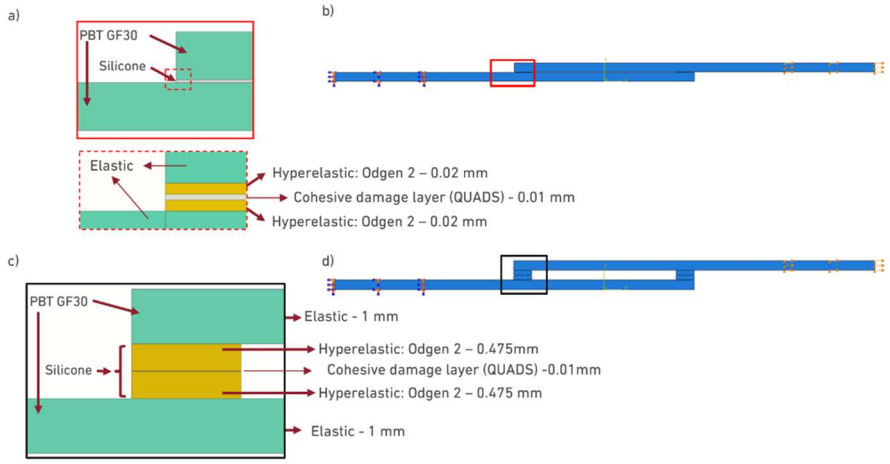


Figure 38 - Representation of joints. a) Division of the joint part and the adhesive layer to 1 mm thickness. b) Boundary condition for the 1 mm thickness. c) Division of the joint part and the adhesive layer to 0.05 mm thickness. d) Boundary condition for the 0.05 mm thickness.

5.2.2.4 Material properties

Table 9 presents the properties used for the numerical simulation of the joint. For the PBT GF30 substrate, the elastic properties studied by Silva et al. (2022) [162], since there is no plastic deformation of the substrate in the test. The properties of the cohesive elements are also represented in Table 9, and an energy criterion, with linear softening was used. For the mode mixity, a power law with a power of 1 was considered.

Table 9 - Properties of the substrate and adhesive layers.

PBT GF 30		
Elastic	Young's Modulus	Poisson's Ratio
	8403.36	0.36

Silicone				
CZM-Quads	Elastic	E/Enn	G1/Ess	G2/Ett
		180	120	120
	DAMAGE	Nominal Stress Normal-only Mode	Nominal Stress First Direction	Nominal Stress Second Direction
		3.4 MPa	4.18 MPa	4.18 Mpa
	DAMAGE EVOLUTION	Normal Mode Fracture Energy	Shear Mode Fracture Energy First Direction	Shear Mode Fracture Energy Second Direction
		4	9	9

The mesh of the joint was set to 1 mm in the substrate, however, in the silicone adhesive the mesh was refined, until a mesh size of 0.1 mm was reached in the cohesive layer, Figure *39*.

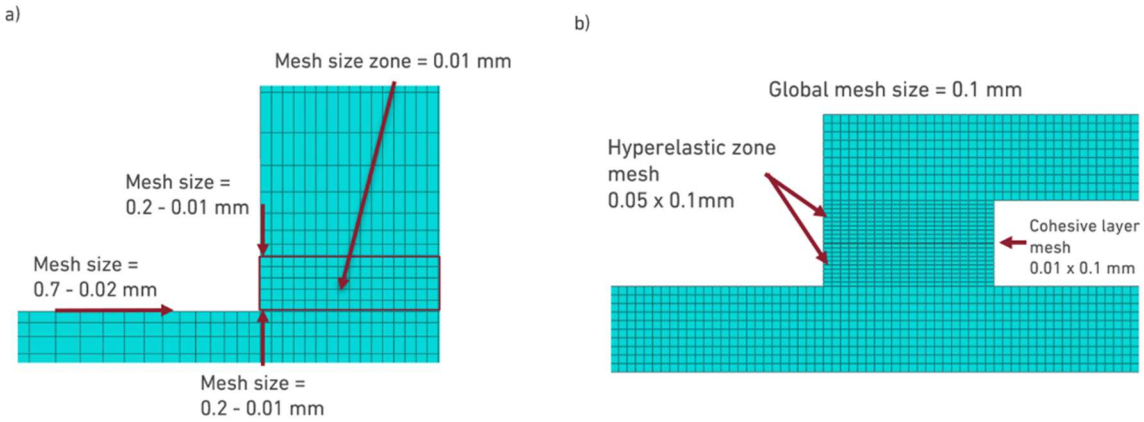


Figure 39 - Meshing details of the adhesive joints.

5.2 COMPONENT LEVEL JOINT

To enhance the understanding of the weld profile and optimize the model developed, a micrographic analysis of the cross-section of the welded joint was conducted, focusing specifically on the welded region, including the geometric characteristics, penetration depth, and interlocking. Furthermore, based on the analysis performed through micro-Raman spectroscopy in the weld region, coupled with the data for thermally treated PBT-GF30 at

temperatures of 225ºC, 237ºC, and 257ºC, the boundaries of the layers in the welded region were defined, as shown in Table 10.

Table 10 - Gradient expressed as a percentage representing the mechanical properties in the weld zone.

External layer	Middle layer	Internal layer
Treated at 225°C	Treated at 237°C	Treated at 257°C
61.60%	15.40%	23%

To represent the welded zone of the actual joint model, geometric measurements obtained through optical microscopy were used, as well as the mechanical property gradient based on the percentage of the layers of PBT-GF30 components presented in Table 10. Figure 40 illustrates the actual joint.

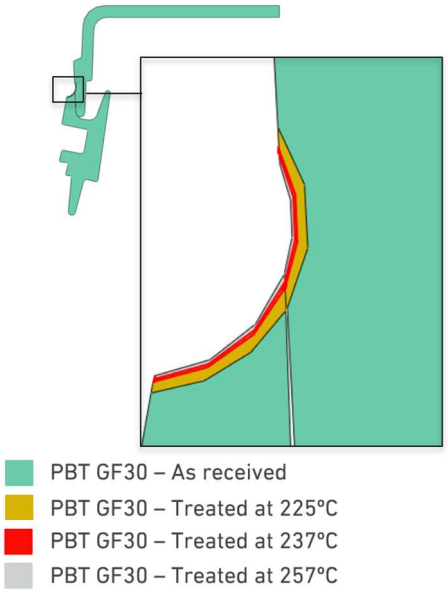


Figure 40 - Representation of layer divisions of the property's gradient – Real joint setting.

Once the properties determined, the boundary conditions were defined in the models. In both configurations, the upper zone was fixed using an encastre, while the lower part was forced to move, through an imposed displacement, as illustrated in Figure 41-a. The joint was generally meshed with a size of 0.5 mm, and locally refined in the welding zone with a mesh size of 0.005 mm, as shown in Figure 41-b.

The numerical model of the real joint was validated based on the model used for the parallel joints of laser-welded PBT-GF30. Consequently, the material properties and fracture

characteristics introduced into the model are also the same, as presented in Table 7, Table 8, and Figure 41.

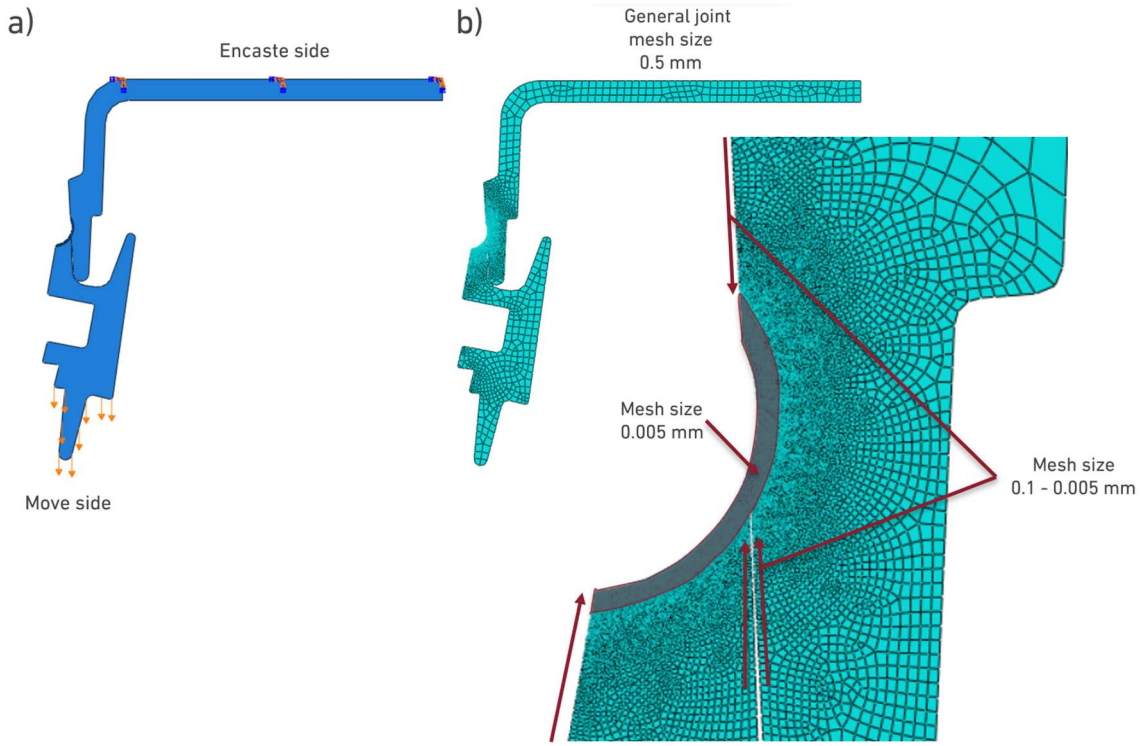


Figure 41 - Schematic representation of the joint model. a) Boundary conditions and b) Mesh size division.

6 CONCLUSIONS

A comprehensive review of the literature was carried out as the first step of this work (Paper 1), showing that a primary research direction in joining is to broaden the spectrum of materials suitable for joining, unlocking the potential for novel designs that fully exploit the capabilities of different materials. Adhesive bonding, mechanical joining, and welding techniques have all been shown to be viable options for these applications, each with varying levels of complexity. Furthermore, a significant trend identified is the development of hybrid joint designs for

polymer bonding, which combine multiple joining processes to create joints with unique and enhanced properties. The literature shows that while these types of joints have historically been confined to academic research, their practical application is now gaining traction.

The initial experimental portion of this work (Paper 2) analysed the thermal, optical, mechanical, and morphological properties of PBT-GF30. The optical analysis indicated that laser welding should be approached using an absorption-based method, focusing on surface welding. Morphological examination revealed that temperatures exceeding the fusion point significantly degrade surface quality, leading to void formation and fiber segregation. This segregation negatively impacts mechanical properties, particularly at higher temperatures. Despite low thermal conductivity, the incident laser energy can still compromise mechanical properties in the weld bead and surrounding areas, emphasizing the importance of studying the thermally affected zone. Numerical models, incorporating ductile damage behaviour for tensile tests, were developed to assess the validity experimentally determined mechanical properties.

Subsequentially, a joint level study was started (Paper 3), which firstly assessed the influence of laser welding parameters on PBT-GF30 joints. Laser diameter was identified as a crucial factor, with small diameters causing perforation and large diameters hindering bonding. For fillet joints, the laser incidence point was found to significantly impact weld strength, with the upper position offering superior performance by reducing undercut and stress concentration. The result data was used to develop full joint models, able to predict failure load and failure mechanisms. While the elastoplastic model was found to simulate the elastic behaviour of laser welded joints, it was found to overestimate maximum forces. Incorporating ductile damage improves convergence for all conditions under analysis

A comparison was then made between joints created with adhesive bonding and laser welding (Paper 4), serving as alternatives for joining electronic housings. The experimental results determined that laser welding is a faster process, while avoiding extra material usage compared to adhesive bonding. A 45-degree laser incidence angle yielded the strongest joints. Laser beam properties like diameter, power, and time also significantly affected the joint strength. This approach allowed to identify optimal settings for power density and power density ratio to avoid burning through the material. For adhesive bonding with silicone, thinner layers performed better due to less air bubble formation and crack propagation.

Finally, it was possible to demonstrate the feasibility of laser welding as a viable joining technique for joining full-scale PBT GF30 components (Paper 5), as commonly used in

automotive electronics. Overlapped and butt configurations, cut from actual components, were found to outperform purely overlapped configurations, likely due to the higher normal stress experienced by the material. The previously developed numerical models, incorporating ductile damage formulation, accurately predicted failure loads, demonstrating their suitability for real-world scenarios.

7 FUTURE WORKS

Based on the insights extracted from this research, the following future research directions are proposed:

- Investigate the potential of laser welding to simultaneously cure adhesives and enhance joint strength by melting thermoplastic materials.
- Explore the application of laser preheating to reduce power requirements and rotational speed in friction stir welding, as well as the use of post-welding laser treatment to consolidate non-joined areas and refine the microstructure.
- Develop laser-assisted techniques to improve the watertightness of mechanical joints. This could involve laser welding at the material interface for transparent substrates or at the joint edge for light-absorbing materials.
- Conduct comprehensive optimization studies to identify optimal process parameters, material combinations, and geometric configurations for various hybrid joining techniques in polymer applications.

REFERENCES

1. Ashby, M.F. and D. Cebon, *Materials selection in mechanical design.* Le Journal de Physique IV, 1993. **3**(C7): p. C7-1-C7-9.
2. Amanat, N., N.L. James, and D.R. McKenzie, *Welding methods for joining thermoplastic polymers for the hermetic enclosure of medical devices.* Medical engineering & physics, 2010. **32**(7): p. 690-699.
3. Marczis, B. and T. Czigány, *Polymer joints.* Periodica Polytechnica Mechanical Engineering, 2002. **46**(2): p. 117-126.
4. Visco, A., et al., *Response to fatigue stress of biomedical grade polyethylene joints welded by a diode laser.* Journal of the mechanical behavior of biomedical materials, 2018. **86**: p. 390-396.
5. Kinloch, A.J., *Adhesion and adhesives: science and technology*. 2012: Springer Science & Business Media.
6. Da Silva, L.F. and R.D. Campilho, *Advances in numerical modelling of adhesive joints*, in *Advances in numerical modeling of adhesive joints*. 2012, Springer. p. 1-93.
7. Da Silva, L.F., A. Öchsner, and R.D. Adams, *Handbook of adhesion technology*. 2011: Springer Science & Business Media.
8. Ravi-Kumar, S., et al., *Laser ablation of polymers: A review.* Polymer International, 2019. **68**(8): p. 1391-1401.
9. Wu, S., *Polymer interface and adhesion*. 2017: Routledge.
10. Hartshorn, S.R., *Structural adhesives: chemistry and technology*. 2012: Springer Science & Business Media.
11. Arteiro, A., et al., *Thin-ply polymer composite materials: a review.* Composites Part A: Applied Science and Manufacturing, 2020. **132**: p. 105777.
12. Yadav, A., et al., *Fabrication of 3D polymeric photonic arrays and related applications.* Materials Today Chemistry, 2020. **15**: p. 100208.
13. Kweon, J.-H., et al., *Failure of carbon composite-to-aluminum joints with combined mechanical fastening and adhesive bonding.* Composite structures, 2006. **75**(1-4): p. 192-198.
14. Friedrich, S., et al. *Hybrid joining technology-a new method for joining thermoplastic-metal-mixed components*. in *AIP Conference Proceedings*. 2014. American Institute of Physics.
15. Ueda, M., et al., *Instantaneous mechanical fastening of quasi-isotropic CFRP laminates by a self-piercing rivet.* Composite Structures, 2012. **94**(11): p. 3388-3393.
16. Machado, J., et al., *Numerical study of impact behaviour of mixed adhesive single lap joints for the automotive industry.* International Journal of Adhesion and Adhesives, 2018. **84**: p. 92-100.
17. Machado, J., et al., *Numerical study of similar and dissimilar single lap joints under quasi-static and impact conditions.* International Journal of Adhesion and Adhesives, 2020. **96**: p. 102501.
18. Machado, J., et al., *Numerical study of the behaviour of composite mixed adhesive joints under impact strength for the automotive industry.* Composite Structures, 2018. **185**: p. 373-380.
19. Nascimento, P.L.d.M.M., et al., *Addition of ammonium-based methacrylates to an experimental dental adhesive for bonding metal brackets: Carious lesion development and bond strength after cariogenic challenge.* American Journal of Orthodontics and Dentofacial Orthopedics, 2017. **151**(5): p. 949-956.

20. Villanueva, J.G.V., et al., *Bio-adhesion evaluation of a chitosan-based bone bio-adhesive.* International Journal of Adhesion and Adhesives, 2019. **92**: p. 80-88.
21. Maurer, P., et al., *Comparison of the bond strength of selected adhesive dental systems to cortical bone under in vitro conditions.* International journal of oral and maxillofacial surgery, 2004. **33**(4): p. 377-381.
22. Kandalam, U., et al., *Novel bone adhesives: a comparison of bond strengths in vitro.* International journal of oral and maxillofacial surgery, 2013. **42**(9): p. 1054-1059.
23. Szymczyk-Ziółkowska, P., et al., *A review of fabrication polymer scaffolds for biomedical applications using additive manufacturing techniques.* Biocybernetics and Biomedical Engineering, 2020. **40**(2): p. 624-638.
24. Pilate, F., et al., *Shape-memory polymers for multiple applications in the materials world.* European Polymer Journal, 2016. **80**: p. 268-294.
25. Butt, H.-J. and M. Kappl, *Surface and interfacial forces*. 2018: John Wiley & Sons.
26. Thakkar, R., et al., *Systematic screening of pharmaceutical polymers for hot melt extrusion processing: A comprehensive review.* International journal of pharmaceutics, 2020. **576**: p. 118989.
27. Clifton, S., et al., *Polymer nanocomposites for high-velocity impact applications-A review.* Composites Communications, 2020. **17**: p. 72-86.
28. Zhang, X., et al., *Design and fabrication of PVAc-based inverted core/shell (ICS) structured adhesives for improved water-resistant wood bonding performance: I. Influence of chemical grafting.* International Journal of Adhesion and Adhesives, 2020. **98**: p. 102522.
29. Shi, J.-W., W.-H. Cao, and Z.-S. Wu, *Effect of adhesive properties on the bond behaviour of externally bonded FRP-to-concrete joints.* Composites Part B: Engineering, 2019. **177**: p. 107365.
30. Rocha, A.V., et al., *Fatigue crack growth analysis of different adhesive systems: Effects of mode mixity and load level.* Fatigue & Fracture of Engineering Materials & Structures, 2020. **43**(2): p. 330-341.
31. Nguyen, K.T., et al., *Fire safety of composites in prefabricated buildings: From fibre reinforced polymer to textile reinforced concrete.* Composites Part B: Engineering, 2020. **187**: p. 107815.
32. Bagherzadeh, A., M. Jamshidi, and F. Monemian, *Investigating mechanical and bonding properties of micro/nano filler containing epoxy adhesives for anchoring steel bar in concrete.* Construction and Building Materials, 2020. **240**: p. 117979.
33. Li, Z., A. Olah, and E. Baer, *Micro-and nano-layered processing of new polymeric systems.* Progress in Polymer Science, 2020. **102**: p. 101210.
34. Cho, B.H., et al., *Waterproofing performance of waterstop with adhesive bonding used at joints of underground concrete structures.* Construction and Building Materials, 2019. **221**: p. 491-500.
35. Ludwig, C.H. and A.W. Stout, *Adhesive composition from lignosulfonate phenoplasts*. 1971, Google Patents.
36. da Silva, L.F., A. Pirondi, and A. Öchsner, *Hybrid adhesive joints*. Vol. 6. 2011: Springer Science & Business Media.
37. Amancio Filho, S.T. and L.-A. Blaga, *Joining of polymer-metal hybrid structures: principles and applications*. 2018: John Wiley & Sons.
38. Chanda, M. and S.K. Roy, *Plastics technology handbook*. 2006: CRC press.
39. Collett, B.M., *A review of surface and interfacial adhesion in wood science and related fields.* Wood Science and Technology, 1972. **6**(1): p. 1-42.
40. El Mansouri, N.-E. and J. Salvadó, *Structural characterization of technical lignins for the production of adhesives: Application to lignosulfonate, kraft, soda-anthraquinone,*

organosolv and ethanol process lignins. Industrial crops and products, 2006. **24**(1): p. 8-16.
41. Valasamudram, V., et al., *Study and evaluation of cold joining on metals and non metals combinations (ss, al, acr) using polymer based adhesive.* Materials Today: Proceedings, 2020. **27**: p. 2806-2810.
42. Weitzenböck, J.R., *Adhesives in marine engineering*. 2012: Elsevier.
43. Kinloch, A., *The science of adhesion.* Journal of materials science, 1980. **15**(9): p. 2141-2166.
44. Higgins, A., *Adhesive bonding of aircraft structures.* International Journal of Adhesion and Adhesives, 2000. **20**(5): p. 367-376.
45. Xie, T., et al., *Preparation and characterization of self-matting waterborne polymer–An overview.* Progress in Organic Coatings, 2020. **142**: p. 105569.
46. Amancio-Filho, S. and J. Dos Santos, *Joining of polymers and polymer–metal hybrid structures: recent developments and trends.* Polymer engineering & science, 2009. **49**(8): p. 1461-1476.
47. Rotheiser, J., *Joining of plastics: handbook for designers and engineers*. 2015: Carl Hanser Verlag GmbH Co KG.
48. Ghassemieh, E., *Materials in automotive application, state of the art and prospects.* New trends and developments in automotive industry, 2011. **20**: p. 365-394.
49. Okada, A., *Automotive and industrial applications of structural ceramics in Japan.* Journal of the European Ceramic Society, 2008. **28**(5): p. 1097-1104.
50. Friedrich, K. and A.A. Almajid, *Manufacturing aspects of advanced polymer composites for automotive applications.* Applied Composite Materials, 2013. **20**(2): p. 107-128.
51. Mitschang, P. and K. Hildebrandt, *Polymer and composite moulding technologies for automotive applications*, in *Advanced materials in automotive engineering*. 2012, Elsevier. p. 210-229.
52. Zimmermann, A. and K.-V. Schütt. *Polymers in power electronics-Performance of thermal interface materials*. in *19th International Workshop on Thermal Investigations of ICs and Systems (THERMINIC)*. 2013. IEEE.
53. Borges, C., et al., *Effect of Water Ingress on the Mechanical and Chemical Properties of Polybutylene Terephthalate Reinforced with Glass Fibers. Materials 2021, 14, 1261*. 2021, s Note: MDPI stays neutral with regard to jurisdictional claims in published ….
54. Cousins, K., *Polymers for electronic components*. 2001: iSmithers Rapra Publishing.
55. Dangel, R., et al. *Development of a low-cost low-loss polymer waveguide technology for parallel optical interconnect applications*. in *Digest of the LEOS Summer Topical Meetings Biophotonics/Optical Interconnects and VLSI Photonics/WBM Microcavities, 2004.* 2004. IEEE.
56. Fink, J.K., *High performance polymers*. 2014: William Andrew.
57. Hergenrother, P.M., *The use, design, synthesis, and properties of high performance/high temperature polymers: an overview.* High Performance Polymers, 2003. **15**(1): p. 3-45.
58. Unterweger, C., O. Brüggemann, and C. Fürst, *Synthetic fibers and thermoplastic short-fiber-reinforced polymers: Properties and characterization.* Polymer Composites, 2014. **35**(2): p. 227-236.
59. Grewell, D. and A. Benatar, *Welding of plastics: fundamentals and new developments.* International polymer processing, 2007. **22**(1): p. 43-60.
60. Kah, P., et al., *TECHNIQUES FOR JOINING DISSIMILAR MATERIALS: METALS AND POLYMERS.* Reviews on Advanced Materials Science, 2014. **36**(2).
61. Troughton, M.J., *Handbook of plastics joining: a practical guide*. 2008: William Andrew.

62. Da Silva, L.F.M. and A. Öchsner, *Modeling of adhesively bonded joints*. 2008: Springer.
63. Rasmussen, P.A. and J.M. Brown, *Integral thermoset/thermoplastic composite joint*. 1997, Google Patents.
64. Schieler, O. and U. Beier, *Induction welding of hybrid thermoplastic-thermoset composite parts.* Applied Science and Engineering Progress, 2016. **9**(1): p. 27-36.
65. Katayama, S., *Handbook of laser welding technologies*. 2013: Elsevier.
66. Dawes, C., *Laser welding: a practical guide*. 1992: Woodhead Publishing.
67. Katayama, S., Y. Kawahito, and M. Mizutani, *Latest progress in performance and understanding of laser welding.* Physics Procedia, 2012. **39**: p. 8-16.
68. Juhl, T.B., et al., *Predicting the laser weldability of dissimilar polymers.* Polymer, 2013. **54**(15): p. 3891-3897.
69. Quazi, M., et al., *Current research and development status of dissimilar materials laser welding of titanium and its alloys.* Optics & Laser Technology, 2020. **126**: p. 106090.
70. Antony, K. and T. Rakeshnath, *Dissimilar laser welding of commercially pure copper and stainless steel 316L.* Materials Today: Proceedings, 2020.
71. Yilbas, B.S., et al., *Life cycle analysis for laser welding of alloys.* Optics & Laser Technology, 2020. **126**: p. 106064.
72. Sakamiti, G.P., et al., *Weldability of a zirconium alloy comparing resistance and pulsed laser methods.* Nuclear Materials and Energy, 2019. **20**: p. 100693.
73. Zhang, Z., J. Shan, and X. Tan, *Evaluation of the CFRP grafting and its influence on the laser joining CFRP to aluminum alloy.* Journal of adhesion science and Technology, 2018. **32**(4): p. 390-406.
74. Rodríguez-Vidal, E., et al., *Experimental investigation into metal micro-patterning by laser on polymer-metal hybrid joining.* Optics & Laser Technology, 2018. **104**: p. 73-82.
75. Tao, W., et al., *Joint formation and fracture characteristics of laser welded CFRP/TC4 joints.* Journal of Manufacturing Processes, 2019. **45**: p. 1-8.
76. Wahba, M., Y. Kawahito, and S. Katayama, *Laser direct joining of AZ91D thixomolded Mg alloy and amorphous polyethylene terephthalate.* Journal of materials processing technology, 2011. **211**(6): p. 1166-1174.
77. Katayama, S. and Y. Kawahito, *Laser direct joining of metal and plastic.* Scripta materialia, 2008. **59**(12): p. 1247-1250.
78. Lambiase, F., S. Genna, and R. Kant, *A procedure for calibration and validation of FE modelling of laser-assisted metal to polymer direct joining.* Optics & Laser Technology, 2018. **98**: p. 363-372.
79. Hirsch, J., et al., *Axisymmetric laser welding of ceramics: comparison of experimental and finite element results.* Optics and lasers in engineering, 1998. **29**(6): p. 465-484.
80. Song, L., et al., *Laser melted oxide ceramics: Multiscale structural evolution with non-equilibrium features.* Journal of Materiomics, 2019. **5**(3): p. 436-445.
81. de Pablos-Martín, A., et al., *Laser welding of fused silica glass with sapphire using a non-stoichiometric, fresnoitic Ba2TiSi2O8· 3 SiO2 thin film as an absorber.* Optics & Laser Technology, 2017. **92**: p. 85-94.
82. Duley, W. and R. Mueller, *CO2 laser welding of polymers.* Polymer Engineering & Science, 1992. **32**(9): p. 582-585.
83. Jansson, A., et al. *The effect of parameters on laser transmission welding of polymers*. in *International Congress on Applications of Lasers & Electro-Optics*. 2003. Laser Institute of America.
84. Van de Ven, J.D. and A.G. Erdman, *Laser transmission welding of thermoplastics—Part I: Temperature and pressure modeling.* 2007.

85. Van de Ven, J.D. and A.G. Erdman, *Laser transmission welding of thermoplastics—Part II: experimental model validation.* 2007.
86. Nonhof, C., *Laser welding of polymers.* Polymer Engineering & Science, 1994. **34**(20): p. 1547-1549.
87. Wissman, L.Y., *Method for laser welding flexible polymers*. 2007, Google Patents.
88. Hilton, P.A., I. Jones, and Y. Kennish. *Transmission laser welding of plastics*. in *First International Symposium on High-Power Laser Macroprocessing*. 2003. International Society for Optics and Photonics.
89. Hubeatir, K.A., *Laser transmission welding of PMMA using IR semiconductor laser complemented by the Taguchi method and grey relational analysis.* Materials Today: Proceedings, 2020. **20**: p. 466-473.
90. Taha, Z., et al., *Mathematical modeling of laser-assisted transmission lap welding of polymers.* Scripta Materialia, 2009. **60**(8): p. 663-666.
91. Acherjee, B., et al., *Effect of carbon black on temperature field and weld profile during laser transmission welding of polymers: A FEM study.* Optics & Laser Technology, 2012. **44**(3): p. 514-521.
92. Casalino, G. and E. Ghorbel, *Numerical model of CO2 laser welding of thermoplastic polymers.* journal of materials processing technology, 2008. **207**(1-3): p. 63-71.
93. Ruotsalainen, S., P. Laakso, and V. Kujanpää, *Laser welding of transparent polymers by using quasi-simultaneous beam off-setting scanning technique.* Physics Procedia, 2015. **78**: p. 272-284.
94. Villar, M., et al., *In-situ infrared thermography measurements to master transmission laser welding process parameters of PEKK.* Optics and Lasers in Engineering, 2018. **106**: p. 94-104.
95. Brodhun, J., D. Blass, and K. Dilger, *Laser transmission welding of thermoplastic fasteners: Influence of temperature distribution in a scanning based process.* Procedia CIRP, 2018. **74**: p. 533-537.
96. Speka, M., et al., *The infrared thermography control of the laser welding of amorphous polymers.* NDT & E International, 2008. **41**(3): p. 178-183.
97. Ilie, M., et al., *Through-transmission laser welding of polymers–temperature field modeling and infrared investigation.* Infrared Physics & Technology, 2007. **51**(1): p. 73-79.
98. Schmailzl, A., et al., *Measurement of core temperature through semi-transparent polyamide 6 using scanner-integrated pyrometer in laser welding.* International Journal of Heat and Mass Transfer, 2020. **146**: p. 118814.
99. Schmitt, R., et al., *3D polymer weld seam characterization based on optical coherence tomography for laser transmission welding applications.* Physics Procedia, 2014. **56**: p. 1305-1314.
100. Chen, M., G. Zak, and P.J. Bates, *Effect of carbon black on light transmission in laser welding of thermoplastics.* Journal of Materials Processing Technology, 2011. **211**(1): p. 43-47.
101. Rodríguez-Vidal, E., I. Quintana, and C. Gadea, *Laser transmission welding of ABS: effect of CNTs concentration and process parameters on material integrity and weld formation.* Optics & Laser Technology, 2014. **57**: p. 194-201.
102. Gisario, A., et al., *Laser transmission welding of poly (ethylene terephthalate) and biodegradable poly (ethylene terephthalate)–based blends.* Optics and Lasers in Engineering, 2017. **90**: p. 110-118.
103. Banea, M.D., et al., *Smart adhesive joints: An overview of recent developments.* The Journal of Adhesion, 2014. **90**(1): p. 16-40.
104. Gierenz, G. and W. Karmann, *Adhesives and adhesive tapes*. 2008: John Wiley & Sons.

105. Hoong, Y.B., et al., *A new source of natural adhesive: Acacia mangium bark extracts co-polymerized with phenol-formaldehyde (PF) for bonding Mempisang (Annonaceae spp.) veneers.* International Journal of Adhesion and Adhesives, 2011. **31**(3): p. 164-167.
106. Ebnesajjad, S., *Handbook of adhesives and surface preparation: technology, applications and manufacturing*. 2010: William Andrew.
107. Da Silva, L.F., et al., *Testing adhesive joints: best practices*. 2012: John Wiley & Sons.
108. Molitor, P., V. Barron, and T. Young, *Surface treatment of titanium for adhesive bonding to polymer composites: a review.* International Journal of Adhesion and Adhesives, 2001. **21**(2): p. 129-136.
109. Sabreen, S., *Plasma surface pretreatments of polymers for improved adhesion bonding.* Tecnology, 2018. **1**(1): p. 1-5.
110. Zhang, D., Q. Sun, and L.C. Wadsworth, *Mechanism of corona treatment on polyolefin films.* Polymer Engineering & Science, 1998. **38**(6): p. 965-970.
111. Nečasová, B., et al., *Comparison of adhesive properties of polyurethane adhesive system and wood-plastic composites with different polymers after mechanical, chemical and physical surface treatment.* Polymers, 2019. **11**(3): p. 397.
112. Bukhari, M.D., et al., *Adhesion Theories and Effect of Surface Roughness on Energy Estimation and Wettability of Polymeric Composites Bonded Joints: A-Review.* VW Applied Sciences, 2020. **2**(1): p. 74-86.
113. Jin, X., et al., *Joining the un-joinable: adhesion between low surface energy polymers using tetrapodal ZnO linkers.* Advanced Materials, 2012. **24**(42): p. 5676-5680.
114. da Silva, L.F.M., et al., *Analytical models of adhesively bonded joints—Part I: Literature survey.* International Journal of Adhesion and Adhesives, 2009. **29**(3): p. 319-330.
115. de Moura, M., et al., *Cohesive and continuum mixed-mode damage models applied to the simulation of the mechanical behaviour of bonded joints.* International Journal of Adhesion and Adhesives, 2008. **28**(8): p. 419-426.
116. Braga, D.F., L.F. da Silva, and P.M. Moreira, *Single lap joints numerical modelling and comparison with experimental testing.* U. Porto Journal of Engineering, 2016. **2**(1): p. 11-20.
117. Adams, R.D. and N.A. Peppiatt, *Stress analysis of adhesive-bonded lap joints.* The Journal of Strain Analysis for Engineering Design, 1974. **9**(3): p. 185-196.
118. Crocombe, A., Adams, and RD, *Influence of the spew fillet and other parameters on the stress distribution in the single lap joint.* The Journal of Adhesion, 1981. **13**(2): p. 141-155.
119. da Silva, L.F.M., et al., *Effect of adhesive type and thickness on the lap shear strength.* The Journal of Adhesion, 2006. **82**(11): p. 1091-1115.
120. Oliveira, J., et al., *Adhesive thickness effects on the mixed-mode fracture toughness of bonded joints.* The Journal of Adhesion, 2019: p. 1-21.
121. Sadeghi, M., et al., *Failure load prediction of adhesively bonded single lap joints by using various FEM techniques.* International Journal of Adhesion and Adhesives, 2020. **97**: p. 102493.
122. Matos-Pérez, C.R., J.D. White, and J.J. Wilker, *Polymer composition and substrate influences on the adhesive bonding of a biomimetic, cross-linking polymer.* Journal of the American Chemical Society, 2012. **134**(22): p. 9498-9505.
123. Hsiao, K.-T., J. Alms, and S.G. Advani, *Use of epoxy/multiwalled carbon nanotubes as adhesives to join graphite fibre reinforced polymer composites.* Nanotechnology, 2003. **14**(7): p. 791.

124. Machado, J., et al., *Numerical study of mode I fracture toughness of carbon-fibre-reinforced plastic under an impact load.* Proceedings of the Institution of Mechanical Engineers, Part L: Journal of Materials: Design and Applications, 2020. **234**(1): p. 12-20.
125. Banea, M., et al., *The effect of environment and fatigue loading on the behaviour of TEPs-modified adhesives.* The Journal of Adhesion, 2020. **96**(1-4): p. 423-436.
126. Akhavan-Safar, A., et al., *Influence of microcork particles on the lap shear strength of an epoxy adhesive subjected to fatigue loading and different environmental conditions.* Proceedings of the Institution of Mechanical Engineers, Part L: Journal of Materials: Design and Applications, 2020: p. 1464420720909848.
127. Borges, C., et al., *Review on the effect of moisture and contamination on the interfacial properties of adhesive joints.* Proceedings of the Institution of Mechanical Engineers, Part C: Journal of Mechanical Engineering Science, 2020: p. 0954406220944208.
128. Sugiman, S., A. Crocombe, and I. Aschroft, *Experimental and numerical investigation of the static response of environmentally aged adhesively bonded joints.* International Journal of Adhesion and Adhesives, 2013. **40**: p. 224-237.
129. Rocha, A., et al., *Numerical analysis of mixed-mode fatigue crack growth of adhesive joints using CZM.* Theoretical and Applied Fracture Mechanics, 2020: p. 102493.
130. Monteiro, J., et al., *Influence of mode mixity and loading conditions on the fatigue crack growth behaviour of an epoxy adhesive.* Fatigue & Fracture of Engineering Materials & Structures, 2020. **43**(2): p. 308-316.
131. Rocha, A., et al., *Paris law relations for an epoxy-based adhesive.* Proceedings of the Institution of Mechanical Engineers, Part L: Journal of Materials: Design and Applications, 2020. **234**(2): p. 291-299.
132. Diebels, S. and S. Rjasanow, *Multi-scale simulation of composite materials: Results from the project MuSiKo*. 2019: Springer.
133. Jansen, K., D. Van Dijk, and M. Husselman, *Effect of processing conditions on shrinkage in injection molding.* Polymer Engineering & Science, 1998. **38**(5): p. 838-846.
134. Köppl, T., et al., *Structure− property relationships of halogen-free flame-retarded poly (butylene terephthalate) and glass fiber reinforced PBT.* Journal of applied polymer science, 2012. **124**(1): p. 9-18.
135. Ehrenstein, G., et al., *Werkstoff-und prozessoptimierte Herstellung flächiger Kunststoff-Kunststoff und Kunststoff-Metall-Verbundbauteile.* Tagungsband zum Berichts-und Industriekolloquium, 2003.
136. Fung, C.-P., J.-R. Hwang, and C.-C. Hsu, *The effect of injection molding process parameters on the tensile properties of short glass fiber-reinforced PBT.* Polymer-Plastics Technology and Engineering, 2003. **42**(1): p. 45-63.
137. Ho, M.H., P.N. Wang, and C.P. Fung. *The effect of Injection molding process parameters on the buckling properties of PBT/short glass fiber composites*. in *Advanced Materials Research*. 2011. Trans Tech Publ.
138. Frick, T. and A. Schkutow, *Laser transmission welding of polymers–Irradiation strategies for strongly scattering materials.* Procedia CIRP, 2018. **74**: p. 538-543.
139. Khosravi, S., *Laser transmission welding of polybutylene terephthalate and polyethylene terephthalate blends*. 2010.
140. Zhang, B.Y., et al., *Thermal, morphological, and mechanical characteristics of polypropylene/polybutylene terephthalate blends with a liquid crystalline polymer or ionomer.* Journal of applied polymer science, 2006. **102**(5): p. 4712-4719.
141. ASTM, C., *ASTM standards.* Philadelphia: American Society for Testing Materials, 1958.

142. ISO, B., *Plastics–determination of tensile properties*. 1997.
143. ASTM, I., *Standard test methods for plane-strain fracture toughness and strain energy release rate of plastic materials.* ASTM D5045-99, 2007.
144. Kuppusamy, N. and R.A. Tomlinson, *Repeatable pre-cracking preparation for fracture testing of polymeric materials.* Engineering Fracture Mechanics, 2016. **152**: p. 81-87.
145. Dean, G., *Adhesives-determination of shear behaviour of structural bonds part 2: thick-adherend tensile-test method.* 1997.
146. Moore, D., *30: Measurement of Creep.* Mechanical Properties and Testing of Polymers: An A–Z Reference, 1999. **3**: p. 137.
147. Banea, M.D. and L.F. da Silva, *Mechanical characterization of flexible adhesives.* The Journal of Adhesion, 2009. **85**(4-5): p. 261-285.
148. Borges, C., et al., *A strain rate dependent cohesive zone element for mode I modeling of the fracture behavior of adhesives.* Proceedings of the Institution of Mechanical Engineers, Part L: Journal of Materials: Design and Applications, 2020. **234**(4): p. 610-621.
149. Rakin, M., et al., *Modelling of ductile fracture initiation in strength mismatched welded joint.* Engineering Fracture Mechanics, 2008. **75**(11): p. 3499-3510.
150. Sugiman, S. and H. Ahmad, *Comparison of cohesive zone and continuum damage approach in predicting the static failure of adhesively bonded single lap joints.* Journal of adhesion science and Technology, 2017. **31**(5): p. 552-570.
151. Huang, H. and R. Talreja, *Numerical simulation of matrix micro-cracking in short fiber reinforced polymer composites: initiation and propagation.* Composites science and technology, 2006. **66**(15): p. 2743-2757.
152. Feng, F., et al., *Application of a GTN damage model predicting the fracture of 5052-O aluminum alloy high-speed electromagnetic impaction.* Metals, 2018. **8**(10): p. 761.
153. Sancho, A., et al., *Experimental techniques for ductile damage characterisation.* Procedia Structural Integrity, 2016. **2**: p. 966-973.
154. Ruzicka, J., et al., *Identification of ductile damage parameters in the ABAQUS.* Bull. Appl. Mech, 2012. **8**: p. 89-92.
155. Ruzicka, P., et al., *Identification of ductile damage parameters.* ENHANCING NUCLEAR POWER PLANT DESIGN WITH REALISTIC SIMULATION, 2013: p. 21.
156. Charitidis, P., *Results of Finite Element Analysis for Interlaminar Fracture Reinforced Thermoplastic Composites.* Adv. Mater. Sci. Eng. Int. J, 2017. **4**: p. 1-17.
157. Chaudri, A.M., M. Suvanto, and T.T. Pakkanen, *Non-lubricated friction of polybutylene terephthalate (PBT) sliding against polyoxymethylene (POM).* Wear, 2015. **342**: p. 189-197.
158. Simon Portillo, F.J., et al., *Mechanical Characterisation and Comparison of Hyperelastic Adhesives: Modelling and Experimental Validation.* Journal of Applied and Computational Mechanics, 2022. **8**(1): p. 359-369.
159. Dias, V., et al., *Development of a constitutive hyperelastic material law for numerical simulations of adhesive steel–glass connections using structural silicone.* International Journal of Adhesion and Adhesives, 2014. **48**: p. 194-209.
160. Mavrodontis, N., *Modelling hyperelastic behavior using test data in abaqus—Simuleon FEA Blog*. 2017.
161. Hu, P., et al., *Strength degradation of adhesively bonded single-lap joints in a cyclic-temperature environment using a cohesive zone model.* The Journal of Adhesion, 2015. **91**(8): p. 587-603.

162. Silva, L.R.R., et al., *Study of the optical, thermal, morphological and mechanical characteristics of a laser weldable fiber reinforced polymer.* Polymer Composites. **n/a**(n/a).

Appendix A

Paper 1: Polymer joining techniques state of the art review

Welding in the World
https://doi.org/10.1007/s40194-021-01143-x

RESEARCH PAPER

Polymer joining techniques state of the art review

L. R. R. Silva[1] · E. A. S. Marques[2] · Lucas F. M. da Silva[1,2]

Received: 23 October 2020 / Accepted: 12 May 2021
© International Institute of Welding 2021

Abstract
Modern products and structures require efficient material joining processes for their construction, able to combine similar or dissimilar materials, which almost always includes high-performance polymers. To design such joints, it is necessary to first understand the techniques currently used in this technological field and how they can be improved using advanced technological joining processes. In this manuscript, a review of several polymer-joining techniques is made, highlighting the recent technological advances in this field. The search for improved mechanical performance and lower costs has led to the development of new, high-performance engineering polymers, which require highly specific joining processes. These can include adhesive bonding, mechanical joining, welding or a combination of different processes, a technique known as hybrid joining. Several experimental works available in the literature have proven the validity of these techniques, although optimization processes are necessary to attain maximum performance. Additionally, extensive numerical with different methods and models has been carried out to better understand the processes and support parametric analysis. The intent of this work is to review studies on the most important polymer bonding techniques, the numerical models applied to simulate these techniques, the use of hybrid joints and describe promising techniques that are being developed and proposed for future use.

Keywords Joining · Polymers · Processing techniques · Numerical model · Adhesive bonding · Welding · Mechanical joining

1 Introduction

Modern society is highly reliant on diverse tools, components and equipment that are only possible due to use of advanced engineering polymers and composites with polymeric matrices. Automobiles, cell phones computers and medical devices are all prime examples of these objects, which must be manufactured in economically in large scale. Due to complex design of these products, joining technologies play a key role in their construction and the importance of joining polymeric materials has thus increased significantly. Significant effort has been dedicated to develop joining technologies that increase design flexibility, improve the mechanical behaviour of polymeric components and improve their durability, reducing failures and increasing service life [1–3]. Polymer-joining techniques now find extensive use in both structural and non-structural applications, for example thermal systems and coatings. Special polymeric-joining techniques are also available for applications where low chemical reactivity is required, as is the case of biomedical components manufactured with biocompatible materials [4–6].

Technical, or engineering polymers have evolved greatly since they were first synthesised in the early twentieth century [7, 8] and, following many decades of evolution, they now present greatly improved properties, achieved with new chemical synthesis and doping methods, forming novel copolymers or composites that meet rigorous industrial technological demands. Such advances have led to drastically improved mechanical, thermal, optical and chemical properties, as well as important manufacturing cost reductions. In addition, significant effort has been made to improve the workability of these materials, which has grown significantly in recent times when compared to metals and ceramics [3, 9–11].

A general analysis of the literature, [12–15] shows that the number of joining processes suitable for use with polymers is very large and is in constant evolution, providing new

Recommended for publication by Commission XVI - Polymer Joining and Adhesive Technology

✉ L. R. R. Silva
luiz.silva@ifes.edu.br

[1] Departamento de Engenharia Mecânica, Faculdade de Engenharia, Universidade do Porto, Rua Dr. Roberto Frias, 4200-465 Porto, Portugal

[2] Instituto de Ciência e Inovação em Engenharia Mecânica e Industrial (INEGI), Rua Dr. Roberto Frias, 4200-465 Porto, Portugal

Published online: 25 May 2021

alternatives that overcome the limitations of classical joining methods. Although the number of techniques available is extensive, methods for joining polymers can all be classified into three main groups. These are adhesive bonding, mechanical joining and welding, as shown in Fig. 1. In addition, hybrid joining methods, combining these different techniques in a single joint are also a valid solution.

One important consideration to be made when analysing polymer-joining techniques is making the distinction between their suitability for use with thermoplastic or thermoset polymers [16, 17]. This is especially important for methods that rely on the fusion of the material to achieve the connection. In addition, some of the methodologies have strict limitations in the applicability to complex geometries, restricting the joint configurations and contours [18]. With these specific particularities in mind, the application of hybrid processes has become increasingly more popular, exploring synergies between multiple joining processes to achieve higher performing joints and design less restricted processes [12, 17].

2 Engineering polymers and their uses

As stated in the introduction, high-performance polymers and its composites now find use in many critical applications and products, supported on decades of research on new material formulations and advanced manufacture techniques. The number of commercially available high-performance polymer formulations is quite large, encompassing a wide range of mechanical, physical and chemical properties. For structural purposes, polymers with high strength to weight ratio are sought, although more often than not they are used integrated in fibre-reinforced composites, due to the significant performance gain that can be obtained. However, high strength and stiffness is not always necessary, and many applications impose other requirements to polymeric materials such as high moldability for injection moulding processes, low transformation energy and good optical properties. However, such variety in requirements can create significant difficulties in the material selection processes [9].

For products which use joining in its construction, it also necessary to understand how the polymeric material properties are affected by the joining solution being employed, which often is performed via experimental testing. An additional issue is the increased interest in expanding the use of bio-degradable and recyclable polymeric materials, which are sometimes compromised with regard to their mechanical properties and durability [19–26].

Engineering polymers are now used in a wide range of industries, including bioengineering applications, the aerospace and automotive sectors, packaging of consumer products and electronics, among others. In all these cases, effective joining processes are essential to create a complete final product. Table 1 summarises the common applications of engineering polymers and provides references on joining materials for each specific application.

Due to the wide diversity chemical formulations of polymers, there is a large number of engineering polymers currently available in the market and which find extensive use. Before the discussion of the most important polymer joining techniques is made, it is important to understand the key engineering polymers that are the target of research on joining methods, their uses and main characteristics. Table 2 lists some of the main engineering polymers and some of their composites and provides examples of research works on joining these materials.

The process of joining polymers can be achieved by diverse methods, which can rely on physical or chemical connections. Mechanical joining, for example using fasteners, relies on a physical load transfer while welding joins the material efficiently at the chemical level. In addition, it is also possible to achieve a strong joint with the combination of physical and chemical connections. This is the case in adhesive bonding, where chemical forces and mechanical interlocking processes are responsible for transferring the load [12, 56, 65]. Hybrid-joining techniques which combine two different joining technologies in a single joint are also an important alternative for joining these materials. An hybrid joint can be attained, for example, by combining fastening with welding, allowing to obtain improved mechanical performance or increase damage tolerance [55, 58].

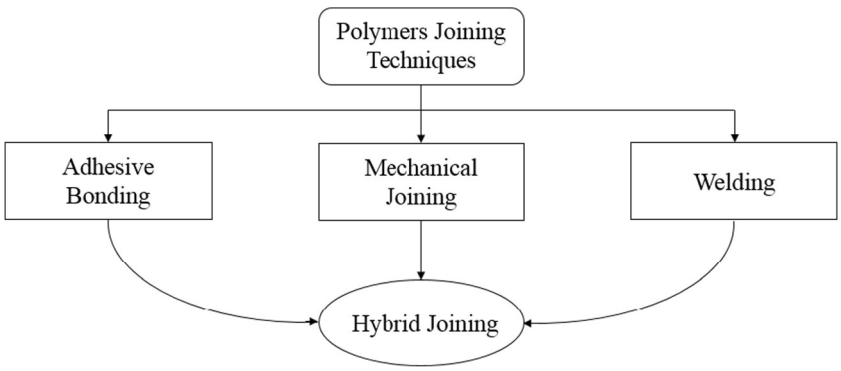


Fig. 1 Main process of joining polymers

Table 1 Main applications of engineering polymers

Main areas	Specific application	References
Aerospace	Airframe structures	[1, 27–32]
Automotive	Headlights, panels, chassis	[1, 27, 28, 30, 31, 33–39]
Biomedicine	Prosthetics	[1, 3, 22, 29, 31, 40–45]
Packaging and food sustainability	Food and drug packaging	[1, 27–31, 46]
Clothing and protection	Clothing coating, ballistic protection	[4, 19, 27, 29–31, 47]
Others	Electronics, Concrete reinforcement, Marine	[1, 28, 29, 31, 48–54]

In this review, adhesive bonding, mechanical joining, friction stir welding and laser welding of polymers and polymeric matrix composites will be discussed in detail, with the following sections describing some of key experimental and numerical works in this field as well as the key lessons learned with these studies. Only two welding processes (friction stir welding and laser welding) are discussed in detail in the following sections as these were considered to be those with the highest industrial and scientific importance, and thus having the greatest potential for improvement. Of course, there are many alternative welding technologies suitable for bonding polymers, although many of them are relatively outdated or of low technological relevance, while other are prospective in nature and still need further maturing before practical usage. These polymer welding techniques can be categorised by their working principle, which can rely on thermal energy, friction or electromagnetic fields [4]. Table 3 lists these polymer welding techniques, indicating their respective advantages and disadvantages.

3 Adhesive bonding

Even though its use for engineering purposes is relatively recent, adhesive bonding is an ancient technique, first used when the early civilizations started to explore the adhesive properties of several natural materials, such as lignin, a natural adhesive extracted from wood fibres, which was used to produce tools and other primitive instruments. Although the mechanical performance of these early adhesives is very limited, subsequent technological advances gradually led to more powerful adhesives. Obtained through chemical synthesis these structural adhesives are able to support much larger, structural mechanical loads. The industrial sectors that spearheaded the application of this technique were the automotive and aerospace industries [1, 5, 57, 59, 60], which have mastered this technique to produce highly complex multi-material vehicle structures where adhesives join metals, polymers and composites.

If used properly, adhesive bonding can enable the design of high-performance structures and research in this field has significantly increased, with many works devoted to experimental and numerical methodologies to predict joint performance and validate its application in industrial applications. Many key works [27, 28, 31, 40, 62–64, 66–68] analyse variables such as stress field and its geometrical dependence, the stress intensity factor for the fracture process and the correlation between adhesive joint performance and the adhesive and substrate behaviour, encompassing thermal, mechanical and chemical parameters.

Table 2 Main polymers and polymer-based composites used for engineering purposes and their main characteristics

Polymers and polymeric composites	Characteristics	References
Epoxy	Resin used as a cohesive material in adhesive, great impact resistance, stiffness and durability	[1, 27, 30, 31, 40, 43, 49, 52, 54–61]
Carbon reinforced epoxy	Material used to ensure cohesion of fibre-reinforced composite	[1, 27, 30, 31, 35–37, 48, 62]
Polyurethane	Material used as thermal insulator and flexible sealant	[1, 27, 30, 31, 57, 62]
Polyethylene	Material used as component of artificial mobile protheses and other biomedical application	[1, 3, 63]
Acrylic	Provides excellent fatigue endurance, impact resistance, and superior toughness when compared to other polymer systems	[30, 31, 52]
Polyamide 6	Typical material used in the automotive sector for moulded components	[1–4, 27, 30, 31, 64]
Polyamide 6 glass reinforced—PA6 GF	Typical material used in the automotive sector for high strength and durable moulded components	[1, 27, 30, 31]
Others	Electronics, concrete reinforcement	[1–4, 27, 30, 31, 49, 54, 63]

Table 3 Different types of techniques for welding polymers and their respective advantages and disadvantages. Adapted from [4]

Characterisation	Welding Method	Advantages	Disadvantages
Thermal	Laser	One-step process, highly localised heating, instantaneous bonding, no vibration, contact or particulates, low residual stresses. Broad range of laser absorbers available and corresponding wavelengths.	Requires laser absorption at interface, requires top part to be laser transmissive, part thickness limitations, may require pigmentation, high capital costs.
	Self-bonding	High joint strength can be achieved.	Entire sample is heated, including internal components.
	Hot-plate	Simple and economical.	Two-step process, contact of heating element, long process time, overheating and degradation can occur, not suitable for polymers with high melting point.
	Hot gas	Economical, complex geometries.	Manual process—operator skill required.
	Extrusion	Shorter process time than hot gas.	Manual process—operator skill required.
	Infrared	Non-contact heating, short process time, suitable for polymers with high melting point.	Two-step process, highly dependent on polymer's absorption characteristics.
Friction or Viscoelastic	Friction Stir Welding	High joint strengths can be achieved.	Entire sample is heated, including internal components.
	Vibration	Short process time.	Limited to larger components, restricted to flat surfaces, not for tight tolerance requirements, not for thin wall parts, high internal bending forces.
	Spin	Simple and economical.	Components must have symmetrical and circular cross-section.
	Ultrasonic	Economical, mass production, short process time.	Requires energy directors to be incorporated at seams. Limitations associated with semi-crystalline polymers.
Electromagnetic	Resistance	Complex geometries.	Slow process time.
	Microwave	Short process time, complex geometries.	Material degradation risk for polymers with polar groups.
	Induction	Short process time, complex geometries.	Expensive machinery. Insert at joint may corrode.
	Radiofrequency	Short process time, simple and economical.	Requires polymers with polar groups and high dielectric loss factor, limited to thin sheets/films.

This technique is suitable for bonding many different materials [41–43, 45, 48, 49, 53, 59, 61, 69, 70], but its true power lies in its unrivalled capability to join dissimilar materials. In many of these applications, one of the two materials to be bonded is often a polymer or a fibre-reinforced polymer composite.

At its most basic, the adhesive bonding technique consists in joining two materials (the substrates) to form the joint, using a fixing material called the adhesive. The adhesive is usually applied between the two substrates in an uncured liquid form or paste form and is later polymerised into a solid final product. It can also be applied in solid form, melted to create the joint and then cooled down to create a solid connection. Both methods may use pressure to create a better-quality, defect-free connection. There are many different types of joint geometries available to assess the strength of an adhesive connection or the strength of the adhesive itself. Figure 2 illustrates examples of some of the most commonly used geometries.

Although highly advantageous for many applications, adhesive bonding of polymeric substrates is notoriously complex, as the surface energy of polymers is quite low. As modern adhesives are also mostly polymeric in nature, they exhibit a low level of surface energy and this almost inevitably leads to low adhesion at the adhesive-polymer interface [1]. It is thus necessary to avoid this issue with the application of suitable surface treatments. These treatments can be passive or active in nature. While the first just modify the morphology of the substrate's surface, active treatments effectively change the chemistry of the substrate, greatly enhancing its surface energy. The work of Ebnesejad et al. [72] details types of surface preparation techniques for polymer adhesive joints.

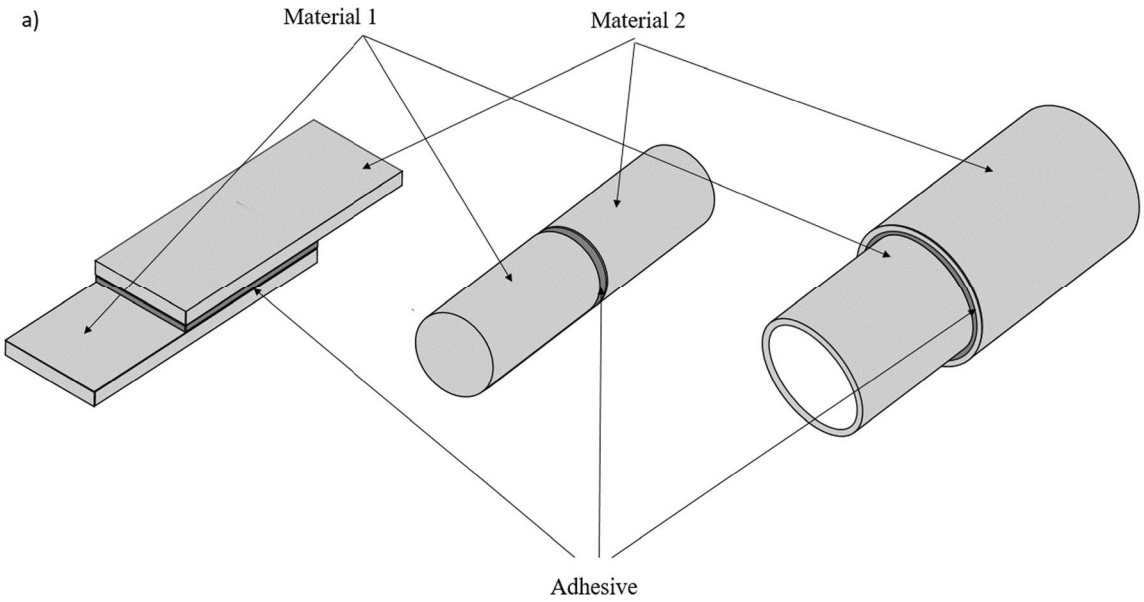


Fig. 2 Examples of specimens used for testing the performance of adhesive joints: single lap shear joint (SLJ), tube butt joint and tube lap shear joint adapted from [71]

Molitor et al. [73] and Sabreen et al. [74] studied the effect of different types of surface treatments for bonding titanium and polymers. The prevalence of treatments that oxidise the surface of the material is observed, with most effective using corona discharge, plasma, flames and laser energy. Zhang et al. [75] report that the effectiveness of the surface treatment for bonding polymers based on corona discharge is proportional to the exposure time. It is also specified that the resting time after the discharge is made on the corona surface is inversely proportional to the effectiveness of the joint strength.

Necasova et al. [76] studied the joining of polyurethane with wood for different types of surface treatments. This included plasma, chemical etching (NaOH based) and sandblasting as well as the addition of a of the primer coating to support these treatments. In this work, it is reported that regardless of the treatments, the addition of the primer coating enhances the joint resistance. It is also observed that the physical based treatment provides better results than the chemical treatments.

Bukhari et al. [77] pointed out that physical-chemical interactions directly interfere in the effectiveness of adhesive joints, specifying the mechanical locking models and their failure modes, the theory of adhesion explaining the theories of adsorption, diffusion, electronic and electrostatic force, chemical bonding and weak forces, wettability, and surface energy. For cases where even after the surface treatment the surface energy of polymeric substrates is still too low to allow bonding with adhesives, Jin et al. [78] propose the use of "tetrapodal ZnO linkers". This technique introduces fixing particles on the surfaces of the two materials, generating an interlock between the two surfaces. The working principle of this technique is illustrated in Fig. 3-a. Experimental testing has shown this to be a very effective solution to increase the peel strength of bonded joints with polymeric substrates (Fig. 3-b).

Irrespective of the type of substrate being bonded, be it metallic, composite or polymeric in nature, proper adhesive joint design is crucial to ensure maximum adhesive joint performance. To aid in this design phase, modelling is often employed, allowing to precisely determine the geometry and the materials which can most efficiently withstand the service loads and conditions. The first approaches for predicting adhesive joint behaviour were based on analytical models, which although limited in scope are quite powerful and fast to use as described by da Silva et al. in a detailed review of these methods [79]. Presently, numerical modelling has become the favoured design methodology for predicting the performance of bonded joints, as it allows for the analysis of highly complex models. Numerical modelling can employ continuum mechanics and simpler stress analysis or it can make use of cohesive zone modelling, which combine continuum mechanics with fracture mechanics, reproducing the onset of damage and its propagation through the adhesive joint [80].

Many research works generate models for the mechanical response of simple specimens used to characterise an adhesive, with the objective of using this data for more complex joint models at a later stage. For example, Braga et al. [81] characterised the behaviour of double cantilever beam (DCB) specimens bonded with an epoxy adhesive using cohesive zone modelling. The results were found to agree with those experimentally obtained, employing a 2D model constructed with a combination in stress plane and cohesive elements, as shown in Fig. 4.

Numerical modelling is also suitable for precisely determining the influence of geometrical parameters on the

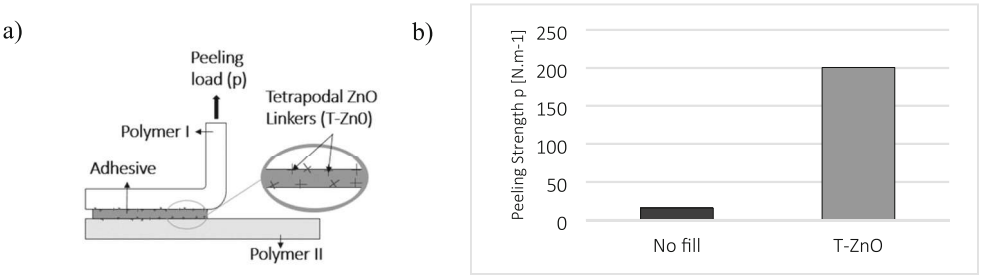


Fig. 3 **a** Application diagram of T-ZnO at the substrate-adhesive interface. **b** Comparison of the joint peeling strength without and with the T-ZnO filling. Adapted from [78]

behaviour of bonded joints. The work of Adams et al. pioneered this approach by studying different effects such as the influence of the spew fillet in the ends of the adhesive layer and the adhesive layer thickness [82, 83]. da Silva et al followed with a detailed experimental study devoted solely to the analysis of the adhesive layer thickness in SLJs [84], stating that the lap shear strength increases as the bond line gets thinner and the adhesive gets tougher. More recently, the work of Silva et al. [85], numerically modelled the behaviour of scarf joints, using three different adhesives formulations and varying the scarf angle. These models employ the cohesive zone model formulation, using three different cohesive zone law shapes. The triangular, trapezoidal and linear-exponential formulation are used, and it is found that for each adhesive formulation there is a specific cohesive law shape that better fits the experimental results. Oliveira et al. [86] carried out several experiments in SLJs, bonded with five different adhesive layer thickness and also determined the corresponding fracture toughness in mode I or mode II using DCB and ENF testing of the adhesive. The results of this work are summarised in Fig. 5-a and Fig. 5-b.

The results show that for this specific joint configuration, a greater load capacity is obtained for larger adhesive thicknesses. As for the G_I and G_{II}, a linear increase was found with the increase of the studied thicknesses up to the value of 1 mm.

In search for a deeper understanding of the influence of the thickness of the adhesive in the performance of a bonded joint, Sadeghi et al. [87] proposed different numerical methods to characterise the behaviour of bonded joints with adhesive layer thicknesses of 0.2 and 0.9. The analysis is performed in a SLJs, using an epoxy adhesive and steel as an adherent material. The models under comparison are cohesive zone modelling, surface-based cohesive model (SBCM), the virtual crack closure technique (VCCT) and the extended finite element method (XFEM). In general, the results show that all techniques can obtain reasonable correlation between the experimental and the numerical results and can capture well the effect of adhesive layer thickness. However, there are varied specificities for each of these methods which requires a critical analysis of their capabilities and limitations in the selection of the most suitable method for each case.

One of the main factors influencing the performance of bonded joints is the interaction between the mechanical behavioir of the substrate and the adhesive, and this especially true when polymeric substrates are used. Pérez et al. [88] carried out a study on two pairs of polymeric substrates (PTFE and PVT), bonded with five different types of adhesives. One of the adhesives is biomimetic, based on 3,4-dihydroxyphenylalanine (DOPA) found in shellfish, the second is based on the same biomimetic adhesive but with the

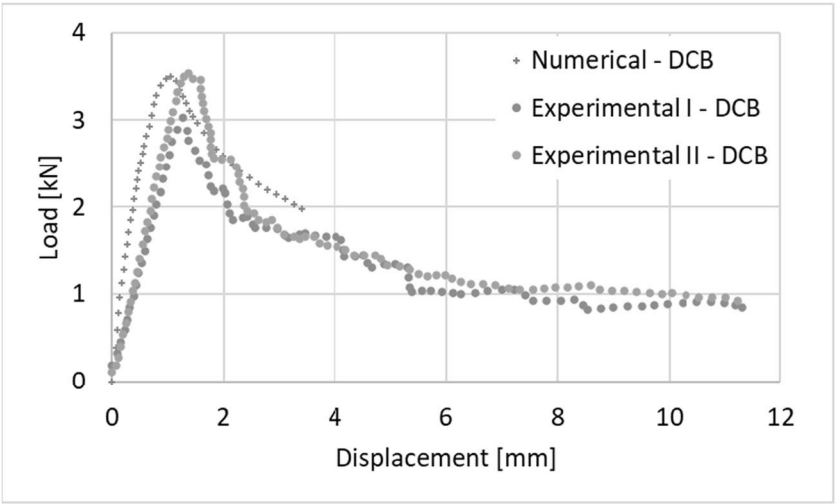


Fig. 4 Load vs. displacement of experimental DCB testing and FEM model. Adapted from [81]

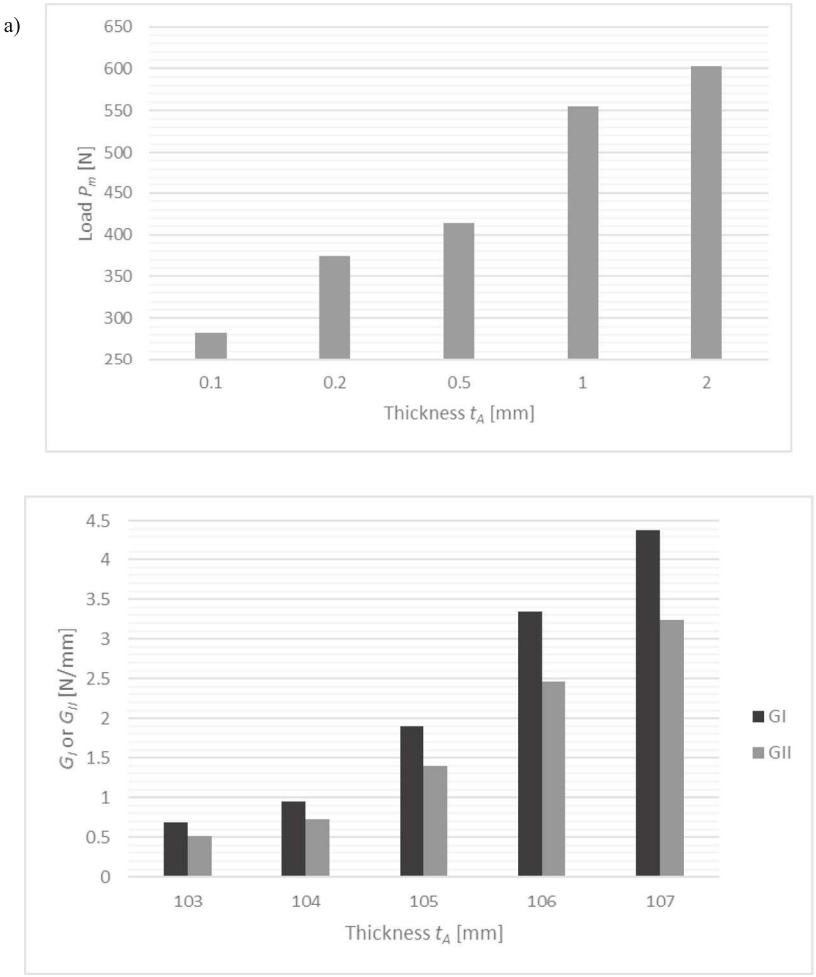


Fig. 5 **a** Average of load - P_m to each adhesive thickness - t_A, **b** energy release rate for mode I - G_I, and mode II - G_{II} to each t_A by the compliance-based beam method (CBBM) adapted from [86]

addition of a periodate (IO4), used to increase the adhesion of the adhesive (DOPA + IO4). Finally, three other synthetic artificial adhesives were considered, and these are polyvinyl acetate (PVA), cyanoacrylate (CNA) and epoxy. The results are shown in Fig. 6.

For the DOPA-IO4 and CNA adhesives applied to the PVT substrate maximum load was of 5.7 MPa because the failure

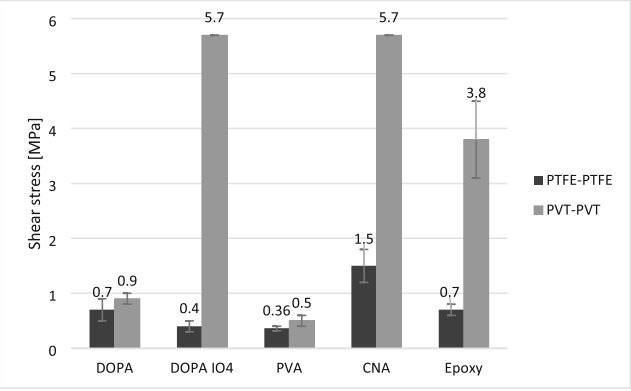


Fig. 6 Maximum shear stress sustained by PTFE-PTFE and PVT-PVT joined with different adhesives adapted from [88]

was always cohesive in the substrate. For the PTFE substrate, the best performing adhesive is the CNA, due to the higher number of cross-links it creates. When bonding PVT, besides the crosslinking relationship of the NAC, there is also a higher interrelation between the forces of the molecules at the interface, simultaneously increasing the adhesion and cohesion. This adhesive and cohesive effect is also pronounced for the other adhesives in PVT. In conclusion, the interface strength is highly dependent on the adhesion and cohesion levels. In another configuration, Hsiao et al. [89] studied the application of multiwalled carbon nanotubes—MCNT in the adhesive. This was carried out to reinforce an epoxy adhesive shear strength in SLJs using graphite composite substrates. The study was done with the addition of 1 and 5% of MCNT, compared with the performance of neat epoxies. The increase in shear stress in response to the addition of 1 and 5%, when compared to the adhesive without MCNT, is 31.2 and 45.6% respectively, showing this to be an effective method to increase joint strength.

In the automotive industry, adhesives are finding greater and greater use for the construction of vehicle bodies. In this specific application, the impact behaviour of the adhesive and

the joints it forms is crucial to ensure occupant safety in the event of a collision [35, 36, 90]. An example of a work in field is the study made by Machado et al. [37] which models the quasi-static and impact behaviour of single lap joints with composite and aluminium substrates, bonded with a high-performance crash resistant adhesive. The proposed cohesive zone model for impact uses material data which has been determined at high strain rates and good agreement is reached between experimental and numerical results.

The behaviour of adhesively bonded joints under harsh environmental conditions has been the target of several studies [91, 92]. As stated by Borges et al. [93], this is a critical subject for the design of bonded polymeric components, as these materials absorb water which can migrate into the adhesive-substrate interface and dimmish joint strength and cause adhesive failure. Banea el al. [91] conducted a study to characterise mechanical properties such as the Young's modulus and failure stress in adhesives subjected to ageing by moisture uptake and reinforced with thermally expandable particles (TEPs). The results are summarised in Fig. 7.

It is observed that the modulus of elasticity is affected by the increased TEP content only in aged materials. Fatigue testing was also carried, and reduction of the fatigue life was also found with an increase in TEP content.

Sugiman et al. [94] has used numerical modelling to analyse the behaviour of monolithic single lap joint (MSLJ) and laminated double in bending (LDB) joints, bonded with a film adhesive and tested under natural and aged conditions (1 year and 2 years). Their methodology allows the models to consider the degradation of the material properties due to ageing. Figure 8 illustrate the relationship of the maximum error between the experimental and the FEM study.

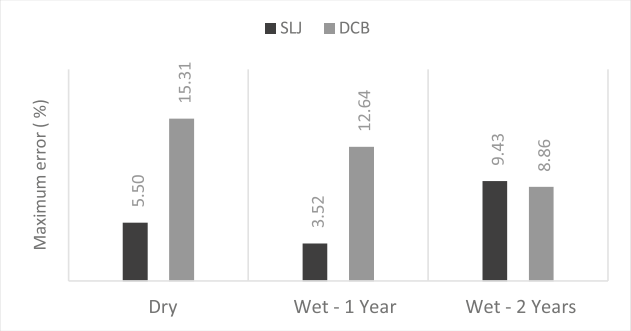


Fig. 8 Comparison of the error between the experimental and numerical results, adapted from [94]

The numerical model can precisely reproduce the experimental fracture process for the LDB test. Showing that it occurs in in the adhesive fillet formed at the ends of the overlap and at an of 45° relative to the load direction, as shown in Fig. 9.

Although adhesively bonded structures perform better under fatigue loads than other joining methods, such as fastening and welding, adhesive joints are still susceptible to fatigue failure and this has been the target of many studies, both experimental and numerical. The work of Rocha et al. [95] is an example of how numerical modelling can be employed to predict the fatigue behaviour of and adhesively bonded joints. In this case, a fatigue crack growth analysis is carried out with a model based on cohesive zone mode (CZM), with triangular cohesive laws. DCB and ENF joints (mode I and mode II) were simulated with Abaqus using a User material subroutine (UMAT) to reproduce the fatigue behaviour of the adhesive. A Paris law-based approach was employed using experimentally obtained adhesive fatigue crack data growth data. The accuracy of the model can be assessed by comparing the predicted number of cycles to failure and by comparing

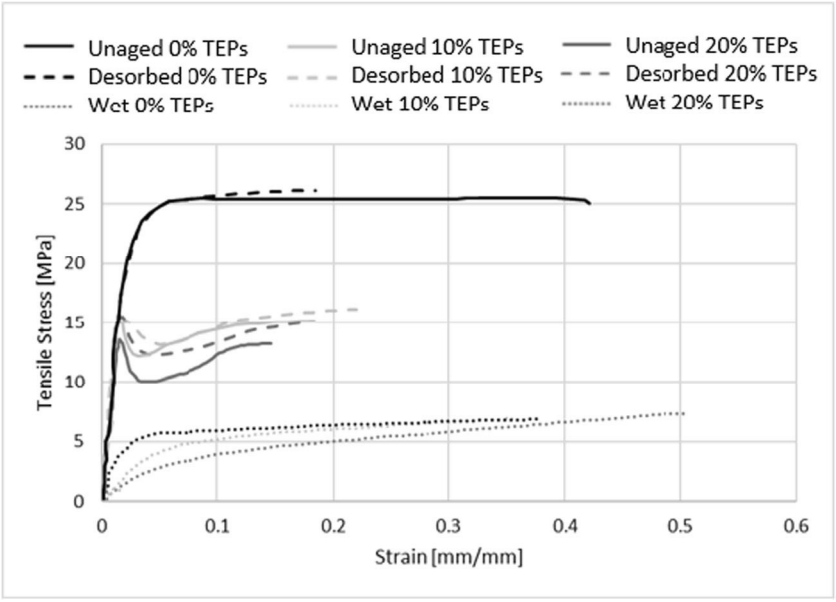


Fig. 7 Representative stress–strain curves of the TEPs-modified adhesive as a function of moisture adapted [91]

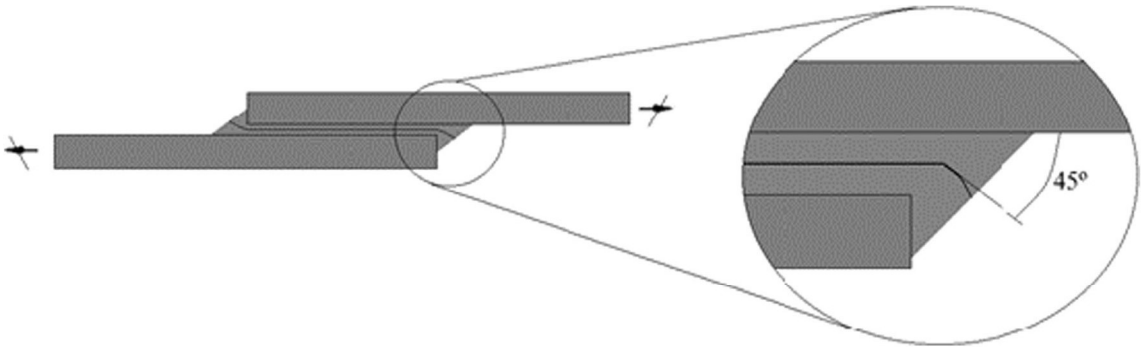


Fig. 9 The static failure characteristic of fillets in SLJ adapted from [94]

experimental and numerical compliance curves as shown in Fig. 10.

Other works [52, 96, 97] have studied the fatigue crack growth in adhesives in order to generate a Paris law. These works have included several different structural adhesives and indicate that greater load amplitudes lead to a faster crack propagation, shortening the service life.

As a summary of this section, it can be stated that adhesive joining is a very powerful technique, suitable to join a wide range of materials, including polymers. However, the specific case of polymer joining requires special attention to be devoted to the surface preparation and many researchers have demonstrated the effectiveness of several surface treatment techniques. It has also been shown that proper geometrical design of a joint can be supported with finite element modelling. Lastly, the degradation of the performance of adhesives under service conditions, such as high humidity environments and fatigue loads, must also be taken into account in the design phase.

4 Mechanical joining

Mechanical joining of polymers consists in the use of mechanical loads or ancillary mechanical components to create connection forces that join two or more materials together. Mechanical joining via plastic deformation is possible in polymers, but it is more common in metals as the low elastic modulus of polymers usually precludes this approach. Thus, mechanical joining of polymers usually employs fasteners, which can take the form of screws, rivets and pins, as shown in Fig. 11 represent single lap joints (SLJ).

Although their use is well-established, the performance of mechanical joints is governed by several different variables and parameters, all of which greatly influence the effectiveness of its application [77]. For high-performance applications this can pose important design challenges, but in many simpler and less costly applications it is widely used, especially when different materials are bonded, and a low sealant capacity is required [98, 99]. One of the main drawbacks of this technique is the fact that it creates highly localised stresses which occur at the location of the fasteners. This means that for soft and low strength materials, such as polymers and some polymer composites, there is a high likelihood of damage in the substrate. This technique is well-established for electronic applications as well as the civil engineering and mechanical construction sectors [100–102].

Despite its popularity, there is only a limited number of studies published regarding its use for joining polymers. Nonetheless, mechanical joining is widely used for bonding

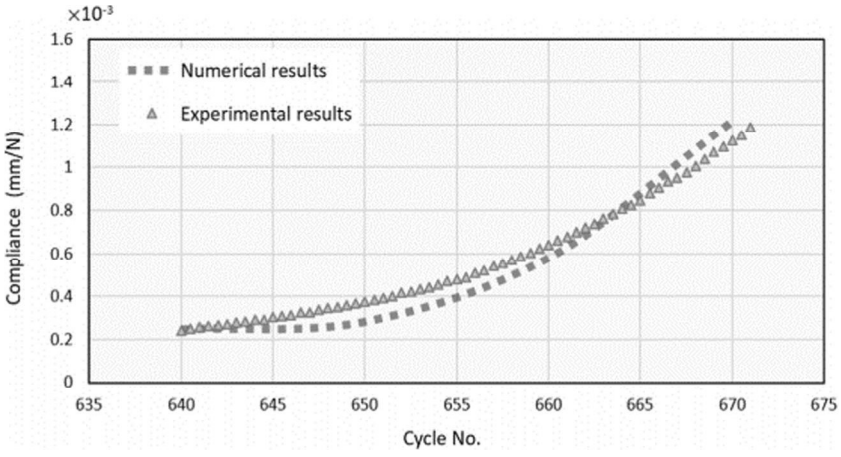


Fig. 10 Compliance as a function of load cycles: comparison between the numerical data and the experimental results adapted from [95]

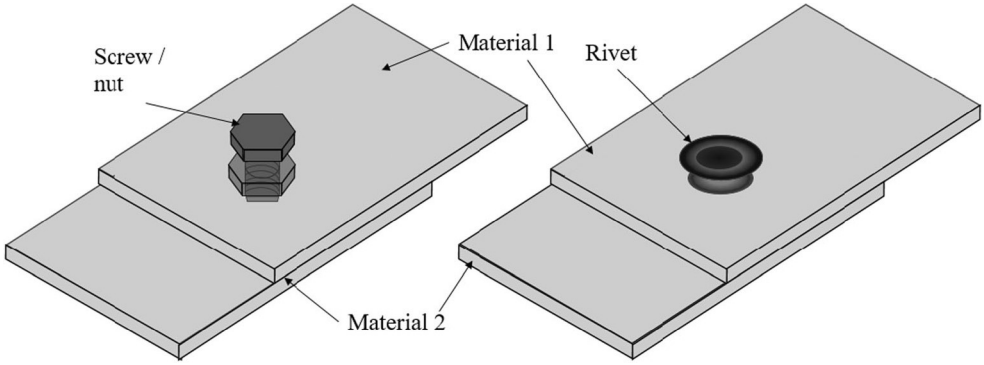


Fig. 11 Types of mechanical joints (general). On the left side shows a SLJ fixed by screw/nut. On the right side it shows a rivet-mounted SLJ

polymers in many applications and many of the recent developments and studies focus on the use of fasteners for joining long fibre-reinforced composites, metals or even concrete [12, 14, 103–105].

As stated in the introductory section of this chapter, mechanical joining by plastic deformation of polymeric substrates is a challenging procedure but can be performed for some materials. Alves et al. [106] published a study on the end-to-end joining of PVC tubes. The tubes are chamfered in such a way that they can fit into each other. After the bevel is made, an axial force is applied to join the two tubes, deforming them by pressure and forming a protuberance in the connection. Finally, a second pressure movement is made through a press external to the pipes, plastically deforming the protuberance region and joining the pipes. The methodology was found to compare well with adhesive bonding and thermal fusion but the relationship between the axial fixation forces and the compression force must be well gauged, otherwise weak spots may appear. The work of Bragança et al. [107] describes an environmentally friendly joining process based on sheet-bulk plastic deformation to connect polymer to polymer or polymer to metal in a perpendicular direction. The concept relies on careful material characterisation and finite element modelling, using an extension of the flow formulation to pressure-sensitive polymers.

An important compilation of numerical models for mechanical fastening techniques, was published by Mackerle et al. [108], covering the period from 1990 to 2002. The present work thus aims to highlight some of the most recent advances in this field and uses this to explain the key factors that govern the performance of these joints. The analysis of a mechanical joint usually requires a study of distinct features of the connection. These include the study of the interactions at the contact interfaces and the stresses generated near the pin. Amancio-Filho et al. (2009) [12] analysed the contact between the surfaces of a SLJ and a fixating pin through a finite element method (FEM) model, aiming to calculate the stress intensity factor for crack propagation. In this work, it was concluded that there is a compressive stress concentration in the hole, by which the plate fails. Bhonge et al. [109] explored the application of a numerical model for 2D and 3D cases in DLJs problems for two distinct cases: when the fixation element is only one pin and for complex situations which require multiple pins. Both analyses were performed for unidirectional tension and fatigue. In the latter case, the load applied can be represented by an oscillatory function. However, for the 3D geometry, the analysis becomes increasingly complex but still can accurately model the joint behaviour.

He et al. [110] complemented this analysis through the comparison between two mechanical fastening techniques and spot welding. The mechanical joining techniques used are self-piercing (SPR) and mechanical clinching, the first is usually applied to join two or more sheets of material, and in the latter the interlocking occurs due to a high pressure, which is a procedure widely spread in the automotive industry to join metallic components. Figure 12 shows that mechanical joining techniques, particularly SPR and clinch, are stronger than spot welding. However, their strength is also more sensitive to the number of loading cycles they are subjected to.

He et al. and Lancu et al. [110, 111] characterised the stress field and the fracture zone in bolted SLJs to validate the simulation against experimental results, Fig. 13. These works show that the stress field analysis is suitable to predict the failure mechanism of these joints. Both authors agree that the higher the torque applied to the screw, the lower is the

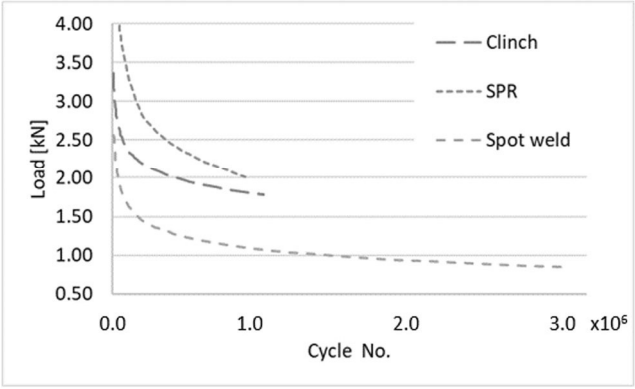


Fig. 12 Comparison between the fatigue behaviour of SPR, clinch and spot weld joint (adapted from (HE, 2013) [110]

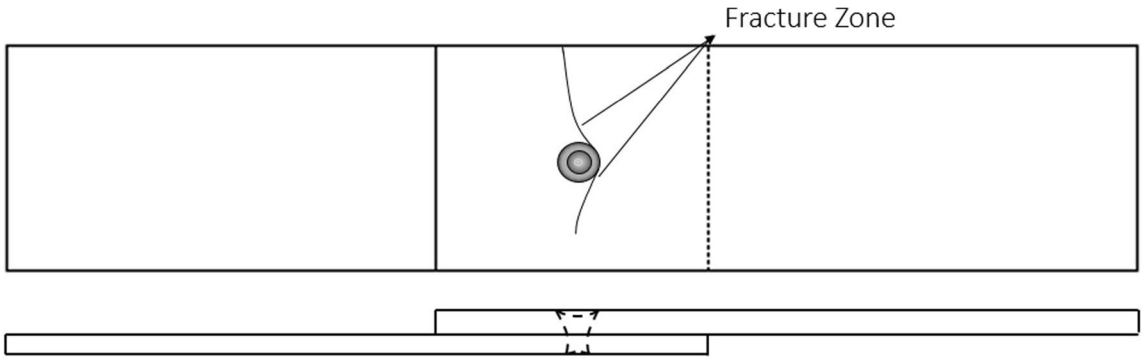


Fig. 13 Schematic representation of the fracture zone near the joint pin adapted from HE et al. (2013) [110]

plate strength under tension, implying the weakening of the region in the contour of the fixing element. Nassar et al. [112] created and validated a similar model that is able to correlate the tightness of the screw on the damage created in composite substrates.

Kweon et al. [34] and Ueda et al. [38] studied the mechanical joining of DSJs with CFRP substrates joined using pins. Both authors conclude that the stress levels in the joint do change significantly with the failure of the fibre reinforcement. Ueda et al. (2012) [34] complemented these studies, analysing the failure of the fibres or rivets under fatigue loading. It was concluded that the failure is similar, and the fibres collapsed on the regions under compression, through the crushing of the fibres until complete failure of the material, Fig. 14 shows that the CFRP fibres fail before the fastener.

To conclude this section, it can be stated that mechanical joining of polymers is a practical and relatively inexpensive procedure. Both the use of plastic deformation and the application of fasteners require careful design using numerical modelling. This is due to difficulty in predicting the material flow during forming and the inherent stress concentrations generated at the locations of the fasteners. The latter case is especially true if fasteners are used to join composites with a polymeric matrix. Finite element modelling allows to determine the stress concentration that occur at the pin locations, as well as the interaction between the compressed contact surfaces of the materials being joined.

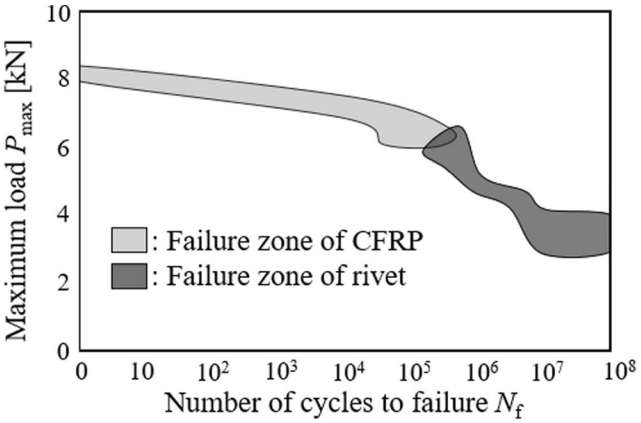


Fig. 14 Maximum load as a function of cycles to failure zone of CFRP laminates jointed using rivet. Adapted from [38]

5 Friction stir welding

Friction stir welding (FSW) is a solid-state joining method that, while relatively recent, has evolved greatly in the last couple of decades. This joining method has the advantage of minimising the thermal energy applied to the substrates, joining materials through friction using equipment that is widely available in industrial environments, such as a lathe, a milling machine, either with manual or with numerical control (CNC) [113, 114].

FSW joins two materials using friction through the rotation of a metallic pin applied at their interface (Fig. 15). A solid connection is achieved because the energy released by friction is paired with the pressure applied by the pin and softens the base material, without melting. This process increases the activation energy between the surfaces causing plastic deformation. The materials are essentially joined through a forging process [114–117].

FSW can be used to join a wide range of different materials and is especially well suited to for use with thermoplastic polymers, joining these materials with minimal energy

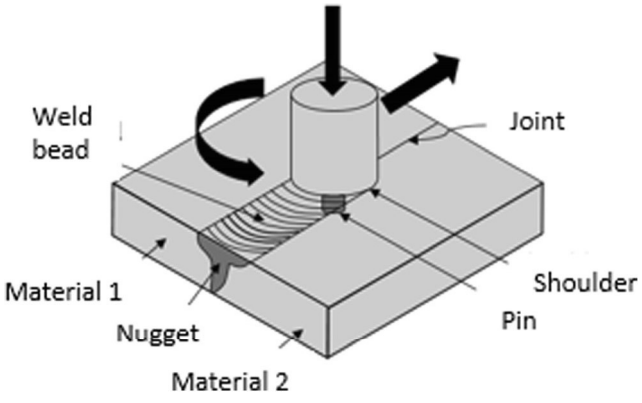


Fig. 15 Friction stir welding technique (adapted from [113])

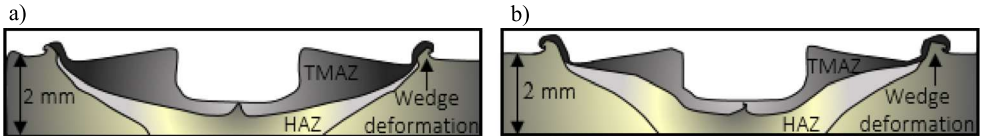


Fig. 16 Evolution of the microstructure during the plunge and dwell phases. **a** 600 rpm after a dwell phase 1.0 s. **b** 1200 rpm after a dwell phase 1.0 s [130]

application. Friction stir welding of thermoset polymers is not possible, as these materials will not soften with temperature and will degrade instead. Nonetheless, this technique is quite flexible and has been further developed to join dissimilar polymers formulations [115, 118, 119] dissimilar metallic alloys [120–124] and polymers to metals [125–129].

Many of the challenges associated with the practical implementation of FSW joints are related to the manufacturing process itself and its key parameters, such as for example the rotational speed of the pin and the pressure it exerts over the substrates. Gemme et al. [130] studied the influence of the rotation speed of the pin on the thermo-mechanically affected zone (TMAZ) and heat-affected zone (HAZ), using an aluminium alloy (Fig. 16-a and Fig. 16-b). The wedge formation in the periphery of the material in contact with the pin was also explored.

It is observed that the greater the rotation, the greater area the HAZ will cover and the greater the wedge deformation of the welded material. It is also shown that as the rotation increases, the temperature of the surface also increases, increasing the softening of the material and lowering the resistance the material imposes to the rotation movement of the pin, i.e., the torque caused by the pin/base material contact (Fig. 16). Figure 17 displays five relevant time steps: t_0, with represents a phase of rotation without contact; t_1, which is the start of the plunge phase, before the shoulder contact; t_2, which is time of the maximum torque after complete plunge; t_3, which is the dwell phase and t_4, which is the end of the process.

The design parameters, such as feed speed, rotation speed and tool depth, were further analysed by Eslami et al. [131] in the joining of polypropylene and polyethylene. It was observed that the tool parameters strongly influence the strength of the joint (Fig. 17). For feed speeds between 20 and 100 mm/s, with, 1500 to 2500 RPM and 2.4 to 2.8 m of tool depth, it is observed that the lower the speeds and the greater the depth of the tool, the greater the resistance of the joint. Adibeig et al. [132] confirms these results with the analysis of strength as a function of pin length using PMMA joints Fig. 18.

The mechanical strength and fatigue behaviour of joints with dissimilar polymers has also been studied by Eslami et al. [133], which have compared the performance of FSW against that of single and double riveting using polypropylene (PP) and polyethylene (PE) substrates. It was shown that FSW provides higher strength and fatigue resistance to the joint than single riveting. However, double riveting exhibited the best mechanical properties. Kredegh et al. [134] analysed the fracture process of aluminium T-joints, bound together through FSW, concluding that, because deformation can occur in different directions, crack progression is also multidirectional, developing towards different areas of the joint.

Additional research has been carried out to understand if reinforcement materials, such as carbon nanotubes, can enhance the performance of polymeric joints created using FSW. The work of Gao et al. [135] studied the joining of a high density polyethylene (HDPE) with a acrylonitrile-butadiene-styrene (ABS) reinforced with carbon nanotubes and determined that, contrary to what was found for metals, the micro hardness of the heat affect zone is higher in the centre (Fig. 19), which has implications in the mechanical performance of the joint.

Numerical simulation of the FSW process is another important topic of research, as it can allow for optimization for optimization of the design parameters especially for joining combinations of polymers. Therefore, the range of numerical examples given for this process will be extended from just polymers to metals [137, 138].

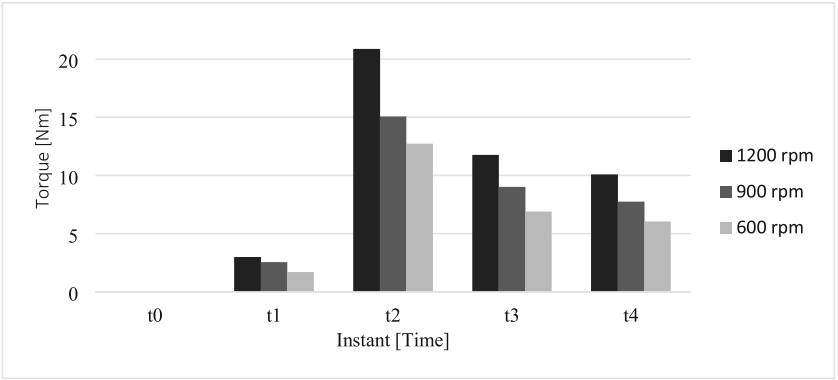


Fig. 17 Experimental recording of torque during the plunge and dwell phases (adapted from [130])

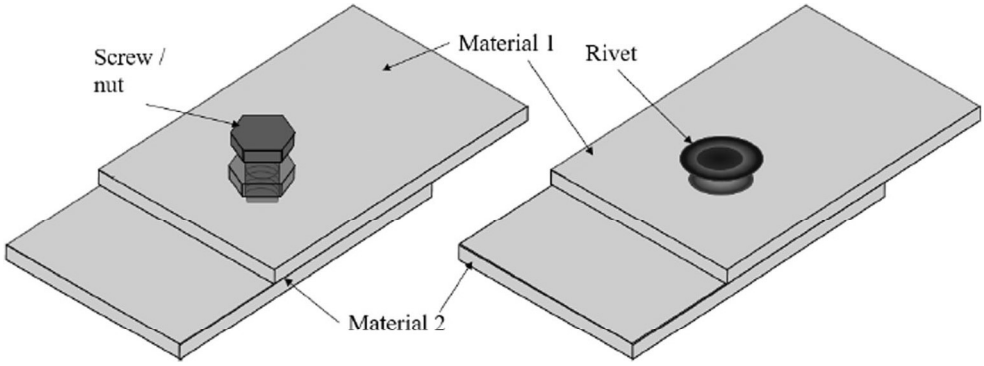


Fig. 18 Contour plots of the maximum tensile load level observed vs different welding parameters [133]

Padmanaban et al. [139] analysed the stresses imposed by the contact between the base material and the pin. The higher stresses were found in the material immediately ahead of the pin, since there is a gradient due to the stress imposed by the pin on the interface of the material and the material is still at its original state. After the pin advances, the stress concentration at that point decreases due do the softening and plastic deformation of the material. The temperature gradient in the vicinity of the pin was also studied [139–141] with aluminium plates as base metal, both in the cross section and across the plate (Fig. 20-a, Fig. 20-b and Fig. 20-c).

The work of Zhao et al. [141] and Kim et al. [136] include the numerical modelling for a thermal analysis of the FSW process and complement it with a study of the material hardness using a quench factor analysis. This allows to understand how the material behaviour is affected by the heat generated during the welding process and enables more precise simulation of the mechanical response of the welded material.

In sum, current research shows that FSW is an efficient and effective method to join thermoplastic polymers and composites. However, the performance of this method is highly dependent on the welding parameters, and this stage it requires careful experimentation. Again, finite element analysis of the FSW process can be used to streamline this parameter tuning process, optimising the joint performance by analysing the stresses and temperature gradients generated.

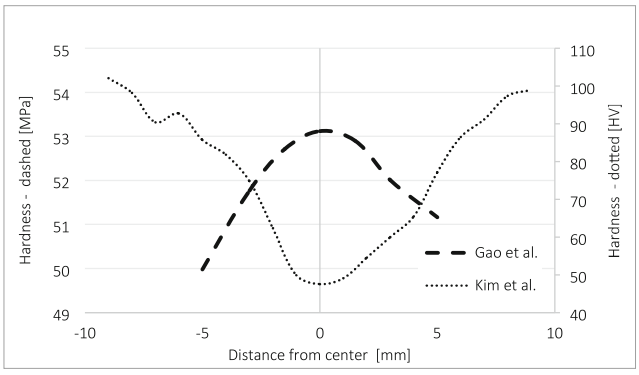


Fig. 19 Hardness profiles in the cross section at HAZ by FSW from the centre of the weld bead (adapted from [136])

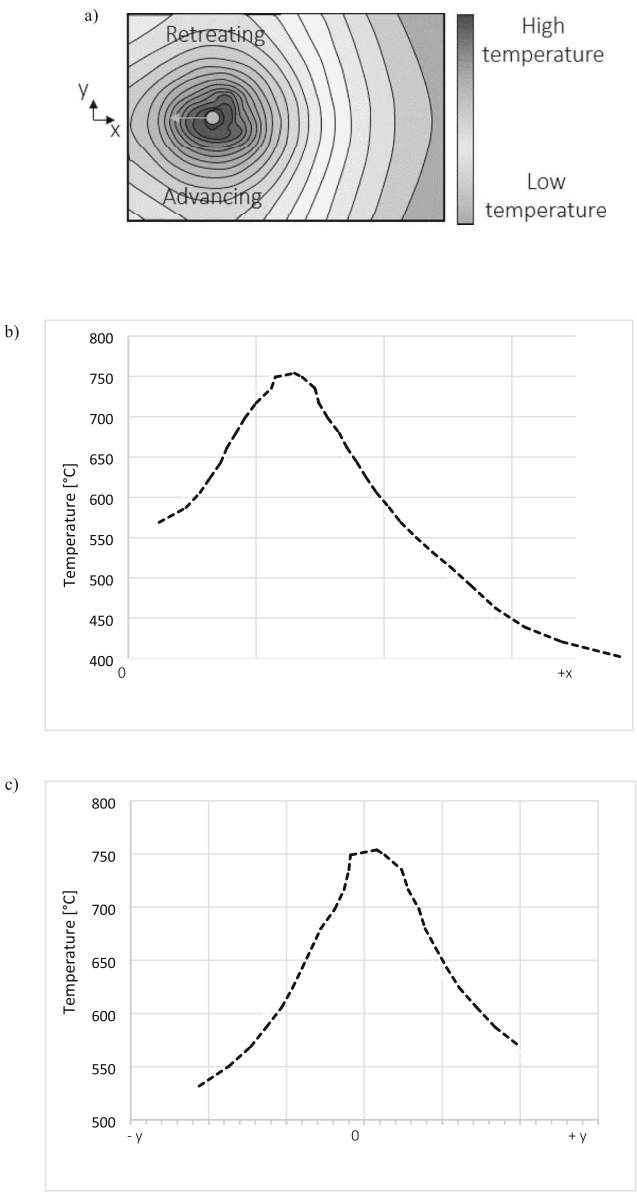


Fig. 20 Variation of temperature. **a** Temperature gradient at t = 180 s. **b** Temperature curve in the cross section of the process. **c**) Temperature curve along the plate in which the process occurs (adapted from [141]

6 Laser welding

Laser welding techniques, although relatively recent, have grown in their capabilities in the last few decades [29, 142–145]. For example, extensive research has enabled this technique to effectively join dissimilar metals, metals with low weldability [146–149] and polymers to metals [150–155]. Technological advances in this technique have even enabled to weld ceramic materials [156–158] mainly because it allows for a large thermal input to be applied in a small region.

This technique has also greatly increased in importance for the joining of thermoplastic materials [159–165] and still possesses a good future growth potential. This opens applications such in the biomedical sector as well as the automotive and aerospace industries, allowing to create high-performing, defect-free joints with good aesthetic qualities.

The laser-joining technique consists in joining two materials through the use of a laser beam that, when aimed at the welded area, releases a large amount of energy. The laser energy is transformed into a wave of thermal energy, fusing the heated region in a localised manner. After cooling, the material solidifies, establishing a strong joint. According to Fig. 21, the technique can be carried out in three different ways, Fig. 21-a represents the optimal technique for materials that have high light absorption. The joint is created in the surface of the material with small thickness, since the laser energy transformed into thermal energy only on the surface of the material. However, this type of process can also be used for thicker materials, if the absorption is suitably low, achieved with a proper selection of the wavelength and material used. Figure 21-b shows a case where one of the materials to be joined has high light transmittance (transparent) and the other material has high absorbance characteristics. The laser beam passes through the first material and is stopped in the second material, in which the beam is converted into thermal energy, heating the interface of the materials and uniting them. For the third case, a pair of materials that have low absorbance is used. For this case, the absorbance of the light is attained by introducing a third material that is placed at the interface of the two transparent materials. This usually takes the form of an absorbing coating, in which the transformation from wave energy to thermal energy takes place (Fig. 21-c).

The laser welding technique is governed by many different parameters, all of which have great importance on the final results. These parameters include the wavelength of the laser radiation, the incident power, the pulse length and shape and the pulse frequency and the welding speed, among many others. Thus, a few authors have produced studies devoted to studying the effect of some of these parameters on joint performance. Hubeatir et al. [166] have carried out a study to analyse the influence of the advance speed in a PMMA polymer, analysing the width and depth of the weld bead. It was found that the width and depth of the weld is inversely proportional to the advance speed, as illustrated in the graph adapted in Fig. 22-a and Fig. 22-b.

Taha et al. [167] performed a study based on mathematical modelling, using heat transfer equations, aiming to quantify

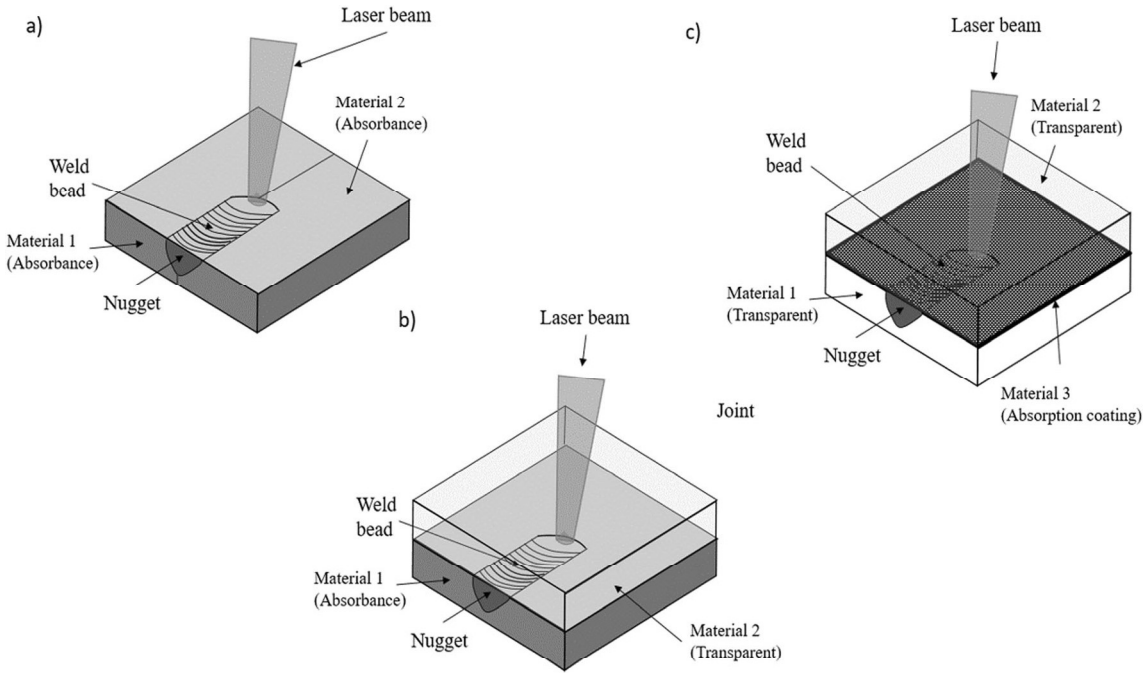


Fig. 21 Different polymer laser welding techniques. **a** Laser welding in pair of absorbent materials, **b** laser welding in different materials, absorbing with transparent material and **c** laser welding in pair of transparent materials with absorption coating

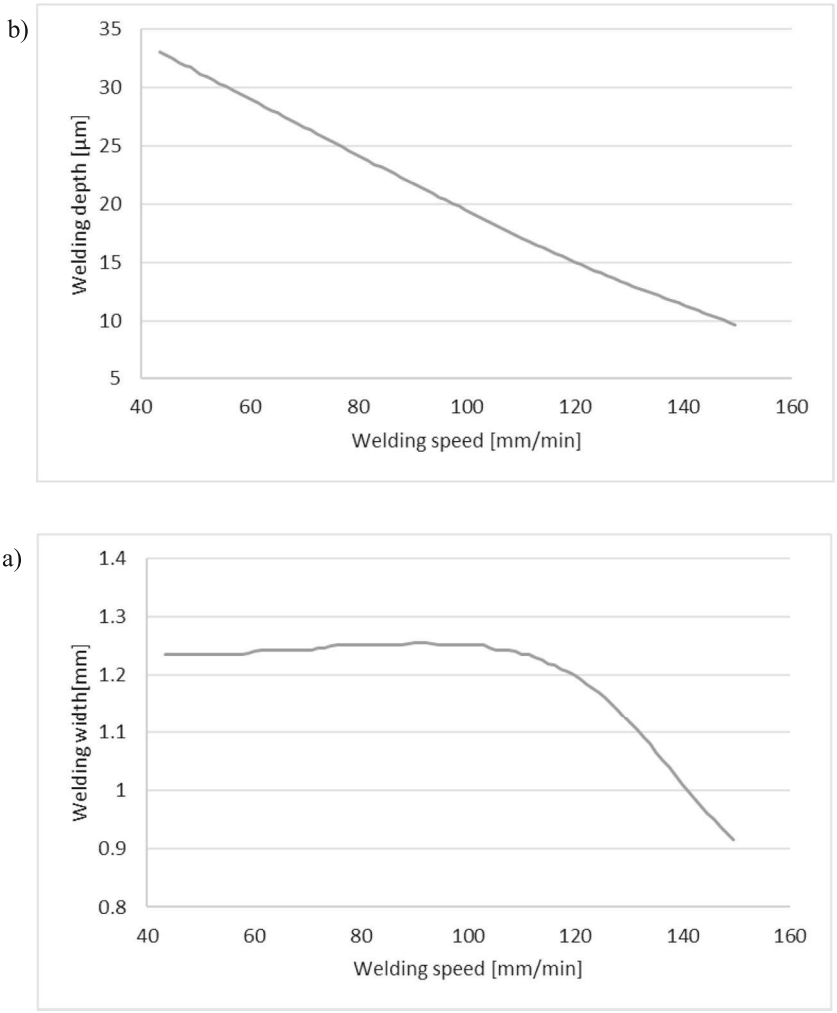


Fig. 22 Correlation between **a** welding depth and welding width with **b** welding speed adapted from [166]

the width and depth of the laser weld bead in a polyethylene. It is concluded that a higher advance speed corresponds to a smaller width and depth of the bead, although it is noted that the discrepancy between the numerical prediction and the experimental data is greater for low speeds.

Acherjee et al. and Casalino et al. have used FEM [168, 169] to reach similar conclusion. Through the results obtained, it is seen that the greater the energy applied during the welding process, the greater the width of the weld bead. The results of Acherjee et al. [168] also corroborate the fact that the greater the amount of black carbon added on the surface of the materials, the greater the energy absorption in the material, conferring a greater width and depth to the weld bead. By comparing the laser power instead of the advance speed, Ruotsalainen [170] studied the welding process of a polyamide, using a 1940 nm wavelength laser. The results show that greater laser power leads to a greater width and depth of the weld bead.

An important consideration in the laser welding process is the effect of the strong energy pulse on the properties of the welded material. Infrared thermography is a well-used method to indirectly characterise and quantify the properties of materials through a temperature gradient. In order to validate studies of the melt pool irradiation process and temperature gradient, several studies [171–174] show experimental and numerical convergence of these results. To quantify and qualify the thermally affected zone of a semi-transparent polyamide 6, using computational methods, Schmailz et al. [175] used a pyrometer integrated with a laser welding process, in which the temperature gradient is correlated with the thermally affected zone. This study confirms that the higher the laser power, the higher the localised temperature. It is also observed that the greater the amount of black carbon resin applied at the polymer interface to increase light absorption, the higher the temperature. These higher temperatures lead to larger heat affected zones. Using the same infrared thermography technology implemented in previous works [173–175] as well as the analysis of the width of the weld bead and the welding power performed by Hubeatir et al. [166], Schmitt et al. [176] have shown that it is possible to combine these techniques to characterise dimensional defects of the weld bead such as residual gap, weld geometry, internal pores and leaks.

Another key area of research associated with laser welding of polymers is the addition of particles and materials that can change how the materials to be joined react to the laser light [168, 175], Chen et al. [177] carried out an experimental study demonstrating and effect of the addition of carbon black to thermoplastics, for cases of welding in transparent materials. The results of this work are summarised in Fig. 23-a, Fig. 23-b and Fig. 23-c. It is observed that the larger the content of carbon black added, the greater is the absorption of the laser energy, optimising the bonding process at the polymer interface. This was found to be true for welding Polyamide 6 to PA 6, glass fibre-reinforced polyamide 6 to PA 6 GF and polycarbonate.

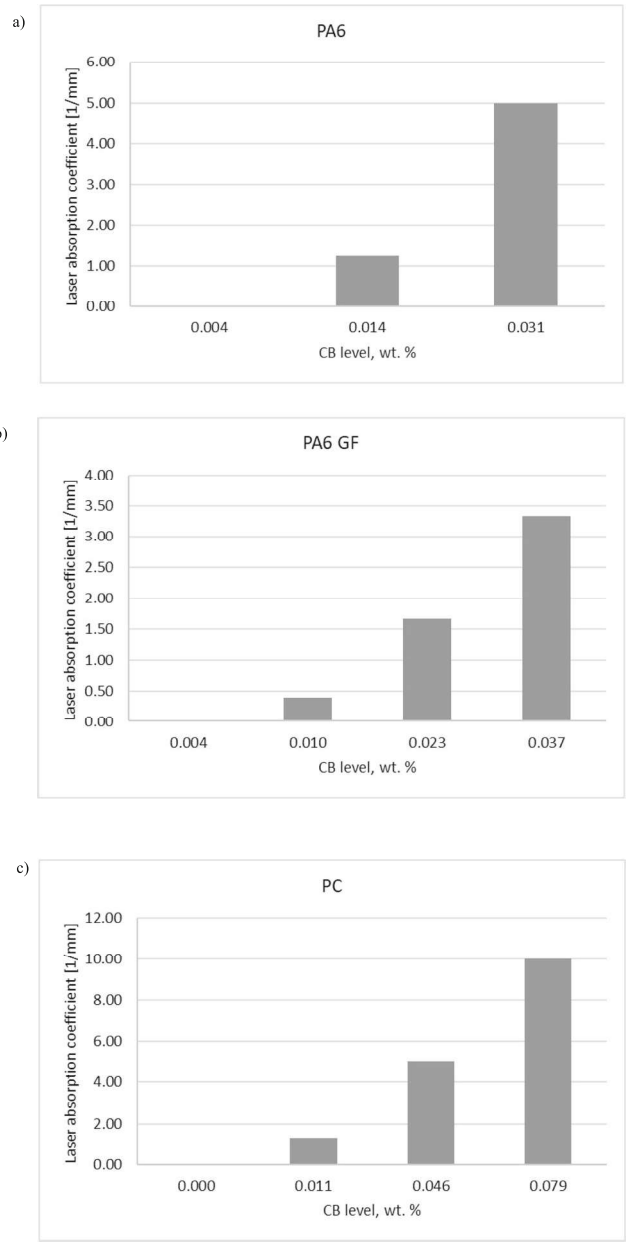


Fig. 23 Laser absorption coefficient vx wt.% black carbon level. **a** PA6, **b** PA6GF **c** and PC adapted from. [177]

Rodríguez-Vidal et al. [178] shows that, due to the low energy absorption in ABS for a 880 nm wavelength diode laser energy absorption in the material can be increased with the application of carbon nanotubes (CNT) in the matrix, which is in agreement with some of the conclusions reached by Chen et al. [177]. This work compares the resistance voltage in relation to the percentage of nanotubes added. It is shown that with 0.01 wt% CNT added, the joining process takes place at 880 nm, however, when placed 0.05 wt% CNT in addition to the joining process, the weld is more resistant because it has better energy absorption to melt the material. Gisario et al. [179] further studied the addition of black carbon at the interface of materials to be laser welded with high transparency. This work considers polyethylene terephthalate (PET) materials in neat state and with 5 wt%, 10 wt% and 15 wt.% of carbon black. Through these fractions, using a 940 nm wavelength laser, it was found that the greater the addition of black carbon, for a weldability map varying the power and the advance speed, the greater the effective welding area, the smaller the area of degradation was obtained.

As the literature shows, laser welding of polymers is seen as a very powerful and advantageous technology which is rapidly becoming ubiquitous as laser welding equipment gradually reduce in price. Research wise, it seen that most of the research is devoted to optimising the wide range of welding parameters that govern this technique, as well as understanding how the highly concentrated incident energy affects the mechanical performance of the base polymeric materials. It is also seen that many research works study methodologies to control the transmission and absorption of the laser light, using transparent polymers or introducing additives that allow to precisely control the location of maximum energy transfer and thus, the location of the weld itself.

7 Hybrid joining process

The idea of a hybrid joint can represent two different concepts in the field of joining. The first corresponds to the union of dissimilar materials, a process which is necessarily more complex than joining similar materials and requires careful study of the compatibility of the materials to be joined. The second concept of a hybrid joint is the case where a single joint includes two or more joining techniques. These techniques can be simultaneously applied and fully complementary in nature or the connection can be assumed mainly by a primary joining technology where a secondary technique only assists or serves as a backup in case of failure of the primary joint [23, 55, 58, 180].

For a case of hybrid joining process, Friedrich et al. [33] have carried out an optimization for PA 6 GF and DC04 steel joints, combining the techniques of mechanical fastening and adhesive bonding to SLJs and T-joints. It is observed that for both types of joints the highest load achieved was with the

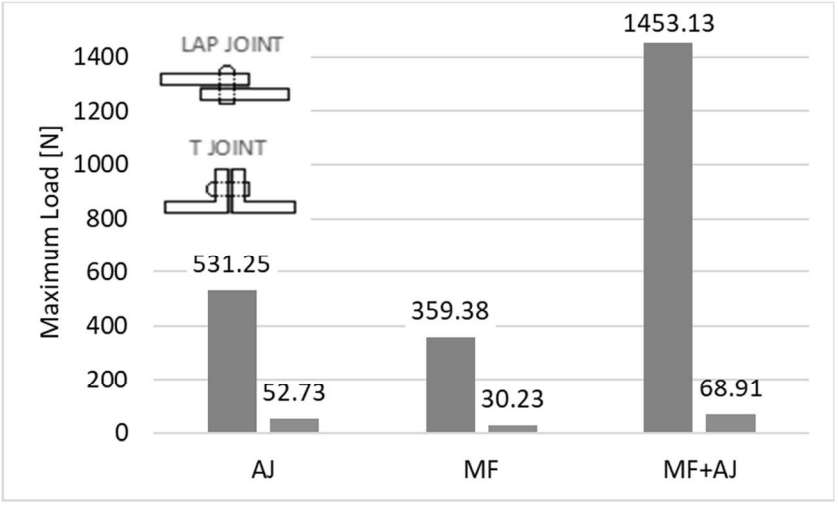


Fig. 24 Maximum load to lap joint and T-joint. AJ, adhesive Joint; MF, mechanical fastening and MF + AJ, mechanical fastening with adhesive joint adapted from [33]

hybrid methodology, while the independent processes performed much poorly, as shown in Fig. 24.

Graham et al. [181] carried out hybrid study in which 306 L steel was joined with a thermoplastic. In this work, the union of the materials using three distinct techniques is compared. The first one is using only an epoxy resin of the LY564 type, while the second one the polymer is fastened to the metal by means of a pin generated on the surface by means of an additive layer method. The hybrid process showed an increase in impact resistance of 300% when compared to the adhesive bonding process, implying higher energy absorption and 67% more shear stress resistance.

In another work, Reisgen et al. [182] studied the hybrid joining of a low carbon steel (DC 01 mild steel) and a fibre-reinforced polymer (FRP) in which thermal energy is electrically transferred through pins machined in the metal surface. When pressed together by external forces, the reinforced polymer adheres to the metal with fusion of the polymer and interpenetration of the two materials, as shown in Fig. 25. A comparison is made between this hybrid joining process and adhesive bonding through ENF testing and the performance of the hybrid joint is found to surpass that obtained only by adhesive bonding.

Abibe and Amancio-Filho [12, 183] propose a novel technique used to bond polymer with metals, also characterised as hybridised mechanical fastening, called injection clinching joining technique (ICJ) in which a polymer sheet moulded with a stud on the surface is first joined to a sheet of metal with a corresponding hole. Joining is achieved by the application of pressure to heated punch, which shapes the stud, consequently fixing the joint. In an alternative method (F-IJC), the punch is also rotated which creates friction, as shown in Fig. 26.

Although the ICJ and F-ICJ techniques require further optimization to their parameters, the results for F-ICJ technique, as reported by the authors, are already superior to those of ultrasonic joining processes.

In a work which has parallels to the work of Graham [181], Engelmann et al. [184] joined P260 steel to a PA 6 polymer, using a laser welding assisted process. Initially, the metal surface is grooved by laser pulses in three powers at the values of 575, 1270 and 1710 W, using 1500, 2000 and 2500 ms pulses. After the grooves are made on the metal surface, the transparent polymeric material is placed into contact with the metal by the application of pressure. The laser is again used and its beam its transmitted through the polymer and absorbed into

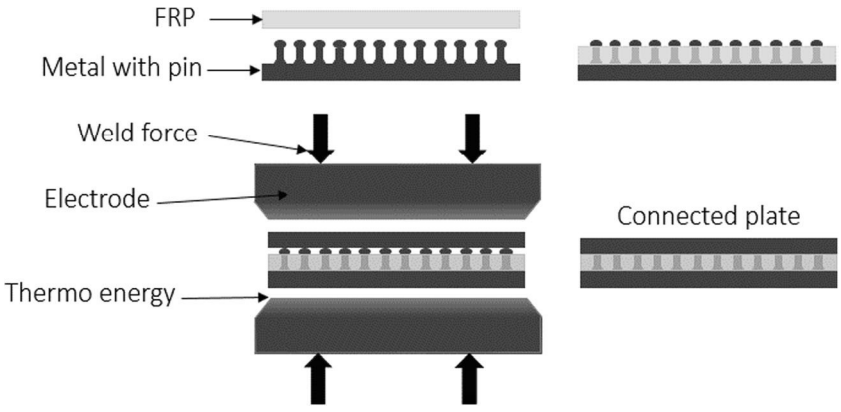


Fig. 25 Adapted layout of Innovative hybrid joining technology of the hot pin adapted from [164]

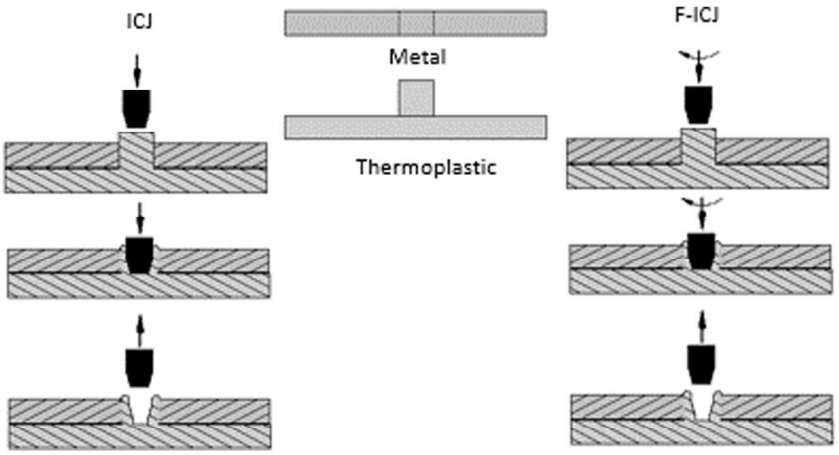


Fig. 26 Steps of the ICJ and F-ICJ process adapted from [12, 183]

the metal. The results show that the greater the power, the greater the shear resistance. In addition, it is also shown that the longer the pulse time, the deeper the groove, thus increasing the joined area and the shear resistance.

Another adhesive bonding application assisted by laser was proposed by Rodríguez-Vidal et al. [181]. In this work, the union of a PA 6 GF with metal was first performed with adhesive bonding on the surface of untreated materials. In the second case, the adherend surfaces were treated by using the laser to etch micro grooves. This allows for a better degree of mechanical interlocking with the adhesive. Finally, in addition to the surface treatment with the laser, laser is also emitted on the surface of the polymer and it transmitted to interface of the metal and polymer, where it creates micro-welds. This study found that the surface treatment improves adhesion performance and that adhesion only with surface treatment, without the assistance of the external laser to assist the joining, actually provides better results.

Save for some special applications in highly technological industrial sectors, such as the aeronautical industry, hybrid joining processes are generally seen as complex and costly to implement, due to the duplication of the equipment associated with their use. However, recent research shows that innovative hybrid joining techniques can in fact simplify the manufacture processes of products, allowing to join unexplored material combinations. Although the implementation of these methods can be technically challenging, it is expectable to see some of these techniques make their way into practical joining of polymeric, composite and metallic components.

8 Conclusions and future trends

Driven by advances in material science and novel technological solutions, adhesive bonding, mechanical joining, laser welding and friction stir welding have all evolved to become mature welding techniques in recent years. As a result, these techniques are already in use in many advanced technological applications, helping create durable and defect-free polymer-based products; yet, their potential can still be improved with further optimization.

An analysis of the literature shows that one of the main current avenues of research is to expand the range of materials that can be joined, a process which enables novel designs that fully explore the capabilities of different materials. Adhesive bonding, mechanical joining and welding techniques are all suitable for these applications, with varied degrees of difficulty. Another important trend that was identified is in the design of hybrid joints for polymer bonding, which combine two or more joining processes to create a joint with unique and synergistically enhanced properties. These types of joints have for long been limited to the academic research works but their use is now becoming attractive for practical application.

Considering these observations on the current research activities, it is possible specify in more detail a set of future trends, listed below:

- Bonding between adhesive joining assisted by laser welding, applied to both cure the adhesive and increase joint strength by melting thermoplastic materials.
- Use of friction stir welding assisted by laser welding, in which the laser has the role of preheating the material, reducing the power and the need for rotation of the friction stir welding pin or performing laser welding after friction stir welding to weld non-joined areas in the bead and improve the uniformity of the microstructure.
- The use of laser welding applied in conjunction with mechanical fastening, has the potential of improving water-tightness of the joint. This can be carried out at the material interface if at least one transparent substrate is used or at the edge of the joint if light absorbent materials are used.
- Optimization of hybrid joining processes in the context of polymer joining, with the objective of determining ideal process parameters, material combinations and geometrical configurations of the different joining methodologies.

References

1. da Silva, L.F., A. Öchsner, R.D. Adams (2011) Handbook of adhesion technology Springer Science & Business Media
2. Marczis B, Czigány T (2002) Polymer joints. Periodica Polytechnica Mechanical Engineering **46**(2):117–126
3. Visco A, Scolaro C, Quattrocchi A, Montanini R (2018) Response to fatigue stress of biomedical grade polyethylene joints welded by a diode laser. J Mech Behav Biomed Mater **86**:390–396
4. Amanat N, James NL, McKenzie DR (2010) Welding methods for joining thermoplastic polymers for the hermetic enclosure of medical devices. Med Eng Phys **32**(7):690–699
5. Banea MD, da Silva LFM, Campilho RDSG, Sato C (2014) Smart adhesive joints: an overview of recent developments. J Adhes **90**(1):16–40
6. Evers F, Schöppner V, Lakemeyer P (2017) The influence of welding processes on the weld strength of flame-retardant materials. Welding in the World **61**(1):161–170
7. Fink JK (2014) High performance polymers William Andrew
8. Unterweger C, Brüggemann O, Fürst C (2014) Synthetic fibers and thermoplastic short-fiber-reinforced polymers: properties and characterization. Polym Compos **35**(2):227–236
9. Ashby MF, Cebon D (1993) Materials selection in mechanical design. Le Journal de Physique IV **3**(C7):C7-1–C7-9
10. Dangel, R. (2004) et al. Development of a low-cost low-loss polymer waveguide technology for parallel optical interconnect applications. In Digest of the LEOS Summer Topical Meetings Biophotonics/Optical Interconnects and VLSI Photonics/WBM Microcavities **1**(1) 29-30
11. Hergenrother PM (2003) The use, design, synthesis, and properties of high performance/high temperature polymers: an overview. High Performance Polymers **15**(1):3–45
12. Amancio-Filho S, Dos Santos J (2009) Joining of polymers and polymer–metal hybrid structures: recent developments and trends. Polym Eng Sci **49**(8):1461–1476
13. Grewell D, Benatar A (2007) Welding of plastics: fundamentals and new developments. Int Polym Process **22**(1):43–60
14. Kah P et al (2014) Techniques for joining dissimilar materials: metals and polymers. Rev Adv Mater Sci **36**(2):152–164
15. Troughton, M.J. (2008) Handbook of plastics joining: a practical guide William Andrew
16. Rasmussen, P.A., J.M. Brown (1997) Integral thermoset/thermoplastic composite joint, Google Patents
17. Schieler O, Beier U (2016) Induction welding of hybrid thermoplastic-thermoset composite parts. Applied Science and Engineering Progress **9**(1):27–36
18. da Silva, L.F.M., A. Öchsner (2008) Modeling of adhesively bonded joints Springer
19. Clifton S, Thimmappa BHS, Selvam R, Shivamurthy B (2020) Polymer nanocomposites for high-velocity impact applications-a review. Composites Communications **17**:72–86
20. El-Abbassi FE et al (2020) A review on alfa fibre (Stipa tenacissima L.): from the plant architecture to the reinforcement of polymer composites. Composites Part A: Applied Science and Manufacturing. A review on alfa fibre (Stipa tenacissima L.): From the plant architecture to the reinforcement of polymer composites. **128**:105677
21. Notario B, Pinto J, Rodriguez-Perez MA (2016) Nanoporous polymeric materials: a new class of materials with enhanced properties. Prog Mater Sci **78**:93–139
22. Pilate F, Toncheva A, Dubois P, Raquez JM (2016) Shape-memory polymers for multiple applications in the materials world. Eur Polym J **80**:268–294
23. Supian A et al (2018) Hybrid reinforced thermoset polymer composite in energy absorption tube application: a review. Defence Technology **14**(4):291–305
24. Wu H, Fahy WP, Kim S, Kim H, Zhao N, Pilato L, Kafi A, Bateman S, Koo JH (2020) Recent developments in polymers/polymer nanocomposites for additive manufacturing. Prog Mater Sci **111**:100638
25. Xia L, Zhang Z, Hong CY, You YZ (2020) Synthesis of copolymer via hybrid polymerization: from random to well-defined sequence. Eur Polym J **122**:109374
26. Zhong Y, Godwin P, Jin Y, Xiao H (2020) Biodegradable polymers and green-based antimicrobial packaging materials: a mini-review. Advanced Industrial and Engineering Polymer Research **3**(1):27–35
27. Kinloch, A.J. (2012) Adhesion and adhesives: science and technology Springer Science & Business Media
28. da Silva LF, Campilho RD (2012) Advances in numerical modelling of adhesive joints. In Advances in numerical modeling of Adhesive Joints 1:93
29. Ravi-Kumar S, Lies B, Zhang X, Lyu H, Qin H (2019) Laser ablation of polymers: a review. Polym Int **68**(8):1391–1401
30. Wu S (1982) Polymer Interface and Adhesion:630
31. Hartshorn, S.R. (2012) Structural adhesives: chemistry and technology Springer Science & Business Media
32. Arteiro A, Furtado C, Catalanotti G, Linde P, Camanho PP (2020) Thin-ply polymer composite materials: a review. Compos A Appl Sci Manuf **132**:105777
33. Friedrich S et al (2014) Hybrid joining technology-a new method for joining thermoplastic-metal-mixed components. in AIP Conference Proceedings. American Institute of Physics **121**(1593):121–127
34. Kweon J-H, Jung JW, Kim TH, Choi JH, Kim DH (2006) Failure of carbon composite-to-aluminum joints with combined mechanical fastening and adhesive bonding. Compos Struct **75**(1-4):192–198
35. Machado J et al (2018) Numerical study of the behaviour of composite mixed adhesive joints under impact strength for the automotive industry. Compos Struct **185**:373–380
36. Machado J et al (2018) Numerical study of impact behaviour of mixed adhesive single lap joints for the automotive industry. Int J Adhes Adhes **84**:92–100
37. Machado J et al (2020) Numerical study of similar and dissimilar single lap joints under quasi-static and impact conditions. Int J Adhes Adhes **96**:102501
38. Ueda M, Miyake S, Hasegawa H, Hirano Y (2012) Instantaneous mechanical fastening of quasi-isotropic CFRP laminates by a self-piercing rivet. Compos Struct **94**(11):3388–3393
39. Yadav A, Kaushik A, Mishra YK, Agrawal V, Ahmadivand A, Maliutina K, Liu Y, Ouyang Z, Dong W, Cheng GJ (2020) Fabrication of 3D polymeric photonic arrays and related applications. Materials Today Chemistry **15**:100208
40. Butt, H.-J., M. Kappl (2010) Surface and interfacial forces Wiley Online Library
41. Kandalam U, Bouvier AJ, Casas SB, Smith RL, Gallego AM, Rothrock JK, Thompson JY, Huang CYC, Stelnicki EJ (2013) Novel bone adhesives: a comparison of bond strengths in vitro. Int J Oral Maxillofac Surg **42**(9):1054–1059
42. Maurer P, Bekes K, Gernhardt CR, Schaller HG, Schubert J (2004) Comparison of the bond strength of selected adhesive dental systems to cortical bone under in vitro conditions. Int J Oral Maxillofac Surg **33**(4):377–381
43. Nascimento PLMM et al (2017) Addition of ammonium-based methacrylates to an experimental dental adhesive for bonding metal brackets: carious lesion development and bond strength after cariogenic challenge. Am J Orthod Dentofac Orthop **151**(5):949–956

44. Szymczyk P et al (2020) A review of fabrication polymer scaffolds for biomedical applications using additive manufacturing techniques. Biocybernetics and Biomedical Engineering **40**(2): 624–638
45. Villanueva JGV et al (2019) Bio-adhesion evaluation of a chitosan-based bone bio-adhesive. Int J Adhes Adhes **92**:80–88
46. Thakkar R, Thakkar R, Pillai A, Ashour EA, Repka MA (2020) Systematic screening of pharmaceutical polymers for hot melt extrusion processing: a comprehensive review. Int J Pharm **576**: 118989
47. Xie T, Kao W, Sun L, Wang J, Dai G, Li Z (2020) Preparation and characterization of self-matting waterborne polymer–an overview. Prog Org Coat **142**:105569
48. Bagherzadeh A, Jamshidi M, Monemian F (2020) Investigating mechanical and bonding properties of micro/nano filler containing epoxy adhesives for anchoring steel bar in concrete. Constr Build Mater **240**:117979
49. Cho BH, Nam BH, Seo S, Kim J, An J, Youn H (2019) Waterproofing performance of waterstop with adhesive bonding used at joints of underground concrete structures. Constr Build Mater **221**:491–500
50. Li Z, Olah A, Baer E (2020) Micro-and nano-layered processing of new polymeric systems. Prog Polym Sci **102**:101210
51. Nguyen KT et al (2020) Fire safety of composites in prefabricated buildings: from fibre reinforced polymer to textile reinforced concrete. Compos Part B **187**:107815
52. Rocha AV et al (2020) Fatigue crack growth analysis of different adhesive systems: effects of mode mixity and load level. Fatigue Fract Eng Mater Struct **43**(2):330–341
53. Shi J-W, Cao W-H, Wu Z-S (2019) Effect of adhesive properties on the bond behaviour of externally bonded FRP-to-concrete joints. Compos Part B **177**:107365
54. Zhang X, Bai L, Sun J, Li Z, Jia Z, Gu J (2020) Design and fabrication of PVAc-based inverted core/shell (ICS) structured adhesives for improved water-resistant wood bonding performance: II. Influence of copolymerizing-grafting sequential reaction. International Journal of Adhesion and Adhesives **99**:102571
55. Amancio Filho ST, LA Blaga (2018) Joining of polymer-metal hybrid structures: principles and applications John Wiley & Sons
56. Chanda, M. (2017) Plastics technology handbook CRC press
57. Collett BM (1972) A review of surface and interfacial adhesion in wood science and related fields. Wood Sci Technol **6**(1):1–42
58. da Silva, L.F., A. Pirondi, and A. Öchsner (2011) Hybrid adhesive joints 6 Springer Science & Business Media
59. El Mansouri N-E, Salvadó J (2006) Structural characterization of technical lignins for the production of adhesives: application to lignosulfonate, kraft, soda-anthraquinone, organosolv and ethanol process lignins. Ind Crop Prod **24**(1):8–16
60. Ludwig, C.H., A.W. Stout (1971) Adhesive composition from lignosulfonate phenoplasts Google Patents
61. Valasamudram V et al (2020) Study and evaluation of cold joining on metals and non metals combinations (ss, al, acr) using polymer based adhesive. Materials Today: Proceedings **27**(3):2806–2810
62. Weitzenböck, J.R. (2012) Adhesives in marine engineering Elsevier
63. Kinloch A (1980) The science of adhesion. J Mater Sci **15**(9): 2141–2166
64. Higgins A (2000) Adhesive bonding of aircraft structures. Int J Adhes Adhes **20**(5):367–376
65. Rotheiser, J. (2015) Joining of plastics: handbook for designers and engineers Carl Hanser Verlag GmbH Co KG
66. Gierenz, G. and W. Karmann (2008) Adhesives and adhesive tapes John Wiley & Sons
67. Wu, S. (1982) Polymer interface and adhesion 188. M. Dekker New York
68. Butt, H.-J., K. Graf, and M. Kappl (2013) Physics and chemistry of interfaces John Wiley & Sons
69. Hoong YB, Paridah MT, Loh YF, Jalaluddin H, Chuah LA (2011) A new source of natural adhesive: Acacia mangium bark extracts co-polymerized with phenol-formaldehyde (PF) for bonding Mempisang (Annonaceae spp.) veneers. Int J Adhes Adhes **31**(3):164–167
70. Zhang X et al (2020) Design and fabrication of PVAc-based inverted core/shell (ICS) structured adhesives for improved water-resistant wood bonding performance: I. Influence of chemical grafting International Journal of Adhesion and Adhesives **98**: 1–23
71. Da Silva, L.F., et al. (2012) Testing adhesive joints: best practices John Wiley & Sons
72. Ebnesajjad, S. (2010) Handbook of adhesives and surface preparation: technology, applications and manufacturing William Andrew
73. Molitor P, Barron V, Young T (2001) Surface treatment of titanium for adhesive bonding to polymer composites: a review. Int J Adhes Adhes **21**(2):129–136
74. Sabreen S (2018) Plasma surface pretreatments of polymers for improved adhesion bonding. Tecnology 1(1):1–5
75. Zhang D, Sun Q, Wadsworth LC (1998) Mechanism of corona treatment on polyolefin films. Polym Eng Sci **38**(6):965–970
76. Nečasová B, Liška P, Kelar J, Šlanhof J (2019) Comparison of adhesive propertiesEEHUKUJ88887666P976311134660-0 of polyurethane adhesive system and wood-plastic composites with different polymers after mechanical, chemical and physical surface treatment. Polymers **11**(3):397
77. Bukhari MD et al (2020) Adhesion theories and effect of surface roughness on energy estimation and wettability of polymeric composites bonded joints: a-review. VW Applied Sciences **2**(1):74–86
78. Jin X, Strueben J, Heepe L, Kovalev A, Mishra YK, Adelung R, Gorb SN, Staubitz A (2012) Joining the un-joinable: adhesion between low surface energy polymers using tetrapodal ZnO linkers. Adv Mater **24**(42):5676–5680
79. da Silva LFM, Das Neves PJC, Adams RD, Spelt JK (2009) Analytical models of adhesively bonded joints—Part I: Literature survey. Int J Adhes Adhes **29**(3):319–330
80. de Moura M et al (2008) Cohesive and continuum mixed-mode damage models applied to the simulation of the mechanical behaviour of bonded joints. Int J Adhes Adhes **28**(8):419–426
81. Braga DF, da Silva LF, Moreira PM (2016) Single lap joints numerical modelling and comparison with experimental testing. U Porto Journal of Engineering **2**(1):11–20
82. Adams RD, Peppiatt NA (1974) Stress analysis of adhesive-bonded lap joints. The Journal of Strain Analysis for Engineering Design **9**(3):185–196
83. Crocombe A, Adams, RD (1981) Influence of the spew fillet and other parameters on the stress distribution in the single lap joint. J Adhes **13**(2):141–155
84. da Silva LFM, Rodrigues TNSS, Figueiredo MAV, de Moura MFSF, Chousal JAG (2006) Effect of adhesive type and thickness on the lap shear strength. J Adhes **82**(11):1091–1115
85. Silva D et al (2018) Experimental and numerical analysis of scarf aluminum adhesive joints. Procedia Manufacturing **17**:705–712
86. Oliveira J et al (2019) Adhesive thickness effects on the mixed-mode fracture toughness of bonded joints. J Adhes:1–21
87. Sadeghi MK et al (2020) Failure load prediction of adhesively bonded single lap joints by using various FEM techniques. Int J Adhes Adhes **97**:1–32
88. Matos-Pérez CR, White JD, Wilker JJ (2012) Polymer composition and substrate influences on the adhesive bonding of a biomimetic, cross-linking polymer. J Am Chem Soc **134**(22):9498–9505

89. Hsiao K-T, Alms J, Advani SG (2003) Use of epoxy/multiwalled carbon nanotubes as adhesives to join graphite fibre reinforced polymer composites. Nanotechnology **14**(7):791 793
90. Machado J, Nunes PDP, Marques EAS, Campilho RDSG, da Silva LFM (2020) Numerical study of mode I fracture toughness of carbon-fibre-reinforced plastic under an impact load. Proceedings of the Institution of Mechanical Engineers Part L. Journal of Materials: Design and Applications **234**(1):12–20
91. Banea M et al (2020) The effect of environment and fatigue loading on the behaviour of TEPs-modified adhesives. J Adhes **96**(1-4):423–436
92. Akhavan-Safar A et al (2020) Influence of microcork particles on the lap shear strength of an epoxy adhesive subjected to fatigue loading and different environmental conditions. Proceedings of the Institution of Mechanical Engineers Part L. Journal of Materials: Design and Applications 0:1–8
93. Borges C et al (2020) Review on the effect of moisture and contamination on the interfacial properties of adhesive joints. Proc Inst Mech Eng C J Mech Eng Sci 0:1–23
94. Sugiman S, Crocombe A, Aschroft I (2013) Experimental and numerical investigation of the static response of environmentally aged adhesively bonded joints. Int J Adhes Adhes **40**:224–237
95. Rocha A et al (2020) Numerical analysis of mixed-mode fatigue crack growth of adhesive joints using CZM. Theor Appl Fract Mech (106):102493
96. Monteiro J, Akhavan-Safar A, Carbas R, Marques E, Goyal R, El-zein M, Silva LFM, Influence of mode mixity, loading conditions on the fatigue crack growth behaviour of an epoxy adhesive (2020) Fatigue Fract Eng Mater Struct **43**(2):308–316
97. Rocha A, Akhavan-Safar A, Carbas R, Marques EAS, Goyal R, El-Zein M, da Silva LFM (2020) Paris law relations for an epoxy-based adhesive. Proceedings of the Institution of Mechanical Engineers Part L. Journal of Materials: Design and Applications **234**(2):291–299
98. Ibrahim R, Pettit C (2005) Uncertainties and dynamic problems of bolted joints and other fasteners. J Sound Vib **279**(3-5):857–936
99. Ageorges C, L Ye (2002) State of the art in fusion bonding of polymer composites, in Fusion Bonding of Polymer Composites Springer 7-64
100. Karpat F, Kucukoglu A (2017) A review of the mechanical joining techniques for thermoplastics. Juniper Online J Mater Sci **3**(2):6–7
101. Vinson JR (1989) Mechanical fastening of polymer composites. Polym Eng Sci **29**(19):1332–1339
102. Thoppul SD, Finegan J, Gibson RF (2009) Mechanics of mechanically fastened joints in polymer–matrix composite structures–a review. Compos Sci Technol **69**(3-4):301–329
103. Arora D (2003) Rapid Strengthening of reinforced concrete bridge with mechanically fastened-fiber reinforced polymer strips. Citeseer. **1**(1):1–166
104. Lambiase F, Durante M, Di Ilio A (2016) Fast joining of aluminum sheets with Glass Fiber Reinforced Polymer (GFRP) by mechanical clinching. J Mater Process Technol **236**:241–251
105. Khoo T et al (2008) Wood filler-recycled polypropylene (WF-RPP) composite pallet: study of fastening method. J Reinf Plast Compos **27**(16-17):1723–1731
106. Alves L, Silva CMA, Santos PD, Martins PAF (2016) Mechanical joining of PVC tubes by their ends. Proceedings of the Institution of Mechanical Engineers Part L. Journal of Materials: Design and Applications **230**(4):860–868
107. Bragança I et al (2017) Lightweight joining of polymer and polymer-metal sheets by sheet-bulk forming. J Clean Prod **145**: 98–104
108. Mackerle J (2003) Finite element analysis of fastening and joining: A bibliography (1990–2002). Int J Press Vessel Pip **80**(4):253–271
109. Bhonge PS, Foster BD, Lankarani HM (2011) Finite element modeling and analysis of structural joints using nuts and bolts. in ASME 2011 International Mechanical Engineering Congress and Exposition. American Society of Mechanical Engineers Digital Collection **1**(1):1–11
110. He X, Gu F, Ball A (2013) Fatigue behaviour of fastening joints of sheet materials and finite element analysis. Advances in mechanical engineering **5**:658219
111. Iancu F, Ding X, Cloud GL, Raju BB (2005) Three-dimensional investigation of thick single-lap bolted joints. Exp Mech **45**(4): 351–358
112. Nassar SA, Virupaksha VL, Ganeshmurthy S (2007) Effect of bolt tightness on the behavior of composite joints **129**(1):43–51
113. Nandan R, DebRoy T, Bhadeshia H (2008) Recent advances in friction-stir welding–process, weldment structure and properties. Prog Mater Sci **53**(6):980–1023
114. Boon T, Thomas WM, Temple-Smith P Friction welding apparatus and method. 2001. Google Patents
115. Inaniwa S, et al. (2013) Application of friction stir welding for several plastic materials. in Proceedings of the 1st international joint symposium on joining and welding. Elsevier 137-142
116. Besharati-Givi, M.-K., P. Asadi (2014) Advances in friction-stir welding and processing Elsevier
117. Lohwasser, D., Z. Chen (2009) Friction stir welding: from basics to applications Elsevier
118. Huang Y, Meng X, Xie Y, Wan L, Lv Z, Cao J, Feng J (2018) Friction stir welding/processing of polymers and polymer matrix composites. Compos A: Appl Sci Manuf **105**:235–257
119. Simões F, Rodrigues D (2014) Material flow and thermo-mechanical conditions during friction stir welding of polymers: literature review, experimental results and empirical analysis. Mater Des **59**:344–351
120. DebRoy T, Bhadeshia H (2010) Friction stir welding of dissimilar alloys–a perspective. Sci Technol Weld Join **15**(4):266–270
121. Shunmugasundaram M, Praveen Kumar A, Maneiah D (2019) An experimental analysis and process parameter optimization on friction stir welded dissimilar alloys. International Journal of Mechanical and Production Engineering Research and Development 9(2):407–414
122. Shen C, Zhang J, Ge J (2011) Microstructures and electrochemical behaviors of the friction stir welding dissimilar weld. J Environ Sci **23**:S32–S35
123. Gupta SK, Pandey K, Kumar R (2018) Multi-objective optimization of friction stir welding process parameters for joining of dissimilar AA5083/AA6063 aluminum alloys using hybrid approach. Proceedings of the Institution of Mechanical Engineers Part L. Journal of Materials: Design and Applications **232**(4): 343–353
124. Shunmugasundaram M et al (2020) Optimization of process parameters of friction stir welded dissimilar AA6063 and AA5052 aluminum alloys by Taguchi technique. Materials Today: Proceedings **27**(2):871–876
125. Ratanathavorn W, Melander A (2015) Dissimilar joining between aluminium alloy (AA 6111) and thermoplastics using friction stir welding. Sci Technol Weld Join **20**(3):222–228
126. Khodabakhshi F, Haghshenas M, Chen J, Shalchi AB, Li J, Gerlich AP (2017) Bonding mechanism and interface characterisation during dissimilar friction stir welding of an aluminium/polymer bi-material joint. Sci Technol Weld Join **22**(3):182–190
127. Patel AR, Kotadiya DJ, Kapopara JM, Dalwadi CG, Patel NP, Rana HG (2018) Investigation of mechanical properties for hybrid joint of aluminium to polymer using friction stir welding (FSW). Mater Today Proc **5**:4242–4249
128. Patel AR, Dalwadi CG, Rana HG (2016) A review: dissimilar material joining of metal to polymer using friction stir welding (FSW). Int J Sci Technol Eng **2**(10):702–706

129. Huang Y, Meng X, Xie Y, Li J, Wan L (2018) Joining of carbon fiber reinforced thermoplastic and metal via friction stir welding with co-controlling shape and performance. Compos A: Appl Sci Manuf **112**:328–336
130. Gemme F, Verreman Y, Dubourg L, Jahazi M (2010) Numerical analysis of the dwell phase in friction stir welding and comparison with experimental data. Mater Sci Eng A **527**(16-17):4152–4160
131. Eslami, S., Farahani B.V., Tavares P.J., Moreira P.M.G.P., Fatigue behaviour evaluation of dissimilar polymer joints: friction stir welded, single and double-rivets. Int J Fatigue, 2018. **113**: p. 351-358.
132. Adibeig MR, Hassanifard S, Vakili-Tahami F, Hattel JH (2018) Experimental investigation of tensile strength of friction stir welded butt joints on PMMA. Materials Today Communications **17**:238–245
133. Eslami S, Ramos T, Tavares PJ, Moreira PMGP (2015) Effect of friction stir welding parameters with newly developed tool for lap joint of dissimilar polymers. Procedia Engineering **114**:199–207
134. Kredegh A, Sedmak A, Grbovic A, Milosevic N, Danicic D (2016) Numerical simulation of fatigue crack growth in friction stir welded T joint made of Al 2024 T351 alloy. Procedia Structural Integrity **2**:3065–3072
135. Gao J, Li C, Shilpakar U, Shen Y (2015) Improvements of mechanical properties in dissimilar joints of HDPE and ABS via carbon nanotubes during friction stir welding process. Mater Des **86**:289–296
136. Kim J-H, Jo D-S, Kim B-M (2017) Hardness prediction of weldment in friction stir welding of AA6061 based on numerical approach. Procedia engineering **207**:586–590
137. Chanakyan C et al (2019) Friction stir processing (FSP) of numerical study based on design of experiment-review. Materials Today: Proceedings **27**(2):748–751
138. He X, Gu F, Ball A (2014) A review of numerical analysis of friction stir welding. Prog Mater Sci **65**:1–66
139. Padmanaban R, Kishore VR, Balusamy V (2014) Numerical simulation of temperature distribution and material flow during friction stir welding of dissimilar aluminum alloys. Procedia Engineering **97**:854–863
140. Zhou X, Pan W, MacKenzie D (2013) Identifying friction stir welding process parameters through coupled numerical and experimental analysis. Int J Press Vessel Pip **108**:2–6
141. Zhao PC et al (2018) Numerical simulation of friction stir butt-welding of 6061 aluminum alloy. Transactions of Nonferrous Metals Society of China **28**(6):1216–1225
142. Katayama, S. (2013) Handbook of laser welding technologies Elsevier
143. Dawes, C. (1992) Laser welding: a practical guide Woodhead Publishing
144. Katayama S, Kawahito Y, Mizutani M (2012) Latest progress in performance and understanding of laser welding. Phys Procedia **39**:8–16
145. Juhl TB, Bach D, Larson RG, Christiansen JC, Jensen EA (2013) Predicting the laser weldability of dissimilar polymers. Polymer **54**(15):3891–3897
146. Quazi M et al (2020) Current research and development status of dissimilar materials laser welding of titanium and its alloys. Opt Laser Technol **126**:106090
147. Antony K, T Rakeshnath (2020) Dissimilar laser welding of commercially pure copper and stainless steel 316 L. Materials Today: Proceedings
148. Yilbas BS, Shaukat MM, Afzal AA, Ashraf F (2020) Life cycle analysis for laser welding of alloys. Opt Laser Technol **126**: 106064
149. Sakamiti GP, Siqueira RHM, Carvalho SM, Meireles JB, Lima MSF (2019) Weldability of a zirconium alloy comparing resistance and pulsed laser methods. Nuclear Materials and Energy **20**:100693
150. Zhang Z, Shan J, Tan X (2018) Evaluation of the CFRP grafting and its influence on the laser joining CFRP to aluminum alloy. J Adhes Sci Technol **32**(4):390–406
151. Rodríguez-Vidal E, Sanz C, Lambarri J, Quintana I (2018) Experimental investigation into metal micro-patterning by laser on polymer-metal hybrid joining. Opt Laser Technol **104**:73–82
152. Tao W, Su X, Chen Y, Tian Z (2019) Joint formation and fracture characteristics of laser welded CFRP/TC4 joints. J Manuf Process **45**:1–8
153. Wahba M, Kawahito Y, Katayama S (2011) Laser direct joining of AZ91D thixomolded Mg alloy and amorphous polyethylene terephthalate. J Mater Process Technol **211**(6):1166–1174
154. Katayama S, Kawahito Y (2008) Laser direct joining of metal and plastic. Scr Mater **59**(12):1247–1250
155. Lambiase F, Genna S, Kant R (2018) A procedure for calibration and validation of FE modelling of laser-assisted metal to polymer direct joining. Opt Laser Technol **98**:363–372
156. Hirsch J et al (1998) Axisymmetric laser welding of ceramics: comparison of experimental and finite element results. Opt Lasers Eng **29**(6):465–484
157. Song L, Ma J, Zhang Q, Shen Z (2019) Laser melted oxide ceramics: multiscale structural evolution with non-equilibrium features. J Mater **5**(3):436–445
158. de Pablos-Martín A, Lorenz M, Grundmann M, Höche T (2017) Laser welding of fused silica glass with sapphire using a non-stoichiometric, fresnoitic Ba2TiSi2O8· 3 SiO_2 thin film as an absorber. Opt Laser Technol **92**:85–94
159. Duley W, Mueller R (1992) CO_2 laser welding of polymers. Polym Eng Sci **32**(9):582–585
160. Jansson A et al (2003) The effect of parameters on laser transmission welding of polymers. in International Congress on Applications of Lasers & Electro-Optics. Laser Institute of America **609**(1):2–12
161. Van de Ven JD (2007) and A.G. Erdman, Laser transmission welding of thermoplastics—Part I: Temperature and pressure modeling **129**(5):849–858
162. Van de Ven JD, Erdman AG (2007) Laser transmission welding of thermoplastics—Part II: experimental model validation **129**(5): 859–867
163. Nonhof C (1994) Laser welding of polymers. Polym Eng Sci **34**(20):1547–1549
164. Wissman LY (2007) Method for laser welding flexible polymers. Google Patents
165. Hilton PA, Jones I, Kennish Y (2003) Transmission laser welding of plastics. in First International Symposium on High-Power Laser Macroprocessing. International Society for Optics and Photonics 4831(1):1–9
166. Hubeatir KA (2020) Laser transmission welding of PMMA using IR semiconductor laser complemented by the Taguchi method and grey relational analysis. Materials Today: Proceedings 20:466–473
167. Taha Z et al (2009) Mathematical modeling of laser-assisted transmission lap welding of polymers. Scr Mater 60(8):663–666
168. Acherjee B, Kuar AS, Mitra S, Misra D (2012) Effect of carbon black on temperature field and weld profile during laser transmission welding of polymers: A FEM study. Opt Laser Technol 44(3):514–521
169. Casalino G, Ghorbel E (2008) Numerical model of CO_2 laser welding of thermoplastic polymers. journal of materials processing technology. 207(1-3):63–71
170. Ruotsalainen S, Laakso P, Kujanpää V (2015) Laser welding of transparent polymers by using quasi-simultaneous beam offsetting scanning technique. Phys Procedia 78:272–284

171. Villar M, Garnier C, Chabert F, Nassiet V, Samélor D, Diez JC, Sotelo A, Madre MA (2018) In-situ infrared thermography measurements to master transmission laser welding process parameters of PEKK. Opt Lasers Eng 106:94–104
172. Brodhun J, Blass D, Dilger K (2018) Laser transmission welding of thermoplastic fasteners: influence of temperature distribution in a scanning based process. Procedia CIRP 74:533–537
173. Speka M, Matteï S, Pilloz M, Ilie M (2008) The infrared thermography control of the laser welding of amorphous polymers. NDT & E International 41(3):178–183
174. Ilie M, Kneip JC, Matteï S, Nichici A, Roze C, Girasole T (2007) Through-transmission laser welding of polymers–temperature field modeling and infrared investigation. Infrared Phys Technol 51(1):73–79
175. Schmailzl A, Käsbauer J, Martan J, Honnerová P, Schäfer F, Fichtl M, Lehrer T, Tesař J, Honner M, Hierl S (2020) Measurement of core temperature through semi-transparent polyamide 6 using scanner-integrated pyrometer in laser welding. Int J Heat Mass Transf 146:118814
176. Schmitt R, Mallmann G, Devrient M, Schmidt M (2014) 3D polymer weld seam characterization based on optical coherence tomography for laser transmission welding applications. Phys Procedia 56:1305–1314
177. Chen M, Zak G, Bates PJ (2011) Effect of carbon black on light transmission in laser welding of thermoplastics. J Mater Process Technol 211(1):43–47
178. Rodríguez-Vidal E, Quintana I, Gadea C (2014) Laser transmission welding of ABS: effect of CNTs concentration and process parameters on material integrity and weld formation. Opt Laser Technol 57:194–201
179. Gisario A, Veniali F, Barletta M, Tagliaferri V, Vesco S (2017) Laser transmission welding of poly (ethylene terephthalate) and biodegradable poly (ethylene terephthalate)–based blends. Opt Lasers Eng 90:110–118
180. Schieler O, Beier U (2016) Induction welding of hybrid thermoplastic-thermoset composite parts. King Mongkut's University of Technology North Bangkok International Journal of Applied Science and Technology 9(1):27–36
181. Graham D et al (2011) A hybrid joining scheme for high strength multi-material joints. in Proceedings of the 18th International Conference on Composite Materials. 1(1):1–6
182. Reisgen U, Schiebahn A, Lotte J, Hopmann C, Schneider D, Neuhaus J (2020) Innovative joining technology for the production of hybrid components from FRP and metals. J Mater Process Technol ((282)):116674
183. Abibe A et al (2011) Development and analysis of a new joining method for polymer-metal hybrid structures. J Thermoplast Compos Mater 24(2):233–249
184. Engelmann C et al (2015) Metal meets composite-hybrid joining for automotive applications. Proceedings of LiM2015. Munich **1**(1):1–10

Publisher's note Springer Nature remains neutral with regard to jurisdictional claims in published maps and institutional affiliations.

View publication stats

Appendix B

Paper 2: Study of the optical, thermal, morphological and mechanical characteristics of a laser weldable reinforced polymer

Check for updates

Received: 14 December 2021 | Revised: 4 April 2022 | Accepted: 11 April 2022

DOI: 10.1002/pc.26677

RESEARCH ARTICLE

Polymer COMPOSITES WILEY

Study of the optical, thermal, morphological and mechanical characteristics of a laser weldable fiber reinforced polymer

Luiz R. R. Silva[1,2] | **Eduardo A. S. Marques**[3] | **Ricardo J. C. Carbas**[3] | **Alireza Akhavan-Safar**[3] | **Lucas F. M. da Silva**[1]

[1]Departamento de Engenharia Mecânica, Faculdade de Engenharia, Universidade do Porto, Porto, Portugal

[2]Departamento de Engenharia Mecânica, Instituto Federal de Educação, Ciência e Tecnologia do Espírito Santo (IFES), São Mateus, Espírito Santo, Brazil

[3]Instituto de Ciência e Inovação em Engenharia Mecânica e Industrial (INEGI), Porto, Portugal

Correspondence
L. R. R. Silva, Departamento de Engenharia Mecânica, Faculdade de Engenharia, Universidade do Porto, 4200-465, Porto, Rua Dr. Roberto Frias, s/n, Portugal.
Email: luiz.silva@ifes.edu.br

Funding information
Fundação para a Ciência e a Tecnologia

Abstract

In recent years, varied industrial users such as the automotive and electronic manufacturers, have greatly expanded the application of technical polymers, exploring the lower weight, improved moldability of complex parts and good mechanical performance that these materials can provide, especially when reinforced with fibers. Among these materials, polybutylene terephthalate reinforced with 30% glass fiber, designated as PBT GF30, is highly interesting, since it combines excellent mechanical properties with watertightness, allowing PBT GF30 to be used in the encapsulation of sensitive electronic elements. However, to maintain access, PBT GF30 products always require the use of joints, which are often created using laser welding. This work presents a detailed characterization of the thermal, optical, mechanical, and morphological characteristics of PBT-GF30 suitable for laser welding, supported by a numerical analysis. This process allowed to determine the influence of thermal energy on the behavior of the material and thus fully understand the mechanical response of the material after laser welding. Testing of the PBT GF30 in the as received state confirmed a fusion temperature of 225°C and large energy absorption for wavelengths around 1000 nm. Exposure to large temperatures leads to increased fiber exposure and matrix degradation, with a deleterious effect on the mechanical properties. When treated at the highest temperature under consideration, the material exhibited a reduction of 66% in its ultimate tensile stress, 67% in the yield at failure, 45% in the Young's modulus and 44% in the stress intensity factor. Hardness was less affected by the temperature increase. From the numerical model for the tensile and the compact tension tests, it was possible to find a good degree of convergence. This material was generally found suitable for laser welding processes and the determined useful to support the modeling the behavior of laser welded joints.

KEYWORDS

fracture toughness, laser welding, material characterization, optical properties, PBT GF 30, thermal treatment

 © 2022 Society of Plastics Engineers.

1 | INTRODUCTION

The automotive and electronic industries have gradually increased the use of engineering polymers in their products, in an effort to reduce weight, increase strength, enhance thermal insulation and to ease forming of more complex parts, among many other uses.[1–3] Following the usage of polymer-only components, products based on polymeric composites have also become commonplace, using fiber reinforcement. This allows to expand the application of polymers to more demanding applications that require superior mechanical properties such as mechanical strength, stiffness, hardness, energy absorption, among many others.[4–10]

According to Schaaf[11] fiberglass reinforced polybutylene terephthalate (PBT GF) has been a reference material among the engineering polymers suitable for automotive application, providing high mechanical properties, good thermal insulation, relatively low cost and allowing high production rates in geometrically complex parts. Koppl[12] also describes the usefulness of PBT GF 30 in electrical and electronic devices, communication, and automotive parts, on account of its excellent mechanical properties. However, it is also stated that this polymer has some limitations regarding its flammability, which can be partially mitigated with the inclusion of anti-flame retardants.

Kopczynska[13] describes the joining process of PBT in electronic components, using a radiation cured epoxy adhesive. Although a good degree of crosslinking was obtained, increasing the strength of the joint, the performance of the bonded joint was not fully satisfactory, owing to difficulties associated to surface preparation. Thus, there has been a growing demand for laser joining of PBT GF 30, since this process increases productivity, with much shorter operation times, especially when compared to adhesive bonding. Laser welding also lends itself to automated processes and for usage in complex geometries. Amanat,[14] in a study on joining processes in thermoplastics, cites the advantages of the laser welding process for polymer joining, describing it consisting of a single step, with highly localized heating and achieving instantaneous joining. The reduction of residual stress field is also generally quite benign, which contributes positively to the joint strength. This process is also reported to be vibration free, highly controllable and with low waste generation. All these advantages make it, for example, highly suitable for hermetically sealing casings for medical devices.

The main aim of this work is to carry out an extensive characterization of the mechanical, optical, morphological and thermal characteristics of PBT GF 30, within the context of the use of this material for laser welding applications. This study determines the material response to the conditions found during a laser welding process, seeking to understand how the properties of the welded region vary, determining not only property gradients within the fusion zone but also within the heat affected zone. Furthermore, the mechanical response of the material to the laser welding process is assessed since there is only very limited information on the welded behavior of PBT-GF30. This is important since the laser welding process, although quite fast, still provides important heating and cooling cycles which can cause changes in the material. The mechanical properties under study include the hardness, strength, and fracture toughness. These include the melting temperature of the material (225°C), a temperature after melting, at the tail-end of the thermogravimetric test (237°C) and a high temperature, selected before the material becomes irreversibly damaged (257°C). The mechanical properties were determined in order to be used in the numerical models for laser welded joints, representing a gradient between the melted material and the heat affected zone, and thus this work includes a numerical validation of the experimentally obtained data, with a focus on the strength and fracture toughness values.

2 | EXPERIMENTAL DETAILS

The PBT GF 30 thermoplastic used in this work is a commercial product. For this work, it was provided in already molded plates with 130 × 20 × 2 mm and 80 × 80 × 2 mm in size, both produced by injection molding of PBT pellets with randomly distributed glass fibers, aiming to reduce the degree of anisotropy.[15] The end result of this process is PBT matrix reinforced with 30% of glass fibers in weight and with non-oriented, homogeneous properties, supplied by BASF (Ludwigshafen, Germany). Its Poisson coefficient is 0.45,[16] its expansion coefficient is 2.4×10^{-5} K^{-1}. It has a thermal conductivity of 0.288 W/m K, thermal capacity of 1600 J/kg K and its melting temperature is of 225°C, according to Jasen and Vendramini.[17,18] According to Koppl[12] the energy absorption capability under impact is 65 kJ/m^2. The density has been determined to be 1525 kg/m^3 by several authors.[16,17,19–21]

2.1 | Thermal treatment of PBT GF 30

To accurately determine the mechanical properties of the PBT GF 30 material that is located in the weld bead and the heat affected zone of laser welded joint, an experimental procedure was devised where the material is submitted to precisely controlled heat treatments in a closed oven. The PBT GF 30 material was supplied in pre-cut sheets and to ensure that the PBT GF 30 sheets do not

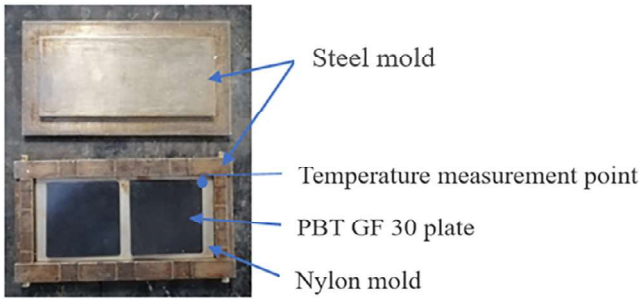


FIGURE 1 Detail of the mold used for heat treatment

deform during the heat treatment, these were placed inside a steel mold, pressed with a load of 8 kg. A 2 mm thick nylon plate was used to control both the shape and the thickness of the samples, as shown in Figure 1.

Three different heat treatment temperatures were considered, as shown in Table 1, with the oven being controlled to ensure that that material is staged at its target temperature for a period of 10 min. The staging temperature was controlled with a K-type thermocouple inserted into the mold and in direct contact with the PBT GF 30 material. After the heat treatment stage, the material was naturally cooled to room temperature.

These heat treatment temperatures were chosen to include the melting temperature of the material (225°C).[17] The end point of melting transition of the DSC curve, (237°C) and finally a temperature of 257°C, slightly before the expected temperature of thermal degradation of the material.

2.2 | Optical properties

To characterize the response of PBT GF 30 to laser radiation, FTIR spectroscopy was performed, allowing to determine the material's transmissivity and absorbance, in a range of wavelengths of 500–1100 nm, which includes the wavelengths typical of laser equipment suitable for joining thermoplastics such as the PBT GF 30. The analyzed specimen has the dimensions of 10 × 20 × 1 mm and is of a dark, almost black color, a characteristic favorable to the absorption of light in these wavelengths. With reference to the work performed by Frick,[22] after performing the test for characterization of transmittance, the Beer–Lambert's law was used to calculate the absorbance of the material at a wavelength of 1064 nm.

2.3 | Thermal properties

Based on the work performed by Khosravi[23] to characterize the thermal properties of the adhesive, such as the level of polymerization in the material, the melting point and temperature of degradation, DSC testing of PBT GF30 was performed. The test was carried out in a NETZSCH DSC 214 Polyma DSC21400-0655-L device in the range of −20 to 300°C, with a heating ramp of 10 K/min, in an N_2 medium.

TABLE 1 Staging temperatures and stage durations used for heat treatment

Staging temperature (°C)	Stage duration (min)
225	60
237	70
257	95

2.4 | Morphological properties

Based on work described in the literature,[12,20,24] the morphology of PBT GF 30 can be generally described as a matrix of polybutylene terephthalate with undirected glass fibers, with diameters of 10–12 μm. The PBT GF 30 used in this work (both in the supplied state and the heat-treated state) was visually characterized via optical microscopy. Concurrently, a macro analysis of the surface of the materials under study was also carried out, comparing their key characteristics.

2.5 | Determination of mechanical properties

The mechanical properties were characterized using three different methodologies, allowing to determine the tensile strength, hardness and fracture toughness of the material in the received and the heat-treated states.

2.5.1 | Tensile testing

Tensile testing was carried out in an INSTRON® (Norwood, MA) 3367 universal testing machine using an extensometer for the strain measurement. The properties directly obtained in this test were the maximum stress and the maximum deformation of the material. The modulus of elasticity was calculated from the stress–strain curves following the ASTM D638-14[25] standard.

The tensile specimen dimensions were based on the BS 2782[26] standard. The specimens for PBT GF 30 in the as received state had different dimensions from those subjected to a heat treatment process. This was mainly due to the dimensional constraints of the mold and the

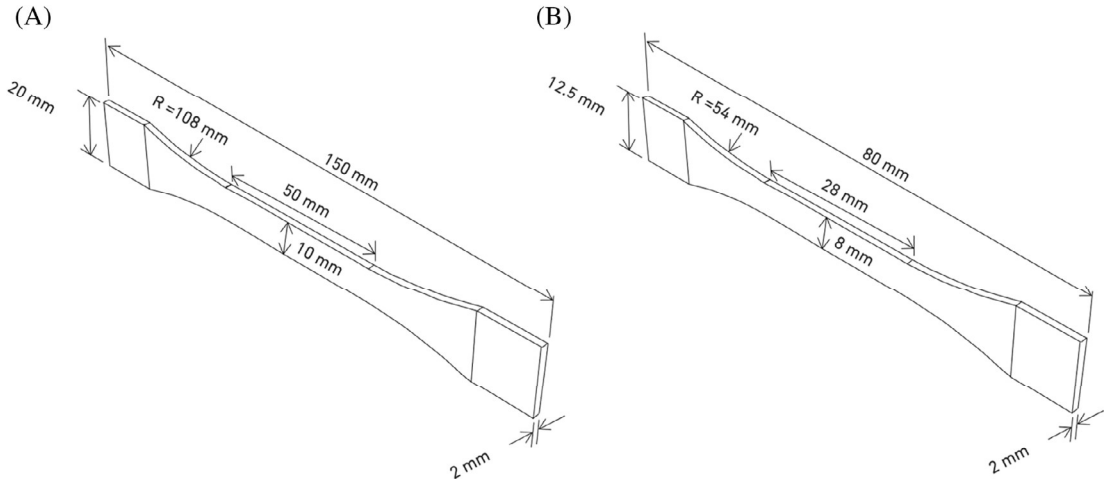


FIGURE 2 Geometry of the dog-bone tensile test specimens. (A) PBTGF30 in as supplied state. (B) PBT GF 30 heat treated state

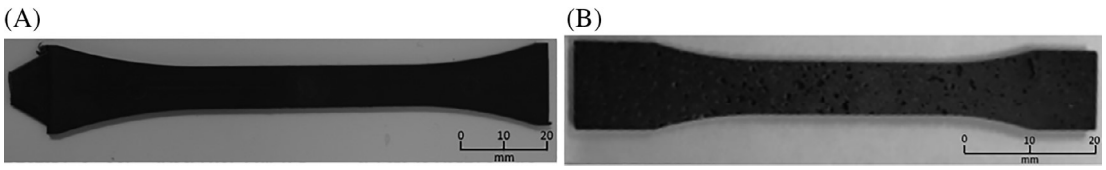


FIGURE 3 Machined tensile testing specimens. (A) PBT GF 30 in as supplied state. (B) PBT GF 30 heat treated state at 257°C

ovens used for heat treatment, which forced a reduction in size. Figure 2A shows the dimensions of the tensile specimens of PBT GF 30 in the as received state and Figure 2B shows the dimensions of the tensile test specimens that were subjected to heat-treatment.

The PBT GF 30 samples in the as received condition were supplied as pre-molded plates which, after machining, could only lead to a tensile test specimen length that was below the recommendation of the BS 2782 standards, as shown in Figure 3A,B. However, no interference was expected to occur with the results, since the specimens were clamped in the universal testing in roughly the same position and the strain was measured in the central region of the specimen using a 25 mm extensometer. Three specimens were tested for each condition of PBT GF 30.

2.5.2 | Hardness testing

The second test characterized the hardness of the PBT GF 30 using a Shore D type durometer, model SAUTER (Balingen, Germany) HBO 100-0. The hardness was measured for material in the as supplied state and following the three different heat-treatment temperatures. A total of 10 indentations were made for each of these four states.

2.5.3 | Fracture toughness testing

The fracture toughness of the PBT GF 30 material was experimentally determined, using the compact test (CT) configuration, as described on ASTM D5045-14.[27] However, considering that the sample thicknesses of 2 mm used were not within the requirement of the standard for characterization in the plane state of deformation, the standard was used instead to determine the stress intensity factor for the PBT GF30 material in the supplied and the heat-treated state.

Figure 4A shows the dimensions of the CT specimen used, while Figure 4B presents an image of a representative specimen after the notch was machined by a 2 mm cutting disc, with a 60° tip angle and a radius of 0.1 mm. A paper scale was bonded to the specimen to serve as a reference of the measurement of crack propagation.

For the crack nucleation, the tapping method was used, using a shaving blade, as cited in.[28] Figure 5A illustrates the notch in the CT specimen caused by the shaving blade and Figure 5B shows the notch with the nucleated crack.

Table 2 shows the initial notch sizes, the crack nucleation length resulting from the tapping method, the effective length and the thickness of the specimens and the results of the function $f(x)$, presented by Equation (1) and explained on the Figure 6 were used for calibration by the standard, considering the sum of the notch and the

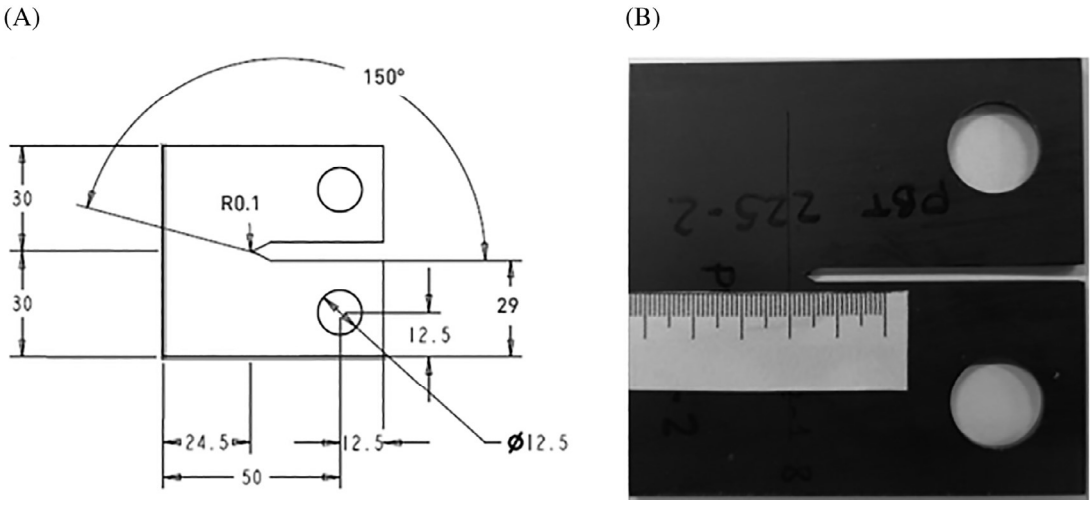


FIGURE 4 (A) Compact tension sample dimensions (in mm). (B) Manufactured sample of compact test

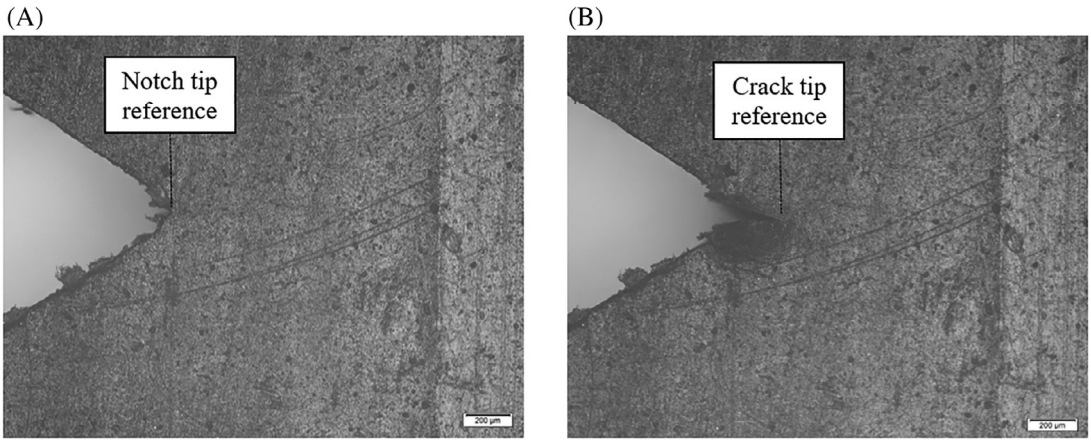


FIGURE 5 Representation of the (A) pre and (B) post crack specimen

TABLE 2 Parameters of the compact test specimens for all PBT GF30 conditions tested

Specimens	Load (N)	Total crack (mm)	Notch size (mm)	Nucleated crack (mm)	Width (mm)	Thickness (mm)	aT/W	$f(x)$
As received	260.00	24.85	23.3	1.55	52.6	2	0.47	8.8933
	265.65	24.5	23.4	1.1	52.6	2	0.47	8.7231
	298.86	25.7	24	1.7	52.5	2	0.49	9.3557
Treated at 225°C	206.00	26	24	2	51.9	2.2	0.50	9.6878
	179.65	26.19	24.8	1.39	51.9	2.2	0.50	9.7982
	194.00	28.72	24.5	4.22	52.2	2.15	0.55	11.3718
Treated at 237°C	162.00	25.78	24	1.78	51	2	0.51	9.8246
	156.30	26.6	23.3	3.3	52.2	2.1	0.51	9.9510
	178.62	24.2	23	1.2	51.5	2.1	0.47	8.8279
Treated at 257°C	122.86	28.9	23.4	5.5	52.7	1.9	0.55	11.3015
	100.80	28.3	23.3	5	52.1	2	0.54	11.1029
	137.00	28.15	23.5	4.65	52	2	0.54	11.0341

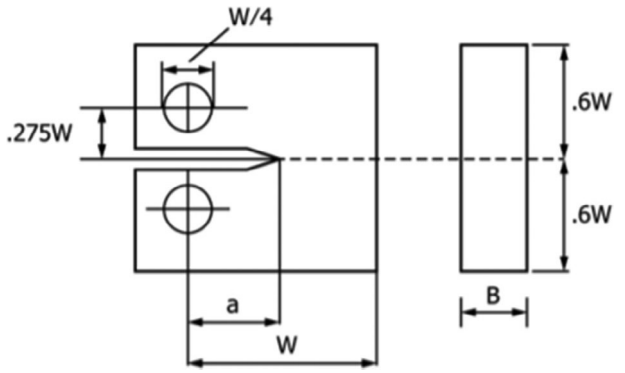


FIGURE 6 Parametric scheme of the compact test sample

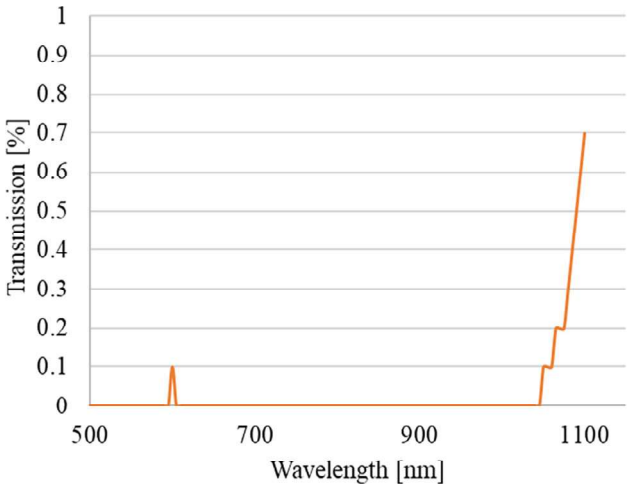


FIGURE 7 Representative FTIR transmittance curve of PBT GF 30 in the as received state

nucleated crack size and the effective length of the specimens.

$$f(x) = 6x^{\frac{1}{2}} \frac{[1.99 - x(1-x)(2.15 - 3.93x + 2.7x^2)]}{(1+2x)(1-x)^{\frac{3}{2}}} \text{ to } x = \frac{a}{W} \quad (1)$$

In order to measure crack propagation, a digital camera was used to capture images every 5 s during the CT test. These images were synchronized with the universal testing machine data, allowing them to be correlated with the force and displacement curves.

3 | EXPERIMENTAL RESULTS

3.1 | Optical properties

To determine the applicability of the PBT GF 30 for laser welding, the absorbance and transmittance of the material was characterized via Fourier-transform infrared spectroscopy (FTIR). Figure 7 shows the transmittance curve obtained for PBT GF 30.

The transmittance curve (T) clearly shows that for most of the wavelengths under analysis the transmittance is low. Applying the Beer–Lambert law, as shown in Equation (2), for the 1064 nm wavelength, the absorbance (A) was determined to be 100% for the used PBT GF 30 material.

$$A = 2 - \log_{10}\%T \quad (2)$$

Thus, as referred in,[29] this type of material is shown to be unsuitable for use in transmission-based laser welding processes, meaning that the material should be used only for laser welding operations in which the fusion and solidification occurs solely at the surface of the materials to be welded, at the initial point of incidence of the laser light.

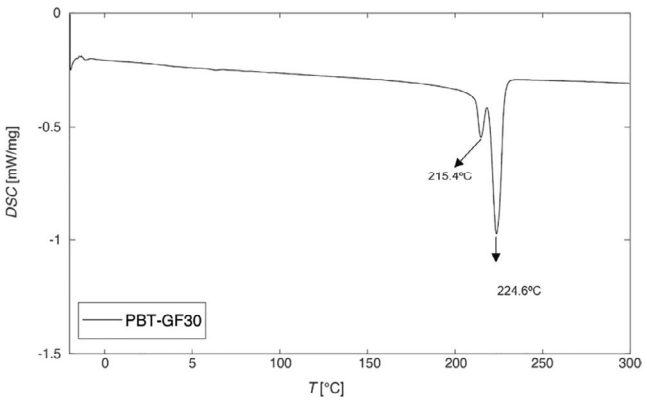


FIGURE 8 Differential scanning calorimetry curve of PBT GF30

3.2 | Thermal properties

The DSC results for PBT GF 30 are represented in Figure 8, which demonstrate that melting occurs at temperature of 225°C. It is observed a second peak at 215.4°C. Segundo Zhang et al.[30] theses peaks are observed in PBT too, they say that origin of this second peak has been ascribed to the presence of different morphologies and simultaneous melting and reorganization of the crystallites.

In the curve shown in Figure 8, considering the range of temperatures at which the DSC was performed, no evidence of material degradation is found up to 300°C. There is also no clear evidence of a glass transition temperature which, according to the literature[31] is around 51°C.

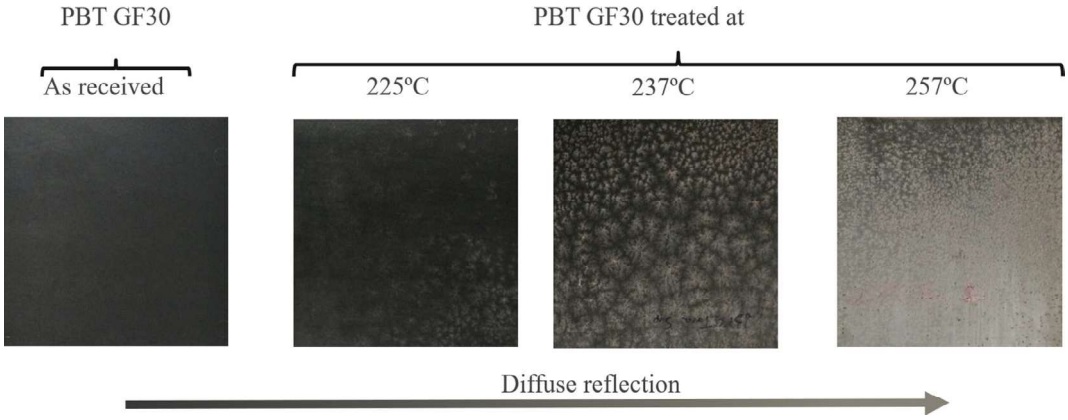


FIGURE 9 Representation of the sample surfaces of PBT GF 30, illustrating the evolution of the material when treated with increasing higher temperatures

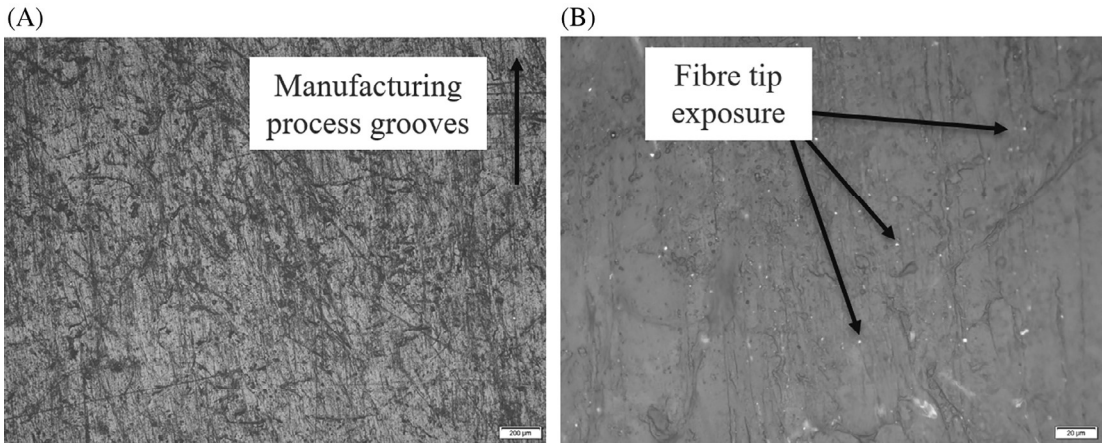


FIGURE 10 Micrography of the surface of the PBT GF 30 as received. (A) Identification of the grooves of the manufacturing process. (B) Exposed fiber tips

3.3 | Morphological properties

The morphological characterization was performed in two phases. The first phase consisted of a visual analysis, comparing the appearance of the PBT GF 30 plates in the as received and after treatment states. Due to the evident degradation of the surface noticed to occur as a function of the temperature, the opacity of the material was gradually and qualitatively characterized, as shown in Figure 9.

In the as received state, the PBT GF 30 samples displayed a uniformly black surface, homogeneous in nature, which absorbs incident light uniformly. The surface becomes increasingly more damaged as the treatment temperature increases, exposing the glass fiber which result in a greyer surface.

The second part of the characterization is based on the analysis of micrographs of the material, which illustrate in detail the surface of the materials, as well as the regions of degradation and exposure of fibers. Figure 10A shows PBT GF 30 in the as received state at 5× magnification, illustrating the direction of the abrasions, grooves and scratches created during manufacturing via injection molding. Figure 10B shows the surface of PBT GF30 as received at 20× magnification, where the tips of the fibers can be seen as sources of light reflection.

Figure 11 shows micrographs of PBT GF 30 for the three heat treatment conditions. It is observed that the material degradation is proportional to the treatment temperature.

This analysis can be further detailed for each specific condition. In Figure 12A, corresponding to treatment at 225°C and magnified five times, it is observed that the overall size of the pores is around 50 μm. For Figure 12B, magnified by 10 times, there is also some exposure of the fibers, either from the tips or in its cross section.

As for the material treated at 237°C, shown in five times magnification in Figure 13A, there is clearly a higher pore density than observed for the 225°C

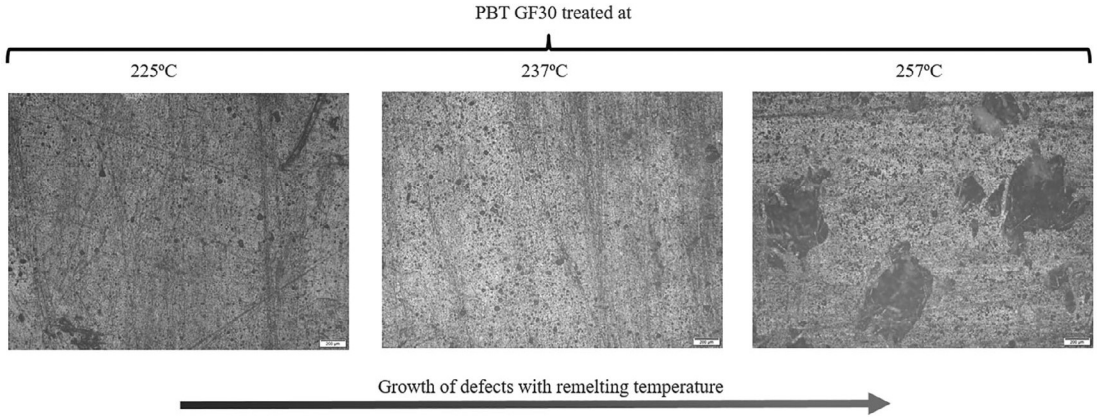


FIGURE 11 Comparison between the degree of porosity in PBT GF30 treated in the three different conditions

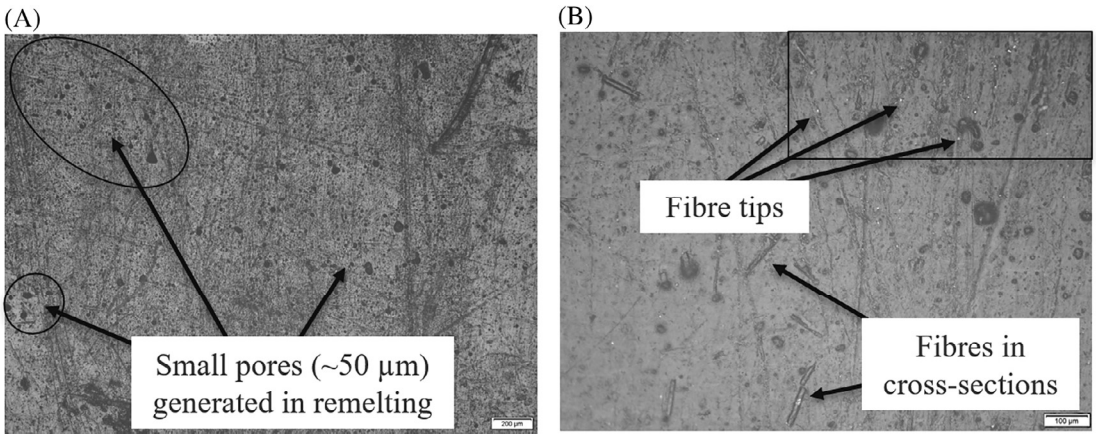


FIGURE 12 Micrography of the surface of the PBT GF30 treated at 225°C. (A) Identification of the pores following the heat-treatment process. (B) Representation of the exposed fibers (tips and cross-section)

condition. By magnifying the image 20 times, it is also more evident that the transversal sections of the fibers are now exposed, as detailed in Figure 13B. Figure 13C then illustrates the appearance of voids, resultant from the surface degradation with an increase of the heat-treatment temperature. Finally, Figure 13D allows the diameter of the fibers to be determined under 20× magnification. This was found to be in the order of 15 µm.

For the last and most severe heat-treatment condition (at 257°C), the micrographs shown in Figure 14A indicate the presence of large voids and widespread exposure of fibers. With greater magnification (Figure 14B,C) the fibers inside these large voids are easily seen.

The degradation of PBT-GF30 when treated at high temperature simulates the result of a direct laser welding process, an autogenous procedure for joining equal materials. In the case of PBT-GF30 this is often achieved using a laser with a relatively long wavelength, in the order of 1000 nm.

The main application of this process is for joining thin plates using butt or fillet type joints. In this case, joining takes place directly in the laser incidence point, melting the matrix and possibly causing partial exposure of the fibers that are close to the surface. In dissimilar joints, PBT-GF30 PBT can also be used as an absorbent material, for use in transmission type welding, under a laser transparent material. In such applications, it can be used for parallel and corner joints, among many others.

3.4 | Mechanical properties

Tensile test results, shown in Figure 15, indicate an important degradation of the properties of PBT GF30 as a result of the heat treatment, showing a large decrease in strength and strain at failure for a temperature of 257°C, a temperature which is significantly above the melting temperature of the material.

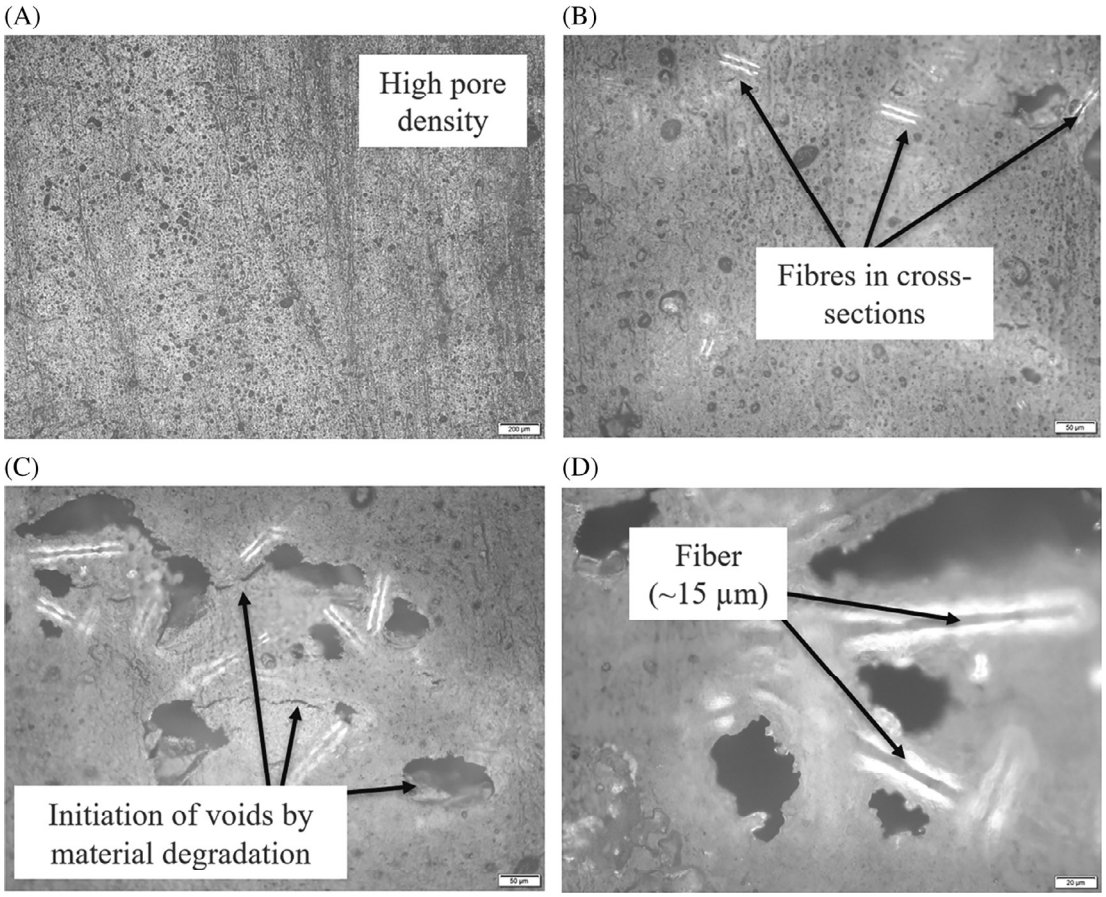


FIGURE 13 Micrography of the surface of the PBT GF30 treated at 237°C. (A) Identification of the pores created after the heat-treatment process. (B) Representation of the exposed fibers (tips and). (C) Void and crack initiation driven by material degradation. (D) Representation of the fibers

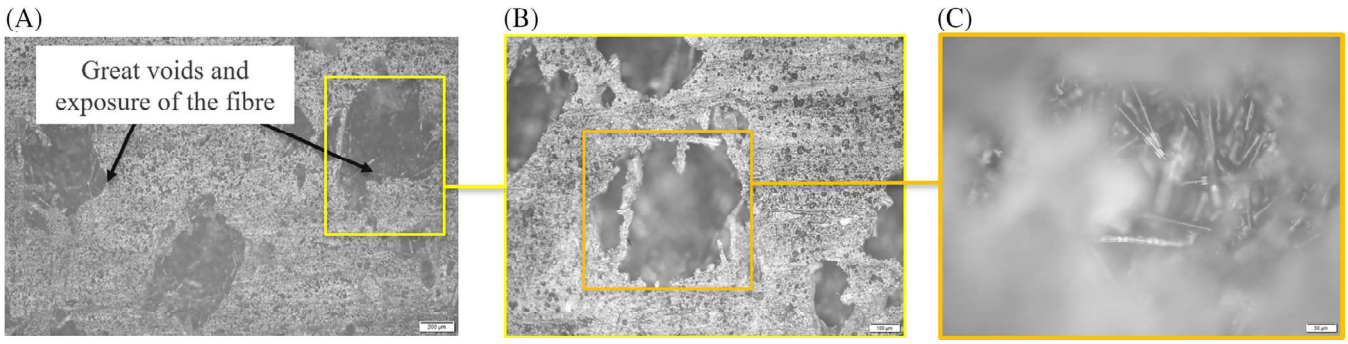


FIGURE 14 Micrography of the surface of the PBT GF30 treated at 257°C. (A) Identification of the large voids, small pores and exposed fibers. (B) Magnification of the voids. (C) Magnification of the fibers

There is thermal degradation of all key mechanical properties such as the modulus of elasticity, failure stress and maximum strain, as illustrated in Figures 16 and 17.

Based on the reference values for the untreated PBT GF 30, the strength values determined in the experimental test are in agreement with studies carried out by other authors.[11,12,20,21,32,33]

According to Figures 16 and 17, the standard deviation for the treated specimens is more significant, since the degradation of the material and the exposure of the glass fibers create a large number of stress concentration points and also reduces the effective cross-section area of the material. The works of Lal et al. and Lazar et al.[34,35] cite debonding as one the most characteristic failure

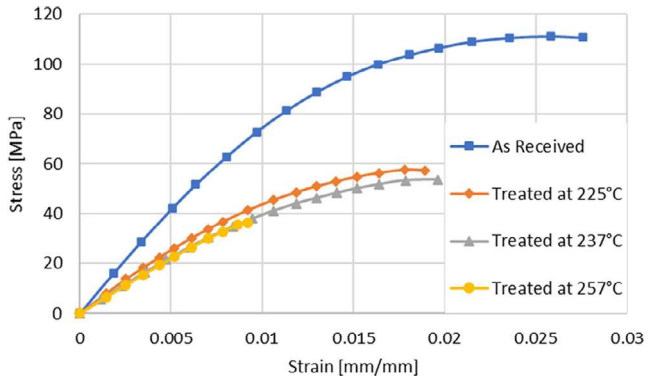


FIGURE 15 Stress–strain tensile test curves of the PBT GF 30 in the as received and treated conditions (at 225, 237, and 257°C)

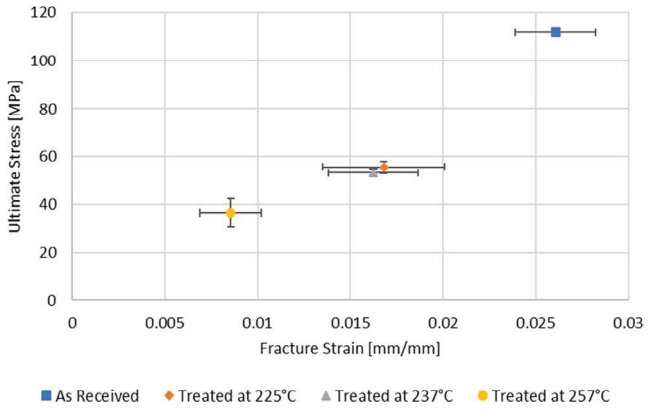


FIGURE 16 Comparison between the ultimate stress and fracture strain between PBT GF 30 in the as received and treated state

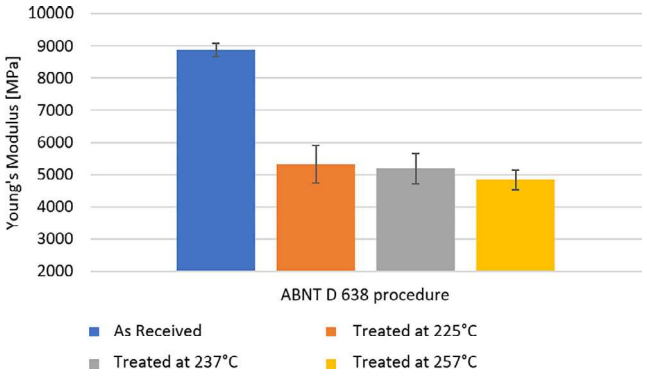


FIGURE 17 Young's modulus comparison between PBT GF30 in the as received and treated state

modes for composites which, in this case, can be the result of the extreme thermal gradients.

Regarding the modulus of elasticity of the PBT GF30 in the received state, the results found are also in agreement with the published data.[11,12,26]

Figure 18 illustrates the difference between the fracture process of tensile specimens of PBT GF30 as received (Figure 18A) and those treated at 225°C (Figure 18B). While the first appear to have undergone a ductile fracture process, with diagonal (45°) crack propagation, the latter exhibit a noticeably more brittle fracture process.

The hardness values measured through the use of a shore D durometer, shown in Figure 19, suggest an increase in the hardness of the material when treated at the temperature of 225°C, followed by a gradual decrease in hardness, roughly proportional to the increase of the treatment temperature.

According to,[36] this increase in hardness can occur for semi-crystalline thermoplastics, caused by normalization of the grain, while the subsequent hardness reduction, proportional to temperature is the result of annealing, leading to a progressive degradation of the material, with an adverse effect on its mechanical properties.

Moreover, according to Figure 8, there is also a peak of polymerization near the fusion temperature, which can also partially explain this slight increase.

For fracture toughness characterization, the stress intensity factor (K_q) was quantified. This was done since the plates used did not have the minimum thickness required by ASTM D5045-14, which would permit the nominal characterization of the K_{Ic} of the material. The results shown in Figure 20, indicate that the values determined for both the PBT GF30 in the as received state and when subjected to heat treatments are well within the range of values published in the literature.[37]

In order to complement the quantitative results reported above, Figure 21A–D representatively show the crack propagation process in the compact test specimens for PBT GF 30 as received, treated at 225, 237, and 257°C, respectively.

It is observed that, for the PBT GF30 material in the as received state, the crack propagation does not occur as linearly as is the case in the treated PBT GF30. According to Naebe et al.,[38] crack propagation in PBT GF30 tends to bypass the fiber and progress through the matrix, where larger changes in the propagation path are more likely, whereas for the treated conditions the crack tends to follow a linear path because there is greater interaction of the weak pores.

According to the results presented above, the degradation of PBT-GF30 when treated at high temperatures can be correlated to the effects of the laser welding process on the material, especially in the case of an autogenous union welding of PBT-GF30 material, where the PBT matrix melts due to the heat front generated by the laser incidence. According to these results, the variation of the mechanical properties of PBT-GF30 is also expected in these joining processes, since the closer the

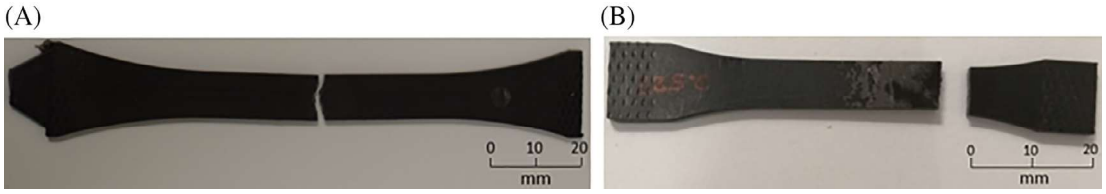


FIGURE 18 PBT GF30 tensile specimens fractured after the tensile test. (A) Specimen representative of the as received condition. (B) Specimen representative of the heat-treated condition

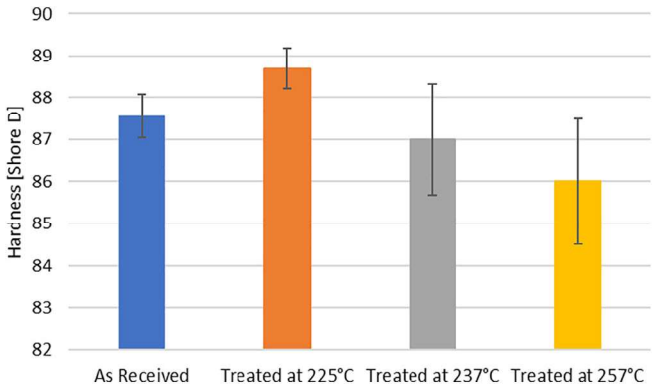


FIGURE 19 Shore D hardness of PBT GF 30 in the as received and treated state

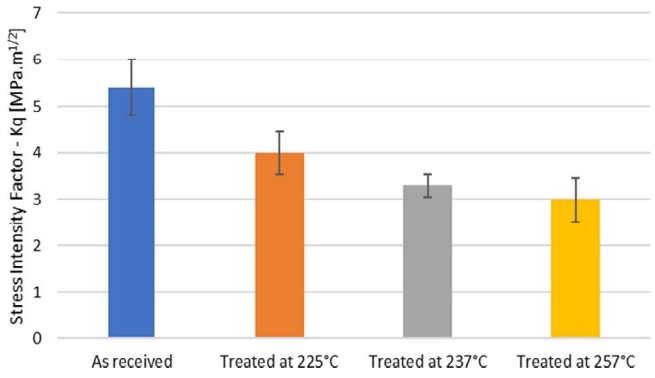


FIGURE 20 Comparison between the experimentally determined stress intensity factor of PBT GF 30

region of laser incidence, the greater the degradation of properties, caused by a melting process which occurs at an increasingly higher temperature.

4 | NUMERICAL PROCEDURE

4.1 | Numerical details

Two different numerical models were created in this work, simulating both the tensile and the compact tension tests. The mechanical properties determined using the experimental testing phase were introduced as inputs in these models, a process which serves to validate the effectiveness of the material models used for reproducing the experimental test.

4.1.1 | Tensile test

For the tensile test, a ductile damage model was used,[39,40] since it enables a better reproduction of the crack path that occurs in this sort of material. In such case, the polymeric matrix (a ductile material) interacts with the high stiffness glass fiber in. Taking into consideration that the bond between the surface of the two materials is often of a low energy nature,[41] many authors in the literature[40,42,43] cite that the application of the ductile damage model is more conducive, with a better applicability of fracture.

In this model, the damage, D, occurs once the maximum stress σ_{y0} is attained. This value is determined using experimental data, based on the peak stress of the elastoplastic behavior. Once the damage is triggered, the material degradation is progressive, based on the relationship $(1-D)E$ from the plastic deformation $\overline{\varepsilon}_0^{pl}$ ε material failure.[43–45] The damage calculation is based on the dissipation of fracture energy G_f (Equation 3), calculated by the integral of the product of the effective stress by the effective element length L within the range from plastic deformation to the maximum deformation $\overline{\varepsilon}_f^{pl}$. Considering that even at the maximum stress the damage is null and that the maximum deformation is the required variable, the base change is made for the displacement of the element until failure occurs.

$$G_f = \int_{\overline{\varepsilon}_0^{pl}}^{\overline{\varepsilon}_f^{pl}} L\sigma_y d\overline{\varepsilon}^{pl} = \int_0^{L\overline{\varepsilon}_f^{pl}} \sigma_y d\overline{u}^{pl} \tag{3}$$

With the change of basis, simplifying the curve by the linear decrease model, without strain hardening rate, the displacement to failure u_f^{pl} is calculated by correlating the maximum strain imposed on the unit length of the characteristic element, according to Equation (4).

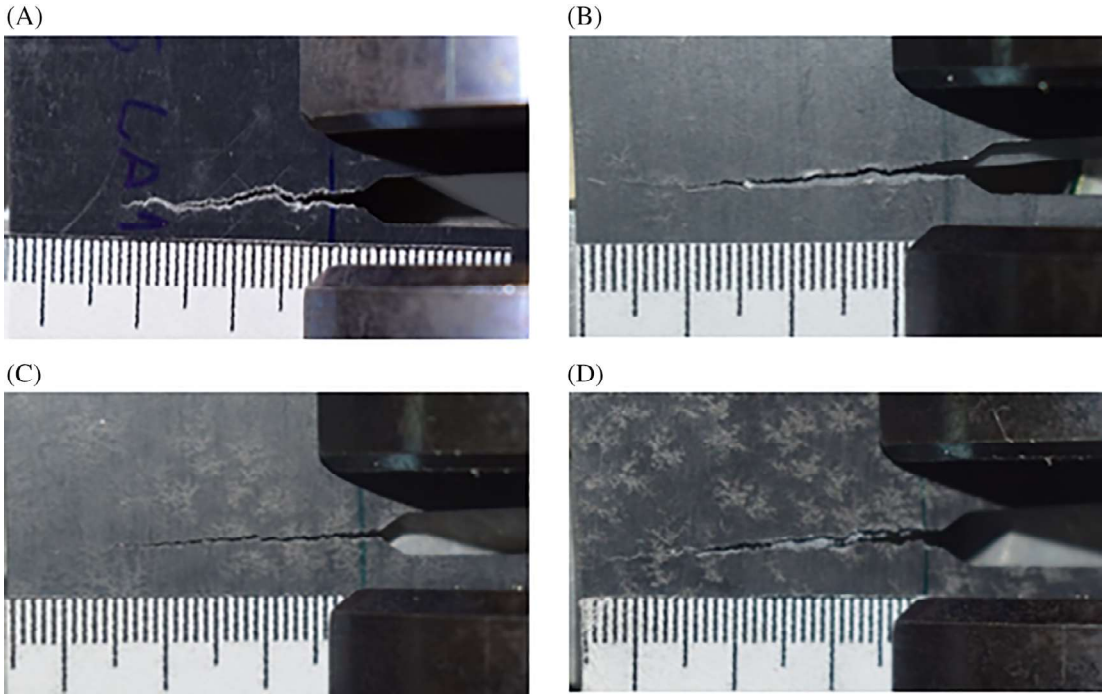


FIGURE 21 Propagation of the crack at the end of the compact test for the PBT GF 30 samples. (A) As received, (B) treated at 225°C, (C) treated at 237°C, and (D) treated at 257°C

TABLE 3 Simulation parameters applied in ductile damage to validate the model in tensile test of PBT GF30

Ductile damage model			
Elastic plastic isotropic			
Material	**Young's modulus (MPa)**	**Poisson ratio**	**Displacement at failure**
As received	8885	0.45	0.1
Treated at 225°C	5317	0.42	0.1
Treated at 237°C	5183	0.42	0.07
Treated at 257°C	4826	0.42	0.07

$$u_f^{pl} = L\bar{\varepsilon}_f^{pl} \tag{4}$$

The material behavior was established as elastoplastic. The mechanical properties used in the model were based on the properties determined in the experimental tests and on literature references. The Poisson's coefficient was set at 0.42 for the conditions of the treated PBT GF 30, reflecting the degradation of the material. Based on the tensile test, carried out at a single test speed, the triaxiality was assumed to be 0.33 and the strain rate as null. The damage evolution was based on displacement type, linear smoothing, with maximum degradation. The simulation conditions used to validate the model are represented in Table 3.

The boundary conditions correspond to a clamped condition on one side of the specimen and the application of a displacement to the other side, as shown in Figure 22 for both tensile test specimens. The mesh size was set to 1 mm for both conditions. Aiming to reach complete failure, the maximum degradation was set at 0.99 and element exclusion was triggered.

4.1.2 | Compact test

For the validation of the compact test a 2D model was used, employing cohesive elements based on a traction separation law. According to the literature,[46] this methodology allows for an accurate simulation of the fracture propagation in reinforced polymers. Furthermore, the thickness of the specimen under study is limited, leading to the application of maximum plane stress damage

(Maxps). The cohesive model is also characterized by a penalty in the material stiffness, with reference to the maximum stress and displacement at damage initiation.

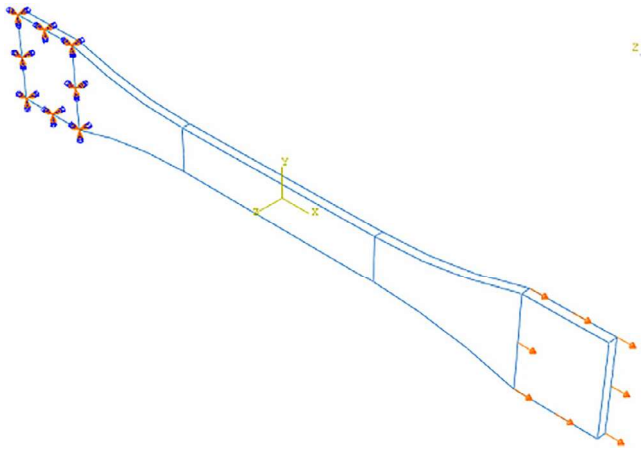


FIGURE 22 Representative configuration of the boundary conditions for the tensile simulation (both as supplied and heat-treated conditions)

For the simulation of the nucleated crack, the extended finite element method (XFEM) was used. Martínez[47] cites that such procedure dispenses with mesh refinement, even for complex geometries, promoting crack propagation instead of momentary stress concentration. Another advantageous factor associated to the use of this model, besides the damage evolution parameters, is the fact that is only really necessary to consider the maximum principal stress.

The material behavior was established as purely elastic. The mechanical properties such as modulus of elasticity and Poisson's ratio were the same used in the numerical model for the tensile test simulation. The damage evolution was based on displacement type, linear smoothing, with maximum degradation. The simulation conditions to validate the model are shown in Table 4.

The specimen measurements are based on Figure 4A, with the model being pinned by one of its holes, while the other hole is forced to displace vertically, as per Figure 23A. The mesh was refined in the crack zone to a 0.5 mm size, with a maximum size of 2 mm away from the crack. The elements used a quad-dominated (free – medial axis) mesh control as per Figure 23B.

TABLE 4 Simulation parameters applied in traction separation law with Maxps and XFEM, to be validated against the experimental compact test results

	Material – PBT GF 30			
	As received	**Treated at 225°C**	**Treated at 237°C**	**Treated at 257°C**
Max principal stress (MPa)	67	40	39	37.7
Displacement at failure	0.33	0.33	0.33	0.12
XFEM – crack size (mm)	1	1	1	1

Abbreviations: Maxps, maximum plane stress damage; XFEM, extended finite element method.

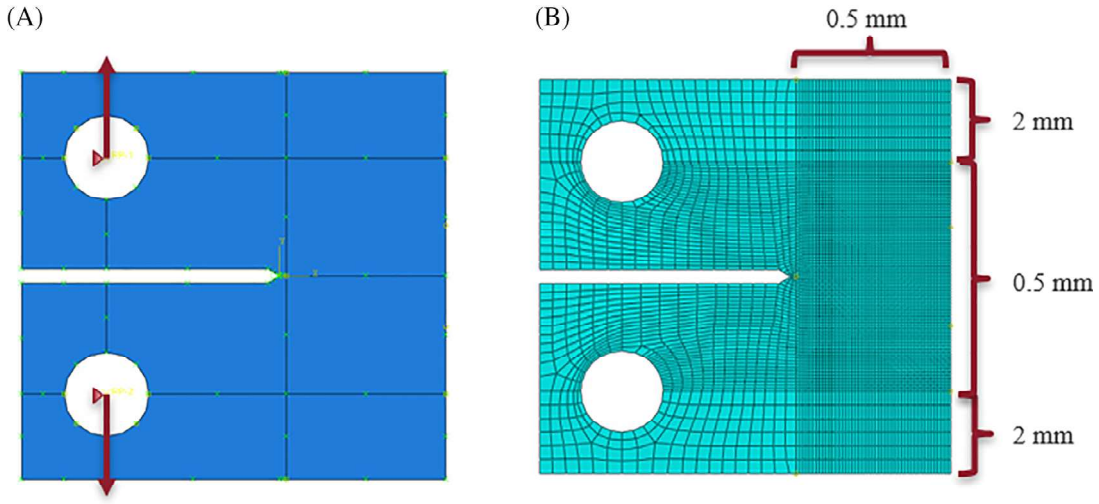


FIGURE 23 Compact test model configuration. (A) Boundary conditions and (B) mesh details

4.2 | Results

4.2.1 | Tensile tests

The results from the ductile damage numerical model (marked as dashed lines) are compared with the experimental curves (marked as continuous lines) in Figure 24. In general, a good degree of convergence was achieved, both for the as received state and for the heat-treated GF30 PBT material (Figure 25).

The error percentages between the experimental and numerical model curves are shown in Table 5.

The largest discrepancy was found for the PBT GF30 thermally treated at 257°C, with an error value of 8.5%, although this can still be considered to be a good degree of convergence.

A comparison of the failure modes of the simulated models, are presented in Figure 26A–D with the failures in the tested specimens of the PBT GF30 as received (Figure 18A) and in for the heat-treated PBT GF30

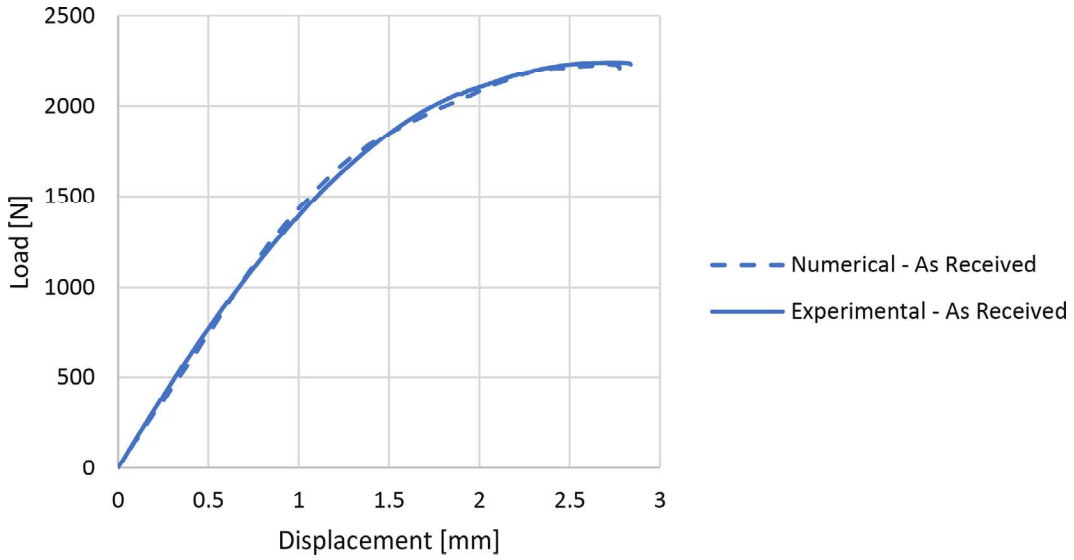


FIGURE 24 Comparison between experimental and numerical results of the force-displacement curve of the tensile test of PBT GF30 in the as received state

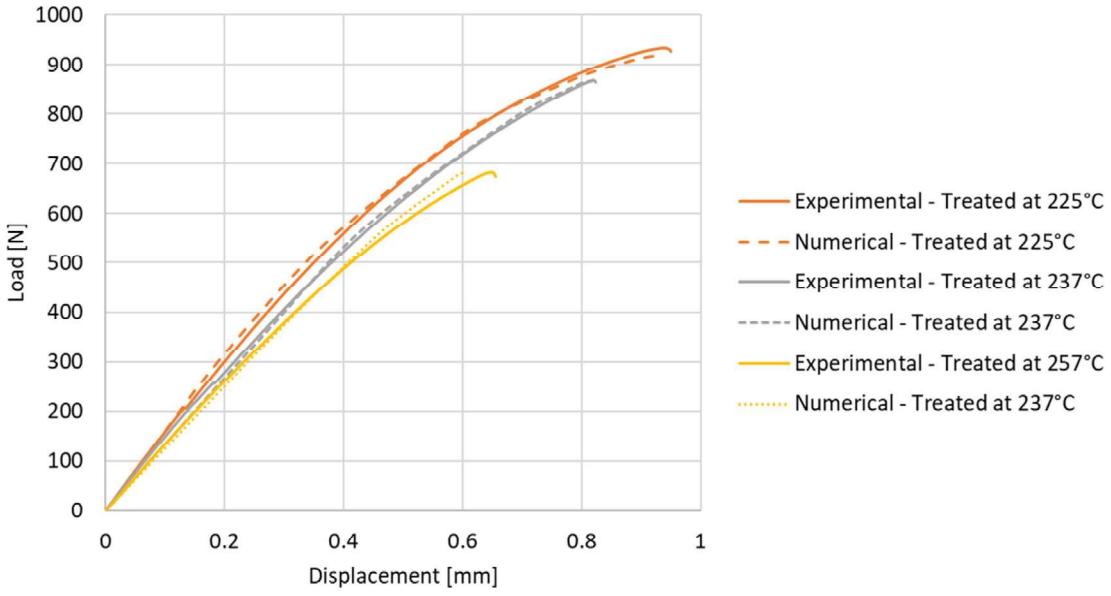


FIGURE 25 Comparison between experimental and numerical results of the force-displacement curves of tensile tests for heat-treated PBT GF30

(Figure 18B). The most representative failure mode is achieved for the PBT GF30 in the as received state, since the material has higher plastic flow.

It is also observed in Figure 26 that the higher the treatment temperature the lower is the concentration of residual stress after failure. This is opposite to what occurs for the PBT GF 30 in the as received state, which possesses greater plasticity. This reflects in higher values of stress concentration in the region of failure.

TABLE 5 Error between experimental and numerical values of maximum strain and maximum stresses

	Error (%)	
	Maximum strain	**Maximum stress**
As received	2.3	0.7
Treated at 225°C	2.2	1.8
Treated at 237°C	5.6	0.3
Treated at 257°C	8.5	0.2

4.2.2 | Compact test

Figures 27 and 28 represent, respectively, the numerical response obtained for the compact tests of the PBT GF 30 material as received and in the heat-treated state. The

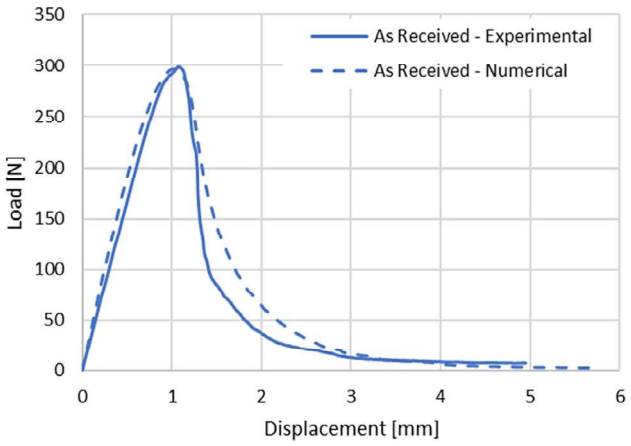


FIGURE 27 Comparison between experimental and numerical force-displacement curves of the compact test of PBT GF30 in the as received state

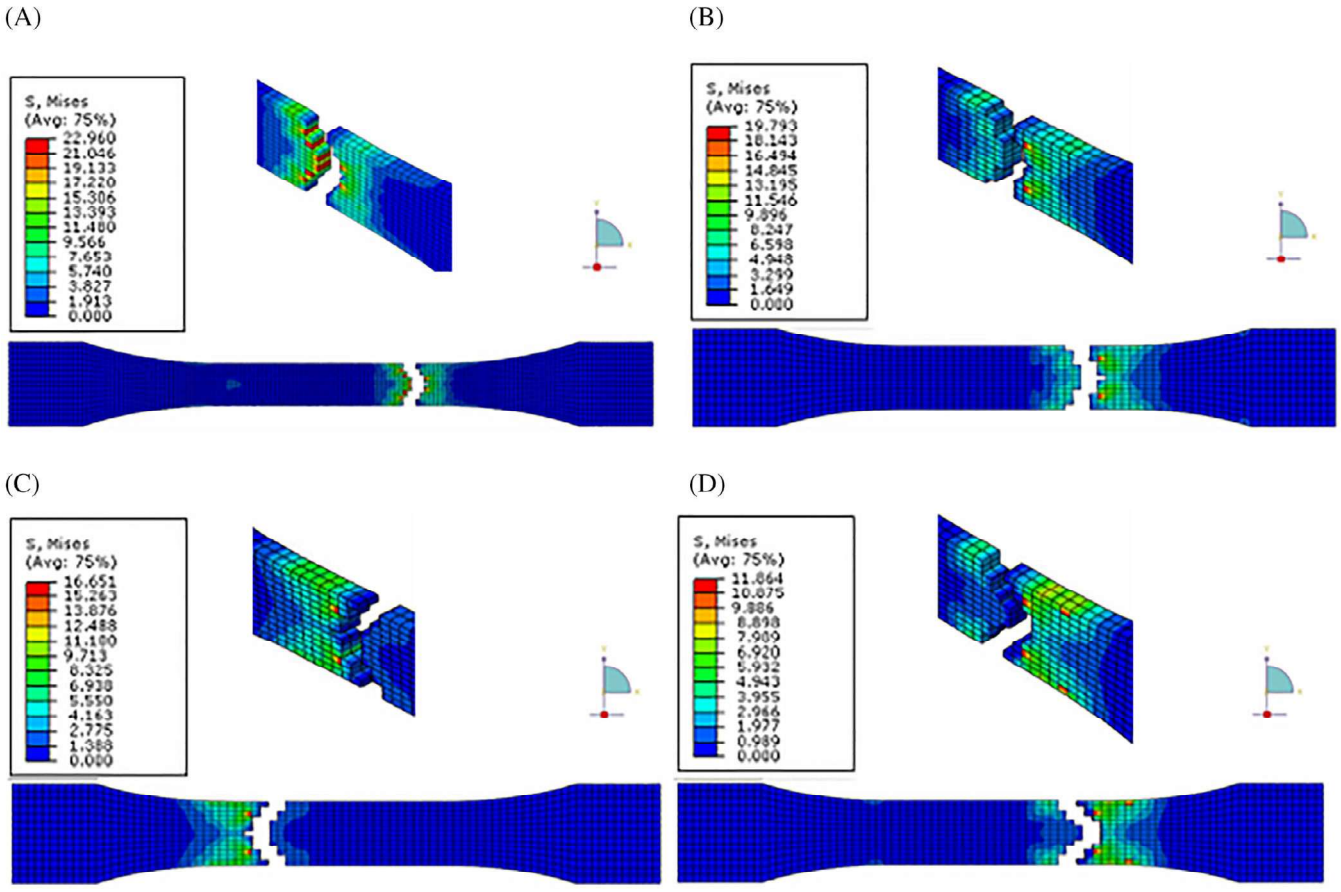


FIGURE 26 Numerical failure mode of PBT GF30 tensile specimens. (A) As received. (B) Treated at 225°C, (C) 237°C, and (D) 257°C

results from the numerical model are represented by the dashed lines and are compared with the experimental results (solid lines).

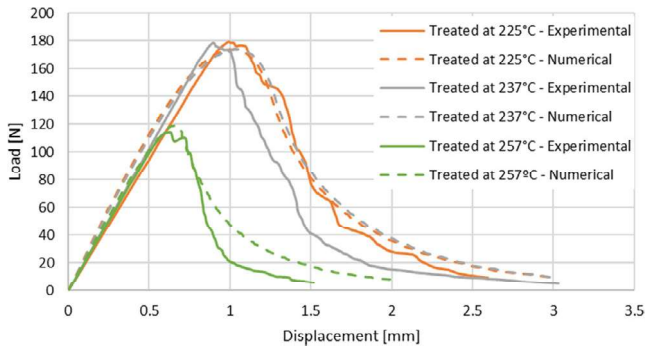


FIGURE 28 Comparison between experimental and numerical force-displacement curves of the compact test of PBT GF30 in the heat-treated states

TABLE 6 Error between experimental and numerical values of the stress intensity factor

	Error (%)
	Stress intensity factor
As received	10.02
Treated at 225°C	7.91
Treated at 237°C	7.51
Treated at 257°C	6.99

The errors between the numerical and experimentally determined stress intensity factor values, are shown in Table 6. Following ASTM D5045-14, the calculation of the stress intensity factor of the numerical curves was achieved by fitting them with a trendline, using a coefficient of determination R^2 of 0.999 for both conditions.

The error values are higher than those obtained for the tensile specimen model, mainly because the numerical curves do not have a clear linear phase, given the gradual degradation of the material property carried out in the numerical model. However, the values shown still indicate that there is good degree of convergence in these representative curves.

The good degree of convergence between the model and the experiment in the compact test is further supported by the crack propagation process. A comparison between the experimental and numerical crack propagation is shown in the representative CT specimens of PBT GF 30 treated at 237°C in Figure 29A,B, which evidence a very similar crack path and fracture process.

The numerical results generally confirm the experimental observations and data. Considering the variation property variations encountered for the tensile test and the fracture toughness test, is becomes evident that for an accurate simulation of the performance of a joint laser-welded PBT-GF30 joint it is indispensable to consider the application of a gradient of the properties along the weld region.

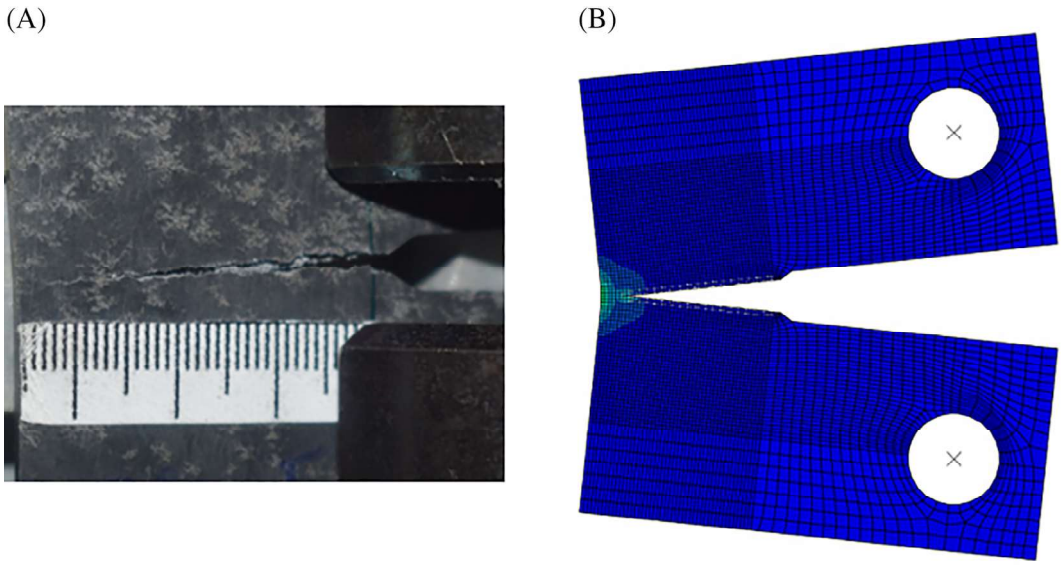


FIGURE 29 Crack propagation process in the compact test. (A) Experimental test. (B) Numerical simulation

5 | CONCLUSIONS

In this work, a detailed characterization of the thermal, optical, mechanical, and morphological characteristic of PBT-GF30 was carried out. The influence of thermal energy on the behavior of the material was also determined, allowing to characterize the response of the material to the thermal conditions encountered during laser welding operations.

The optical analysis of the PBT GF 30 material demonstrated that the application of this material in laser welding should follow an absorption-based approach, that is, weld will be formed at the surface of the contact interfaces.

With regards to the morphological study, it was observed that exposure to temperatures above the fusion temperature noticeably influences the quality of the surface. This is explained by the presence of voids emerging on an increasingly damaged surface. It was also found that when the material is heated at temperatures above or above the fusion temperature, there is a degree of segregation and exposure of the fibers, a process which has a deeply negative effect on the mechanical properties and with an evolution which is roughly proportional to the temperature.

The thermal and mechanical analysis carried out implies that even if the conductivity coefficient is low, the incident laser energy can still lead to a drop in the mechanical properties in the weld bead and its surroundings, which makes it absolutely crucial to study the properties of the thermally affected zone.

Finally, numerical models were created to assess the experimentally determined mechanical properties. A ductile damage behavior was found to be able to reproduce the tensile test, while the compact test employed Maxps implemented in XFEM.

DATA AVAILABILITY STATEMENT

The data that support the findings of this study are available from the corresponding author upon reasonable request.

ORCID

Luiz R. R. Silva https://orcid.org/0000-0002-1815-6842
Alireza Akhavan-Safar https://orcid.org/0000-0002-7168-7079

REFERENCES

[1] A.-D. Bendrea, L. Cianga, I. Cianga, *J. Biomater. Appl.* **2011**, *26*(1), 3.
[2] J. K. Fink, *High Performance Polymers*, William Andrew, Waltham, United State, **2014**.
[3] P. M. Hergenrother, *High Perform. Polym.* **2003**, *15*(1), 3.
[4] S. Clifton, B. H. S. Thimmappa, R. Selvam, B. Shivamurthy, *Compos. Commun.* **2020**, *17*, 72.
[5] K. Friedrich, A. A. Almajid, *Appl. Compos. Mater.* **2013**, *20*(2), 107.
[6] G. C. Jacob, J. F. Fellers, S. Simunovic, J. M. Starbuck, *J. Compos. Mater.* **2002**, *36*(7), 813.
[7] A. Supian, S. M. Sapuan, M. Y. M. Zuhri, E. S. Zainudin, H. H. Ya, *Defence Technol.* **2018**, *14*(4), 291.
[8] C. Unterweger, O. Brüggemann, C. Fürst, *Polym. Compos.* **2014**, *35*(2), 227.
[9] K. Wang, J. Wu, *Key Eng. Mater.* **2000**, *177-180*, 363.
[10] H. Wu, W. P. Fahy, S. Kim, H. Kim, N. Zhao, L. Pilato, A. Kafi, S. Bateman, J. H. Koo, *Prog. Mater. Sci.* **2020**, *111*, 100638.
[11] A. Schaaf, M. de Monte, E. Moosbrugger, M. Vormwald, M. Quaresimin, *Materialwiss. Werkstofftech.* **2015**, *46*(2), 214.
[12] T. Köppl, S. Brehme, F. Wolff-Fabris, V. Altstädt, B. Schartel, M. Döring, *J. Appl. Polym. Sci.* **2012**, *124*(1), 9.
[13] A. Kopczynska, G. W. Ehrenstein, *Adhäsion Kleben Dichten* **2004**, *48*(9), 37.
[14] N. Amanat, N. L. James, D. R. McKenzie, *Med. Eng. Phys.* **2010**, *32*(7), 690.
[15] S. K. Kugler, G. M. Lambert, C. Cruz, A. Kech, T. A. Osswald, D. G. Baird, *Polym. Compos.* **2020**, *41*(7), 2542.
[16] S. Diebels, S. Rjasanow, *Multi-scale Simulation of Composite Materials: Results from the Project MuSiKo*, Springer, Berlin, Germany, **2019**.
[17] K. Jansen, D. Van Dijk, M. Husselman, *Polym. Eng. Sci.* **1998**, *38*(5), 838.
[18] J. Vendramini, C. Bas, G. Merle, P. Boissonnat, N. D. Alberola, *Polym. Compos.* **2000**, *21*(5), 724.
[19] G. Ehrenstein, S. Amesöder, L. F. Díaz, H. Niemann, R. Deventer, *Werkstoff-und prozessoptimierte Herstellung flächiger Kunststoff-Kunststoff und Kunststoff-Metall-Verbundbauteile*, Tagungsband zum Berichts-und Industriekolloquium, Erlangen, Germany, **2003**.
[20] C.-P. Fung, J.-R. Hwang, C.-C. Hsu, *Polym.-Plast. Technol. Eng.* **2003**, *42*(1), 45.
[21] M. H. Ho, P. N. Wang, C. P. Fung, *Adv. Mater. Res.* **2011**, *284-286*, 550.
[22] T. Frick, A. Schkutow, *Proc. CIRP* **2018**, *74*, 538.
[23] S. Khosravi, *Laser transmission welding of polybutylene terephthalate and polyethylene terephthalate blends* **2010**.
[24] B. Y. Zhang, Q. J. Sun, Q. Y. Li, Y. Wang, *J. Appl. Polym. Sci.* **2006**, *102*(5), 4712.
[25] ASTM C, *ASTM Standards*, American Society for Testing Materials, Philadelphia, PA **1958**.
[26] ISO, B, *Plastics–determination of tensile properties* **1997**.
[27] ASTM C, *Standard test methods for plane-strain fracture toughness and strain energy release rate of plastic materials*. ASTM D5045-99 **2007**.
[28] N. Kuppusamy, R. A. Tomlinson, *Eng. Fract. Mech.* **2016**, *152*, 81.
[29] L. Silva, E. Marques, L. F. da Silva, *Weld. World* **2021**, *65*(10), 2023.
[30] D. Zhang, M. He, S. Qin, J. Yu, J. Guo, G. Xu, *Polym. Compos.* **2018**, *39*(1), 63.
[31] J. Vendramini, P. Mele, G. Merle, N. D. Alberola, *J. Appl. Polym. Sci.* **2000**, *77*(11), 2513.

[32] B. Klimkeit, S. Castagnet, Y. Nadot, A. E. Habib, G. Benoit, S. Bergamo, C. Dumas, S. Achard, *Mater. Sci. Eng., A* **2011**, *528*(3), 1577.
[33] C. Okeke, A. Thite, J. Durodola, M. Greenrod, *Proc. Struct. Integr.* **2017**, *5*, 600.
[34] L. Lal, S. Ramesh, S. Parasuraman, E. Natarajan, I. Elamvazuthi, *Materials* **2019**, *12*(19), 3057.
[35] P. J. L. Lazar, R. Sengottuvelu, E. Natarajan, *Materials* **2018**, *11*(11), 2186.
[36] E. de Avila, J. Eo, J. Kim, N.P. Kim, presented at MATEC Web of Conferences, EDP Sciences 2019, 264.
[37] K. Friedrich, *Application of Fracture Mechanics to Composite Materials*, Elsevier, North Holland, **2012**, pp. 231.
[38] M. Naebe, M. M. Abolhasani, H. Khayyam, A. Amini, B. Fox, *Polym. Rev.* **2016**, *56*(1), 31.
[39] M. Rakin, N. Gubeljak, M. Dobrojević, A. Sedmak, *Eng. Fract. Mech.* **2008**, *75*(11), 3499.
[40] S. Sugiman, H. Ahmad, *J. Adhes. Sci. Technol.* **2017**, *31*(5), 552.
[41] H. Huang, R. Talreja, *Compos. Sci. Technol.* **2006**, *66*(15), 2743.
[42] F. Feng, J. Li, P. Yuan, Q. Zhang, P. Huang, H. Su, R. Chen, *Metals* **2018**, *8*(10), 761.
[43] A. Sancho, M. J. Cox, T. Cartwright, G. D. Aldrich-Smith, P. A. Hooper, C. M. Davies, J. P. Dear, *Proc. Struct. Integr.* **2016**, *2*, 966.
[44] J. Ruzicka, M. Španiel, A. Prantl, J. Kuželka, M. Moravec, *Bull. Appl. Mech* **2012**, *8*, 89.
[45] P. J. Ruzicka, M. Spaniel, M. Moravec, *Identification of ductile damage parameters*, **2013**, 21.
[46] P. Charitidis, *Adv. Mater. Sci. Eng. Int. J* **2017**, *4*, 1.
[47] XPCI, *J. Appl. Mech.* **2017**, *6*(1), 1000251.

How to cite this article: L. R. R. Silva, E. A. S. Marques, R. J. C. Carbas, A. Akhavan-Safar, L. F. M. da Silva, *Polym. Compos.* **2022**, 1. https://doi.org/10.1002/pc.26677

View publication stats

Appendix C

Paper 3: Numerical study of double fillet lap joint by spot laser welding in overlap joint of PBT-GF30

Numerical study of double fillet lap joint by spot laser welding in overlap joint of PBT-GF30

L. R. R. Silva[1], E. A. S. Marques[1], R. J. C. Carbas[2], Lucas F. M. da Silva[1]

[1]Departamento de Engenharia Mecânica, Faculdade de Engenharia, Universidade do Porto, Rua Dr. Roberto Frias, 4200-465 Porto, Portugal

[2]Instituto de Ciência e Inovação em Engenharia Mecânica e Industrial (INEGI), Rua Dr. Roberto Frias, 4200-465 Porto, Portugal

Abstract

This study presents a numerical investigation of elastoplastic damage in laser-welded double fillet lap joints fabricated from PBT GF30. Experimental testing was conducted on joints with varying laser beam diameters and incidence positions to determine the optimal welding parameters. The results revealed that a 1.5 mm diameter beam incident on the upper surface (US) of the joint yielded the highest joint strength of 51.8 ± 1.6 N. To accurately simulate the mechanical behaviour of these joints, a numerical model incorporating elastoplastic and ductile damage models was developed. The model demonstrated good agreement with the experimental force-displacement curves, especially for the US position, where the error was just 1.08%. This level of precision highlights the model's ability to capture the complex deformation and failure mechanisms inherent to laser-welded joints. The successful validation of this numerical model provides a powerful tool for future design and optimization of laser-welded joints in PBT GF30. By accurately predicting joint strength and failure modes, engineers can tailor welding parameters to achieve desired mechanical performance and minimize the risk of premature failure.

Keywords

Joining, polymers, processing techniques, numerical model, adhesive bonding, welding, mechanical joining.

1. Introduction

It is widely known that multiple industries continuously invest in advanced joining equipment and processes, aiming to optimize production and increase efficiency in their industrial processes [1]. Among

these, the automotive and aeronautical industries stand out, using advanced joining methods to create high performance, highly optimized products, combining multiple materials for their mechanical, electronic, thermal and structural components. [2-5].

Silva (2021) [6] mentions that, among the countless joining processes, laser welding has gained importance in multiple uses, as it provides continuous and high performing joints in an efficient and clean manner, with less variation in properties. Done properly, it allows to reduce stress concentrators in the joints, doing so with a high productivity as well as a high-quality visual finish [7-9].

Currently, the laser welding process has been advanced to the point that it can be used to join a wide range of material pairs, whether similar or dissimilar in nature [10]. In electronic applications, this process has multiple uses. One of this is the joining of polymeric enclosures and panels, as they have the role of storing electronic boards and electrical circuits, which distribute the commands to the general equipment, an application which demands lightness [11], tightness, electrical insulation [12] and thermal transfer capabilities [13].

According to Starzhinsky (2020) [14], Irish (2020) [15] and Silva (2021), among the advanced engineering polymers, Polybutylene Terephthalate (PBT) appears to be the better suited for this application, especially when reinforced with glass fibres, increasing its strength and durability when compared to other polymers. Moreover, PBT is a thermoplastic, facilitating the manufacture of complex parts and enabling joining through fusion based processes, such as laser welding.

Furthermore, more detailed numerical study of joining processes has been progressing in parallel with the growth of experimental studies. For the laser welding case, the use of numerical modelling to achieve a detailed analysis of the variables of the experimental process is a key step to guide the manufacture of higher performing and more efficient joints, achieving this by improving the understanding of the process and also allowing to reduce the costs by eliminating repetitive tests and waste of raw material associated with exhaustive manufacturing and testing in laboratories [16] Silva (2021).

Thus, the current paper supports this development path by presenting a procedure adequate to optimize the joining process by laser welding in Polybutylene Terephthalate reinforced with 30% glass fiber (PBT GF30), while proposing to develop a model for double fillet welded joints applied in electrical circuit enclosure boxes. This work provides a novel numerical model for this type of joint application from representative parameters of the pulsed manual Nd:Yag 1064 nm laser.

2. Experimental details

The experimental component of this study involved the manufacture of laser spot welded double fillet welds, conducting strength tests on these joints, and performing micro and macrographic analyses to characterize the welded joint morphology. The characterization of the base material, PBT-GF30, necessary for subsequent modelling activities was based on the work of Silva (2021).

2.1. Laser welding procedure

The equipment used to create the welded joints in this work was a SISMA LM-D 180 (SISMA, Italy), using a Nd:YAG 1064 nm laser source, and with a maximum laser power of 80 W, as shown in Figure 1.



Figure 1 - Nd:YAG spot laser welding machine used in this work, SISMA LM-D 180

The parameters used for the laser welding were a lens-to-incidence-point distance of 70 mm, maintaining the microscope focus at this distance, a peak power of 36 W, a rectangular pulse time of 1.5 ms, with a low pulse frequency of 1 Hz, configuring the feed as manual spot laser welding, as shown in Figure 2. To achieve the laser incidence point, a visible target projected by the microscope lens of the laser was used. Knowing that the laser process can be conducted through conduction-limited welding or keyhole, a better visual analysis was sought to initiate the experimental study. The variable analyzed was the beam diameter, which took values of 0.5, 1.0, 1.5, and 2.0 mm, as measured using the machine's own microscope.

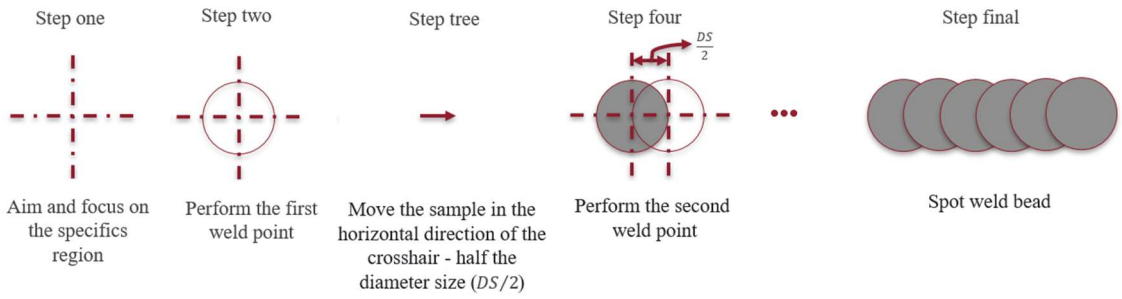


Figure 2 - Step-by-step procedures followed for manufacturing the spot weld bead.

2.2. **Geometry analysis of the welded double fillet lap joint**

The welded joint was created by joining two 10x40x1 mm (width x length x height) plates with an overlap zone (l_o) in the longitudinal region of 20 mm in length (Figure 3-a). The laser beam incidence configuration on the joint was conducted with an inclination (β) of 45°, as shown in Figure 3-b, based on the study of [17] which cites the efficiency of two different absorbent base materials. The laser incidence study was carried out in three positions: the first position was made at the upper edge of the overlapping plate (US), the second position was performed in the middle of the thickness of the upper plate (MS) and the third position was at the interface of the two plates (DS), with welding performed on both sides of the joint, without the introduction of additional material, as shown in Figure 3-c.

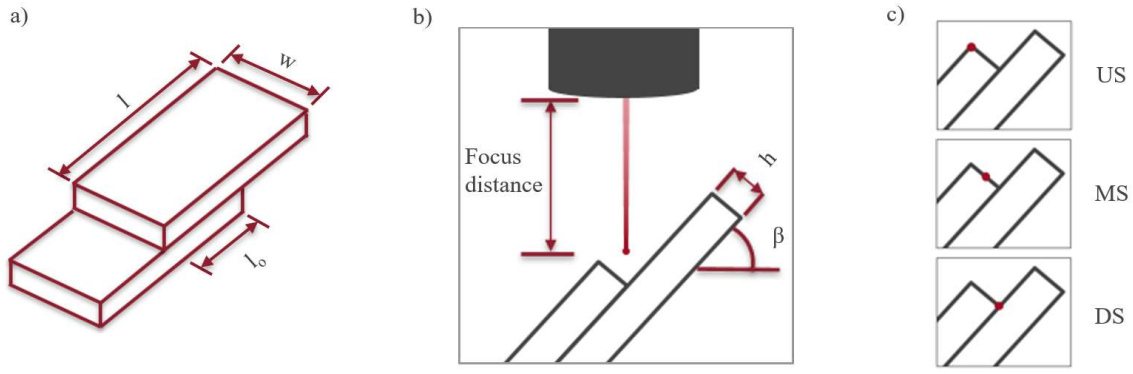


Figure 3 - Geometrical configuration of the joint. b) Inclination of the sample in relation to the laser beam and c) Positions of incidence of the laser on the samples.

2.3. **Macroscopic and microscopic analysis of the spot weld**

To perform the macroscopic analysis, a camera was fixed to the microscope integrated with the laser machine's sight, and photos of the laser welding points were taken individually, representing each incidence position of the laser (US, MS, and DS), for each defined beam diameter (0.5, 1.0, 1.5, and 2.0 mm).

For microscopic analysis, used to characterize the transverse zone of the welded region, aspects such as the dimension the weld depth, defects such as undercut, the geometric profile of the surface, and the actual spacing between the plates were analyzed. For this purpose, a set of welds was made on 10x15x2 mm rectangles of PBT-GF30 material. Since the welding profile is small and could easily fracture during the sanding and polishing process, a notch was made on the surface of each rectangle, where on one side of the notch the edge of the material would be welded according to the pre-established parameter and on the other side of the notch the plates were joined with adhesive, increasing the joint strength. This allowed for a more

solid joint, enabling sanding of the cross-section (Figure 4). Sanding was done with water and sandpaper with grain sizes of 220, 320, 800, 1200, and 4000 grit. This procedure was followed by air drying of the sample.

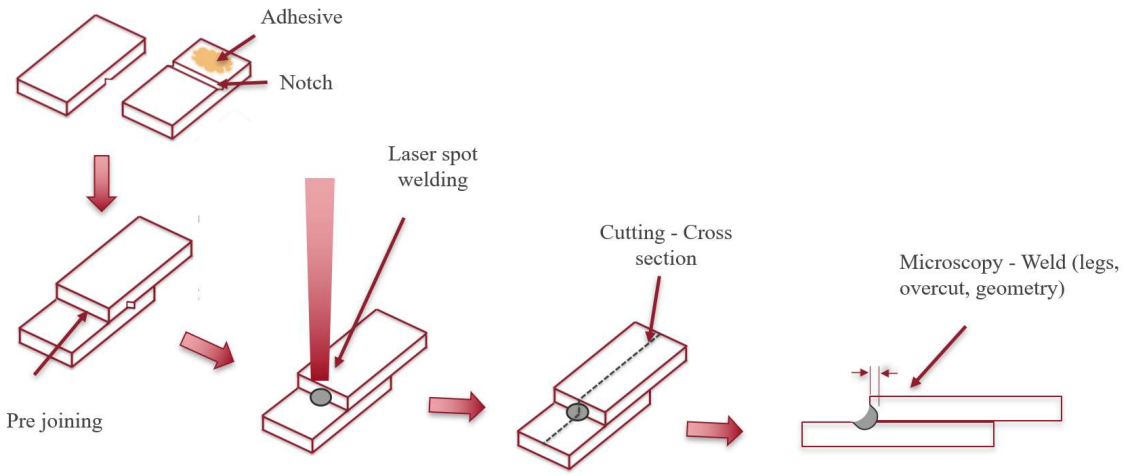


Figure 4 - Scheme of the procedures adopted to analyse the weld region on the optical microscopy.

2.4. **Double fillet lap joint test**

To ensure perfect load alignment during testing of double fillet lap joint test, rectangular PBT-GF30 plates, measuring 10 x 10 mm, were glued with cyanoacrylate to the ends of the joints, where the joint is clamped to the testing machine. For all tests, a universal testing machine, INSTRON® 3367, was used (Figure 5). This test entails a shear configuration, carried out according to the relevant standard [18]. The test was performed at a test speed of 1 mm/min, with three specimens for each condition.



Figure 5 - Universal test machine showing double fillet lap joint under test.

3. Experimental results

The experimental part of this work sought to determine the characteristics and behaviour of the joint to serve later as input data for the numerical simulation of double fillet lap joints, modelling their behaviour according to different laser incidence positions. These procedures include macroscopic analysis by verifying the external quality of the weld, determining the laser beam diameter that provides a consistent penetration and defect free joint. It also includes the results of the double fillet lap joint tests for each beam position and, finally, an analysis is provided of the configuration and characteristics of the weld's geometry section, aided by an optical microscopy analysis.

3.1. Macroscopic analysis of the spot laser weld

Considering that many of the laser beam parameters such as focal distance, pick power, and pulse time were already pre-established and with manually controlled transverse of the laser beam, a qualitative visual control of the weld was carried out first. Following the procedure illustrated in Figure 2, welding points were performed by varying the laser beam diameter and the incidence positions of the laser, forming a 3x4 combination matrix of data points. The images of the weld points captured were taken in the order of US, MS, and DS positions, respectively shown in Figure 6, Figure 7 and Figure 8, ordered by the decreasing size of beam diameter.

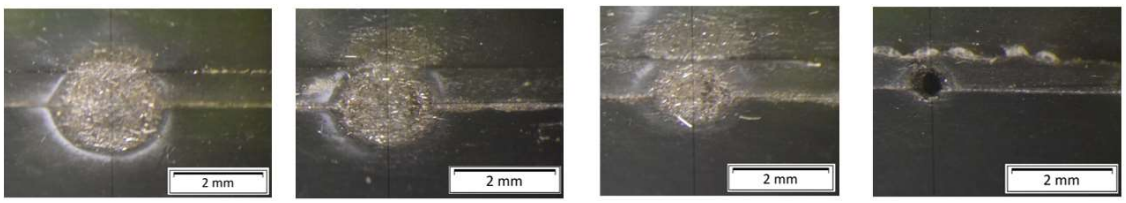


Figure 6 - Macrograph of the welding points for the US position, for beam diameters of 2.0, 1.5, 1.0 and 0.5 mm.

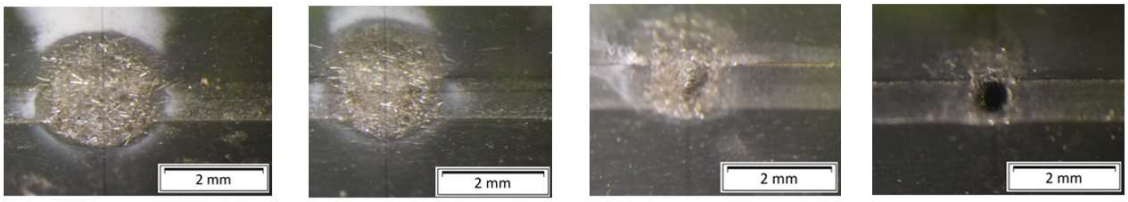


Figure 7 - Macrograph of the welding points for the MS position, for beam diameters of 2.0, 1.5, 1.0 and 0.5 mm.

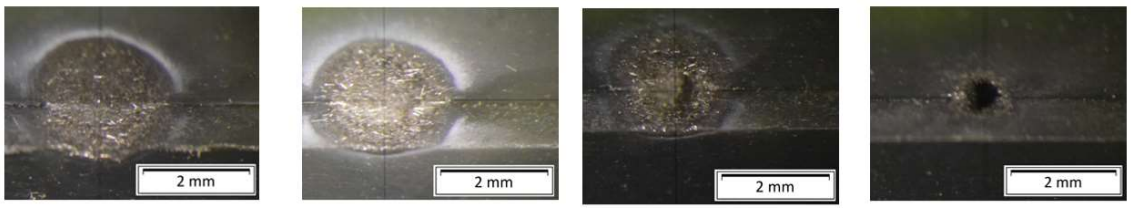


Figure 8 - Macrograph of the welding points for the DS position, for beam diameters of 2.0, 1.5, 1.0 and 0.5 mm.

Based on the data presented in these figures, it is evident that for smaller diameters of 1 and 0.5 mm, the high laser energy flux is observed in the laser incidence region, with material melting through the keyhole method, resulting in holes being formed in the plates. In contrast, the larger diameter of 2 mm exhibits insufficient energy for adequate penetration, with the melting occurring via the conduction-limited welding method. However, the 1.5 mm diameter consistently provides ideal weld quality and appearance, regardless of the beam's angle of incidence, and thus appears to be the best-performing condition.

3.2. **Microscopic analysis of the spot laser weld**

For the micrographic analysis of the cross section, a weld bead was produced by applying spot welds with diameters of 1.5 mm, aiming to analyze the geometrical parameters and characteristics of the weld bead. Figure 9-a, 10-a, and 11-a indicate the weld lengths in the direction parallel and adjacent to the plate interfaces. Figures 9-b, 10-b, and 11-b also illustrate the overcut dimensions in the lower plates and the geometrical characteristic of the surface which interfaced with the laser beam, shown for the US, MS, and DS positions, respectively.

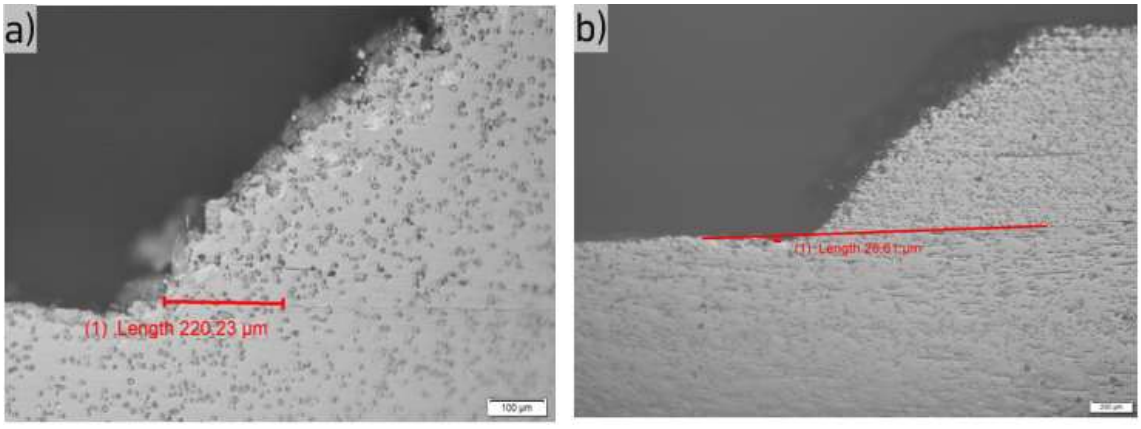


Figure 9 - Microscopic analysis of the sample in the US position. a) Representative measurement of the weld length of 220.23 µm at 50x magnification. b) Representation of the final shape of the weld, showing an overcut of 28.61 µm at 100x magnification.

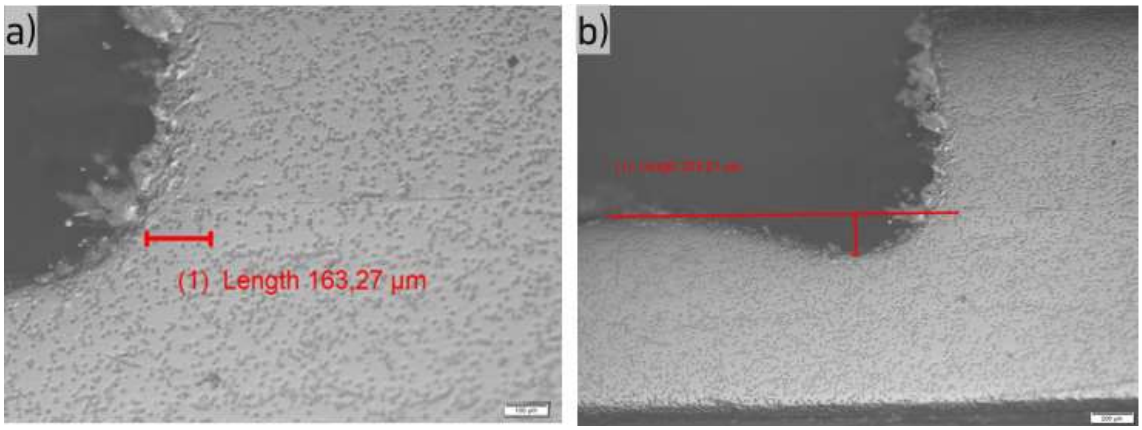


Figure 10 - Microscopic analysis of the sample in the MS position. a) Representative measurement of the weld length of 163.27 µm at 50x magnification. b) Representation of the final shape of the weld, showing an overcut of 203.21 µm at 100x magnification.

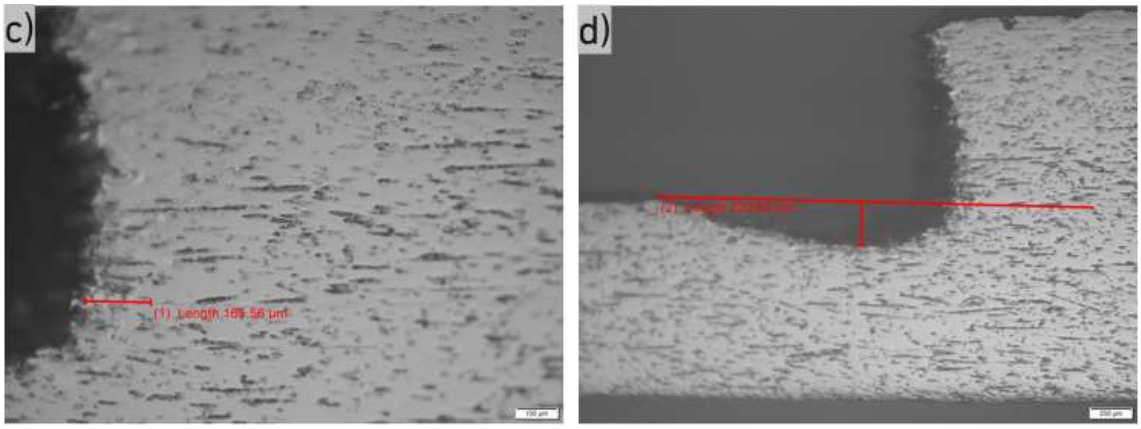


Figure 11 - Microscopic analysis of the sample in the DS position. a) Representative measurement of the weld length of 165.56 µm at 50x magnification. b) Representation of the final shape of the weld, showing overcut of 220.68 µm at 100x magnification.

When comparing Figure 9,Figure **10**Figure 11, it can be observed that the undercut length increases as the laser is directed closer to the interface of the plates. The curvature of the surface geometry is also more pronounced for the MS and DS positions. For the US surface, the weld length is greater, with a smaller surface curvature, since the melting process occurs more explicitly in the upper plate.

Looking at the plate spacing, *t*, is represented by a weld in the US position, as shown in Figure 12. This is representative for all cases under analysis, since the welding process was performed with the same procedure, maintaining the same level of contact between the plates and the same manual pressure applied by the same operator.

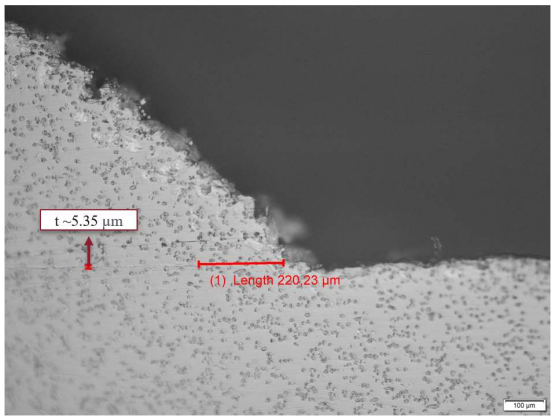


Figure 12 - Microscopic analysis, showing a measurement of plate spacing.

Figures 13-a and 13-b represent, respectively and in a quantitative manner, the weld lengths and undercut lengths for each welding position."

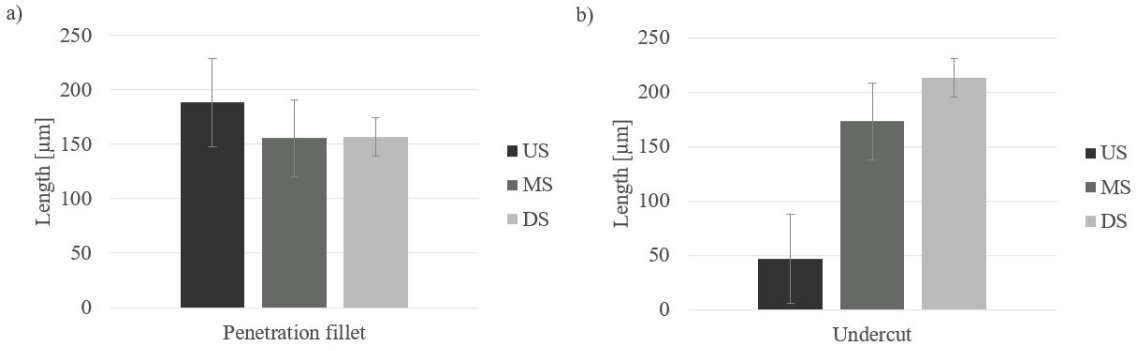


Figure 13 - a) Fillet penetration length and b) undercut length for the US, MS and DS positions.

Figure 12-a indicates a trend towards a greater weld penetration in the fillet for the US position. Looking at Figure 12-b, which represents the measurement of the undercut, for the US position the size of this parameter is smaller, when compared to the MS and DS positions. Figure 13 represents a schematic representation of the typical bead shapes of the welds for each welding position

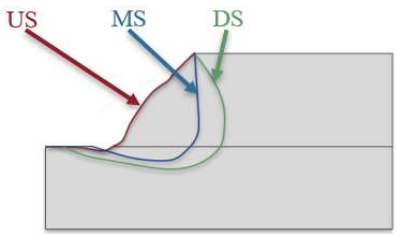


Figure 14 - Qualitative comparison of weld bead characteristics for the US, MS and DS positions.

Figure 14 demonstrates that, for the US, MS, and DS positions in the US, a decrease in the radius of curvature leads to a geometrically driven increase in the stress concentration factor. This observation aligns well with the findings of [19].

3.3. **Double fillet lap joint test**

Figure 15 provides a representative illustration of the typical load-displacement response of the weld for each analyzed configuration. It also provides a summary of the average failure loads obtained for each condition.

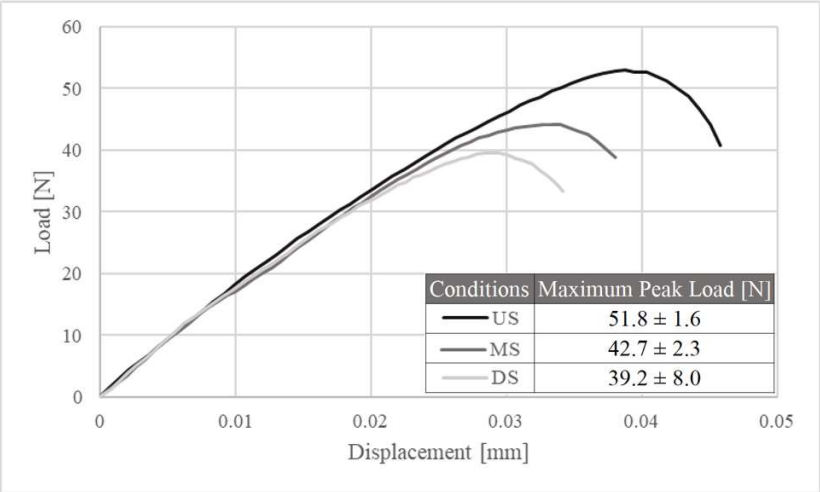


Figure 15 – Representative load-displacement curves for the different welding positions: US, DS and DS.

The results show that while all joints exhibit similar stiffness, the US position clearly corresponds to greater joint strength and displacement at failure. This can be attributed to the greater level of penetration achieved and, consequently, lower stress concentration achieved in this joint.

4. **Numerical details**

To analyse the performance of the different double fillet lap joints configurations, models were developed for each of the potential positions of the double fillet lap joint under analysis, including elastoplastic material behaviour and damage mechanics from the ductile damage model. Such models can account for the effects of different process parameters and variation of geometric parameters to increase the strength of the joints.

4.1. **Elastoplastic and ductile damage model**

Lemaitre and Bouktir et al. [20, 21] proposed an elastoplastic model with ductile damage, based on the concept of the continuous damage mechanism (CDM), accounting for the laws of plastic behaviour. Damage is introduced through isotropic scalar degradation of elastic properties. With this, the constitutive equation of the effective stress of the undamaged $\bar{\boldsymbol{\sigma}}$ derived from the Cauchy stress tensor, $\boldsymbol{\sigma}$, Equation 1, is thus formulated by:

$$\bar{\boldsymbol{\sigma}} = \frac{\boldsymbol{\sigma}}{1-d} \tag{1}$$

The scalar damage variable d, varying from 0 to 1 (with d = 0 for an undamaged material, and d = 1 for a fully damaged material), and is defined by the following relationship by Equation 2. The variable S_d is the surface of defects (cavities and cracks), S_{eff} denotes the effective surface (undamaged surface), and S is the total surface.

$$d = \frac{S_d}{S} = 1 - \frac{S_{eff}}{S} \tag{2}$$

As Pirondi (2003) [22] and also Sadhinoch (2017) [23]described the effect of damage on elastic deformation is characterized by addressing the fact that potential plastic deformation and damage can be separated. In this way, the set of constitutive equations for the damaged material can be written as shown in Equations 3, 4, 5, 6 and 7, which represent, respectively, the effective elastic deformation tensor ε_{ij}^{e},, the plastic deformation tensor ε_{ij}^{p} where F_p and the variables s_{ij} and X'_{ij} are deviatoric components of the stress and kinematic hardening tensor, $f\left(\frac{\sigma_m}{\sigma_{eq}}\right)$ is the triaxility stress formed by the hydrostatic stress σ_m and equivalent stress σ_{eq}, the accumulated strain rate $\dot{r}$, leading to R stress due to isotropic hardening and the plastic multiplier λ, finally the damage based on the displacement $\dot{u}^p$.

$$\varepsilon_{ij}^{e} = \frac{1+\nu}{E}\frac{\sigma_{ij}}{1-d} - \frac{\nu}{E}\frac{\sigma_{kk}}{1-d}\delta_{ij} \tag{3}$$

$$\varepsilon_{ij}^{p} = \dot{\lambda}\frac{\partial F_p}{\partial \sigma_{ij}} = \frac{3}{2}\dot{\lambda}\frac{(s_{ij} - X'_{ij})}{\sigma_{eq}} \tag{4}$$

$$f\left(\frac{\sigma_m}{\sigma_{eq}}\right) = \frac{2}{3}(1+\nu) + 3(1-2\nu)\left(\frac{\sigma_m}{\sigma_{eq}}\right)^2 \tag{5}$$

$$\dot{r} = -\dot{\lambda}\frac{\partial F_p}{\partial R} = \dot{\lambda} = p(1 \dot{-} d) \tag{6}$$

$$\dot{u}^p = L\dot{\varepsilon}_{ij}^p \tag{7}$$

4.2. **Double fillet lap joint test**

To validate the joint behaviour, a 2D model was created, using the Dynamics Explicit model, in an elastoplastic configuration with a ductile damage model. The step was configured with a time period of 0.2 seconds, allowing for geometric nonlinearity of the system. The integration was based on a time scale factor of 1 second, with a scale factor of 10000 and target time increment of 10^{-10} seconds.

4.2.1. Model geometry

The geometry was based on the measurements in Figure 3-a, with length, width and height of 40 mm, 10 mm and 1 mm respectively. The plates were overlapped by a length of 20 mm. The separation between the samples was 5.35 µm. A friction coefficient of 0.2 [24]was used to set the contact interaction between the plates. Figure 16 shows a macro representation of the configuration of the plates, illustrating the overlapping region in general and the boundary conditions. An encastre was applied on the left side of the joint and a displacement was imposed on the left side, of 0.2 mm in the x direction.

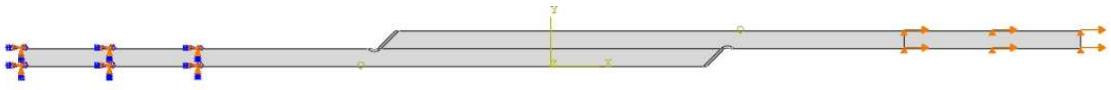


Figure 16 – Illustration of a joint model (US), used as a representative joint, showing the boundary conditions.

Figure 17-a, Figure 17-b and Figure 17-c illustrate the geometry of the fillet region (weld) and the base material for the US, MS and DS positions, respectively.

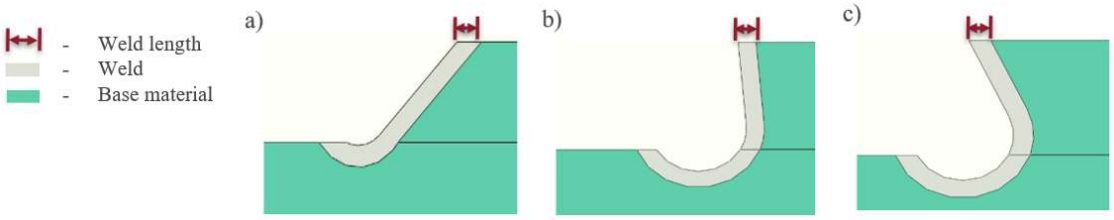


Figure 17 – Material partition, showing weld and base material in the a) US model, b) MS model and c) DS model.

The meshing process considers a 0.01 mm element size in the weld region and 0.1 mm in the base material. The model employed a plane stress condition, modelled using the CPS4R element.

4.2.2. Material properties

The physical and mechanical properties of the PBT GF30 material used in the simulation were based on the study carried out by Silva (2021). Table 1 shows the physical and mechanical properties of the material, such as densities, moduli of elasticity, Poisson's ratio and stress-strain plastic zone for the purely elastoplastic simulation. For the elastoplastic simulation together with the damage, Table 2 shows the failure deformations, triaxialities, deformation rates and displacements up to failure for the implementation of ductile damage. Finally, Figure 17 illustrates the stress and strain curves in the plastic regions of the materials, detailing the characteristics of PBT GF 30 in three different states: “As received”, “Treated at 225ºC”, “Treated at 237ºC” and “Treated at 257ºC”.

Table 1 - Physical and mechanical properties of PBT GF30

Material	Density [g/cm^3]	Young's Modulus [MPa]	Poisson Ratio
As received	1.31	8398	0.45
Treated at 225°C	1.31	5317	0.42
Treated at 237°C	1.31	5183	0.42
Treated at 257°C	1.31	4826	0.42

Table 2 - Properties of the PBT GF30 material for the implementation of ductile damage.

Material	Fracture Strain [mm/mm]	Stress Triaxiality	Strain rate [s^{-1}]	Displacemnt at Failure [mm]
As Received	0.011492123	-0.33	0	0.001
Treated at 225°C	0.006559261	-0.33	0	0.001
Treated at 237°C	0.003570756	-0.33	0	0.0007
Treated at 257°C	0.000821712	-0.33	0	0.0007

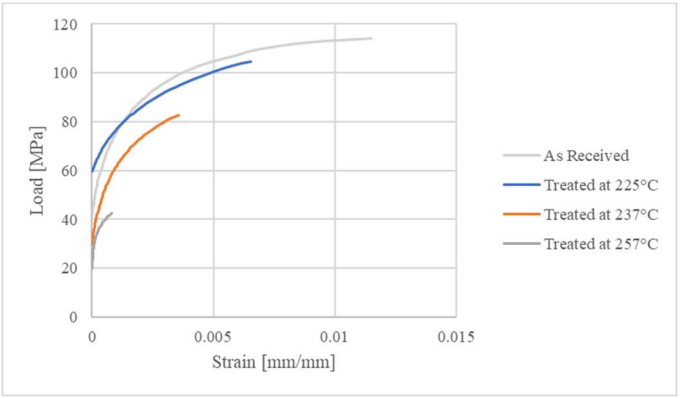


Figure 18 – Experimental curves representing the plastic region of PBT GF 30. Adapted from [].

5. Numerical results

For model validation, a simulation was conducted for three positions: US, MS, and DS. Initially, the numerical results for the double fillet lap joint model are treated in a purely elastoplastic manner, encompassing all combinations of base material and weld pairs. Finally, the model is followed by the implementation of ductile damage, represented by the scheme shown in Figure 19.

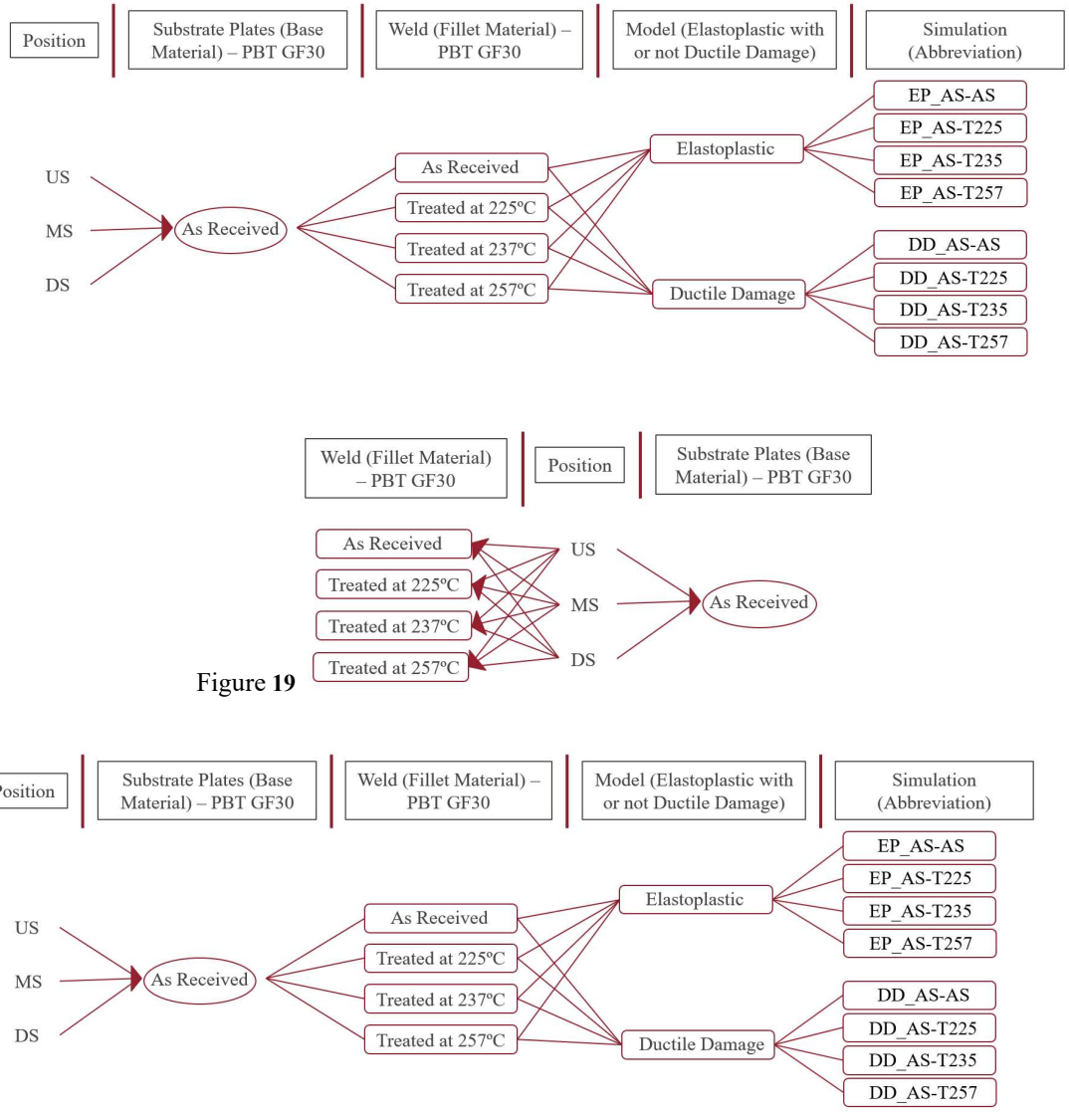


Figure **19**

Figure 19 – Diagram of the general matrix of simulations describing the position, base material, fillet weld, models and reference.

5.1. **Double fillet lap joint test – Elastoplastic model**

Figure 20 shows the load-displacement curves for the material pairs (base material-weld) in the purely elastoplastic model for the US position, comparing this data with experimental results.

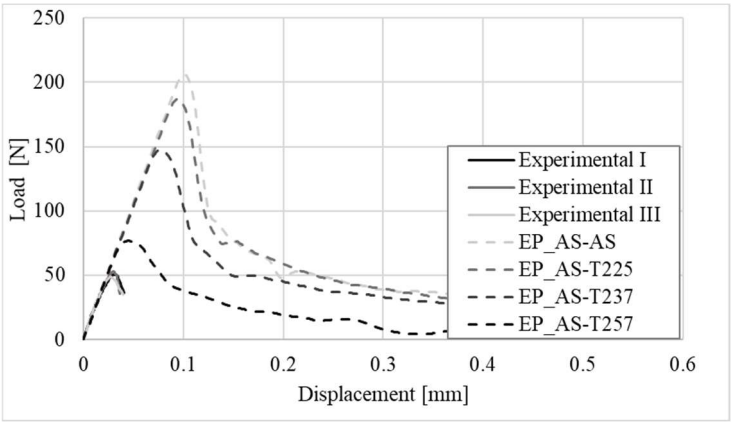


Figure 20 – Comparison of elastoplastic model results, for the US position, between different materials joints pairs and experimental results.

Figure 21 shows load-displacement curves for the material pairs (base material-weld) in the purely elastoplastic model for the MS position, again comparing it with the experimentally obtained curves.

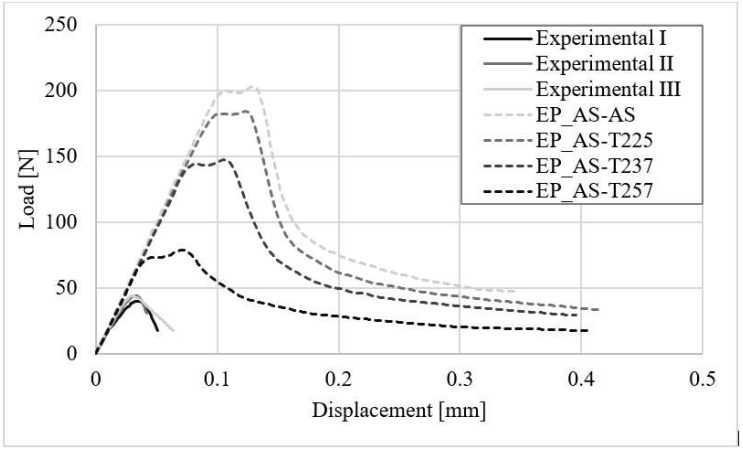


Figure 21 – Comparison of elastoplastic model results, for the MS position, between different materials joints pairs and experimental results.

Figure 22 shows the stress-strain curves for different combinations of base material and weld metal, assuming a perfectly elastoplastic material behaviour at the DS location

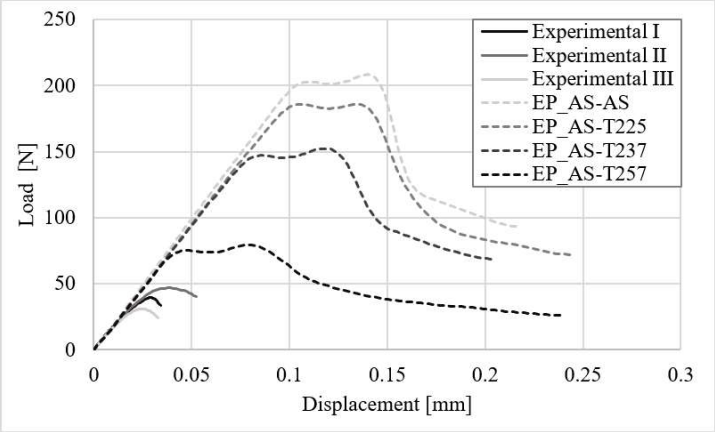


Figure 22 – Comparison of elastoplastic model results, to DS position, between different materials joints pairs and experimental results.

In Figure 20, Figure 21 and Figure 22, it is observed that for the elastoplastic model, for all pairs of base material and weld, the numerical strength is above the forces measured in the experiments, something which is also observed for all positions. However, the slope of the curves, in the initial regions, maintains convergence. In general, it is observed that the maximum force recorded in the simulation curves in the pair of materials (base material and weld) compared to the experimental curves is about four times greater.

It can also be analysed that in Figure 20 there is a small difference from the curves shown in Figure 21 and Figure 22, especially in the region where maximum load is attained. For Figure 20, there is a convergence of softening with the friction of the contact between the plates, characterizing a peak in the maximum force zone. However, for the curves of Figure 21 and Figure 22, there is a characteristic plateau accompanied by a peak located to the right of the plateau, corresponding maximum stress of the weld material, followed by softening of the same. This process also accounts for the contact between the plates, with a slight increase in force due to friction, followed with the decrease in force, due to the softening of the material.

For the comparison of the stress fields in the region adjacent to the weld in the base material and in the weld before softening, considering the maximum allowable stress, Figure 23-a, 23-b, and 23-c are presented for the positions US, MS, and DS respectively.

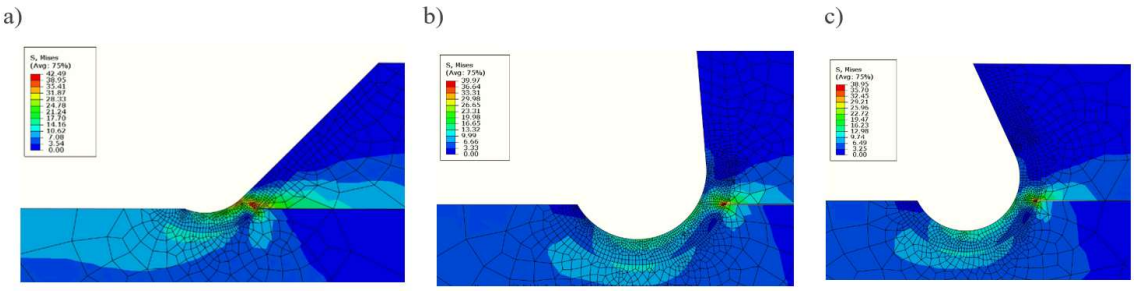


Figure 23 – Stress field of fillet weld joint in US, MS and DS models. a) Macro stress field – Von Misses US position. b) Macro stress field – Von Misses MS position. c) Macro stress field – Von Misses DS position.

As illustrated in Figure 23, it is evident that there is more extensive plastic development in the US model, reaching a maximum stress higher than the MS and DS positions. There is a higher stress concentration in the lower region of the weld for the MS and DS positions. To better characterize the weld stress concentration, Figure 24 details the Von Mises stress distribution curve in a horizontal path along the weld, adjacent to the plate surfaces.

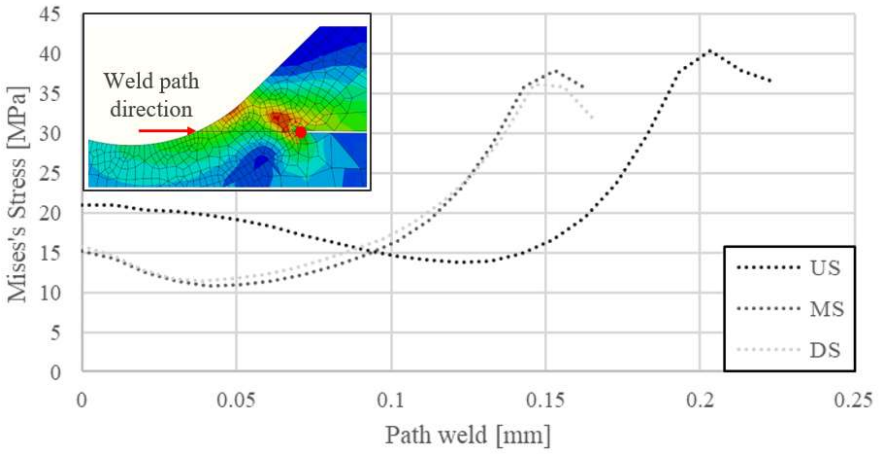


Figure 24 – Von Mises's stress distribution through weld fillet path.

The results show the contrast between the stress generated within the US model and the MS and DS models, illustrating a maximum stress before elastoplastic decay. The MS and DS models show similar characteristics, reaching a peak stress which is lower but more concentrated along the path.

5.2. **Double fillet lap joint test – ductile damage model**

Considering that for both pairs of materials, in each position US, MS, and DS, the curves of the elastoplastic models attained a higher strength than the forces of the experimental curves, the elastoplastic model is not

sufficient for validation. Therefore, ductile damage was added to the elastoplastic model, which was simulated only for the pair of base material as PBT-GF30 “As received” and the weld with PBT-GF30 “Treated at 257ºC”, using the parameters in Table 2.

To smooth the noise oscillation caused by the dynamic explicit model, as cited by [25], a Butterworth filter was used with a cutoff correction frequency of 40 Hz, with the same condition being used for all ductile damage simulations. The curves in Figure 25 below show the comparison of the numerical model with ductile damage and the experimental curves for the US position.

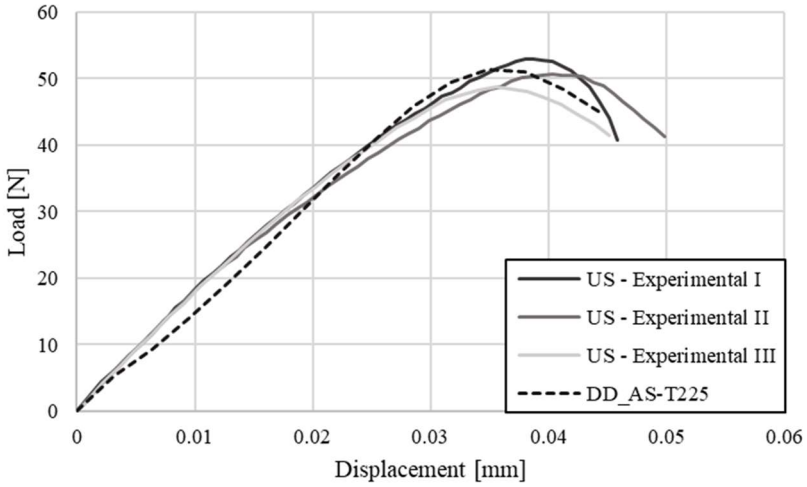


Figure 25 – Comparison of the performance of the elastoplastic model with ductile damage results for PBT-GF30 material treated at 257ºC, base material with PBT-GF30 against experimental results, for US position.

Even though a strain gauge wasn't used to verify displacement, the simulation curve in Figure 25 maintains a similar displacement. There's a slight variation in stiffness in the intermediate zone of the curve, slightly altered by the Butterworth filter. The average joint strength with the standard deviation of the experimental curves is 50.82 ± 2.07 N. The maximum force value from the simulation is 51.37 N, which falls within the standard deviation, providing just 1.08% of error above the average.

In line to what is shown in Figure 25, Figure 26 and Figure 27, respectively, show the comparison of the numerical model with ductile damage to the experimental curves for positions MS and DS.

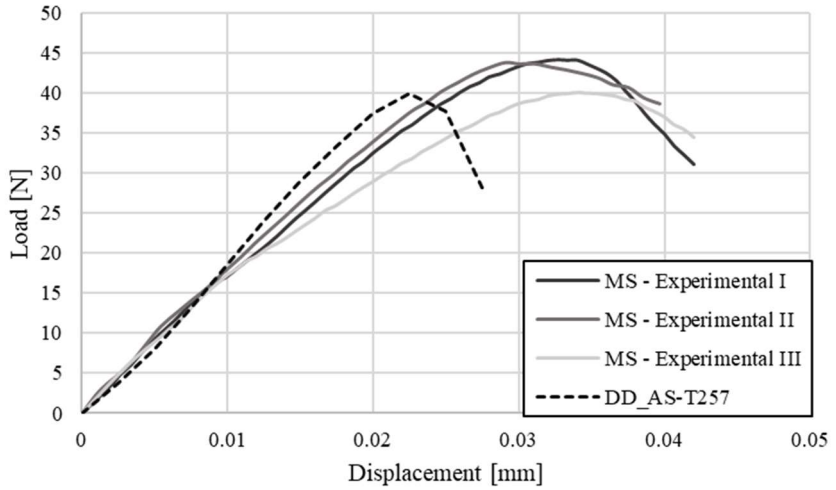


Figure 26 – Comparison of the performance of the elastoplastic model with ductile damage results for PBT-GF30 material treated at 257ºC, base material with PBT-GF30 against experimental results, for MS position.

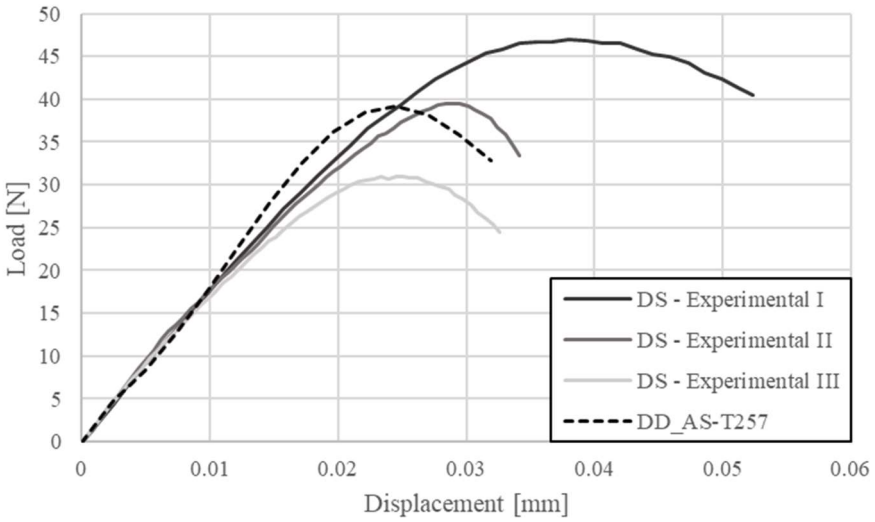


Figure 27 – Comparison of the performance of the elastoplastic model with ductile damage results for PBT-GF30 material treated at 257ºC, base material with PBT-GF30 against experimental results, for DS position.

For Figure 26, under identical simulation conditions as used for the US position, the simulated displacement representation deviates slightly from the US position's accuracy. Nonetheless, considering the mean and standard deviation of the experimental resistance forces (39.94 ± 2.30 N), the model error remains relatively low at approximately 6.43%. Figure 27 exhibits a similar convergence between the model curve and experimental results, especially at the DS position. Here, the numerical simulation resistance force aligns closely with the experimental value of 39.17 ± 7.99 N, resulting in a minimal error of 0.12%.

Overall, the numerical model's elastoplastic simulation with ductile damage validation corroborates the experimental procedure for all three welding positions.

6. Conclusions

This work provides a systematic analysis of the effect of different parameters in laser welded joints of PBT-GF30 material, supported by the development of damage models able to reproduce the failure processes. Within the analysed laser parameters, post-manual welding, laser diameter emerges as a critical factor. A small diameter can lead to material perforation, while a large diameter compromises bonding between plates due to reduced energy density. For fillet joints, the laser incidence point significantly impacts weld strength. The US position, targeting the upper plate's edge, offers multiple advantages. For example, by reducing the undercut on the fillet surface and stress concentration, this position promotes increased weld strength. The elastoplastic numerical model accurately simulates the elastic region. However, the maximum forces predicted for various material combinations (As received and treated at 257°C) exceed experimental averages. This discrepancy necessitated the incorporation of damage modelling to refine the simulation. The introduction of ductile damage significantly improved convergence for both analysed models. While both models converge, the US model exhibits superior convergence in terms of force prediction. Ultimately, to optimize welding parameters and further enhance simulation accuracy, future research is essential. A promising approach might involves incorporating a gradual variation of weld properties along the fillet length, more realistic reflecting the variation in material behaviour stemming from the interaction of the material with the laser light.

References

1. Chan, F., et al., *Investment appraisal techniques for advanced manufacturing technology (AMT): a literature review.* Integrated Manufacturing Systems, 2001.
2. Taub, A.I. and A.A. Luo, *Advanced lightweight materials and manufacturing processes for automotive applications.* Mrs Bulletin, 2015. **40**(12): p. 1045-1054.
3. Sivanur, K., K. Umananda, and D. Pai. *Advanced materials used in automotive industry-a review*. in *AIP Conference Proceedings*. 2021. AIP Publishing LLC.
4. Nirudhoddi, B.S., et al., *Journal of Advanced Joining Processes.*
5. Bahl, S., et al., *A systematic review on recent progress in advanced joining techniques of the lightweight materials.* AIMS Materials Science, 2021. **8**(1): p. 62-81.
6. Silva, L., E. Marques, and L.F. da Silva, *Polymer joining techniques state of the art review.* Welding in the World, 2021: p. 1-23.
7. Chowdhury, S., et al., *Identification of modes of welding using parametric studies during ytterbium fiber laser welding.* Journal of Manufacturing Processes, 2020. **57**: p. 748-761.
8. Acherjee, B., *Laser transmission welding of polymers–A review on process fundamentals, material attributes, weldability, and welding techniques.* Journal of Manufacturing Processes, 2020. **60**: p. 227-246.
9. Acherjee, B., *Laser transmission welding of polymers–A review on welding parameters, quality attributes, process monitoring, and applications.* Journal of Manufacturing Processes, 2021. **64**: p. 421-443.
10. Muhammad, N., et al. *Experimental study on laser welding dissimilar materials*. in *AIP Conference Proceedings*. 2021. AIP Publishing LLC.
11. Mallick, P., *Joining for lightweight vehicles*, in *Materials, design and manufacturing for lightweight vehicles*. 2021, Elsevier. p. 321-371.
12. Katayama, S., *Features of Laser Welding or Joining of Various Materials*, in *Fundamentals and Details of Laser Welding*. 2020, Springer. p. 145-165.
13. Rudrapati, R., *Parametric studies on transmission laser welding of acrylics*, in *Acrylate Polymers for Advanced Applications*. 2020, IntechOpen.
14. Starzhinsky, V., et al., *Plastic gears: State-of-the-art design and technology.* Machines. Technologies. Materials., 2020. **14**(3): p. 100-105.
15. Irish, J.R., *Polybutylene terephthalate*, in *Engineering Thermoplastics*. 2020, CRC Press. p. 19-27.
16. Wu, J., et al., *A review on laser transmission welding of thermoplastics.* The International Journal of Advanced Manufacturing Technology, 2021: p. 1-17.
17 Berger, S., F. Oefele, and M. Schmidt, *f.* Journal of Laser Applications, 2015. **27**(S2): p. S29009.
18. ASTM. *Standard test method for determining strength of adhesively bonded rigid plastic lap-shear joints in shear by tension loading*. 2014. ASTM West Conshohocken, PA.
19. Cerit, M., O. Kokumer, and K. Genel, *Stress concentration effects of undercut defect and reinforcement metal in butt welded joint.* Engineering Failure Analysis, 2010. **17**(2): p. 571-578.
20. Lemaitre, J., *A course on damage mechanics*. 2012: Springer Science & Business Media.
21. Bouktir, Y., H. Chalal, and F. Abed-Meraim, *Prediction of necking in thin sheet metals using an elastic–plastic model coupled with ductile damage and bifurcation criteria.* International Journal of Damage Mechanics, 2018. **27**(6): p. 801-839.
22. Pirondi, A. and N. Bonora, *Modeling ductile damage under fully reversed cycling.* Computational Materials Science, 2003. **26**: p. 129-141.
23. Sadhinoch, M., et al. *Numerical and experimental validation of a new damage initiation criterion*. in *Journal of physics: Conference series*. 2017. IOP Publishing.
24. Chaudri, A.M., M. Suvanto, and T.T. Pakkanen, *Non-lubricated friction of polybutylene terephthalate (PBT) sliding against polyoxymethylene (POM).* Wear, 2015. **342**: p. 189-197.
25. Dantas, M., et al., *Numerical study of flexible tubular metal-polymer adhesive joints.* The Journal of Adhesion, 2020: p. 1-23.

Appendix D

Paper 4: Experimental and numerical study for the optimization of process parameters in laser welded and adhesively bonded PBT GF30 fillet joints

Experimental and numerical study for the optimization of process parameters in laser welded and adhesively bonded PBT GF30 fillet joints

Luiz RR Silva, Eduardo AS Marques, Ricardo JC Carbas, Lucas FM da Silva

ABSTRACT With the advancement of technological processes and the application of fibre-reinforced polymer matrices in elements of vehicles, there has been a demand for the optimization of productivity, enhancing automation, reduction in process time and increasing the quality of part joining, allowing to manufacture high performance protective enclosures for electrical circuits. In this context, the laser welding process has gained importance especially when the polymer matrix is thermoplastic. On the other hand, adhesive bonding also has a wide application in this market, although it often harder to automate and requires a longer time for the curing of the process, which can reduce productivity. This work aims to study and optimize the laser welding parameters in overlapped joints of PBT GF30, joined by fillets at the ends performed through manual laser spot welding, to experimentally compare with joints with similar geometries joined by adhesive joints, validated by numerical models for the experimental conditions. The model identified the most effective parameters and was found to replicate the experimental results with a high degree of accuracy.

Keywords thermoplastic composites · laser welding· adhesive bonding · joint characterization · hyperelastic modelling

Eduardo AS Marques (✉)
Institute of Science and Innovation in Mechanical and Industrial Engineering (INEGI), Rua Dr. Roberto Frias, 4200-465 Porto, Portugal
e-mail: emarques@fe.up.pt

Luiz RR Silva
Fatigue and Fracture Research Laboratory, Center of Excellence in Experimental Solid Mechanics and Dynamics, School of Mechanical Engineering, Iran University of Science and Technology, Narmak, 16846 Tehran, Iran
e-mail: luiz.silva@ifes.edu.br

Ricardo JC Carbas (✉)
Institute of Science and Innovation in Mechanical and Industrial Engineering (INEGI), Rua Dr. Roberto Frias, 4200-465 Porto, Portugal
e-mail: rcarbas@fe.up.pt

Lucas F. M. da Silva
Department of Mechanical Engineering, Faculty of Engineering, University of Porto, Portugal
e-mail: Lucas@fe.up.pt

1 Introduction

For decades, the automotive industry has been updating its components and designs, selecting materials with high rigidity and weight reduction, while exploring new manufacturing processes, aimed at increased productivity. [1-3]. This process goes hand in hand with advances in new materials, especially when it comes to thermoplastic polymeric matrices, which are often reinforced with fibres. In the automotive industry, these are often applied to headlights, panels, protective casings for electronic peripherals, coatings, etc. [4, 5]. There are multiple manufacturing processes available for joining these types of components, which can be used by themselves, or in conjunction with others, then characterised as hybrids [6]. However, most research shows that, accounting for the automation of processes, the homogeneity of properties in the joint without the need for extra elements and the speed with which the process is carried out, laser welding is a great option. [7-11]. As it is still a recent manufacturing process compared to other processes, it is often costly. However, because it is also being used in applications other than manufacturing, this limitation has been reduced in recent years[11], and laser welding is found mainly in applications in the automotive and aeronautics industries, as well as in the biomedical and electronics fields. [7, 12]. When it comes to applying the laser welding process to polymeric materials, its application is more restricted to thermoplastic matrices, often with the addition of reinforcing fibres [13]. For materials with high absorption of light, joints are restricted to the surface of laser incidence, while for transmissive materials, since there is the possibility of applying an absorption film at the interface of the materials, the range of joints is extended. [14]. Amanat et al (2010) [15] studied the optimisation of laser welding parameters on PEEK, pointing out that at lower speeds, i.e. between 4 and 8 mm/s, the joint strength is more effective. Jones (2002) [14]. cites that for polyethylene, in a study on thin plates of 0.1 mm, a high speed of around 100 m/min is required. However, this parameter depends on the polymer and the thickness to be welded. Kim et al (2009) [16], Volpe et al (2015) [17] and Klotzbuecher et al (2006) [18] studied the analysis of the parameters in the joint welding of a PMMA pair, optimising the parameters, making the union between pure materials effective. Kim et al. (2013) [19] also demonstrated the possibility of welding different polymers together, as in the case of joining polypropylene and polycarbonate. Visco et al (2018) [20] and Galtieri et al (2016) [21] also demonstrated the optimisation of polyethylene with the addition of carbon particles, increasing weldability, raising resistance to a weight of up to 1% of particles. PBT is seen as a high-strength polymer with a low relative cost, as well as thermal and optical properties with great performance, according to Antic et al. (2011). [22], mainly with the addition of fibre reinforcement, its application has been extensive in the automotive sector [23-27]. Generally speaking, Klein (2012) [28] reported on the compatibility of PBT in the laser welding process with other thermoplastics. Furthermore, Okuizumi et al. (2011) [29] proved that the weldability of PBT joints applied to electrical housings is efficient. For this application, a PBT with high transmissivity and a PBT with high absorption are used in which the joint is made at the contact interface. Wang et al. (2016) [30] carried out a study on dissimilar PBT joints with PMMA, in which even though small bubbles appeared, the weld was effective. They point out that the study of clamping pressure is very important. Laser welding can also be carried out on fibre-reinforced polymers, but due to the high absorption of energy, the practical geometry is restricted to a framework of specific joints, where the joining takes place on the surface where the laser hits. Berger et al. [31] has shown this effect for the 35% glass fibre-reinforced PA6.6 used in

solenoid valve housings. When it comes to adhesive bonding, its application has been widespread in all industrial sectors. However, the automation of this process is complex, since each adhesive has its own specific characteristics for use, be it curing time, the temperature of the application medium, or the influence of contact pressure. [32]. However, it still has features advantages over the laser welding process due to its low cost, low stress concentration and high fatigue life [6, 33]. Its characteristics have been studied extensively, using multiple numerical modelling approaches, allowing joint performance to be reproduced and costs reduced once it has been validated before it makes its way to real joints. [34, 35]. As a result, there has been an increase in the analysis of more complex shapes, even studying the implementation of adhesives and their characteristics. The aim of the current work, based on an industrial demand, is to experimentally study the application of laser welding to joints made of Polybutylene Terephthalate reinforced with 30% glass fibre by weight (PBT GF30), overlapped and joined at the ends by fillet, with a view to optimising the static parameters and comparing the process with adhesive joints in similar joints, both numerically and experimentally. This work provides a methodology to optimize and fine tune the process parameters of complex bonded-welded joints, for thermoplastic composite components.

2 Experimental procedure

2.1 Laser welding

In order to study the process variables and optimise its parameters, analyses were started based on two main conditions. The first condition was the angle of inclination of the laser in question on the joint, which was taken from the study by Berguer et al. (2015) [36] which states that for a fillet joint the optimum angle is 45º. The second condition was used to define the location of the laser incidence on the joint, because as studied by the authors, the best position is when the laser is incident on the upper edge of the welded joint, as shown in Figure 1.

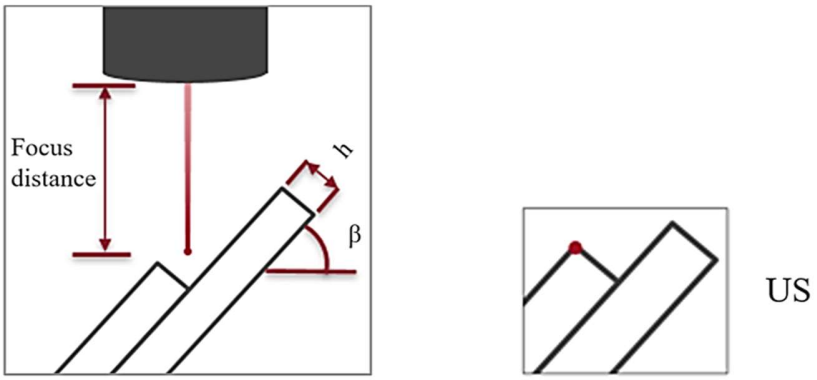


Fig. 1 - Scheme of sample inclination angle, showing the laser beam and the laser incidence positions on the samples.

The machine used in the process to make the welded joint was a SISMA LM-D 180, with a Nd:Yag 1064 nm laser, and an average laser power of 80 W, shown in **Erro! A origem da referência não foi encontrada.Erro! A origem da referência não foi encontrada.**.



Fig. 2 - Spot laser welding machine.

In accordance with the recommendations of the laser welding equipment manufacturer, the baseline configuration for laser welding was a focal length of the lens to the incidence point of 70 mm, and a power level in the range of 24 W to 80 W. A rectangular pulse was used, with the time interval between 0.5 and 3.5 ms with a laser beam diameter between 1.3 and 1.9 mm, with a base frequency of 1 Hz. To generalise the study, tests were carried out at three different inclinations (β), 30º, 45º and 60º. This was implemented as a manual spot laser welding procedure, as shown in Figure 3.

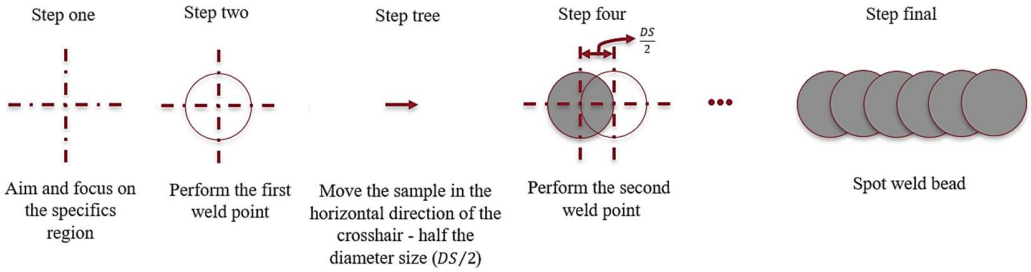


Fig. 3 - Step-by-step procedures used for the determining the advance on the spot weld bead.

2.1.1 Joint configuration and testing procedures

A microscopic analysis was carried out to characterize a transverse section of the welded region, allowing to determine the penetration of the weld, the geometric profile of the surface and the actual spacing between the plates. For this analysis, laser welding was performed experimentally on 10x15x2 mm samples of PBT-GF30 material. Since the welding profile is small and may fracture with the large loads encountered during the grinding and polishing process, a notch was made in the surface of each rectangle, where on one side of the notch the material would be welded according to the pre-established parameters and on the other side of the notch the plates were joined with a supporting adhesive, increasing the resistance of the joint and allowing for easier sanding of the cross section, as shown in Fig. **4** - - Scheme of the procedures used for the analysis of the welded region with optical microscopy.

. The sanding process was carried out was done with emery paper of 220, 320, 800, 1200 and 4000 grain sizes and in water. After the grinding process was complete, the specimens were dried and analysed with an optical microscope (Carl Zeiss El-Einsatz HAL 100).

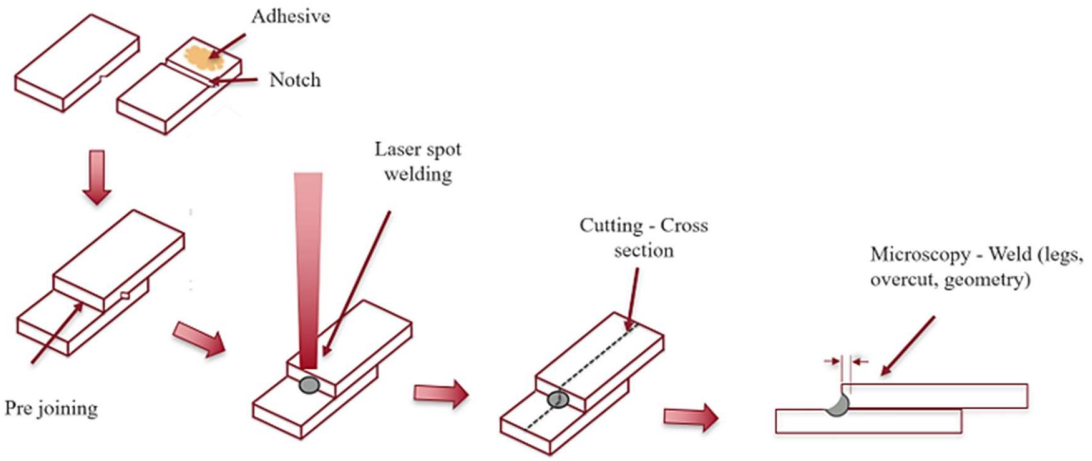


Fig. 4 - - Scheme of the procedures used for the analysis of the welded region with optical microscopy.

The PBT GF 30 thermoplastic used in this work is a commercial product. The specimens were made from square plates measuring 80 x 80 x 1 mm, both produced by injection moulding using PBT pellets with undirected glass fibres as the raw material, forming a matrix of PBT and reinforced with 30% of glass fibres in weight with homogeneous characteristic properties, regardless of direction, supplied by BASF (Ludwigshafen, Germany). Its Poisson coefficient is 0.45 [37]. Based on the format supplied by the company, sections were made in the boards to make the rectangular samples for the formation of the 60 x 10 mm long and wide joints, which were positioned along their length with a 20 mm overlap, welding only at the ends of the joint, of the fillet type as shown in Figure 5.

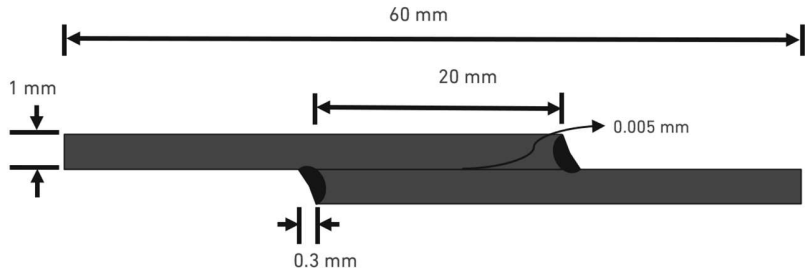


Fig. 5 - - Scheme of double single lap joint configuration, joined by laser welding.

Testing of the welded joints was carried out in an INSTRON® (Norwood, Massachusetts, USA) 3367 universal testing machine, as shown in Figure 6. In order to linearise the force in the shear zone in the double fillet lap joint test, rectangular PBT-GF30 plates measuring 10 x 10 mm were glued to the ends of the joints, in the area where the test machine's clamp is attached. The test was based on the shear standard [38], using a speed of 1 mm/min, carrying out three tests in each pre-set condition.



Fig. 6 - - Universal machine test showing the double fillet lap joint in test.

2.2 Adhesive bonding

2.2.1 Characterization of adhesive properties

A one component silicone adhesive was used in this work. For the mechanical characterisation of this silicone, two main tests were carried out, one for the characterisation of the ultimate normal stress based on ISO BS 2782 [39] and another for the ultimate shear stress based on ISO 11003-2:1993 [40], both properties being necessary for the application of the numerical simulation approach, presented later in this document.

2.2.2 Single lap joint configurations and manufacturing procedures

In order to allow for a comparison between the two different joining processes, two configurations of adhesive joints were designed this purpose. The first configuration, as shown in Fig. **7** - Adhesive joint geometry with low thickness (0.05 mm). b) Adhesive joint geometry with reference thickness (1 mm).

-a, includes a free space between the plates of the substrate and has an adhesive layer thickness of 0.05 mm, a value which is consistent with the minimal gap introduced during compared with the thickness used in the laser welding. The second configuration, shown in Fig. **7** - Adhesive joint geometry with low thickness (0.05 mm). b) Adhesive joint geometry with reference thickness (1 mm).

-b, used a thickness of 1 mm, which is often reported to be the optimal thickness for obtaining maximum performance with a silicone adhesive [41]. For both configurations, the overlap length can be adjusted to ensure mechanical performance which is consistent with that of the laser welded joint.

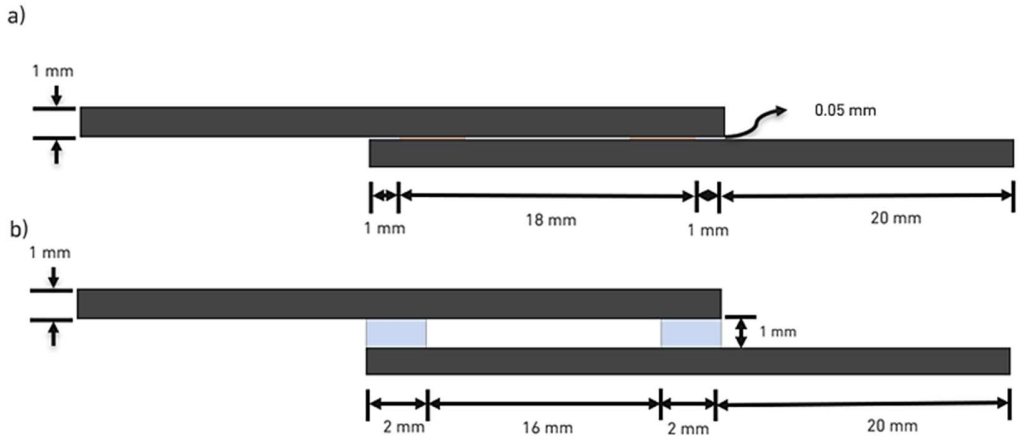


Fig. 7 - Adhesive joint geometry with low thickness (0.05 mm). b) Adhesive joint geometry with reference thickness (1 mm).

The adhesive joints were manufactured with the assistance of rubber frames which included rectangular notches of 10 x 60 mm that allowed to manufacture three joints in each desired condition, as shown in Fig. **8** - a) Rubber frame configuration. b) Adhesive joint configuration with low thickness. c) Adhesive joint configuration with reference thickness.

-a. To maintain parallelism, the rubber frames were assembled between thick aluminium plates. The curing process was assisted by a hot plate press, set to a pressure of 300 bar and a temperature of 120ºC for 25 minutes. After the curing process was completed, the specimens were allowed to cool down naturally until room temperature was reached. To control the spacing between the plates, a 0.05 mm Kapton tape was used for the first configuration (Fig. 8 - a) Rubber frame configuration. b) Adhesive joint configuration with low thickness. c) Adhesive joint configuration with reference thickness.

-b), whereas a 1 mm thick rubber tape was used (Fig. 8 - a) Rubber frame configuration. b) Adhesive joint configuration with low thickness. c) Adhesive joint configuration with reference thickness.

-c) for the thicker joints. For both configurations, 1 mm stainless steel tapes were used as spacers to compensate for joint thickness.

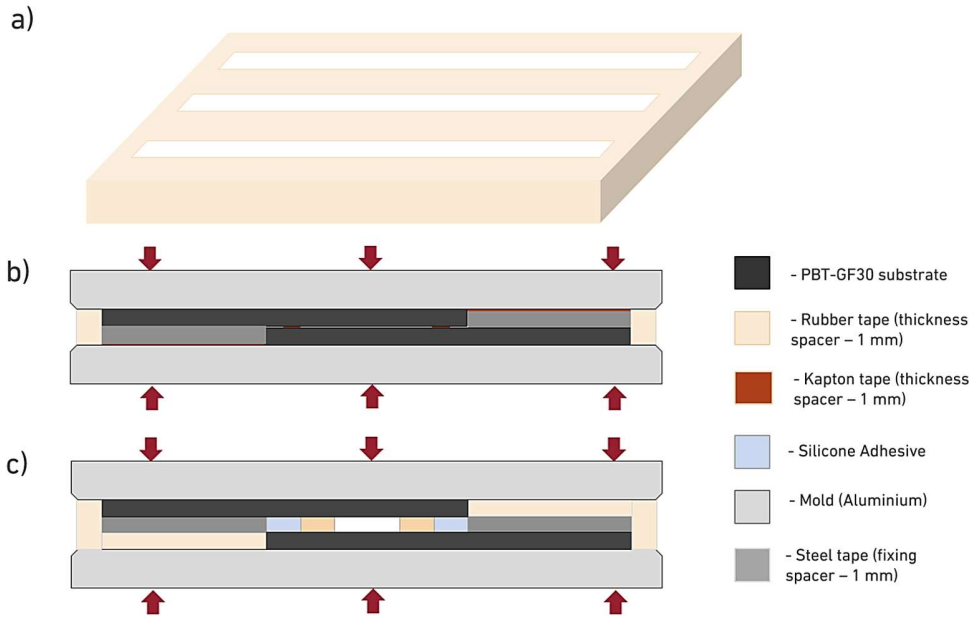


Fig. 8 - a) Rubber frame configuration. b) Adhesive joint configuration with low thickness. c) Adhesive joint configuration with reference thickness.

All bonded joints were tested using the same procedures as described for the welded joints.

3 Experimental results

3.1 Laser welding bonding

Once a baseline analysis was completed, it was possible to expand the range of parameters under analysis beyond the laser incidence point and the beam diameter. The initial parameters for testing consisted in a pulse time of 1.5 ms, laser beam diameter of 1.5 mm and manually controlled pulse frequency. **Erro! A origem da referência não foi encontrada.** demonstrates that peak strength is achieved for a 45° inclination, being proportional to the average power.

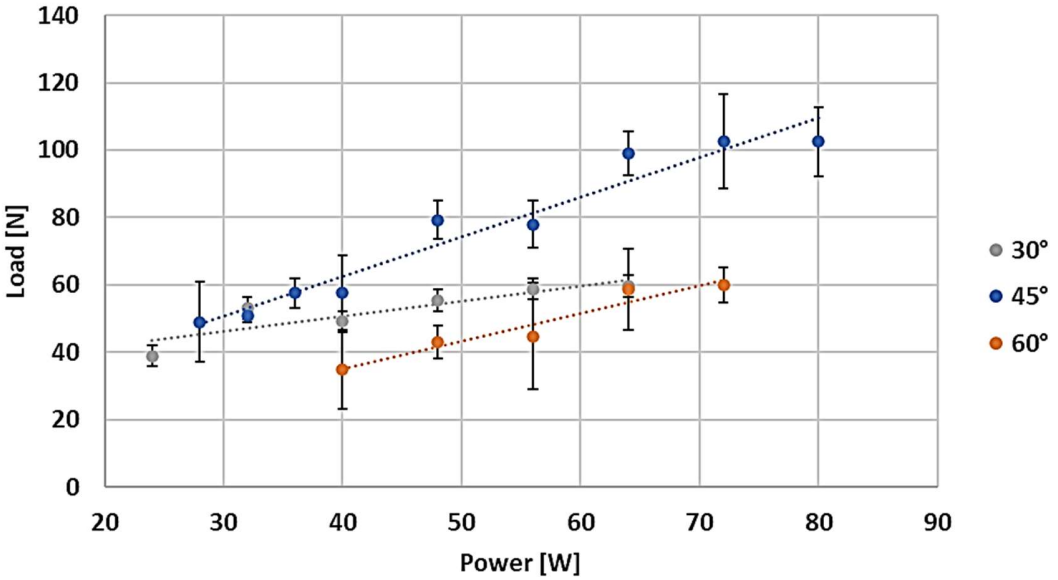


Fig. 9 - Results of the failure load in relation to the angle of incidence and average power.

These results are consistent with those obtained by Berger (2015) [187], which state that for a fillet type of joint the 45º angle leads to a higher joint strength. Comparing angles of incidence between 30º and 60º, one can see that low power levels appear to favour the 30º angle while higher power levels work better with 60º angles. Overall, these results suggest that the higher the beam power, the stronger is the resultant joint, considering a configuration where the laser beam diameter and the pulse duration are fixed at 1.5 mm and 1.5 ms. It was then possible to return to a study of the laser beam diameter, fixing the incidence position and the incidence angle (at 45º) but varying the power level. The resulting specimens were tensile tested, and the results are shown in Fig. **10** - Failure load study for 45º angles, with pulse time fixed in 1.5 ms varying the average power and the laser beam diameter.

.

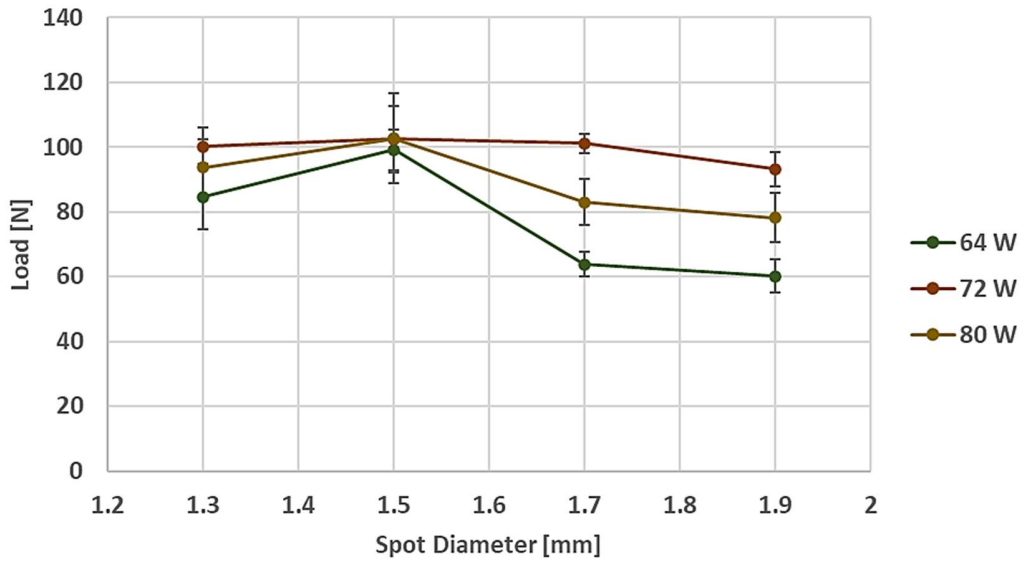


Fig. 10 - Failure load study for 45º angles, with pulse time fixed in 1.5 ms varying the average power and the laser beam diameter.

From this analysis, it was clear that the laser beam with 1.5 mm of diameter has the best performance, providing results which are very consistent, even with varied power levels. Furthermore, it was also possible to observe that the samples with 1.3 diameter suffered excessive penetration for the 72W and 80W power, exhibiting holes, as shown in Fig. **11** - Representative sample of the excess power degradation, pointing to the perforation of the PBT-GF30 plate.

.

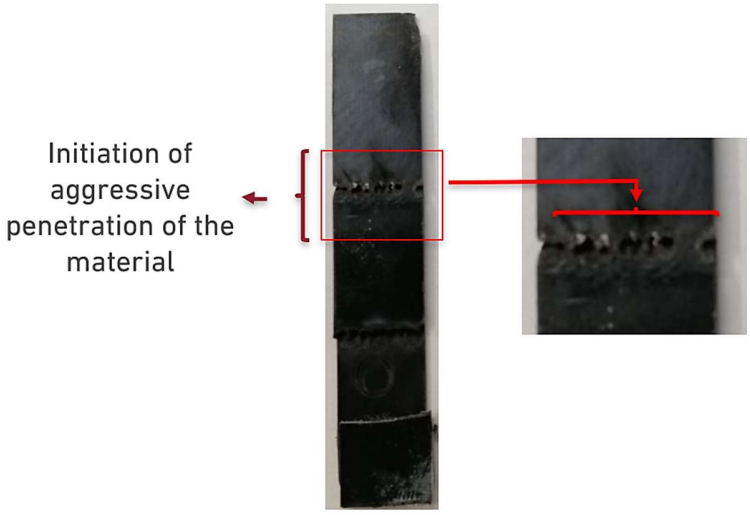


Fig. 11 - Representative sample of the excess power degradation, pointing to the perforation of the PBT-GF30 plate.

Calculating the minimal power density (p) from the minimal power (P) and the beam area (A) (Equation 1) one can define the power density boundaries that lead to material degradation, which for the case under analysis was found to be 53 W.mm^{-2}.

$$Power\ density\ (p) = \frac{P}{A} \tag{1}$$

Using this data, it becomes possible to create a two-dimensional plot, establishing a relationship between the failure load of the joints, beam power and the diameter of the laser beam, while defining the boundaries that lead to excessive degradation of the base materials. This plot is shown in Fig. **12** - Failure load map for 45º angles varying the average power and the laser beam diameter.

.

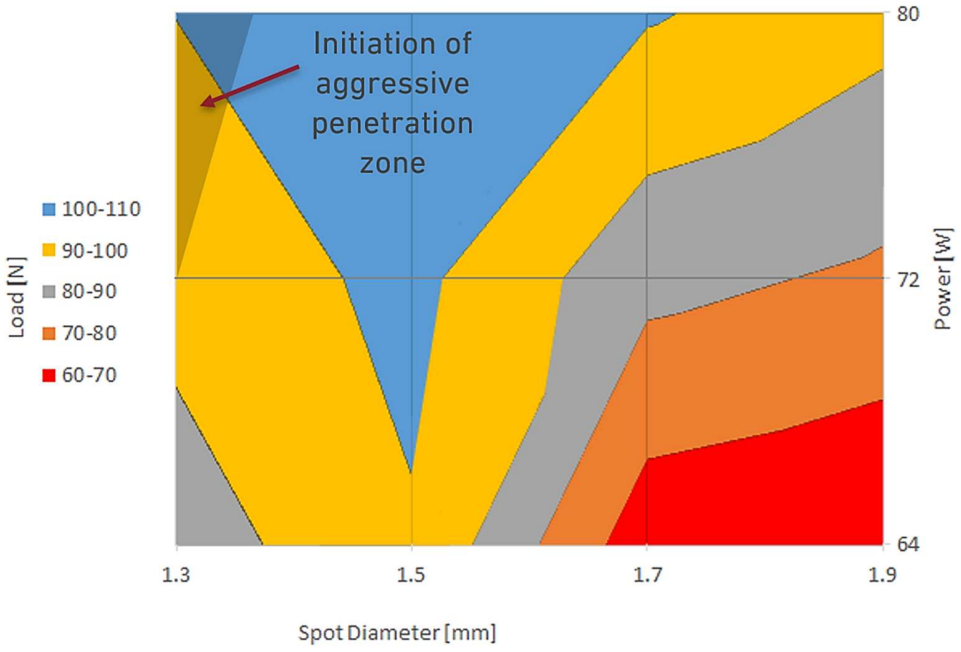


Fig. 12 - Failure load map for 45º angles varying the average power and the laser beam diameter.

In an analogous form, one can seek the ideal pulse width time by fixing the laser beam diameter to 1.5 mm and incident angle of 45º. The pulse time was then varied (0.5, 1.5, 2.5 and 3.5 ms) and three different power levels being considered (64, 72 and 80 W).

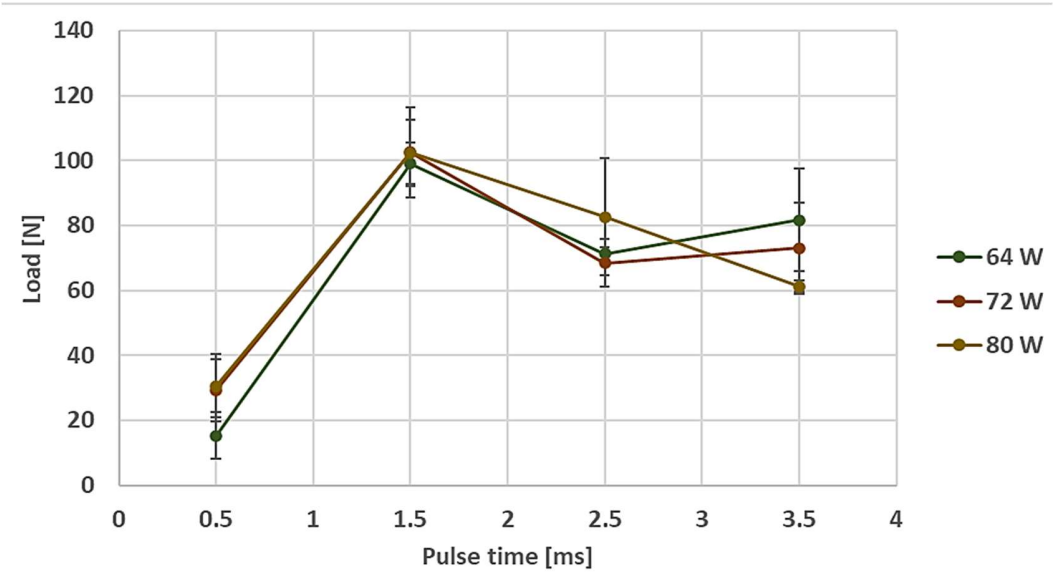


Fig. 13 - Failure load study for 45º angles, with the optimized laser beam diameter in 1.5 mm varying the average power and the pulse time.

As shown in Fig. **13** - Failure load study for 45º angles, with the optimized laser beam diameter in 1.5 mm varying the average power and the pulse time.

the best joint performance was found for 1.5 ms of pulse time. In line to what occurred during the laser diameter optimization process, excessive degradation was found for the longest pulse diameter, independently of the power level. Considering the minimal power density flux ($\dot{p}$) that degrades the material as being the result of the multiplication of the minimum power density (p) by the minimal pulse time (t_p), stated in Equation 2, one can determine a boundary value of 0.13 J.mm^{-2}.

$$Power\ density\ flux\ (\dot{p}) = p.t_p \qquad (2)$$

According to this data, one can again design a chart (Fig. **14** - Failure load map for 45° angles, varying the average power and time of the laser pulse.

) which provides information on the dependency of the joint performance with the laser pulse time and the overall power, while defining a clear boundary for excessive material degradation.

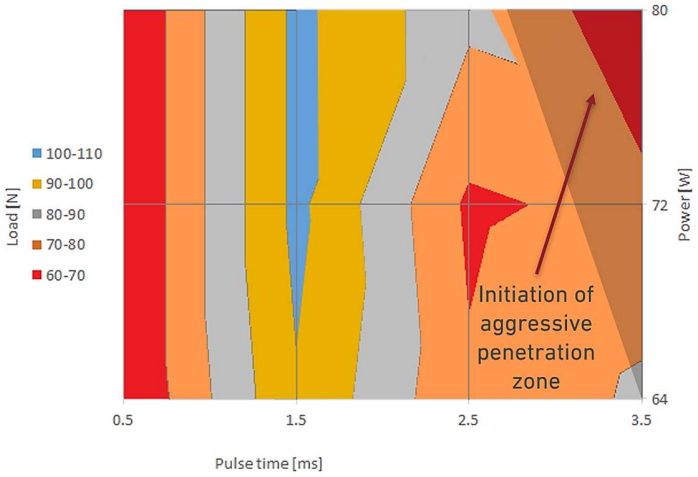


Fig. 14 - Failure load map for 45° angles, varying the average power and time of the laser pulse.

This chart indicates that optimal joint performance is attained with an inclination of 45º and a laser beam with 1.5 mm of diameter, a pulse time of 1.5 ms and a power of 64W. Such configuration results in the joint morphology shown in the micrograph of Fig. **15** - Microscopy analysis with the measurement of weld length and the thickness at the approximation 100x magnification.

, where the length of the welded area is of 0.306 mm and the gap between the substrates of $6.25x10^{-3}$ mm.

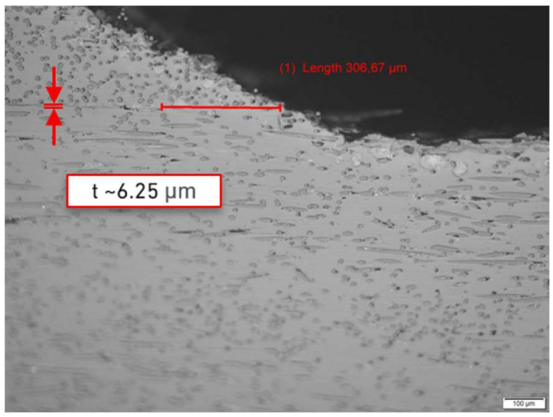


Fig. 15 - Microscopy analysis with the measurement of weld length and the thickness at the approximation 100x magnification.

3.2 Adhesive bonding

3.2.1 Mechanical characterization of the adhesive

A microscopic analysis was carried out to characterize a transverse section of the welded region, allowing to determine the penetration of the weld, the geometric profile of the surface and the actual spacing between the plates.

For this analysis, laser welding was performed experimentally on 10x15x2 mm samples of PBT-GF30 material. Since the welding profile is small and may fracture with the large loads encountered during the grinding and

polishing process, a notch was made in the surface of each rectangle, where on one side of the notch the material would be welded according to the pre-established parameters and on the other side of the notch the plates were joined with a supporting adhesive, increasing the resistance of the joint and allowing for easier sanding of the cross section, as shown in Fig. **4** - - Scheme of the procedures used for the analysis of the welded region with optical microscopy.

. The sanding process was carried out was done with emery paper of 220, 320, 800, 1200 and 4000 grain sizes and in water. After the grinding process was complete, the specimens were dried and analysed with an optical microscope (Carl Zeiss El-Einsatz HAL 100). The tensile and shear behaviour of the silicone adhesive is illustrated in Figure 16 and Figure 17, respectively, by the curves representing the tensile test and the shear test. For the tensile test, the maximum stress value is 3.40 ± 0.10 MPa. For the shear test, the value is 2.78 ± 0.01 MPa.

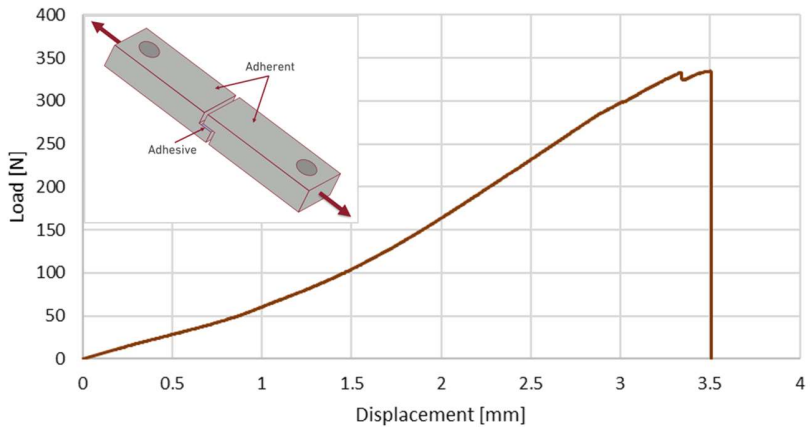


Fig. 16 - Representative force-displacement curve for the shear test.

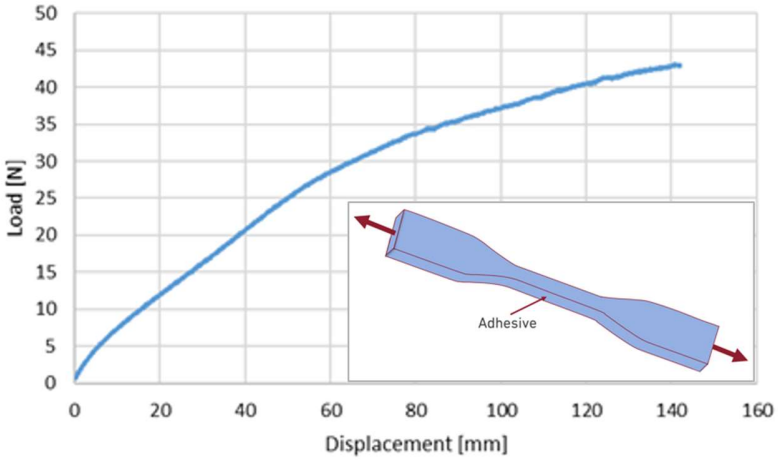


Fig. 17 - Representative force-displacement curve for the tensile test.

3.2.2 Single lap joint results

To provide a comparison between the optimal laser welded configuration, the two adhesive joint configurations under study were tensile tested to determine their mechanical performance and its fracture mechanism. The fracture surfaces of the first configuration (with 0.05 mm of adhesive thickness and 1 mm of overlap) are shown in Fig. **18** - Double fillet adhesive fracture surfaces

. These results indicate that the failure mode is of mixed nature.

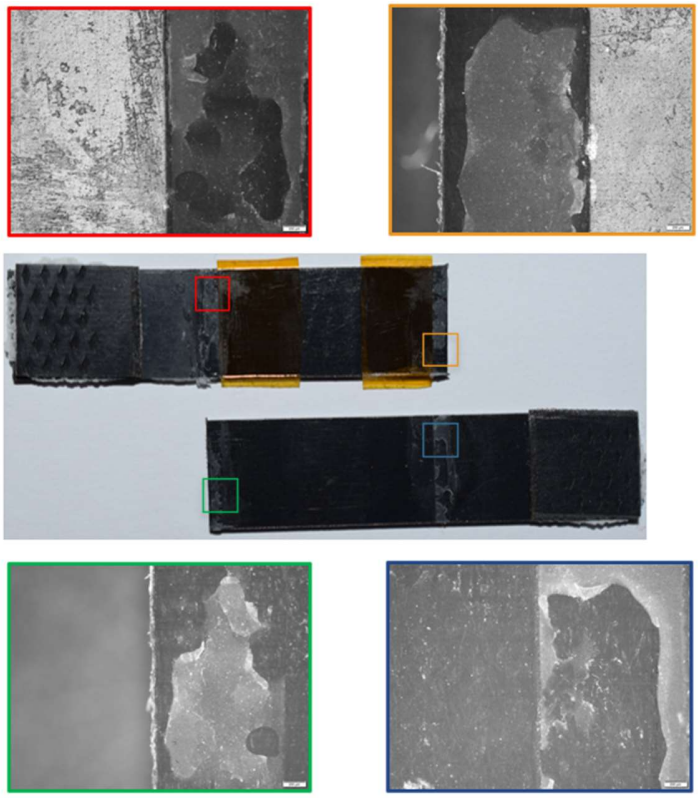


Fig. 18 - Double fillet adhesive fracture surfaces

The fracture surfaces of the second configuration (with 1 mm of adhesive thickness with 2 mm of overlap) are shown in Figure 19. These results indicate that the failure mode is mostly cohesive in nature, although voids are easily seen. These voids also appear to have been the starting points for crack propagation and demonstrate the difficulty in ensuring that large adhesive layer thicknesses are defect free.

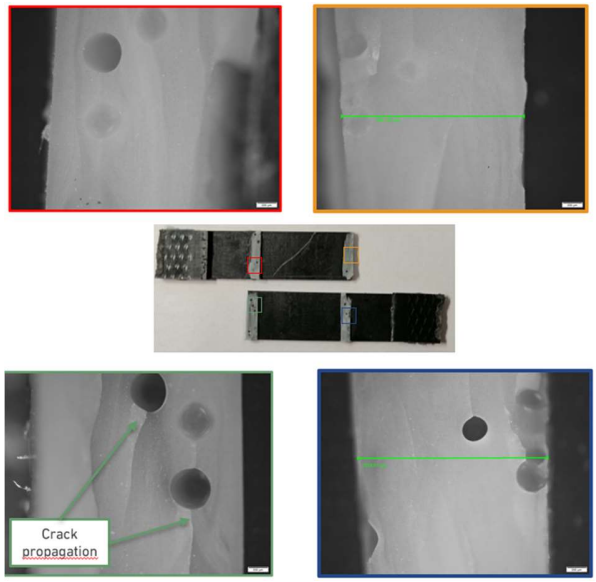


Fig. 19 - Double fillet cohesive fracture. with fracture comparison side by side showing cohesive fracture.

The load-displacement curves resulting from the tensile test of the two adhesively bonded configurations are shown in Fig. **20** - Experimental curves of the single lap joint by adhesive bonding obtained in the first attempt with 0.05 mm thickness.

and Fig. **21** - Experimental curves of the single lap joint by adhesive bonding obtained in the first attempt with 1 mm thickness.

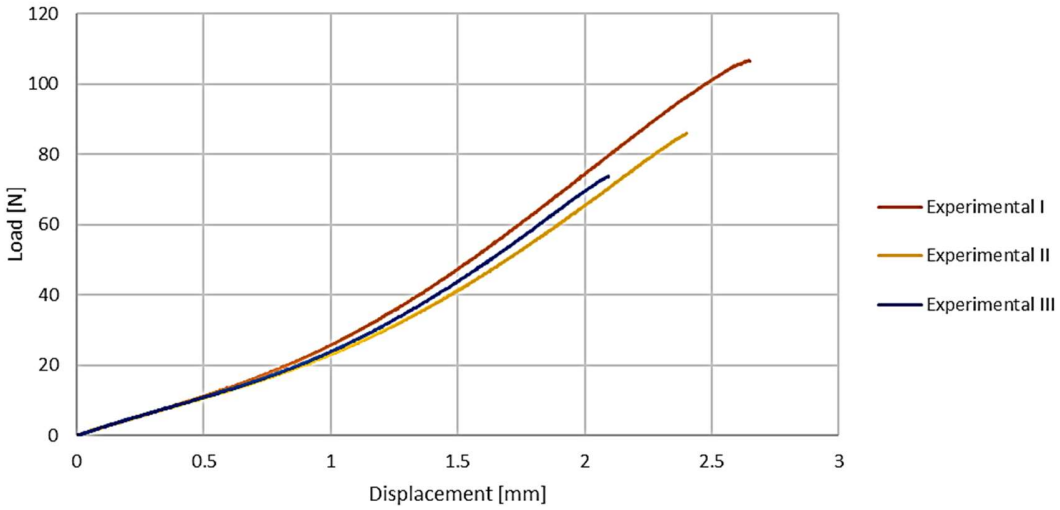


Fig. 20 - Experimental curves of the single lap joint by adhesive bonding obtained in the first attempt with 0.05 mm thickness.

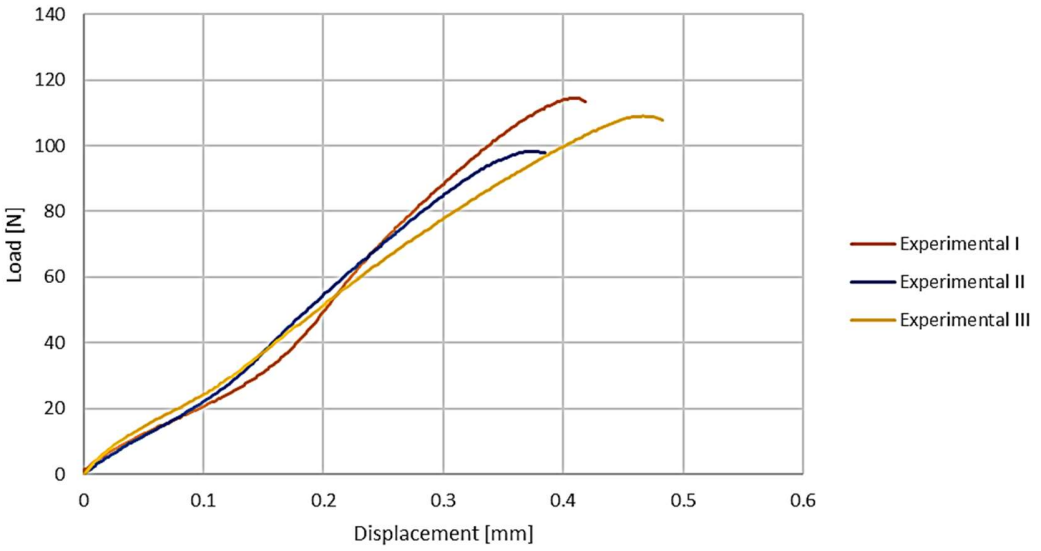


Fig. 21 - Experimental curves of the single lap joint by adhesive bonding obtained in the first attempt with 1 mm thickness.

Fig. **22** - Comparison between the maximum load obtained in the joint processes, adhesive joint and spot laser welding.

compares the maximum load supported with these two adhesively bonded configurations and compares it with the maximum load supported by a joint created with the optimal laser welded configuration.

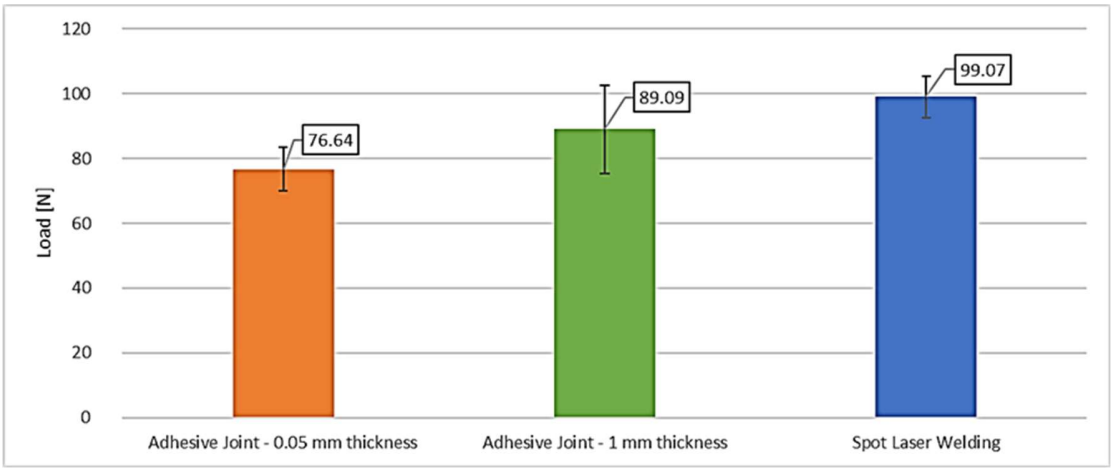


Fig. 22 - Comparison between the maximum load obtained in the joint processes, adhesive joint and spot laser welding.

These results indicate that the adhesive joint provides higher strength for the lowest adhesive thickness, following the results reported by Chéron 1998 [42], although the difference is not very significant. At this stage, it

also clear that the laser welded joint configuration under study has a similar performance to the bonded joint configurations, and thus all these joints are, at least in strength, suitable for the intended application.

4 Numerical procedure

4.1 Adhesive bonding

The aim of the numerical simulation of the adhesive joint is to validate the model based on the properties characterised using the mechanical characterisation tests of the silicone adhesive. A complex model, using hyperlastic considerations was employed for this purpose.

4.1.1 Hyperelastic model

Based on the principle of hyperelasticity theory, it is necessary to analyse and validate the constitutive laws applied to the Abaqus finite element model for silicone. As Simon et al. (2022) [43] and Dias et al. (2014) [44] stated, the hyperelastic laws available for this case in ABAQUS are shown in Fig. **23** – Map of the hyperelastic constitutive laws available.

.

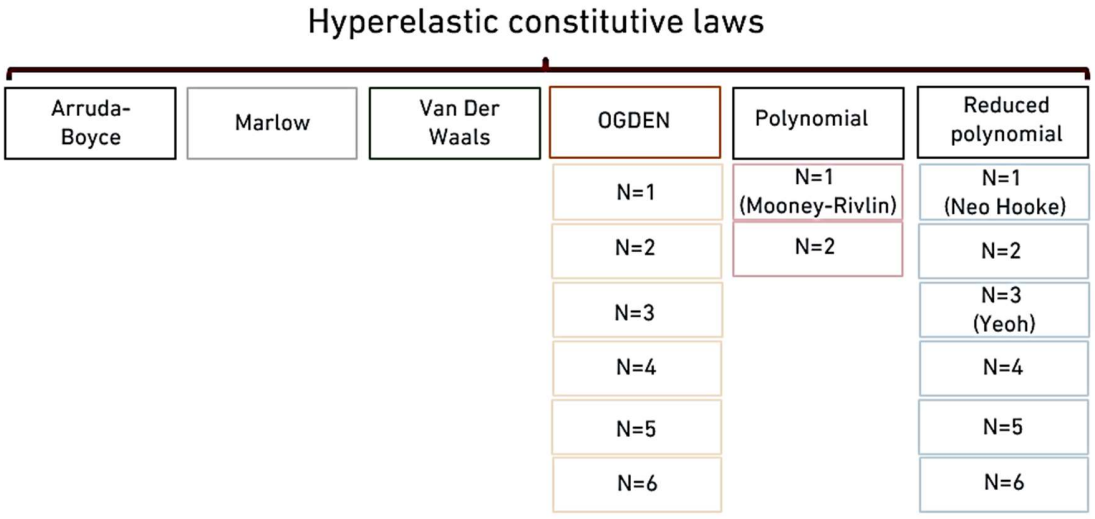


Fig. 23 – Map of the hyperelastic constitutive laws available.

As pointed out by Mavrodontis (2017) [45], the general equation for hyperelastic modelling is based on Equation 3, which identifies the deformation potential energy (U). The first deviatoric part depends on the invariant term (I), according to Equation 4, and the second part is volumetric.

$$U = \sum_{i+j=1}^{N} C_{ij}\,(\bar{I}_1 - 3)^i(\bar{I}_2 - 3)^j + \sum_{i=1}^{N} \frac{1}{D_i}(J_{el} - 1)^{2i} \quad (3)$$

$$\bar{I}_1 = \lambda_1^2 + \lambda_2^2 + \lambda_3^2 \quad \text{and} \quad \bar{I}_2 = \lambda_1^{-2} + \lambda_2^{-2} + \lambda_3^{-2} \quad (4)$$

In each constitutive law shown in Fig. **23** – Map of the hyperelastic constitutive laws available.

, there is a model of the invariant term, i.e. for each type of experiment, be it uniaxial, planar, equibiaxial or volumetric. However, based on the uniaxial traction experimental analysis, the main extension functions can be given by Equation 5.

$$\lambda_1 = \varepsilon_u + 1 \quad \text{and} \quad \lambda_2 = \lambda_3 = \frac{1}{\sqrt{\varepsilon_u + 1}} \quad (5)$$

Knowing that the term ε_u refers to the nominal principal deformation.

4.1.2 Cohesive zone modelling (CZM)

Knowing that failure fracture follows a non-linear behaviour, the cohesive model is often employed in these cases, especially when it comes to adhesive joints. As a result, it allows for the application of damage, which is simpler depending on the need for few variables, especially when it comes to the experimental tests carried out to characterise silicone adhesives. The CZM model reproduces the separation of surfaces, following a triangular relation between stress and displacement. The traction increases to its maximum value (maximum stress of the material) and continues to decrease until it is cancelled, based on the Fig. **24** – Damage process using a triangular cohesive zone model in single lap joint.

.

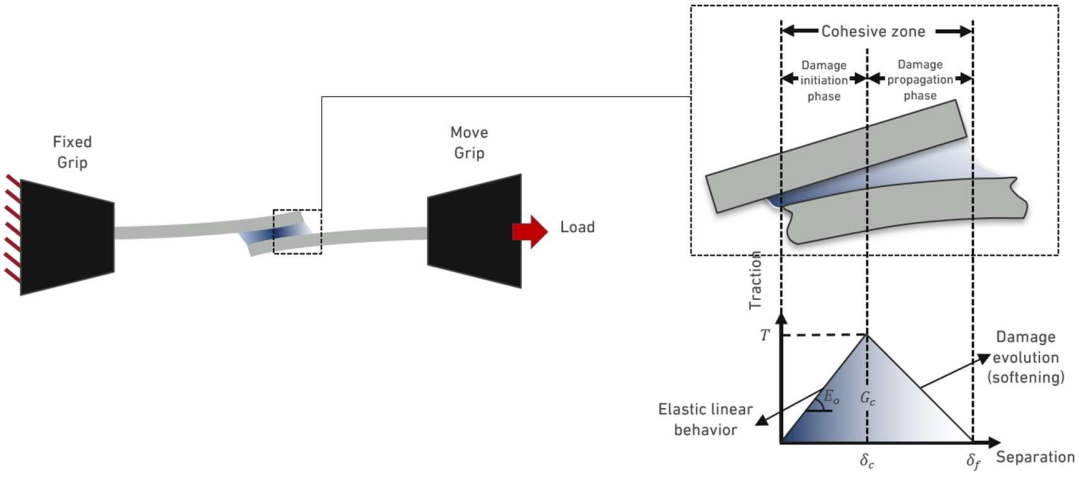


Fig. 24 – Damage process using a triangular cohesive zone model in single lap joint.

4.1.3 Damage model - Quadratic nominal stress (QUADS)

As shown in Fig. **24** – Damage process using a triangular cohesive zone model in single lap joint.

, damage after the elastic phase can be reproduce using various models, however, the quadratic normal stress model directly satisfies the approach to the two experiments performed, proposing the two main directions, either normal or shear according to the Fig. **25** – Traction separation law for multiple modes.

.

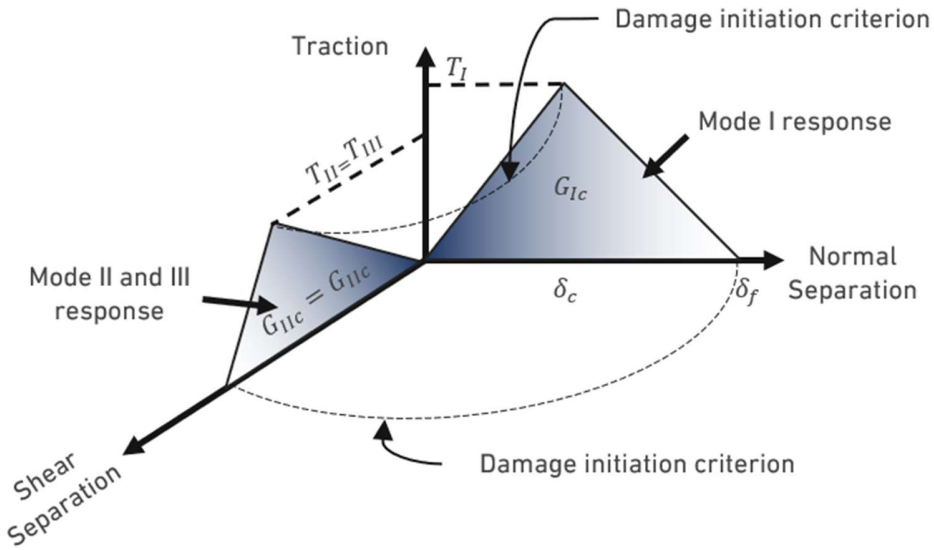


Fig. 25 – Traction separation law for multiple modes.

Based on the relationship between the normal principal stress $T_{I,c}$ and the shear stresses, especially in the simplification where the sliding and tearing shear stresses are equal $T_{II,c} = T_{III,c}$, the damage model can be represented by Equation 6.

$$\left(\frac{T_I}{T_{I,c}}\right)^2 = \left(\frac{T_{II}}{T_{II,c}}\right)^2 = \left(\frac{T_{III}}{T_{III,c}}\right)^2 = 1 \quad (6)$$

4.1.4 Single lap joint modelling

The model geometries for the joint simulations were based on the measurements provided in Fig. **7** - Adhesive joint geometry with low thickness (0.05 mm). b) Adhesive joint geometry with reference thickness (1 mm).

a and Fig. **7** - Adhesive joint geometry with low thickness (0.05 mm). b) Adhesive joint geometry with reference thickness (1 mm).

b, with 10 mm of width. The thickness of the adhesive was divided into three parts, the parts in contact with the substrate modelled with hyperelastic material and the central part, where the failure occurs with cohesive elements with QUADS damage as shown Fig. **28** – Comparison between experimental curve and numerical validation curve attained using the Ogden N=2 model.

The results of the simulations are shown in the figures below. Figure 29 shows the comparison between the numerical result and the experimental curves for the 0.05 mm thick adhesive. Figure 30 shows the comparison between the numerical result and the experimental curves for the 1 mm thick adhesive.

-a e Fig. **28** – Comparison between experimental curve and numerical validation curve attained using the Ogden N=2 model.

The results of the simulations are shown in the figures below. Figure 29 shows the comparison between the numerical result and the experimental curves for the 0.05 mm thick adhesive. Figure 30 shows the comparison between the numerical result and the experimental curves for the 1 mm thick adhesive.

-c.

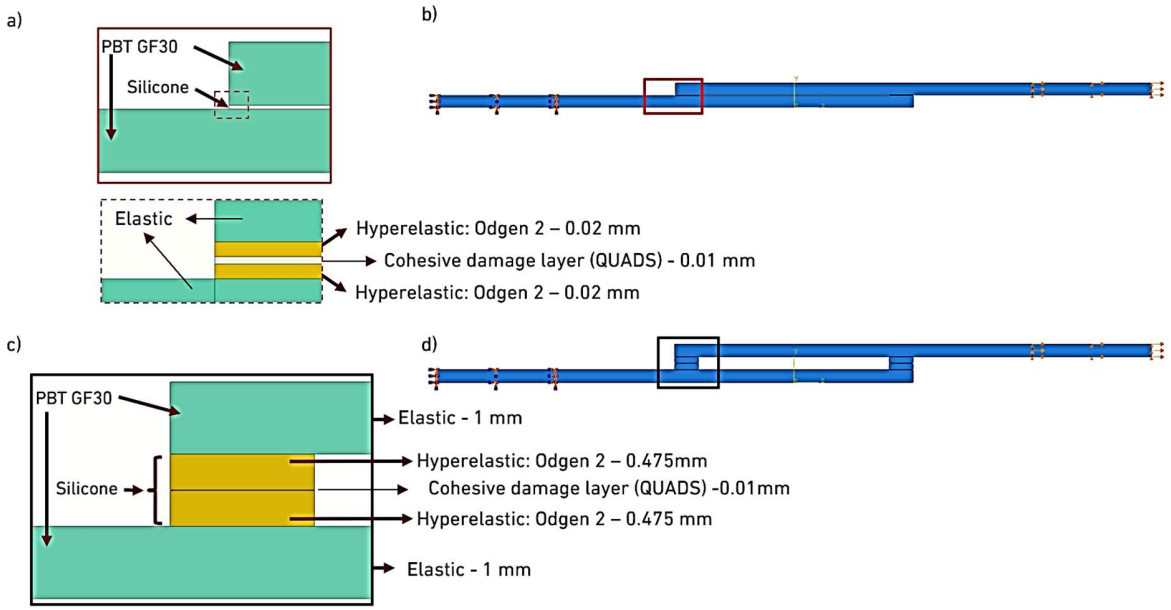


Fig. 26 – Representation of joints. a) Division of the joint part and the adhesive layer to 1 mm thickness. b) Boundary condition for the 1 mm thickness. c) Division of the joint part and the adhesive layer to 0.05 mm thickness. d) Boundary condition for the 0.05 mm thickness.

For the boundary conditions (Fig. **28** – Comparison between experimental curve and numerical validation curve attained using the Ogden N=2 model.

The results of the simulations are shown in the figures below. Figure 29 shows the comparison between the numerical result and the experimental curves for the 0.05 mm thick adhesive. Figure 30 shows the comparison between the numerical result and the experimental curves for the 1 mm thick adhesive.

-c e Fig. **28** – Comparison between experimental curve and numerical validation curve attained using the Ogden N=2 model.

The results of the simulations are shown in the figures below. Figure 29 shows the comparison between the numerical result and the experimental curves for the 0.05 mm thick adhesive. Figure 30 shows the comparison between the numerical result and the experimental curves for the 1 mm thick adhesive.

-d), an encastre fixation was used on the left and unidirectional displacement on the right, with movement corresponding to a total displacement of 10 mm. **Erro! A origem da referência não foi encontrada.** presents the properties used in the simulation. For the PBT GF 30 substrate, purely elastic properties were used since the adhesive is much less stiff than the adherend. For the hyperelastic zone in the adhesive, the relevant constants are shown in Fig. **28** – Comparison between experimental curve and numerical validation curve attained using the Ogden N=2 model.

The results of the simulations are shown in the figures below. Figure 29 shows the comparison between the numerical result and the experimental curves for the 0.05 mm thick adhesive. Figure 30 shows the comparison between the numerical result and the experimental curves for the 1 mm thick adhesive.

. **Erro! A origem da referência não foi encontrada.** also shows the properties for the cohesive elements, the elastic part, the damage part and the damage evolution. For damage evolution, energy type, linear softening, maximum degradation, Power law mixed mode behaviour, mode mix ratio energy was used.

Table 1 - Properties of the substrate and adhesive layers.

PBT GF 30		
Elastic	Young's Modulus	Poisson's Ratio
	8403.36 MPa	0.36

Silicone				
CZM-Quads	Elastic	E/Enn	G1/Ess	G2/Ett
		180 MPa	120 MPa	120 MPa
	DAMAGE	Nominal Stress Normal-only Mode	Nominal Stress First Direction	Nominal Stress Second Direction
		3.4 MPa	4.18 MPa	4.18 Mpa
	DAMAGE EVOLUTION	Normal Mode Fracture Energy	Shear Mode Fracture Energy First Direction	Shear Mode Fracture Energy Second Direction
		4 N/mm	9 N/mm	9 N/mm

The mesh size in the joints was mostly 1 mm for the substrate. However, when approaching the silicone adhesive zone, the mesh was refined to allow it to be consistent with the mesh size of the cohesive elements, as detailed in **Erro! A origem da referência não foi encontrada.**.

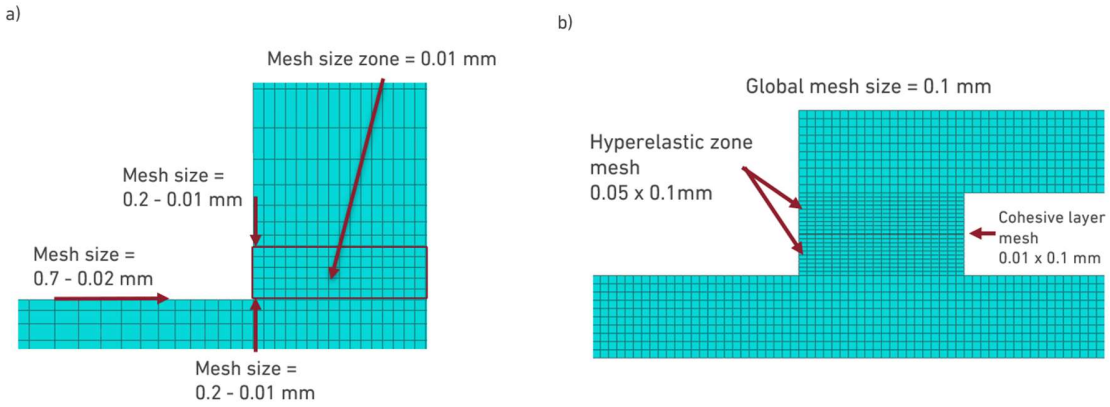


Fig. 27 – Meshing details for the adhesive joint models

5 Numerical results of adhesive bonding

In this way, from the traction curve based on the work of Esmail et al (2020) [46], all the constitutive laws represented in Fig. **23** – Map of the hyperelastic constitutive laws available.

were analysed. However, convergency was only obtained for the Arruda-Boyce, Marlow, OGDEN 1, OGDEN 2, and Reduced polynomial 1, 2 and 5. However, the best convergence was obtained with OGDEN 2, as shown in Fig. **28** – Comparison between experimental curve and numerical validation curve attained using the Ogden N=2 model.

The results of the simulations are shown in the figures below. Figure 29 shows the comparison between the numerical result and the experimental curves for the 0.05 mm thick adhesive. Figure 30 shows the comparison between the numerical result and the experimental curves for the 1 mm thick adhesive.

, which also highlights the governing equation and and the values of the constants of the constitutive law.

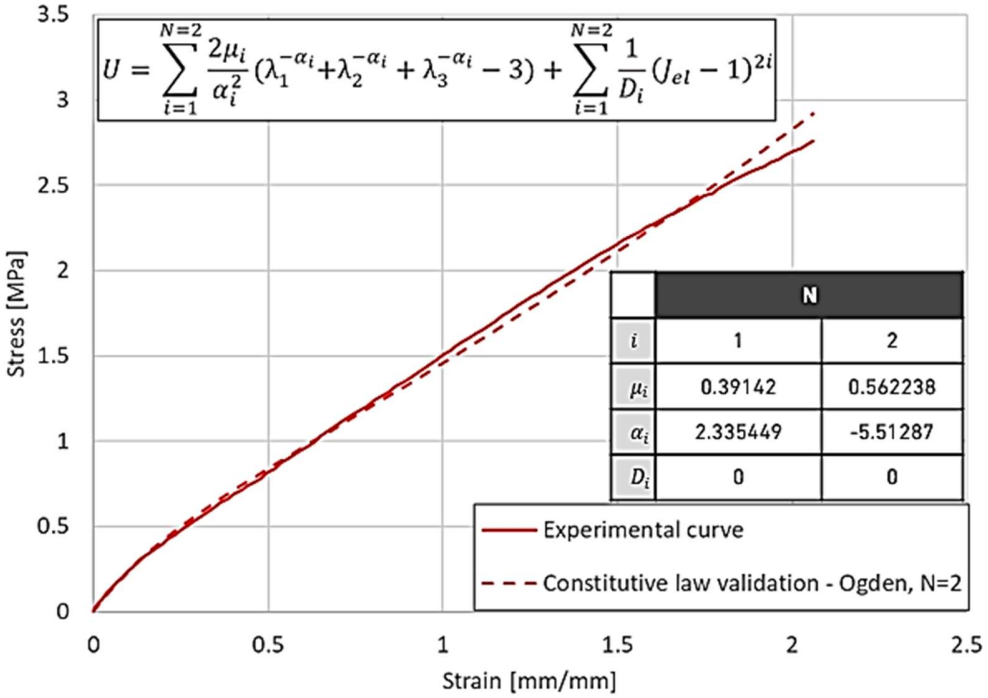


Fig. 28 – Comparison between experimental curve and numerical validation curve attained using the Ogden N=2 model.

The results of the simulations are shown in the figures below. Figure 29 shows the comparison between the numerical result and the experimental curves for the 0.05 mm thick adhesive. Figure 30 shows the comparison between the numerical result and the experimental curves for the 1 mm thick adhesive.

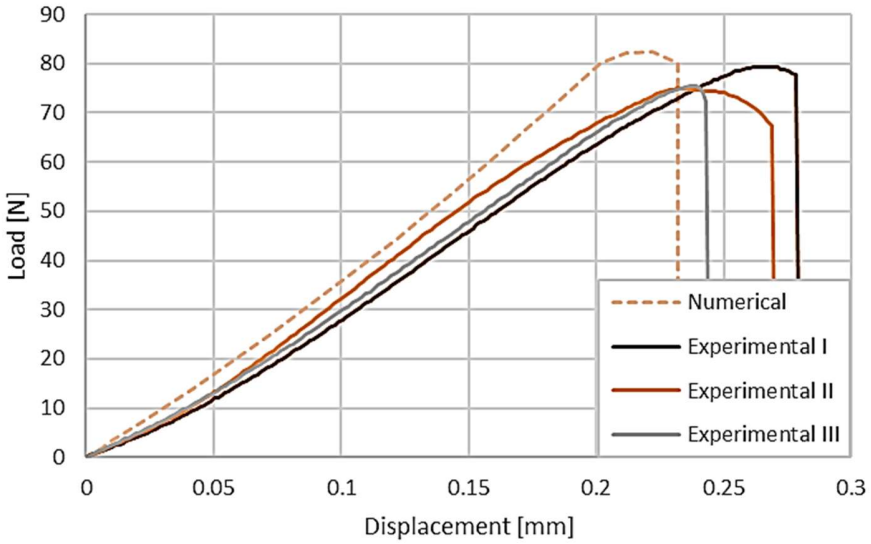


Fig. 29 – Adhesive joint – 0.05 mm thickness. Comparison results between experimental and numerical simulation with hyperelastic-quad damage (CZM) model.

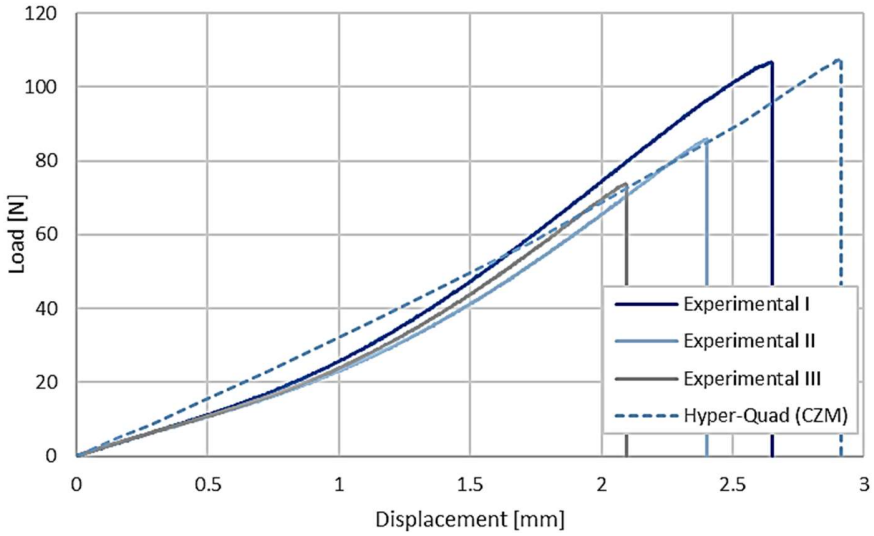


Fig. 30 – Adhesive joint – 1 mm thickness. Comparison results between experimental and numerical simulation with hyperelastic-quad damage (CZM) model.

Figure 29 and Figure 30 show a high degree of convergence in the results. According to the analysis of the comparative curves, there is a slight change in stiffness between the experimental and numerical curves, taking into account that the simulation disregards the added displacement that is calculated in the elements of the universal traction

machine. Another analysis that can also be made is that the maximum force of the simulation for both configurations is slightly higher than the experimental curves. The validation of the properties of the experimental tests provides excellent results for adhesive joints, making it possible to apply the model to real-life studies applied in an industrial environment.

6 Conclusions

This work, using optimized laser spot welding parameters in PBT-GF30 fillet joints, allowed to determine that this technique provides in an efficient response when compared to adhesive bonding in similar configurations, avoiding the addition of material and resulting in a faster joining process. According to the parameters and configurations discussed, it was confirmed that the joint's tensile strength is higher at an angle of 45° than at 30° and 60°. Furthermore, the diameter, power and time of the laser beam were also found to be highly relevant parameters to study, having and independent response on joint performance. It was also determined that the optimal parameters for welding PBT-GF30 necessitate a power density and power density ratio of 53 W.mm-2 and 0.13 J.mm-2 respectively, so that the material does not perforate the 1 mm thick sheets.

For adhesive joints, with silicone as the adhesive on a PBT-GF30 substrate, it can be seen that the thickness of the adhesive directly influences the response of the joint strength. For a thickness of 0.05 mm, the joint performance is greater than that encountered for a thickness of 1 mm, which is explained by the formation of air bubbles and the propagation of cracks at greater thicknesses.

As for the validation of the model in adhesive joints, especially for materials such as silicone, it can be seen that there is a good degree of convergence in the results when applying the hyperelastic material joint with the cohesive damage elements based on QUADS.

References

[1] De Camargo, D. Z., Zancanella, A. C. B., Da Silva, L. R. R., Maziero, R., De Castro, B. D., and Rubio, J. C. C., "Selection of Materials for Weight Reduction in Sports Cars," in *Advanced Materials Research*, 2019, pp. 73-82.

[2] Lyu, M.-Y. and Choi, T. G., International journal of precision engineering and manufacturing, **16**, 213-220 (2015)

[3] Taub, A. I. and Luo, A. A., Mrs Bulletin, **40**, 1045-1054 (2015)

[4] Borges, M., Laser Technik Journal, **13**, 26-29 (2016)

[5] Friedrich, K. and Almajid, A. A., Applied Composite Materials, **20**, 107-128 (2013)

[6] Silva, L., Marques, E., and Da Silva, L. F., Welding in the World, **65**, 2023-2045 (2021)

[7] Schubert, E., Klassen, M., Zerner, I., Walz, C., and Sepold, G., Journal of Materials Processing Technology, **115**, 2-8 (2001)

[8] Hirose, A. and Kobayashi, K. F., "Laser beam welding of automobile materials for lightweight car body," in *Materials Science Forum*, 2005, pp. 487-492.

[9] Vaamonde Couso, E. and Vázquez Gómez, J., Structural connections for lightweight Metallic Structures, (Springer, 2010). 59-84
[10] Kacar, I., Ozturk, F., and Yilbas, B., Lasers in Engineering (Old City Publishing), **33**, (2016)
[11] Acherjee, B., Journal of Manufacturing Processes, **64**, 421-443 (2021)
[12] Quazi, M., Ishak, M., Fazal, M., Arslan, A., Rubaiee, S., Aiman, M.*, et al.*, Critical Reviews in Solid State and Materials Sciences, **46**, 109-151 (2021)
[13] Gonçalves, L. F., Duarte, F. M., Martins, C. I., and Paiva, M. C., Infrared Physics & Technology, **119**, 103931 (2021)
[14] Jones, I., Assembly automation, (2002)
[15] Amanat, N., Chaminade, C., Grace, J., Mckenzie, D. R., and James, N. L., Materials & design, **31**, 4823-4830 (2010)
[16] Kim, H.-J., Jeon, J.-A., Choi, J.-Y., Kim, J., Hong, J.-T., Seo, H.*, et al.*, Optical Engineering, **48**, 084301 (2009)
[17] Volpe, A., Di Niso, F., Gaudiuso, C., De Rosa, A., Vàzquez, R. M., Ancona, A.*, et al.*, "Femtosecond fiber laser welding of PMMA," in *Laser-based Micro-and Nanoprocessing IX*, 2015, pp. 32-40.
[18] Klotzbuecher, T., Letschert, M., Braune, T., Drese, K.-S., and Doll, T., "Diode laser welding for packaging of transparent micro-structured polymer chips," in *Laser-based Micropackaging*, 2006, p. 610704.
[19] Kim, D.-J., Jeon, I.-R., Park, H.-Y., and Seo, K.-H., Polymer (Korea), **37**, 753-763 (2013)
[20] Visco, A. and Scolaro, C., International Journal of Polymer Analysis and Characterization, **23**, 354-361 (2018)
[21] Galtieri, G., Visco, A., Nocita, D., Torrisi, L., Ceccio, G., and Scolaro, C., Journal of Instrumentation, **11**, C04013 (2016)
[22] Antic, V. and Pergal, M. V., Handbook of Engineering and Specialty Thermoplastics, Volume 3: Polyethers and Polyesters, **3**, 127 (2011)
[23] Borges, C. S., Akhavan-Safar, A., Marques, E. A., Carbas, R. J., Ueffing, C., Weißgraeber, P.*, et al.*, Materials, **14**, 1261 (2021)
[24] Pham, N. T.-H., Lu, H.-K., Nguyen, N. T.-N., Huynh-Nhat Do, H., Doan, D.-Q., and Van Huong, H., Polymer Science, Series A, 1-6 (2022)
[25] Li, X., Xia, M., Qiu, D., Long, R., Huang, Z., Li, J.*, et al.*, Macromolecular Materials and Engineering, **306**, 2000638 (2021)
[26] Li, Z., Li, J., Chen, Y., Ye, J., Song, X., Jin, Y.*, et al.*, Polymers for Advanced Technologies, (2022)
[27] Davoodi, M., Sapuan, S., Ahmad, D., Aidy, A., Khalina, A., and Jonoobi, M., Materials Letters, **67**, 5-7 (2012)
[28] Klein, R., Laser welding of plastics: materials, processes and industrial applications, (John Wiley & Sons, 2012).
[29] Okuizumi, R., Hirota, S., Takagi, Y., Sudoh, M., and Okano, Y., "Process analysis of laser welding method with polybutyleneterephthalate (PBT)," in *Advanced Materials Research*, 2011, pp. 150-153.
[30] Wang, X., Zhong, X., Liu, W., Liu, B., and Liu, H., Journal of Applied Polymer Science, **133**, (2016)
[31] Berger, E. A. and Milos, L., MATERIALE PLASTICE, **51**, 45-47 (2014)

[32] Brockmann, W., Geiß, P. L., Klingen, J., and Schröder, K. B., Adhesive bonding: materials, applications and technology, (John Wiley & Sons, 2008).
[33] Humbe, A., Deshmukh, P., Jadhav, C., and Wadgane, S., Int. J. Res. Eng. Technol, **2**, 191-206 (2014)
[34] Tserpes, K., Barroso-Caro, A., Carraro, P. A., Beber, V. C., Floros, I., Gamon, W.*, et al.*, The Journal of Adhesion, 1-61 (2021)
[35] He, X., International Journal of Adhesion and Adhesives, **31**, 248-264 (2011)
[36] Berger, S., Oefele, F., and Schmidt, M., Journal of Laser Applications, **27**, S29009 (2015)
[37] Diebels, S. and Rjasanow, S., Multi-scale simulation of composite materials: Results from the project MuSiKo, (Springer, 2019).
[38] Astm, "Standard test method for determining strength of adhesively bonded rigid plastic lap-shear joints in shear by tension loading," 2014.
[39] Standard, B. and Iso, B. E.,
[40] Dean, G., (1997)
[41] Banea, M. D. and Da Silva, L. F., The Journal of Adhesion, **85**, 261-285 (2009)
[42] Chéron, B. B. J. M., "Adhesive properties of silicone resins," Massachusetts Institute of Technology, 1998.
[43] Simon Portillo, F. J., Cuadrado Sempere, Ó., Marques, E. A., Sánchez Lozano, M., and Da Silva, L. F., Journal of Applied and Computational Mechanics, **8**, 359-369 (2022)
[44] Dias, V., Odenbreit, C., Hechler, O., Scholzen, F., and Zineb, T. B., International Journal of Adhesion and Adhesives, **48**, 194-209 (2014)
[45] Mavrodontis, N., "Modelling hyperelastic behavior using test data in abaqus—Simuleon FEA Blog," ed, 2017.
[46] Esmail, J. F., Mohamedmeki, M. Z., and Ajeel, A. E., "Using the uniaxial tension test to satisfy the hyperelastic material simulation in ABAQUS," in *IOP Conference Series: Materials Science and Engineering*, 2020, p. 012065.

Appendix E

Paper 5: Experimental and numerical study of laser beam welding of PBT-G30 for electronic housings in automotive applications

Experimental and numerical study of laser beam welding of PBT-G30 for electronic housings in automotive applications

L. R. R. Silva[1,2], P. D. P. Nunes[3], E. A. S. Marques[1*](emarques@fe.up.pt), R. J. C. Carbas[3], Lucas F. M. da Silva[1]

[1]Departamento de Engenharia Mecânica, Faculdade de Engenharia, Universidade do Porto, Rua Dr. Roberto Frias, 4200-465 Porto, Portugal

[2]Instituto Federal de Educação, Ciência e Tecnologia do Espírito Santo (Ifes), Rodovia BR Norte Km 58, São Mateus, 101 - Litorâneo, ES, 29932-540, Brasil

[3]Instituto de Ciência e Inovação em Engenharia Mecânica e Industrial (INEGI), Rua Dr. Roberto Frias, 4200-465 Porto, Portugal

Abstract

This study investigates the application of laser spot welding to join protective housing components in the automotive electronics industry. The PBT GF 30 components were joined using two primary configurations: a purely overlapping joint and a top-overlap joint, both autogenous (i.e., without filler material). To complement the experimental analysis, a numerical model, previously validated for a simpler joint configuration, was adapted and applied to these more complex joint configurations. The results demonstrated that butt-overlap joints exhibited significantly higher strength (85% increase) than purely overlapping joints. This enhancement is attributed to the combined effect of normal and shear stresses in the top-overlap configuration, whereas purely overlapping joints rely solely on shear stress. The validated numerical model accurately predicted the experimental results, including displacement and force values. While minor deviations were observed, the numerical model's predictions converged within the average experimental values and standard deviation, demonstrating that such model can be used to precisely design laser welded joints for similar applications.

Keywords

Laser welding , PBT GF30, housing, automotive, numerical modeling.

1. Introduction

With the increasingly tighter regulations and demands facing the automotive industry, one of the most key priorities of the companies operating in this sector has been the usage of lighter and more resistant

materials, in an effort to reduce weight and energy consumption, while ensuring maximum functionality [1]. While most of the effort is being devoted to new structural designs, other components, such as electronic systems have also been adopting lighter materials. However, according to Begum et al [2]and Patil et al [3], for these smaller components, especially electrical box protection, it is also necessary to analyse a wide range of parameters, such as flame protection, flame retardancy and water tightness, ensuring that the systems can operate without issues. Due to their versatility, polymers dominate this field of application, especially those which employ short fibre reinforcement, increasing their performance at a relatively low cost and without adding complexity to the manufacturing process [4-6].

Among all the possible polymeric matrices for these short fibre composites, Polybutylene Terephthalate (PBT) has multiple advantages compared to other polymers, such as its good chemical resistance and electrical properties, it is relatively and hard, shows limited water absoprtion [7]. It also has very good resistance to dynamic stress [8]and excellent thermal and dimensional stability [9]. PBT is relatively economical and simple to manufacture due to fast crystallization and fast cooling. Accordingly, it finds extensive usage in electronics protection housings but it can also be used in many other other applications, such as fog lamp housings and bezels, sun-roof front parts, locking system housings, door handles, bumpers, carburettor components, among many others.

The application of reinforced PBT, mainly with glass fibers (PBT GF-30, reinforced with 30% glass fiber by weight), has increased in the market due to the the excellent mechanical properties it provides. It is also very important in dynamic applications, providing high hardness and a low friction coefficient, reducing wear [10]. Furthermore, it is relatively easy to recycle, placing itself as a more sustainable polymer according to Pegoretti et al. [11].

When using such materials it also important to master a set of joining processes that allow to assemble them into more complex components. Of course, for thermoplastic polymers, laser welding is almost always one of the most significant joining methods, also supported with ultrasonic welding and adhesive bonding Silva et al (2021) [12]. Looking specifically at the laser welding application, Silva et al (2022) has carried out a characterization study of PBT GF30, demonstrating the good weldability in this material. Silva et al (2022) also carried out a study which defined the most suitable parameters for laser welding PBT-GF30 joints in overlapped joints, joined at the ends by a fillet. Furthermore, and aiming to optimize the production process in the industrial application of the laser welding process, Silva et al (2022) and Silva et al (2022)

furhter developed and optimized a model for predicting the performance of laser welded joints in PBT GF30, demonstrating its suitability for simple joint geometries.

This work, stemming from an industrial demand, aims to study the application of laser welding in real PBT-GF30 component, adopting specimen configurations that are closely related to those found in industrial applications. This is achieved through and experimental procedure and the use and validation model of the real joint, providing a new methodology to predict the performance of complex laser welded joints.

2. Experimental methodology

This work, based on an industrial demand from the automotive sector, seeks to join housing components for electronic components. These housings, as shown in **Figure 1**, are usually comprised of two separate halves, which are bonded together to seal the electronic boards placed inside them. However, adhesive bonding has some limitations in what concerns long term durability, as water ingress can in some cases damage the bonding interfaces. In this work, laser welding is instead used to achieve this joint, with the aim of providing a monolithic connection, less vulnerable to the environment. To prepare specimens for testing, small substrates were cut from the complete samples of the electronic housing. Since the goal is to assess the performance of the joint and not of the complete housing, 10 mm wide samples were extracted from different areas of the box, allowing to better study how the parts can be connected.

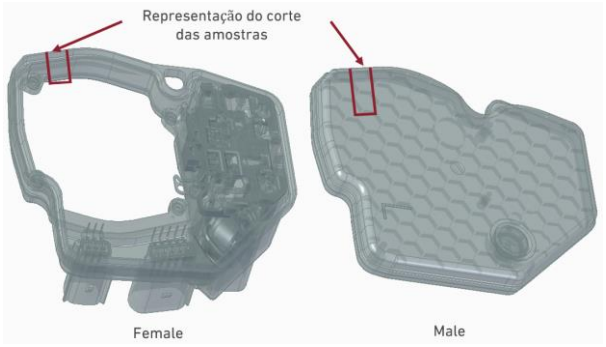


Figure 1 – Illustration of the electronics housing, showing the location of the cut made to extract the test specimens.

A cross-section of these cut specimens can be found in **Figure 2**. It is possible to see that the housing uses a male-female fitting to achieve a precise alignment, which is then usually bonded and sealed with the use of a flexible adhesive.



Figure 2 - Representation of the cross-sectional view of the joint samples, highlighting the female and male parts.

2.1. **Laser welding process**

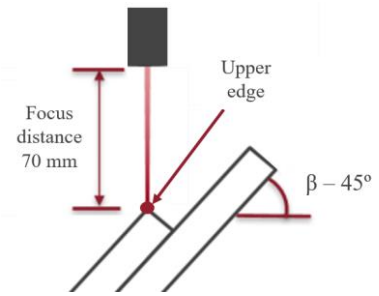
The equipment used to create the welded joints was a SISMA LM-D 180 (SISMA, Italy), which uses a Nd:YAG 1064 nm laser source, and with a maximum laser power of 80 W, as shown in Figure 3.



Figure 3 - Nd:YAG spot laser welding machine used in this work, SISMA LM-D 180

Following previous work by the authors, the optimal parameters to join GF30 PBT overlap joints, in 1 mm thick plates, fillet welded at their ends, are presented in Table 1. As the material used and the sheet thickness is the same, these procedures and parameters were directly adopted for the current work.

Table 1 - Optimized parameters and setting spot laser welding to PBT GF30.

<table>
<tr><td>Power</td><td>64 W</td><td rowspan="8">Scheme picture
 
</td></tr>
<tr><td>Inclination</td><td>1.5 mm</td></tr>
<tr><td>Aim position</td><td>1.5 ms</td></tr>
<tr><td>Frequency</td><td rowspan="2">Manual operation</td></tr>
<tr><td>Speed rate</td></tr>
<tr><td>Focus distance</td><td rowspan="3">See scheme</td></tr>
<tr><td>Inclination</td></tr>
<tr><td>Aim position</td></tr>
</table>

As the experimental testing seeks to provide data that can enable further optimization of the joints found in the full scale component, in addition to carrying out the test in which the real joint is purely overlapped, a test was also carried out in which the joint is partially overlapped and partially butt-jointed, as shown in **Figure 4**.

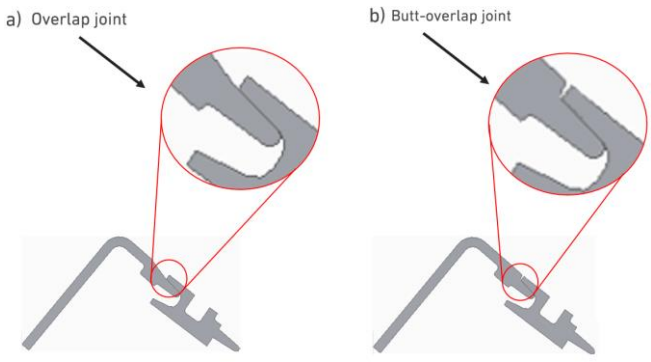


Figure 4 - Joint configurations for laser beam welding. a) Overlap joint. b) Butt-overlap joint.

2.1.1. Welding fixtures

In order to join these complex joints, which have non-standard specimens which are difficult to clamp, a specific jig had to be developed to support the welding process, as shown in **Figure 5**.

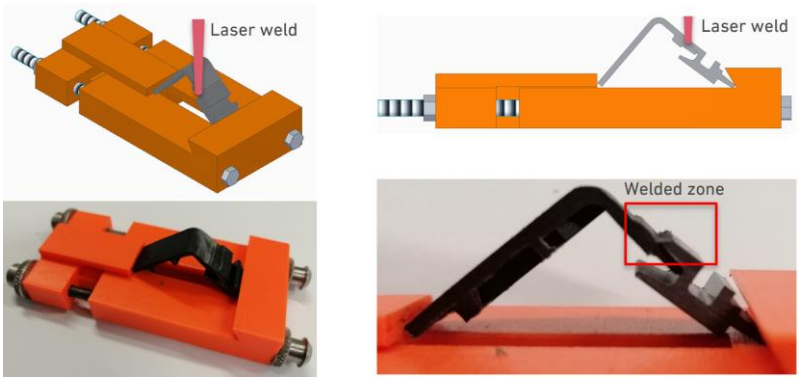


Figure 5 - Jig for fixing parts for joining by spot laser beam welding.

This jig, custom design and manufactured using additive manufacturing, has the role of ensuring that the the substrates are consistently located during welding. This is achieved by tightening two parallel screws, which keep the joint parts aligned and with a positive contact force during the welding process.

2.1.2. Test fixtures

In order to allow the specimens to be tested in a universal testing machine, the male part of the joint was fixed to a rectangular ABS block using a structural adhesive, while an additively manufactured fixing mold was bonded to the female part, also using a structural adhesive. This allowed both ends of the specimen to be clamped to the testing machine, in such a way that the surface of the block was perpendicular to the fixing mold, as shown in **Figure 6**.

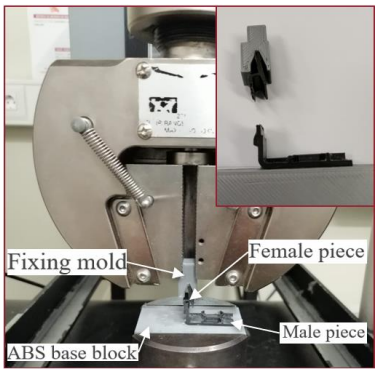


Figure 6 - Real joint test fixing configuration.

2.1.3. Displacement measurement

The INSTRON® 3367 universal testing machine was used to carry out the tensile tests. The crosshead speed setting was 1 mm/min, as used in the tests carried out by Silva et al. (2022). Three tests were carried

out for both configurations. For measuring displacement, the digital image correlation (DIC) method was used, based on the studies carried out by Borges et al. (2020) [13] using the GOE Correlate Pro program. The sample was speckled using black and white paint and filmed during the test. After completion of the test, the displacement was extracted using the GOE Correlate Pro software.

3. Experimental results

Experimental testing allows to accurately compare the performance of the two configurations under analysis. **Figure 7** shows the results of the overlapped only configuration, showing the crosshead displacement and the same value corrected using the DIC method.

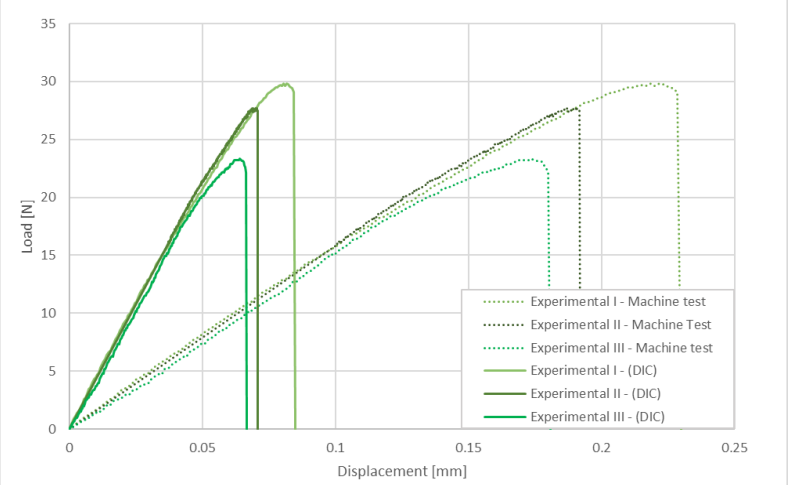


Figure 7 – Load displacement curves of for the overlapped configuration, showing a comparison between the crosshead displacement and the displacement obtained via DIC.

These results show the necessity of carrying out a DIC analysis, since the displacement is extremely small in relation to the size of the joint. Furthermore, the DIC displacement reading is determined solely in the region close to the weld, providing a value that is more representative of the actual joint performance, In contrast, using the testing machine data adds up all the deformation between the joint and the fixtures as well as the displacement corresponding to flexibility and clearances of the elements in the clamping jaw.

For the butt-overlap joints, the results show a similar variation between the displacement measured for the crosshead of the machine and by the DIC method, as shown in **Figure 8**.

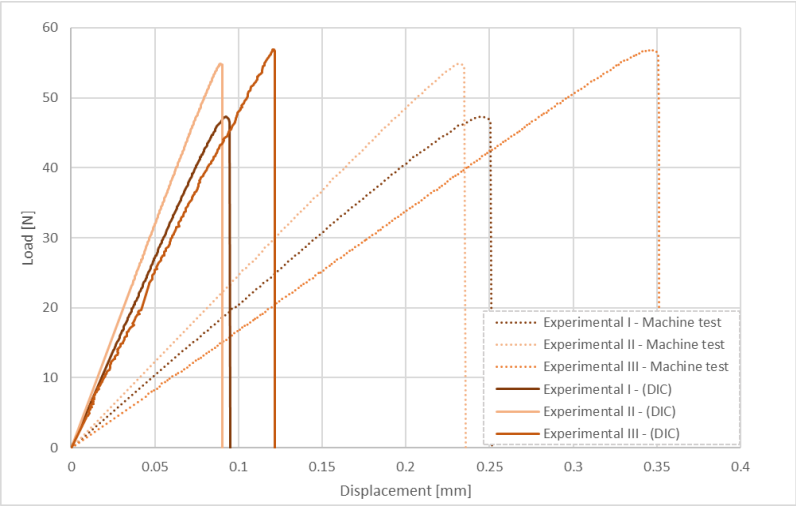


Figure 8 – Load displacement curves of for the butt-overlap configuration, showing a comparison between the crosshead displacement and the displacement obtained via DIC.

When comparing the load displacement curves of the two configurations, as shown in **Figure 9**, it becomes evident that both the strength and the displacement of the butt-overlap joint configuration are significantly higher than that found for the overlap joint, reaching almost the double of the peak strength.

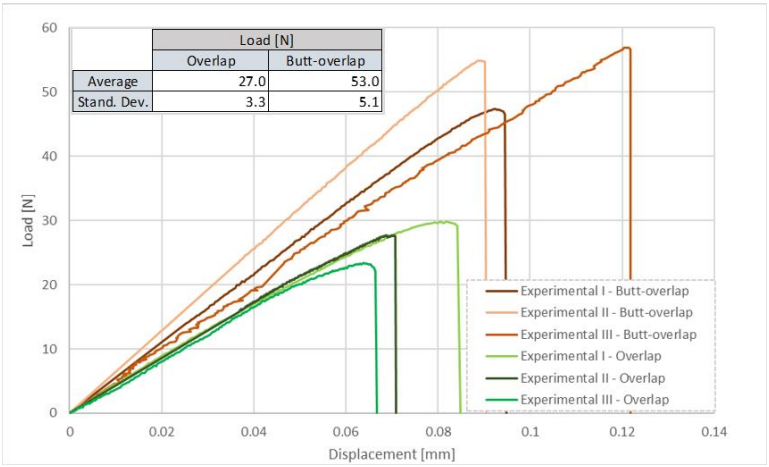


Figure 9 – Load-displacement curves of the purely overlapped configuration and the butt-overlap configuration (displacement measured by the DIC method).

This difference is explained in the work of Kagan et al. [14], which describes that, in lap welding, a fused zone is formed both in the overlapped part, which resists mainly to shear stress, and in the top region, which resists mainly the normal stress. This will increase the overall strength of the joint. Given the results displayed in **Figure 9**, it becomes evident that, if possible, laser welding in this type of connection should adopt a butt-overlap combination, ensuring maximum performance.

4. Numerical details

As the displacement of the joint has been calibrated using DIC, it becomes feasible to develop a numerical model which is able to precisely model the behaviour of the real joint. This can be achieved using the physical and elastic properties of PBT GF30 obtained after exposures to different temperatures (proposed for laser welding in the work of Silva et al.) shown in **Table 2**. Furthermore, the curves shown in **Figure 10** provide the deformation and stress in the plastic zone of PBT GF30 and were also used to model the elastoplastic behaviour of this material, detailing the behaviour of PBT GF 30 in three different states: "As received", "Treated at 225ºC", "Treated at 237ºC" and "Treated at 257ºC".

Table 2 – Main physical and mechanical properties of PBT GF30 in different states

Material [PBT GF30]	Young´s modulus [MPa]	Poisson ratio	Density [g/cm^3]
As received	8398	0.45	1.31
Treated at 225°C	5317	0.42	1.31
Treated at 237°C	5183	0.42	1.31
Treated at 257°C	4826	0.42	1.31

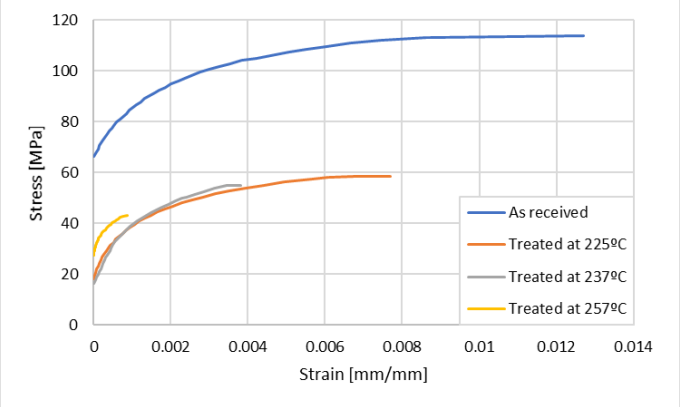


Figure 10 – Experimental curves representing the plastic region of PBT GF 30. Adapted from [].

Further using the ductile damage enabled numerical model previously developed by the authors, Table 3 shows the failure deformations, triaxialities, deformation rates and displacements up to failure for the implementation of ductile damage. Finally, Figure 17 illustrates the stress and strain curves in the plastic regions of the materials, detailing the characteristics of PBT GF 30 in three different states: "As received", "Treated at 225ºC", "Treated at 237ºC" and "Treated at 257ºC".

Table 3 - Properties of the PBT GF30 for implementing ductile damage.

Material	Fracture strain [mm/mm]	Stress triaxiality	Strain rate [s^{-1}]	Displacemnt at failure [mm]
As received	0.011492123	-0.33	0	0.001
Treated at 225°C	0.006559261	-0.33	0	0.001
Treated at 237°C	0.003570756	-0.33	0	0.0007
Treated at 257°C	0.000821712	-0.33	0	0.0007

Following the refinement of the characterization of the gradient of the PBT GF30 weld carried out through characterization by Raman spectroscopy, it is possible to establish the percentage of the welded zone which follow a given material behaviour (stemming from exposure to a given temperature range), resulting in the gradient of mechanical properties at the three temperatures under study shown in Table 4.

Table 4 - Representative percentages of the mechanical properties within the weld zone.

External layer	Middle layer	Internal layer
Treated at 225°C	Treated at 237°C	Treated at 257°C
61.60%	15.40%	23%

4.1. **Microscopical analysis**

In order to characterize the cross-section geometry and to measure the effective length of the weld, a micrographic analysis was carried out for the lap joint (**Figure 11**) and the butt-overlap joint (**Figure 12**).

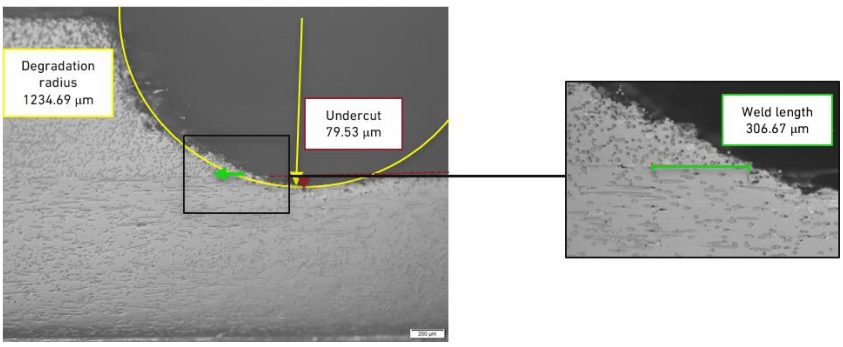


Figure 11 – Geometrical characterization of the weld in the purely overlapping configuration.

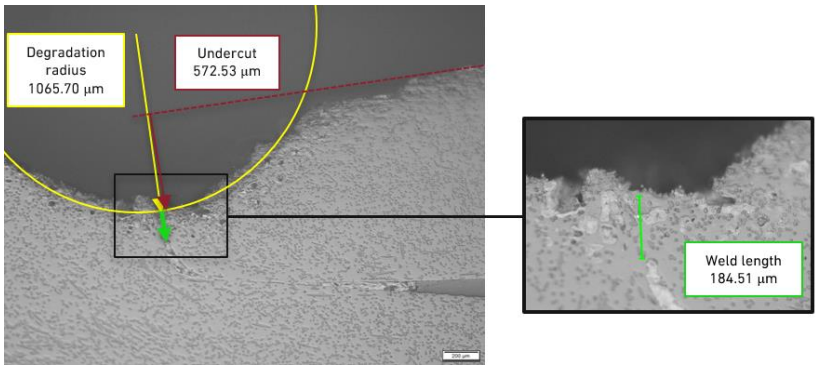


Figure 12 – Geometrical characterization of the weld in the butt-overlap configuration.

This exercise also shows that while the effective weld length for the purely overlapped joint is higher, the undercut is also significantly higher, which justifies the low performance of this joint. The degradation radius stemming from exposure to laser beam is quite similar, which is also expectable, given that the same welding parameters were used for both cases.

4.2. **Modeling details**

The models of the joint were generated in Abaqus, using the geometric measurements presented in **Figure 11** and **Figure 12**, using the percentual distributions of the mechanical properties shown in **Table 4**. The model for the purely overlapped configuration is shown in **Figure 13-a** while **Figure 13-b** shows the butt-overlapped configuration, highlighting the different properties applied to different regions around the welded area.

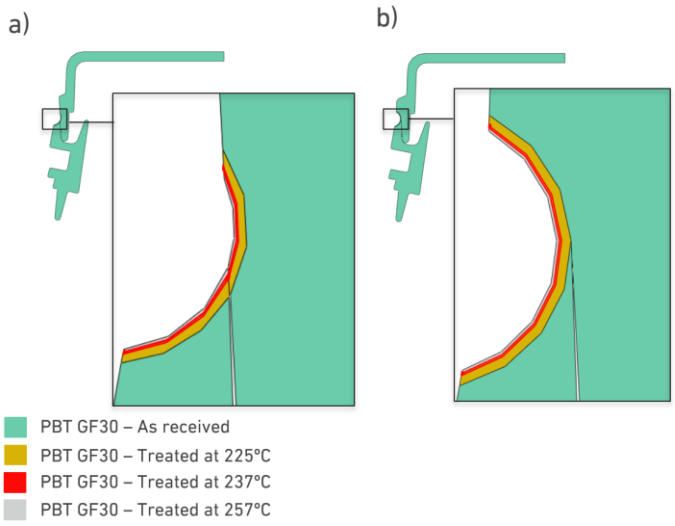


Figure 13 – Representation of distribution of different material properties along the join. a) Overlap joint and b) Butt-overlap joint.

Once the properties were defined, the boundary conditions for the simulation of the joints were configured. In both configurations, the upper zone (male part) was fully fixed with an encastre, with an imposed movement to the female part, as shown in **Figure 14-a**.

In what concerns the element size, the joint generally meshed with 0.5 mm elements and refined in the welding zone with 0.005 mm elements, both in the layers with the different properties (corresponding to different exposures of the material to temperature) and in the regions adjacent to these layers shown in **Figure 14-b**.

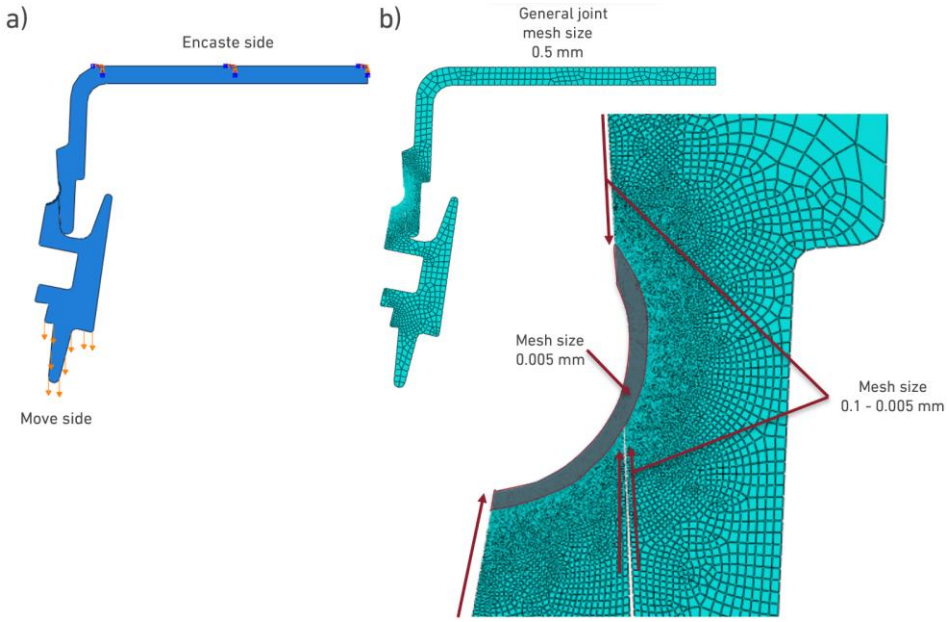


Figure 14 – Schematic representation of the joint model. a) Boundary conditions and b) Mesh size.

5. Numerical results

To validate the model, the simulation was run for both configurations. The numerical results for the model for the purely overlaped configaration are shown in **Figure 15**, where the dotted line represents the numerical model results.

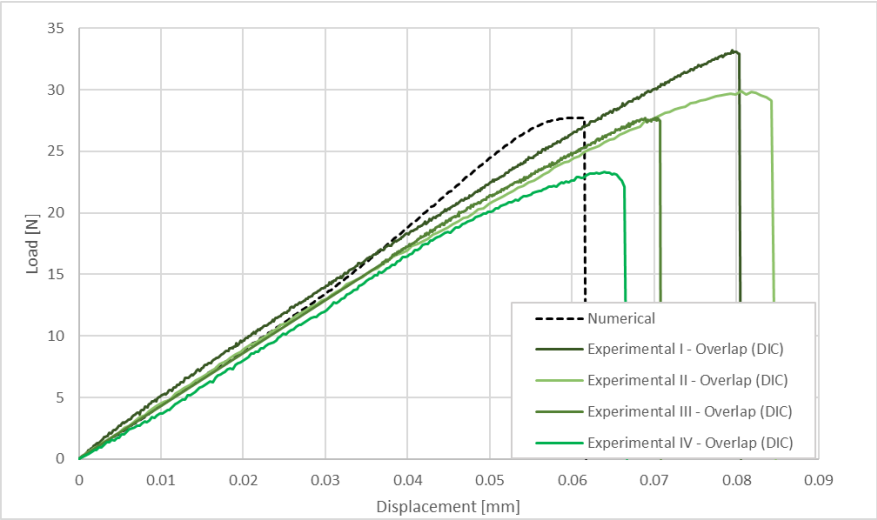


Figure 15 – Comparison between experimental load-displacement curves (corrected by DIC) and numerical curves for the purely overlap configuration

The numerical model for the overlapped joint has good agreement with the experimental data for both the maximum strength and the displacement at failure. Analysing the fracture process (**Figure 16**) for the joint in the purely overlapped configuration, it is noticeable that there is an asymmetry in the stress field, showing a concentration of stress on the right side at the bottom, stemming from the greater shear stress generated in that region of the joint.

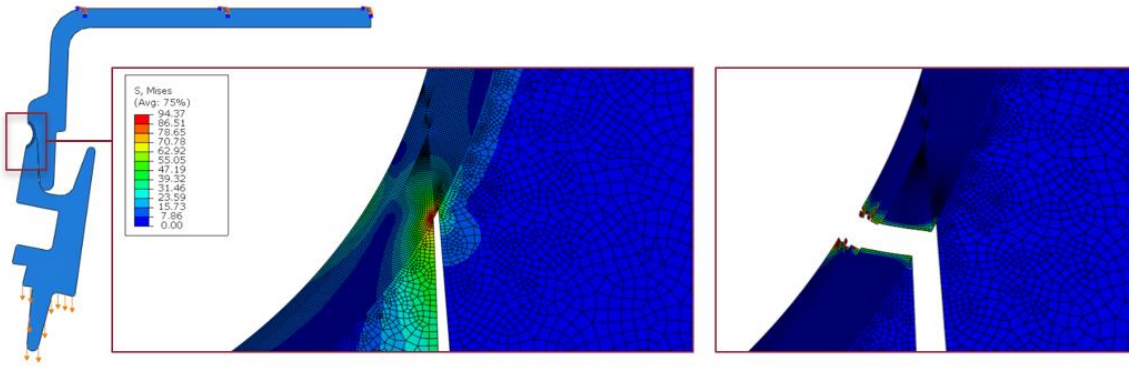


Figure 16 – Numerical characterization of the von Mises stress field before failure and representation of the failure mode for the purely overlapped configuration.

Comparing the numerical simulation for the butt-overlap joint with the experimental results shown in **Figure 17**, the failure load has a good level of agreement. However, the displacement expressed in the simulation is slightly lower than the displacement of the experimental curves.

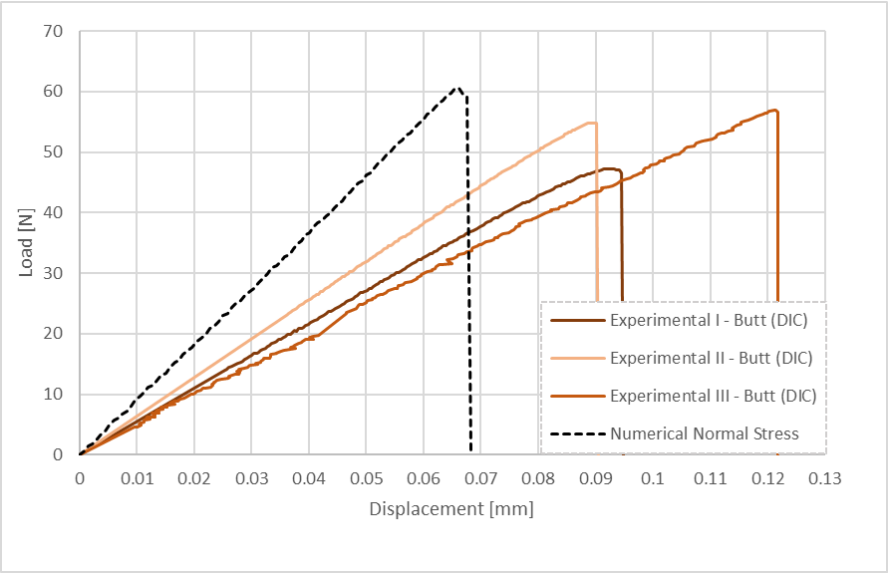


Figure 17 – Comparison between experimental load-displacement curves (corrected by DIC) and numerical curves for the butt-overlap configuration

The damage in the model for the butt-overlap joint is driven by stresses acting mostly in the normal direction, exhibiting a typical crack opening process. This is due to fact that there is a more symmetrical stress field at the crack tip, as shown in **Figure 18**. In fact, in addition to supporting a large amount of load through shear, the same joint is also able to support normal strength, delating damage and crack formation, explaining the increased performance over the purely overlapped joint.

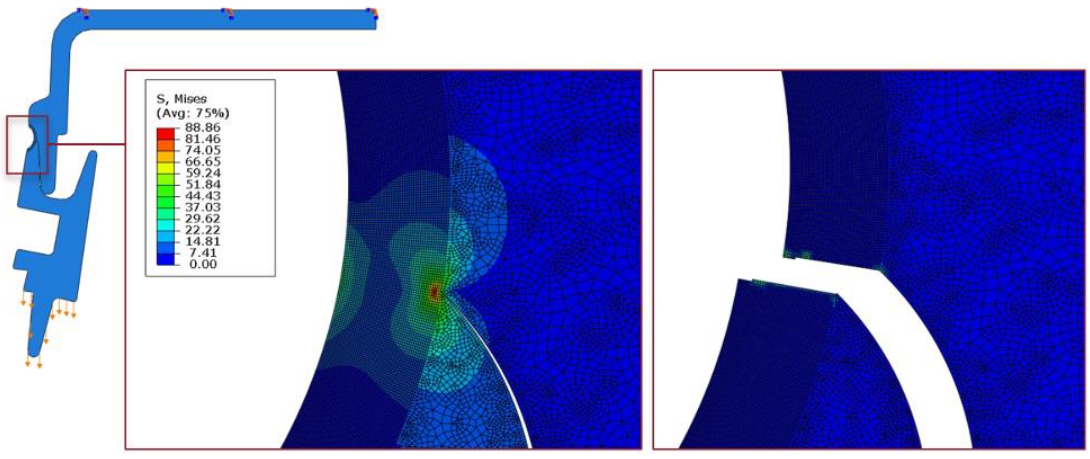


Figure 18 – Numerical characterization of the von Mises stress field before failure and representation of the failure mode for the butt-overlap configuration.

6. Conclusions

The feasibility of laser welding as a viable joining technique for PBT GF30 components, commonly employed in automotive electronical housings, has been successfully demonstrated. The process was found to be an effective method, resulting in successful component joining. DIC was shown to be a robust method for assessing the performance of these joints, providing accurate and reliable displacement data. Furthermore, a significant observation emerged: laser-welded joints incorporating overlapped and butt configurations outperformed purely overlapped configurations. This enhancement in joint strength can be attributed to the higher normal stress experienced by the material relative to shear stress. Furthermore, the employed elastoplastic numerical models, which incorporated ductile damage formulation, demonstrated satisfactory convergence in both scenarios under analysis, especially in what concerns the failure load prediction. This finding underscores the potential applicability of these models to real-world joint scenarios, offering valuable insights into the mechanical behaviour of the joints. To further optimize the welding process for these specific applications, future research should prioritize the evaluation of pulse frequency and advance rate of the laser, aiming to maximize joint strength. Additionally, exploring the potential of robotization in the process could significantly enhance efficiency and precision, leading to improved overall performance and reduced production costs.

Conflicts of interest

The authors declare that there exists no competing financial interest or personal relationships that could have appeared to influence the work reported in this paper.

Funding

No funding was obtained for this study

References

1. Taub, A., et al., *Materials for automotive lightweighting.* Annual Review of Materials Research, 2019. **49**: p. 327-359.
2. Begum, S.A., A.V. Rane, and K. Kanny, *Applications of compatibilized polymer blends in automobile industry*, in *Compatibilization of Polymer Blends*. 2020, Elsevier. p. 563-593.
3. Patil, A., A. Patel, and R. Purohit, *An overview of polymeric materials for automotive applications.* Materials today: proceedings, 2017. **4**(2): p. 3807-3815.
4. Olhan, S., V. Khatkar, and B. Behera, *Textile-based natural fibre-reinforced polymeric composites in automotive lightweighting.* Journal of Materials Science, 2021. **56**(34): p. 18867-18910.
5. Patel, M., et al., *Lightweight composite materials for automotive-a review.* Carbon, 2018. **1**(2500): p. 151.
6. Pervaiz, M., et al., *Emerging trends in automotive lightweighting through novel composite materials.* Materials Sciences and Applications, 2016. **7**(01): p. 26.
7. Borges, C.S., et al., *Effect of water ingress on the mechanical and chemical properties of polybutylene terephthalate reinforced with glass fibers.* Materials, 2021. **14**(5): p. 1261.
8. Mortazavian, S. and A. Fatemi, *Tensile and fatigue behaviors of polymers for automotive applications: Zähigkeits-und Ermüdungsverhalten von Polymeren für Automobilanwendungen.* Materialwissenschaft und Werkstofftechnik, 2015. **46**(2): p. 204-213.
9. Niu, L., et al., *Study on the synergetic fire-retardant effect of nano-Sb2O3 in PBT Matrix.* Materials, 2018. **11**(7): p. 1060.
10. Mu, B., et al., *Tribological and mechanical properties of PBT composites with microcapsules and potassium titanate whiskers.* Polymer Engineering & Science, 2019. **59**(3): p. 490-499.
11. Pegoretti, A., *Towards sustainable structural composites: A review on the recycling of continuous-fiber-reinforced thermoplastics.* Advanced Industrial and Engineering Polymer Research, 2021. **4**(2): p. 105-115.
12. Silva, L., E. Marques, and L.F. da Silva, *Polymer joining techniques state of the art review.* Welding in the World, 2021. **65**(10): p. 2023-2045.
13. Borges, C., et al., *A strain rate dependent cohesive zone element for mode I modeling of the fracture behavior of adhesives.* Proceedings of the Institution of Mechanical Engineers, Part L: Journal of Materials: Design and Applications, 2020. **234**(4): p. 610-621.
14. Kagan, V. and G. Pinho, *Laser transmission welding of semicrystalline thermoplastics-part II: Analysis of mechanical performance of welded nylon.* Journal of reinforced plastics and composites, 2004. **23**(1): p. 95-107.

Appendix F

Additional paper 1 : Raman microspectroscopy applied in the characterization of the properties of the weld in PBT GF 30 with numerical validation

Raman microspectroscopy applied in the characterization of the properties of laser welded PBT GF 30 with numerical validation

L. R. R. Silva[1,3], E. A. S. Marques[1], R. J. C. Carbas[2], A. Q. Barbosa[2], A. Guedes [4], Lucas F. M. da Silva[1,2]

[1]Departamento de Engenharia Mecânica, Faculdade de Engenharia, Universidade do Porto, Rua Dr. Roberto Frias, 4200-465 Porto, Portugal

[2]Instituto de Ciência e Inovação em Engenharia Mecânica e Industrial (INEGI), Rua Dr. Roberto Frias, 4200-465 Porto, Portugal

[3]Instituto Federal de Educação, Ciência e Tecnologia do Espírito Santo (Ifes), Rodovia BR Norte Km 58, São Mateus, 101 - Litorâneo, ES, 29932-540, Brasil

[4] Departamento de Geociências, Ambiente e Ordenamento do Território da Faculdade de Ciências and Instituto de Ciências da Terra-Pólo Porto, Universidade do Porto, Rua do Campo Alegre s/n, 4169-007, Porto, Portugal

Abstract

Automotive electronics demand compact, robust sealing solutions. Laser welding of fiber-reinforced polymer matrixes offers a promising approach to solve this challenge. This research aims to optimize a numerical model of a laser-welded joint, based on the Raman microspectroscopy characterisation of the properties of a glass fibre reinforced polymer. The study was developed considering autogenous overlapped joints, of the fillet type at the ends, with Polybutyleneterephthalate with a 30% glass fibre reinforced (PBT GF30) as the substrate material, welded by the laser welding process. The spectra of melted and solidified PBT GF30 material at three different temperatures was compared. This data was used to construct a numerical model with variable mechanical properties along the transverse region, using optical microscopy for geometry. The performance was compared with the results of the tensile test of the joints showing good convergence with the failure process of the joint.

Keywords

Joining, PBT GF30, numerical model, laser welding, Raman microspectroscopy.

1. Introduction

With advancements in technology and the increasing demand for lighter, more efficient components, it becomes imperative to invest in the development of advanced joining processes to optimize final product performance. High-technology industries, such as aerospace and automotive, have responded by investing in the development of mechanically and thermo-chemically resistant materials. The integration of composite materials and the use of dissimilar materials in structural components necessitates the selection of optimal joining methods that transcend traditional techniques like welding and riveting. These traditional methods often prove inadequate or inapplicable to modern materials. Therefore, the need to optimize joining techniques, that traditionally were not applied in the industry, arises [1-4]. Silva (2021) [5] cites that, among the dozens of joining processes, laser welding has stood out in the market because it provides monolithic joints, with less variation of properties. This technique allows to produce high quality joints, in a flexible manner, maintaining tightness, high productivity, with a great visual finishing [6-8].

In automotive electronic applications, the laser welding process is increasingly being implemented, as it improves the finishing of enclosures that store boards and electrical circuits of the controls for the general equipment. According to Zhao (2019) [10] and Wang et. al. (2015) [11] PBT GF30 is one of the main polymers in the selection of these enclosures, since it can be moulded in complex shapes, besides having high mechanical strength and also good thermal properties [12-15].

In a study conducted on transparent PBT GF30 made by Frick et al. (2018) [16], analysed only the optical properties stating that it can be used for laser welding when additive and reinforcing fibres are used. Silva et. al. (2021) [5], conducted a research of

characterization of the properties of absorbent PBT GF30 after thermal cycles at temperatures characteristic of the component, prospecting the analysis of weldability performed by the laser welding process, suitable for joints where the joint is made on the outside. This work also validates the properties in numerical models, aiming to apply the same properties in models of welded joints.

Based on preliminary results of laser welding in overlapped joints of PBT GF30, Silva et al (2022) developed a numerical model that validates the optimisation of the laser beam position in the welded joint, simulating the weld as a heterogeneous region. Confirming the weldability of absorbent PBT GF30, Silva et. al. (2022) [6] conducts the analysis on the optimization of laser welding process parameters in PBT GF30 joints and proves that the weld property is not heterogeneous, with the need for further study, since there is a gradient of properties in the weld.

In order to better understand the characteristic of the melt zone, due to its heterogeneity according to the thermal cycle, and based on the studies of Ishak et al. (2000) [17], Schaaf et al. (2014)[18] and Showaib et al. (2020) [19] a SEM analysis was performed on PBT GF 30. This analysis was performed aiming at the characterization of the chemical composition of the matrix and the reinforcement fibre. This also sought to identify possible changes of the chemical composition with the effect of thermal treatment, aiming to predict characteristic of the weld melted zone.

In addition to this, taking based on the studies done by Mermoux et al. (2018) [20] and Ta et al. (2021) [21] where a Raman spectroscopy analysis is performed to analyse the variation of materials and their chemical bonds by comparing the spectra from the variation of the altered properties due to the temperature effect. Both conclude the possibility of characterising the material based on qualitative analysis of the spectra with the influence of temperature.

This research aims to optimise the simulation of the joining process by laser welding in 30% glass fibre reinforced polybutylene terephthalate (PBT GF30), providing a gradient in the welding property and, at the same time, aiming to achieve a more qualitative response to the temperature effect on the component through the characterisation of PBT GF30 in the weld gradient by Raman microspectroscopy analysis, numerically validating the optimised experimental results of the laser welding process.

2. Experimental Procedure

2.1 - Materials and properties

For this research, PBT GF30 was used in three different states: as received, treated at different temperatures (225, 237 and 257 ºC). The material as received has the original properties of the material analysed in the work of Silva et. al. (2022) [5]. Table 1 presents the samples that were analysed in this research

Table 1 - Source of sample for Raman microspectroscopy.

Sample	*State*	*Density (g/cm^3)*	*Young's Modulus (MPa)*	*Poisson ratio*	*Reference*
1	As received	1.31	8398	0.45	Silva et. al. (2022)
2	Treated at 225°C	1.31	5317	0.42	
3	Treated at 237°C	1.31	5183	0.42	
4	Treated at 257°C	1.31	4826	0.42	

2.2 – Single lap joint test

In a study aimed at better laser spot welding efficiency of PBT GF30, Silva et. al (2022) [6] performed the optimization of static parameters such as laser diameter, incidence position, inclination angle, pulse time and power. As previously stated by Silva et. al (2022), the weld has a gradient of properties along the length between the laser incidence surface and the non-melted zone. To characterize the weld and its limitations in which properties change in this gradient, based on the properties of PBT GF30 received and treated in Table 1, it is hereby proposed to use Scanning electron microscopy with X-ray Microanalysis and Raman microspectroscopy to characterize the properties of the weld.

It was assumed that the PBT G30 treated at 257ºC is the outermost layer of the weld, since at this temperature the degradation of the material begins and the inner part of the weld is the beginning of the delimitation in which the material undergoes fusion and solidification, i.e., the beginning of PBT GF30 treated at 225ºC, which is the fusion temperature. The scheme presented in Figure 1 points the direction of the line of study of this work.

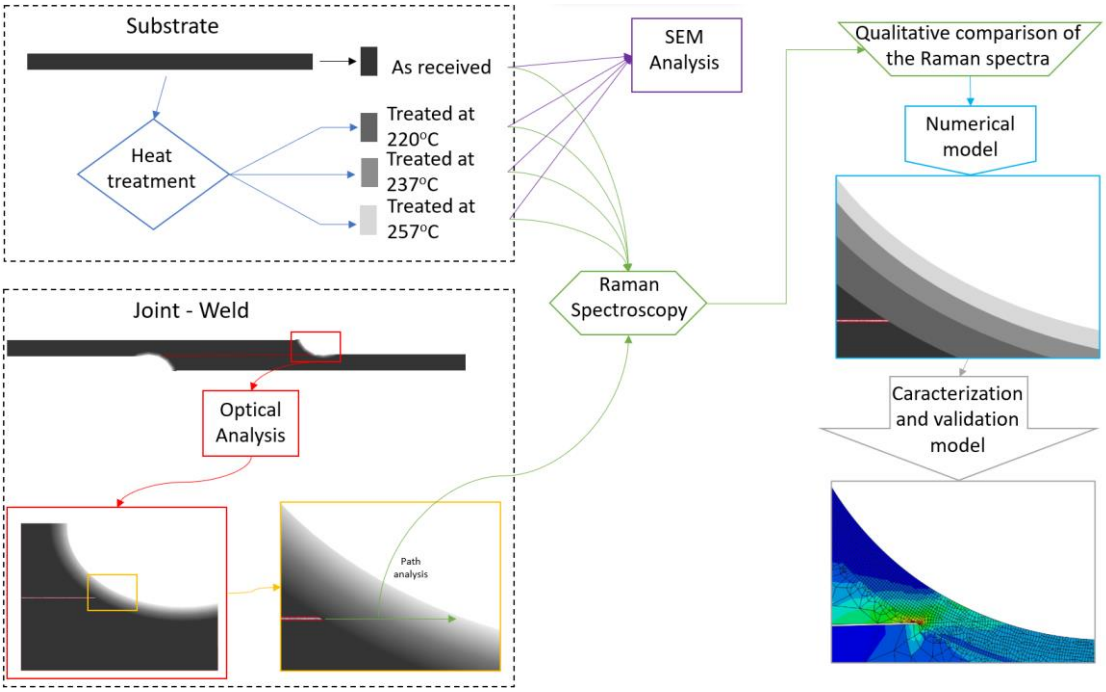


Figure 1 - Schematic diagram of the characterization and validation procedure of the optimized numerical model.

2.3 – Optical Microscopy

Optical microscopy was used to observe the weld bead and precept the surface preparation of the specimens to be used for Raman analysis. For this analysis a Carl Zeiss El-Einsatz HAL 100 was employed.

2.4 – Scanning electron microscope with X-ray Microanalysis

To better understand the influence of temperature on the interaction between the PBT matrix and the glass fibre, a Scanning electron microscope (SEM) with X-ray Microanalysis was performed, analysing the fracture surface of the conditions listed in table 1. These analyses were conducted at CEMUP (University of Porto, Portugal) using a JEOL JSM 6301 F/Oxford INCA Energy 350/Gatan Alto 2500 (Tokyo, Japan)

microscope. The samples were sputtered with an Au/Pd thin film for 120 seconds at 15 mA, using a SPI Module Sputter Coater.

2.5 - Raman microspectroscopy

Raman spectroscopy is a molecular spectroscopy technique that uses the interaction of light with the material to be analysed to determine its structure and chemical composition. The information provided by Raman spectroscopy is the result of a light scattering process and results in information about intra- and intermolecular vibrations providing additional understanding about a reaction. Thus, when analysing a material using Raman spectroscopy, it is very important the state of the surface to be analysed, since the analysis of a material's characteristics is more effective when the surface is perpendicular to the incidence of light. For this purpose, the surface to be analysed was sanded to obtain a better Raman characterisation, but also to quantify the weld region. The samples are passed through several sandpapers of different granulometry: 200, 340, 600, 800, 1200 mesh. On the welding sample, prior to grinding, a cut was made in the cross section of the weld bead. After the grinding process was complete, the samples were cleaned with ultrasound and compressed air to remove any remaining water and impurities.

Raman spectroscopy was performed on the GF30 PBT components at random points within the material, as mentioned in Table 1, to compare and characterize the reference base spectra of PBT. This spectroscopy analysis also sought to correlate the constituents of PBT GF30 and the mechanical properties stemming from the characterization of the autogenous weld performed by the laser welding process.

The characterization of the welded region followed a different procedure. In this regard, 14 equidistant points were analysed, scanning from the laser incidence surface (external zone of the weld) to the end of the weld length where there is the delimitation of the

material as received (internal zone) through a horizontal path parallel and adjacent to the joint plate interface. Once the spectra were obtained in the weld region and in the GF30 PBT components, two Raman shift intervals were randomly chosen in the spectra and the deconvolution of the observed bands performed for such intervals. Lastly, the position in the weld region where there is a transition between the characteristics of the treated PBT GF30 components was qualitatively classified. All Raman measurements were carried out using a LabRAM Microscope XploRA^{TM} from Horiba Scientific equipped with a Nd:YAG 532 nm laser as the excitation source.

3. Numerical details

The numerical model was developed using the optimized results of the laser spot welding process on PBT GF30 joints, performing this analysis on 1 mm thick plates, modelling the welded joint at the ends by fillet welding, with no addition of material, i.e. autogenous welding.

The weld, as described in the methodology used for the Raman microspectroscopy, is divided into three layers, from the surface to the interior. Thus, it presents the gradient of mechanical properties according to the components of PBT GF30 treated at temperatures of 257ºC, 237ºC, 225ºC and the substrate material as received that was not cast.

Since the numerical model had already been developed for a non-optimised homogeneous type weld, for this research, aiming at addressing the gradient of properties in the weld, i.e. heterogeneous weld, the behaviour used remains the same (elastoplastic), adding ductile damage.

4.1. **Elastoplastic and ductile damage model**

Lemaitre and Bouktir et al. [17, 18] present the elastoplastic model with ductile damage in a detailed way, starting from the concept of continuous damage mechanism (CDM), addressing the plasticity behaviour laws. The damage is introduced through the isotropic scalar degradation of the elastic property. Through this, the constitutive equation of the effective stress of the undamaged $\overline{\sigma}$ is presented, derived from the Cauchy stress tensor, σ equation 1.

$$\overline{\boldsymbol{\sigma}} = \frac{\boldsymbol{\sigma}}{1-d} \tag{1}$$

The scalar damage variable d, varying from 0 to 1 (with d = 0 for an undamaged material, and d = 1 for a fully damaged material), and is defined by the following relationship by equation 2. The variable S_d is the surface of defects (cavities and cracks), S_{eff} denotes the effective surface (undamaged surface), and S is the total surface.

$$d = \frac{S_d}{S} = 1 - \frac{S_{eff}}{S} \tag{2}$$

As stated by Pirondi et al. [19, 20] and also Sadhinoch et al. [19, 20], the effect of damage on elastic deformation is characterized by approaching that potential plastic deformation and damage can be separated. Accordingly, the set of constitutive equations for the damaged material can be defined according to Equations 3, 4, 5, 6 and 7, which represent, respectively the effective elastic deformation tensor ε_{ij}^{e}, the plastic deformation tensor $\varepsilon_{ij}^{p}$where F_p and the variables s_{ij} and X'_{ij} are deviating part of stress and kinematic hardening tensor, $f\left(\frac{\sigma_m}{\sigma_{eq}}\right)$ is the triaxility stress formed by hydrostatic stress $\sigma_m$and

equivalent stress $\_\sigma_{eq}$, the cumulative strain rate $\dot{r}$, having R stress due to isotropic hardening and plastic multiplier λ, finally the displacement-based damage $\dot{u}^p$.

$$\varepsilon_{ij}^{e} = \frac{1+\nu}{E}\frac{\sigma_{ij}}{1-d} - \frac{\nu}{E}\frac{\sigma_{kk}}{1-d}\delta_{ij} \tag{3}$$

$$\varepsilon_{ij}^{p} = \dot{\lambda}\frac{\partial F_p}{\partial \sigma_{ij}} = \frac{3}{2}\dot{\lambda}\frac{(s_{ij} - X'_{ij})}{\sigma_{eq}} \tag{4}$$

$$f\left(\frac{\sigma_m}{\sigma_{eq}}\right) = \frac{2}{3}(1+\nu) + 3(1-2\nu)\left(\frac{\sigma_m}{\sigma_{eq}}\right)^2 \tag{5}$$

$$\dot{r} = -\dot{\lambda}\frac{\partial F_p}{\partial R} = \dot{\lambda} = p(1\dot{-}d) \tag{6}$$

$$\dot{u}^p = L\varepsilon_{ij}^{p} \tag{7}$$

4.2. **Double fillet lap joint test**

To validate the joint using the optimized welding parameters, layers with different properties were applied to the weld in two dimensions using the Dynamics Explicit model, featuring an elastoplastic behavior with ductile damage. The step was configured with a time period of 1 second, with the aid of the activated non-linear configuration. The integration was based on a scale time factor of 1 s, with a scale factor of 10000 and target time increment of 10^{-10} s.

4.2.1. Geometry model

Measurements in the welded area, represented in Figure 5 and Figure 6, were used as a basis for the construction of the numerical model. A PBT GF30 plate separation of 6.25

µm, a weld length of 306.67 µm, a surface radius of curvature of 1234.69 µm and an undercut of 79.53 µm were used.

The geometry of the overlapped joint was based on Figure 2. The plates overlapped by a length of 20 mm and the measures of length, width and height respectively were 40 mm, 10 mm and 1 mm. Also presented in Figure 2 are the boundary conditions regarding the loading, encasement on the left side of the joint and the displacement on the right side, with only the degree of freedom in the xx direction set to 0.2 mm and the constraint of movement in the yy direction set to zero.

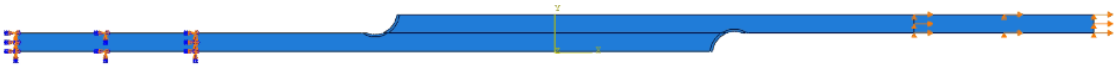


Figure 2 - Geometry and load scheme in the double single lap joint.

To configure the contact interaction between the plates, a friction coefficient of 0.2 [21] was set. Figure 3 illustrates, in a macro way, the welded joint, the layers in the weld and the size of the elements in the weld region. It should be noted that for the joint, generically, the elements were predefined with the size of 1 mm. Plane stress elements were used, of the CPS4R type.

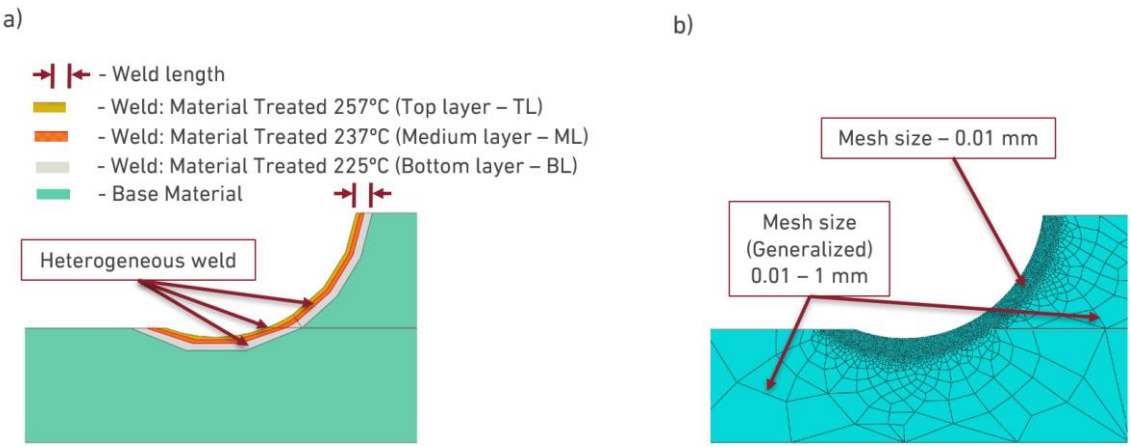


Figure 3 - a) Material partition of model showing weld layers and base material b) Refined mesh size configuration.

4.2.2. Material properties

The physical and mechanical properties of PBT GF30 used in the simulation were derived from the study performed by Silva (2021). Table 1 presents the material properties that supported the construction of the model for the purely elastoplastic simulation. For the elastoplastic simulation along with the damage, Table 2 shows the failure strains, triaxialities, strain rates and displacements until failure for the implementation of ductile damage. Finally, Figure 4 illustrates the stress-strain curves in the plastic regions of the materials, detailing the characteristics of PBT GF 30 as received and thermally treated at 225, 237 and 257 ºC. These results have been previously presented and discussed in Silva et. al (2022).

Table 2 - Properties of PBT GF30 for implementation of ductile damage obtained by Silva et. al (2022).

PBT GF30 state	Fracture strain [mm/mm]	Stress triaxiality	Strain rate [s^{-1}]	Displacement at failure [mm]
As received	0.011492123	-0.33	0	0.001
Treated at 225°C	0.006559261	-0.33	0	0.001
Treated at 237°C	0.003570756	-0.33	0	0.0007
Treated at 257°C	0.000821712	-0.33	0	0.0007

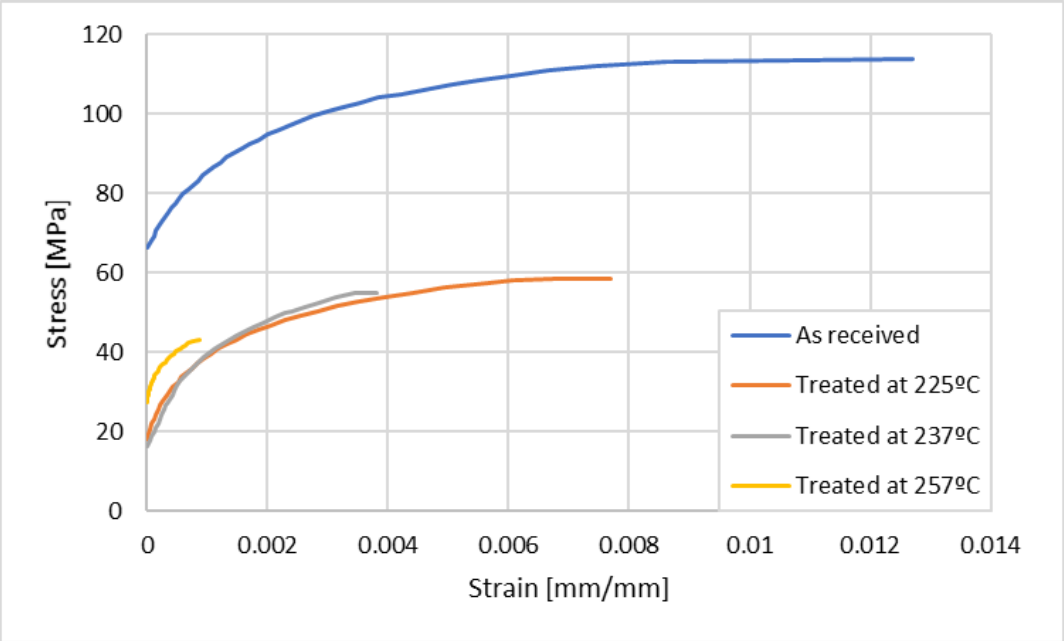


Figure 4 - Experimental curves representative of the plastic region of PBT GF 30 components obtained by Silva et. al. (2022) [5].

4. Experimental results

3.1 – *Optical Microscopy*

According to the analysis made of the welded joint, the effective weld length was 306.67 µm, as shown in Figure 5. Figure 6 a) shows, the effective welding zone in a more magnified view and the distinction between the PBT matrix and the glass fibres can be seen more clearly. The spacing between the top and bottom plates is also visible, measuring 6.25 µm. Figure 5 b) shows the lower plate undercut of 79.53 µm and Figure 5 c) shows a circular feature on the laser incidence surface of approximately 1234.69 µm. These measurements will be used to develop the numerical model of the welded joint.

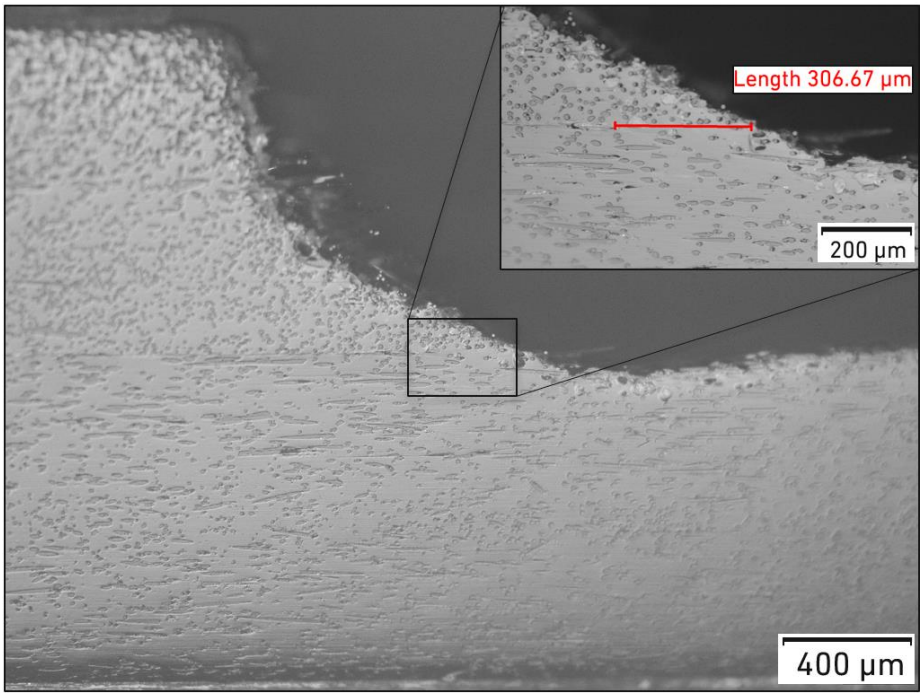


Figure 5 - Microphotograph in reflected light showing the welded area and measurement of the effective weld length.

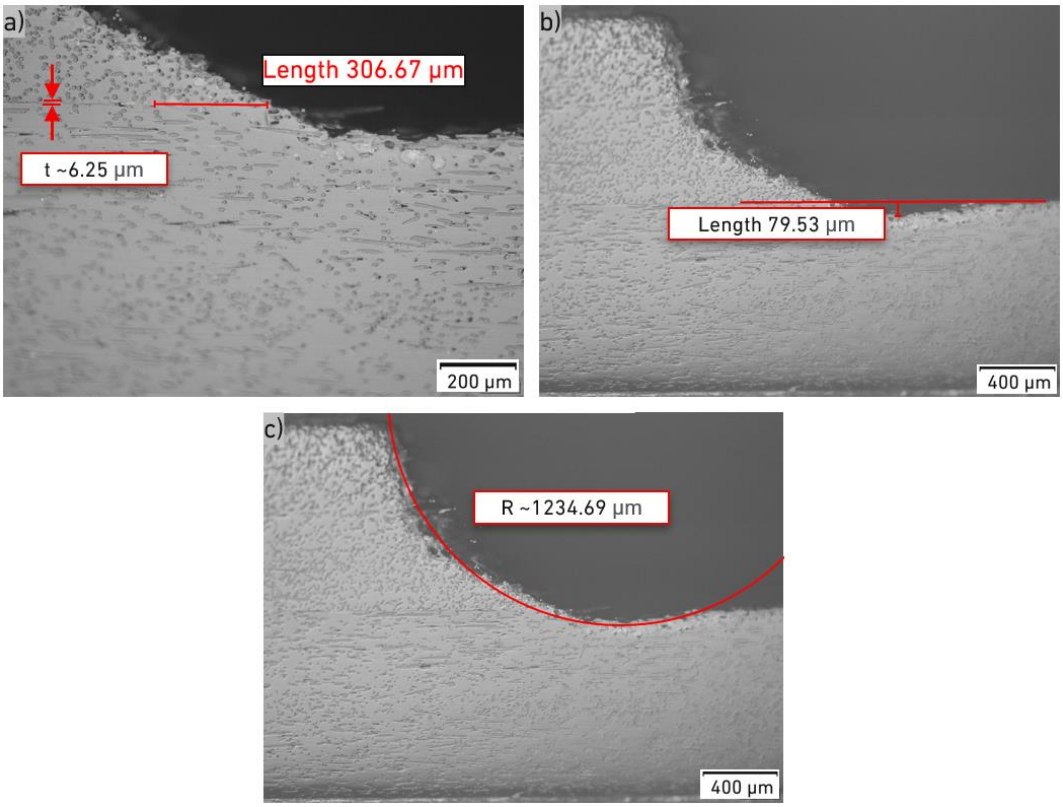


Figure 6 - Microphotograph of the welded area a) measurement of the effective weld length and of the spacing between the PBT GF30 plates, b) measurement of the undercut and c) measurement of the surface curvature radius.

3.2 – *Scanning electron microscopy results*

SEM analysis allowed to understand the influence of temperature on the interaction of the matrix with the fibres. The study was done for PBT GF30 as received, treated at 225ºC, treated at 237ºC and treated at 257ºC, along with their compositional spectra (X-ray microanalysis). In Figure 7, it is possible to observe the interaction between the matrix and the fibres in the as received state. It can be observed that the fibres present a smooth surface without a strong interfacial bond between the matrix and the fibres. In general, the matrix fracture is fragile. EDS spectrum 1 represents the elemental chemical composition of the matrix and spectrum 2 shows the elemental composition of the fibres. Polybutylene terephthalate ($(C_{12}H_{12}O_4)_n$) is composed of carbon, hydrogen and oxygen, so when you analyse its composition chemically by EDS you just get the peaks in oxygen and carbon. The remaining peaks are representative of the coating and their influence should be neglected. In the fibre, it is clear the predominant presence of silicon, pointing to silica (SiO_2) and the identification of other possible components such as $CaCO_3$, MgO, Al_2O_3, Wollastonite and Feldspar.

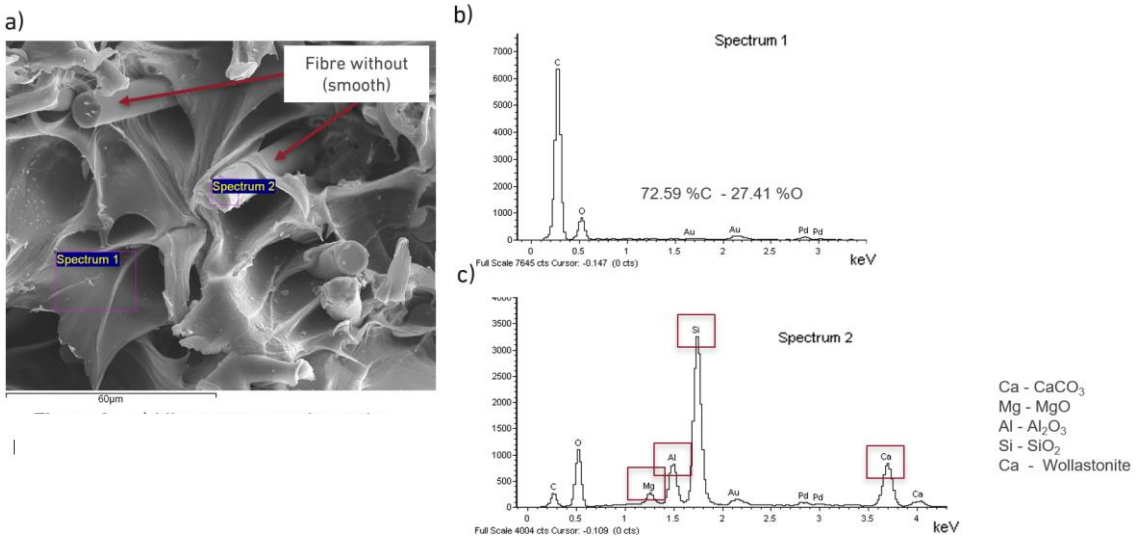


Figure 7 - a) SEM Microphotograph at the PBT-GF30 As received. b) PBT EDS spectrum and c) Fibre EDS spectrum.

In the other hand, when PBT is thermally treated at 225ºC, 237ºC and 257ºC, it is observed that the matrix and the fibres have a different behaviour, as represented in Figure 8, Figure 9 and Figure 10 respectively. For the GF30 PBT component treated at 225ºC there is an adhesive effect on the fibre surface, there is a fusion of the PBT matrix over the glass fibres, which leads to a deeper and stronger interfacial bond. This contamination effect is intensified when raising the treatment temperature to 237ºC, giving a characteristic of high roughness. For the treatment at 257ºC this characteristic of the matrix on the glass fibre is altered again, showing PBT plaques retained on the fibres.

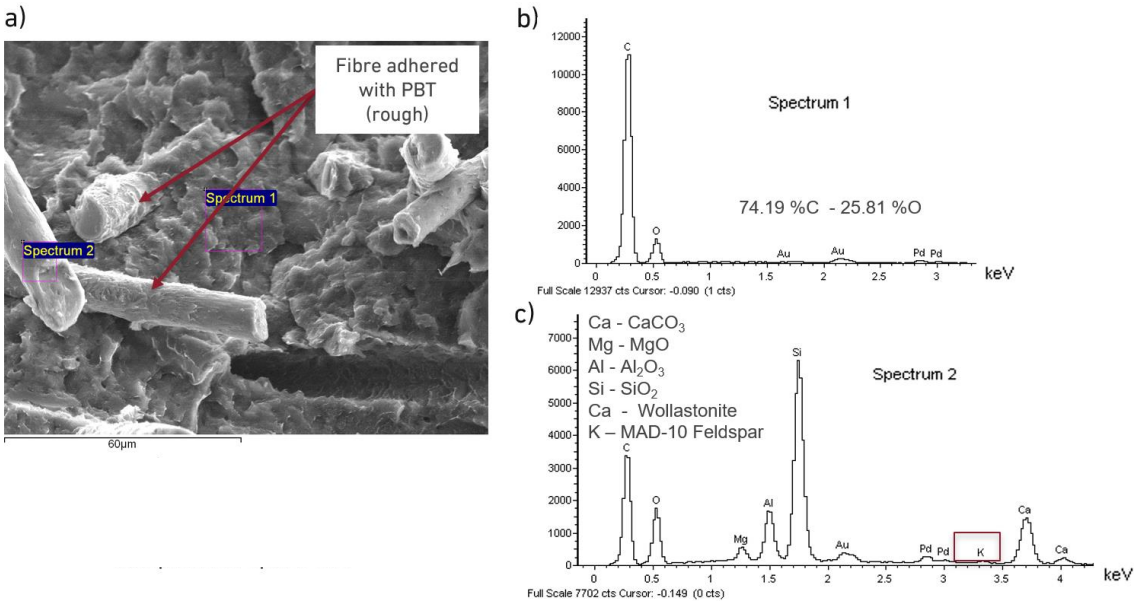


Figure 8 - a) SEM microphotograph of the PBT-GF30 treated at 225º. b) PBT EDS spectrum and c) fibre EDS spectrum.

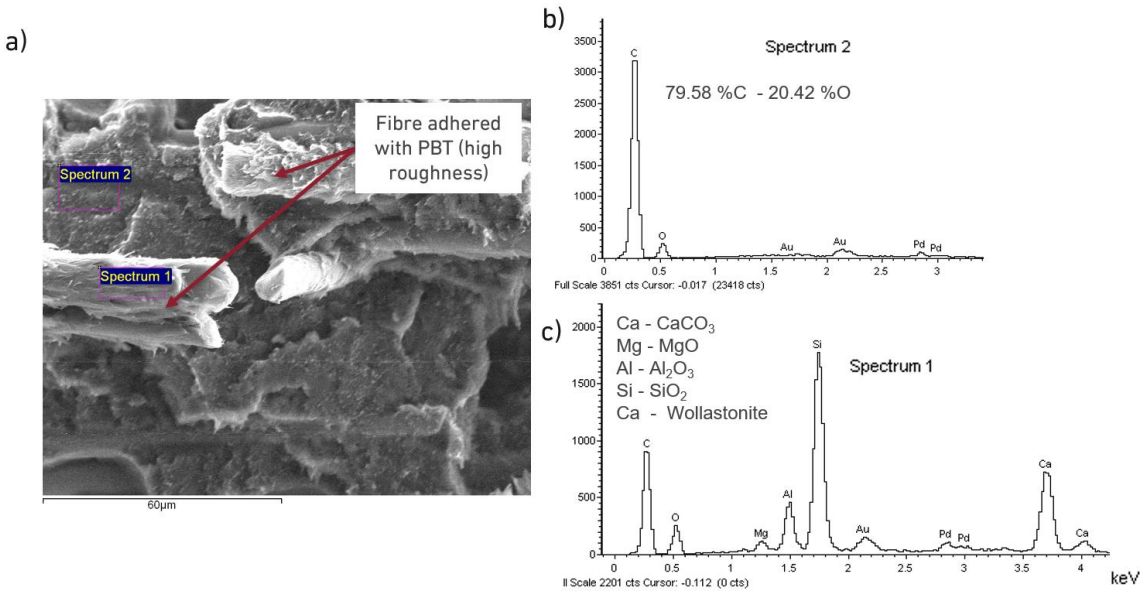


Figure 9 – a) SEM microphotograph of the PBT-GF30 treated at 237º. b) PBT EDS spectrum and c) fibre EDS spectrum.

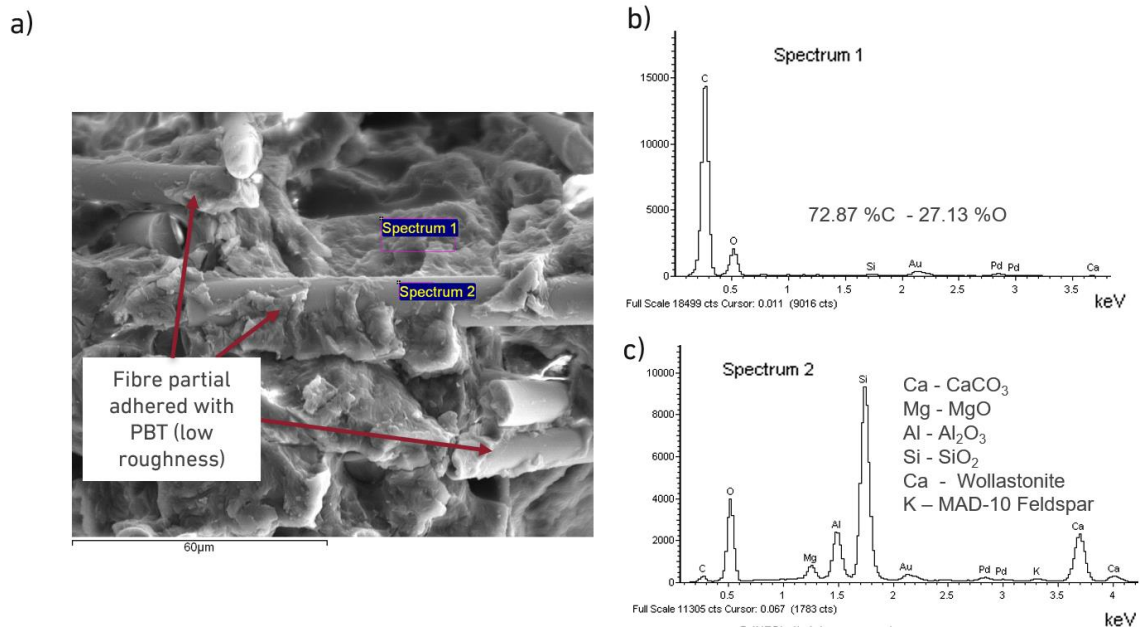


Figure 10 - a) Microscopy results at the PBT-GF30 treated at 257º. b) PBT composition spectrum and c) Fibre composition spectrum.

3.3 - Raman spectroscopy

The Raman analysis started with the study of the base material (PBF GF30) within the range 500-2000 cm^{-1}. To this end, the spectrum obtained was compared with those found for PBT in the literature (Agbenyega,1992). By analysing Figure 11, it is observed that there is a similarity between both Raman spectrum and the peaks are nearly coincident. The recurrent divergence between GF30 PBT spectrum and the spectrum of pure PBT is in the low defined peaks assigned to ring CH in plane bend or C-O (1110 cm^{-1}), ring CH in plane bend (1184 cm^{-1}) and Glycol C-H (def) (1456 cm^{-1}). On the opposite, there is a loss of the right shoulder of the peak located around approximately (1200 cm^{-1}) and assigned to Ring carbonyl (str), O-C- (str), Ring C-H in plane bend

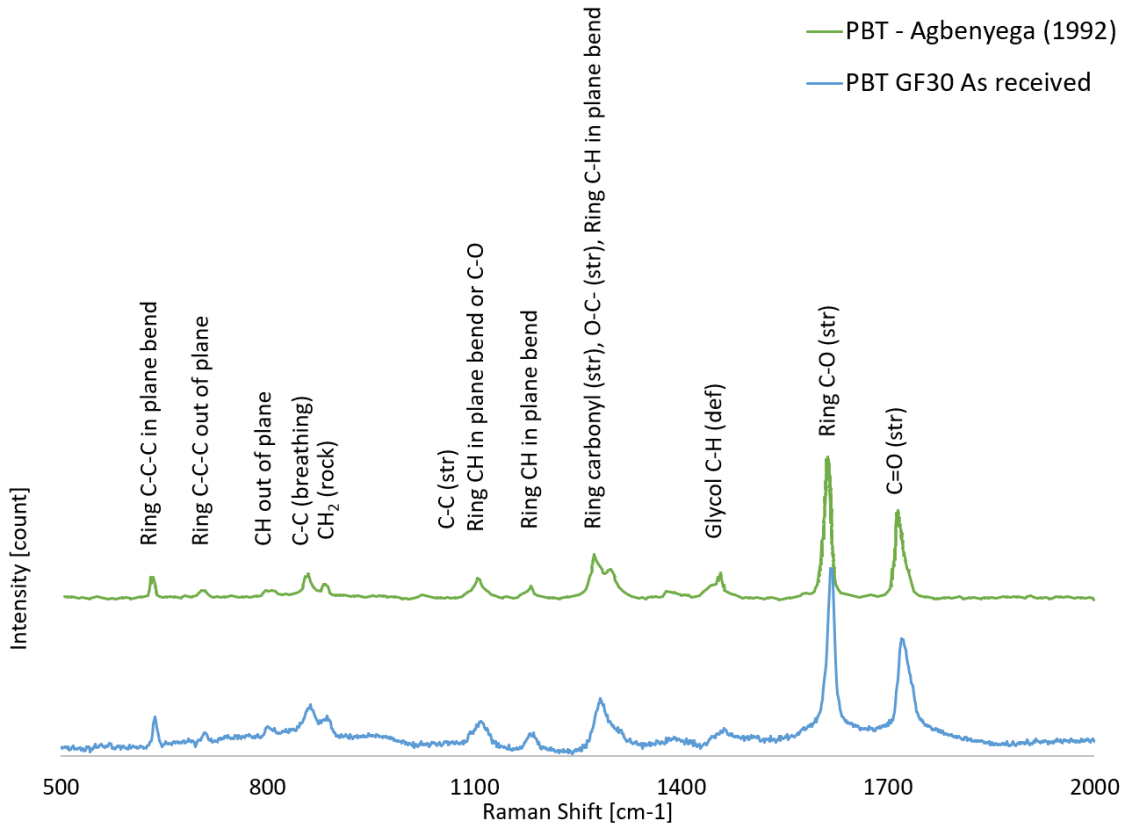


Figure 11 - Comparison between the Raman spectra of PBT obtained by Agbenyega (1992) (at the top) and GF30 PBT obtained experimentally (at the bottom).

When comparing the overall characteristics of the spectra, PBT GF30 shows a fluorescence that is not perceived in PBT. Doumeng et. al (2019) [16], reports very similar findings to those obtained in this research. These authors compare the spectra obtained between Polyether ether ketone (PEEK) and Polyether ether ketone reinforced with glass fibre (PEEK GF30). It is likely that this behaviour is due to the inclusion of glass fibre. After the identification of the main PBT peaks, the results obtained for the different thermal conditions under analysis were compared (see Figure 12). Comparing the PBG GF30 as received and the treated PBT GF30, a shoulder can be observed to the right of the 1722 cm^{-1} peak (C=O (str)) peak at . The pronounced formation of new bands is also noticeable, softening the peaks, as is the case of the peak at 639 cm^{-1} assigned to ring C-C-C in plane bend -, and the 862 cm^{-1} peak assigned to C-C (breathing) -. In parallel, the disappearance of the peak assigned to CH_2 (rock) at 890 cm^{-1} and finally a peak at 1471 cm^{-1} assigned to ring CH in plane bend - is observed, probably resulting by the interference of the medium in the solidification process, leaving changes at the interface between fibre and matrix, a characteristic that is pointed out in the SEM analysis specifically for PBT GF30 treated at 257ºC. On the other hand, the temperature change propitiates the formation of a shoulder on the left of the Ring CH in plane bend, observing more clearly the C-C (str), in the region between 922 and 1022 cm^{-1}.

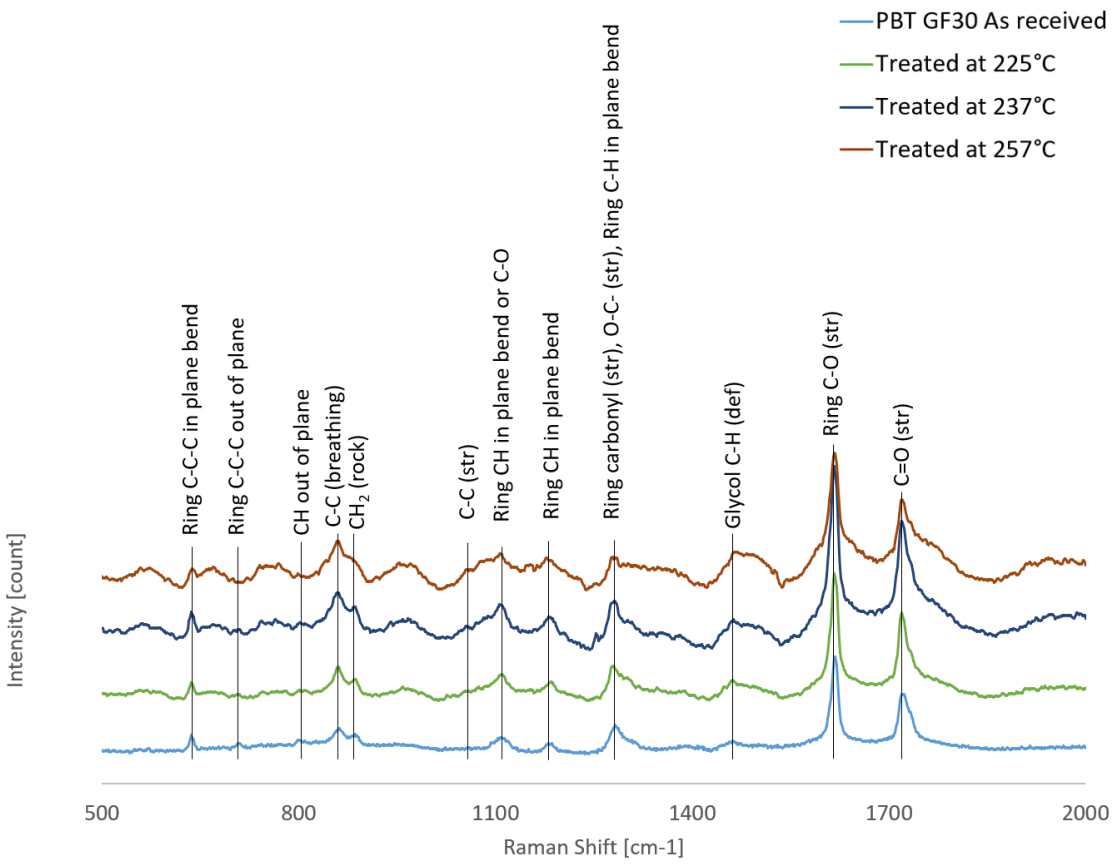


Figure 12 - Comparative PBT GF30 Raman spectra at different thermal conditions.

Once the GF30 PBT spectra were analysed for the different thermal conditions, the Raman spectroscopy analysis of the welded zone was performed. A full-length examination was performed along the length of the weld, analysing 14 equidistant points, considering the beginning of the measurement as 0% until the end of the measurement at 100%, as represented in Figure 133.

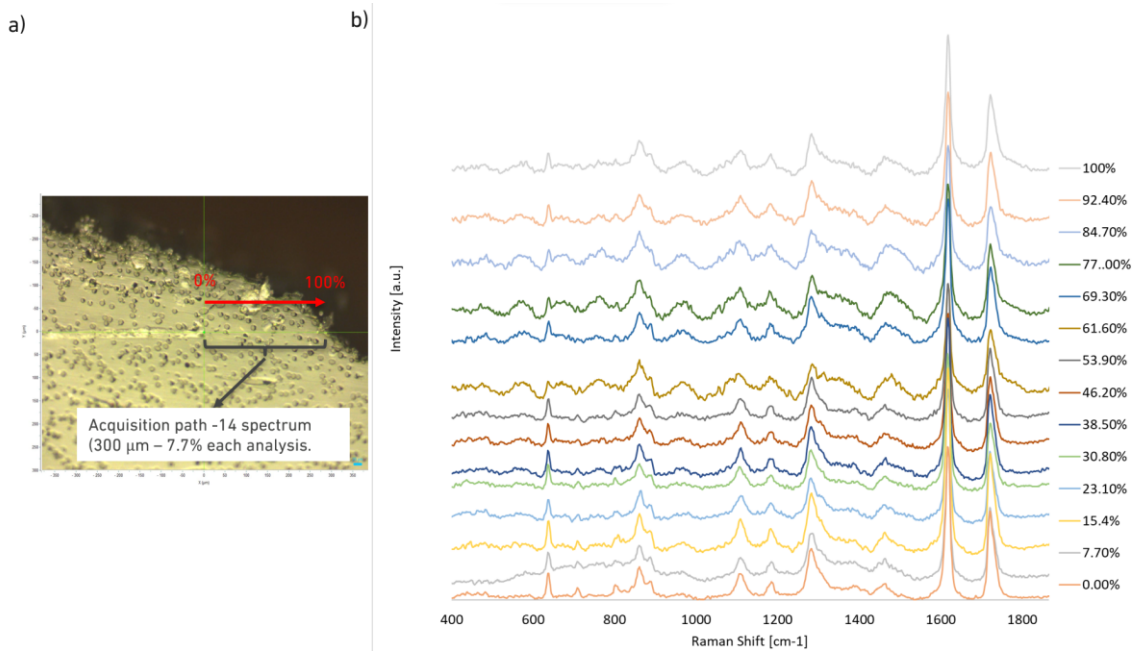


Figure 13 - a) Microphotograph of the Raman mapping scheme at the weld joint path. b) Raman spectra obtained through the acquisition weld path.

Comparing the analysis made along the sole zone with PBT in different thermal conditions the differences are not clear and therefore two spectral regions that had been previously specified in the comparison between the GF30 PBT components were randomly selected. Being the regions of the peak at 1722 cm^{-1}, with the particularity of the presence of a shoulder to the right side of the peak, appointed as region A1 from 1675 to 1865 cm^{-1} and a second region in which is pronounced the formation of a new band smoothing the peak at 862 cm^{-1} in parallel to the disappearance –the peak at 890 cm^{-1} appointed as region B1 from 819 to 909 cm^{-1}. In order to better perceive the differences between the spectra, the zones corresponding to A1 and B1 were zoomed in. Comparing the spectrum of the welded zone with the heat-treated PBT GF30 spectra, it is possible to gain a better understanding of the boundary area of the material.

By enlarging the spectra in these regions A1 and B1, shown respectively in Figure 14 and Figure 15, it is possible to compare the spectra of the weld and the spectra of the GF30

PBT components. This process allows a clear identification of the boundaries of the material in the weld zone.

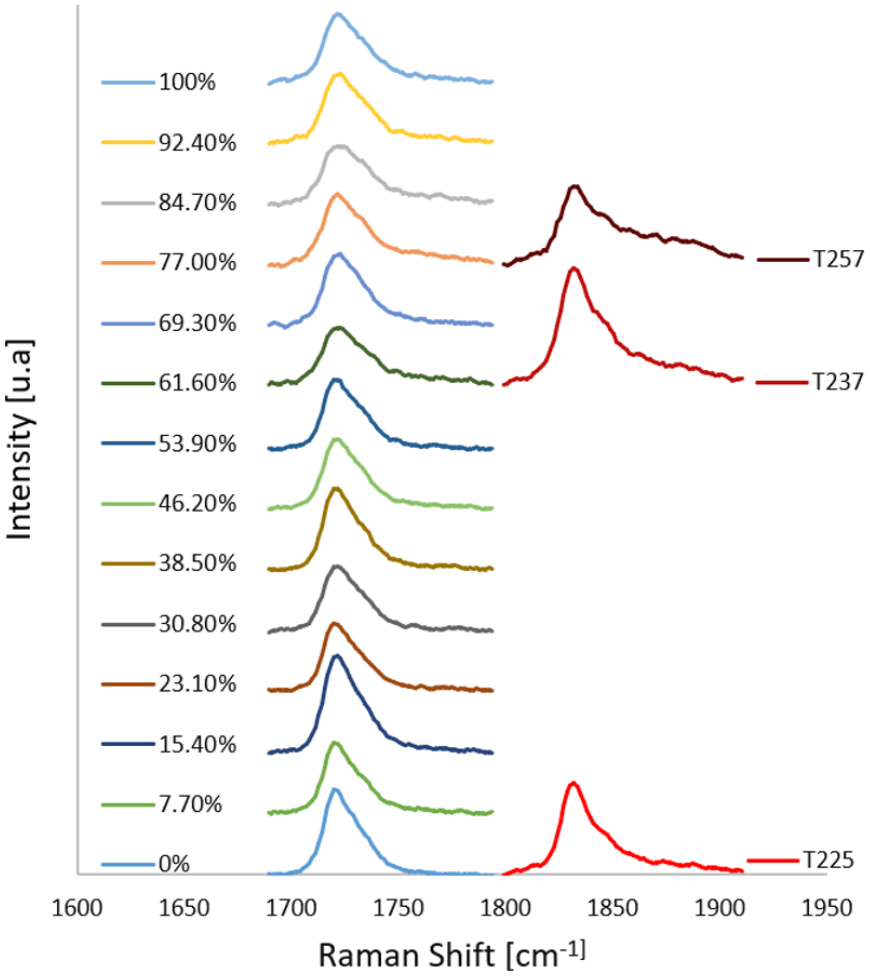


Figure 14 - Comparison between spectra obtained in scanning along the welded zone and the spectra for temperatures of 257, 237 and 225 ºC in A1 area.

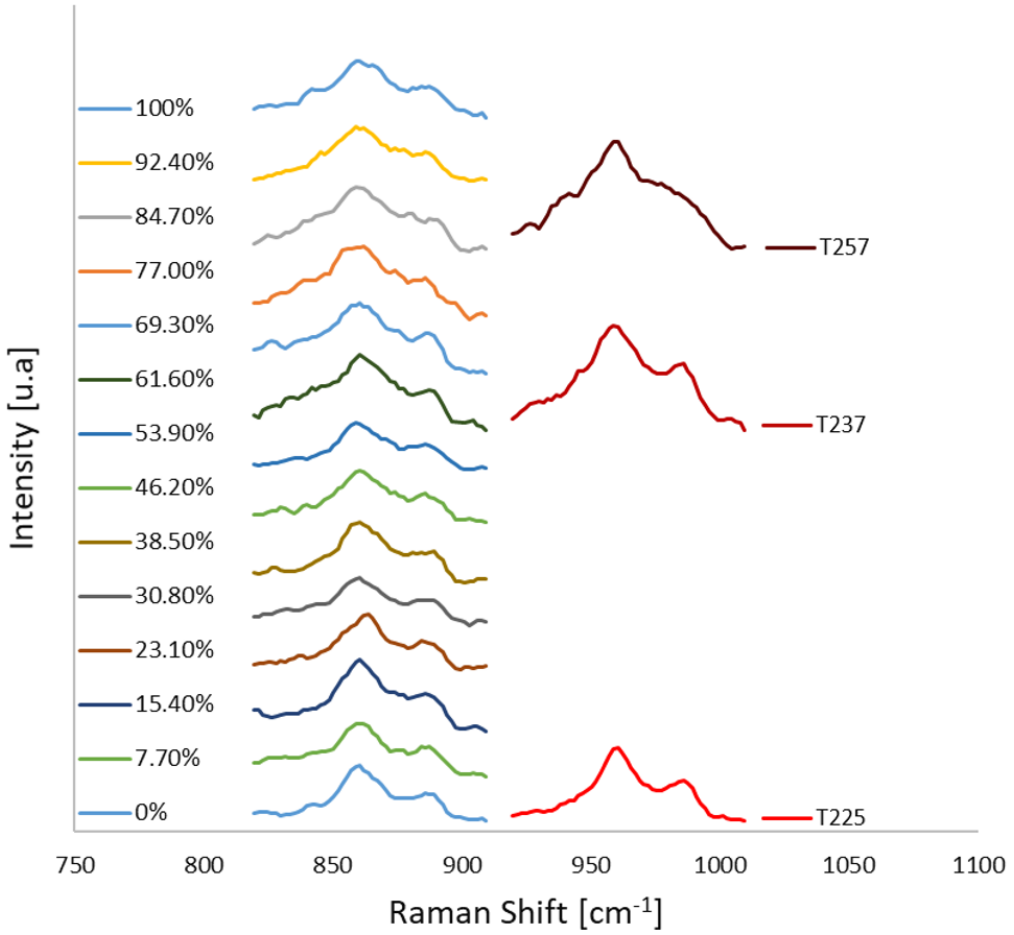


Figure 15 - Comparison between spectra obtained in scanning along the welded zone and the spectra for temperatures of 257, 237 and 225 ºC in B1 area.

Analysing the A1 and B1 zones, it is observed that there is a great similarity between the spectrum of the initial position (0%) with the spectrum obtained for the PBT GF30 treated at its fusion temperature of 225ºC. This feature is characteristic of the weld zone, where there is a boundary between the fused zone and the non-fused zone.

Analysing the similarity of the spectra for higher temperatures, especially in zone A1, it is observed that the spectrum obtained for 61.6% is quite similar to that obtained for PBTGF30 treated at 237 ºC. Since there is a more pronounced elongation of the base of the curve on the right side of the peak shown in Figure 14. The spectrum obtained for 77% is quite similar to that obtained for PBTGF30 treated at 257 ºC, noting the more intense shoulder formation on the right side of the peak in Figure 14.

Examining zone B1, it is observed that there is quite a high degree of similarity between the spectrum obtained for 61.6% and that obtained for PBT GF30 treated at 237 ºC Figure 15. The characteristic isosceles triangle is denoted, but with a slight protuberance on the right side of the peak. This protuberance to the right of the peak becomes less pronounced in the weld region at 84.7%, revealing a clearer similarity with the PBT GF30 component treated at 257 ºC. In order to improve the clarity of the results, the spectra were deconvoluted in these regions, both in the GF30 PBT (treated at different temperatures) and in the weld spectra. Figure 16 shows the analysis performed in region A1, in which the spectra were deconvoluted. Performing the comparisons regarding the curve fittings and the integrated intensity (area) of the bands of PBT GF30 at temperatures of 237ºC and 257ºC, it is noticeable that the greatest similarity happens respectively in the curves of 61.6% and 77.0% (Figure 166).

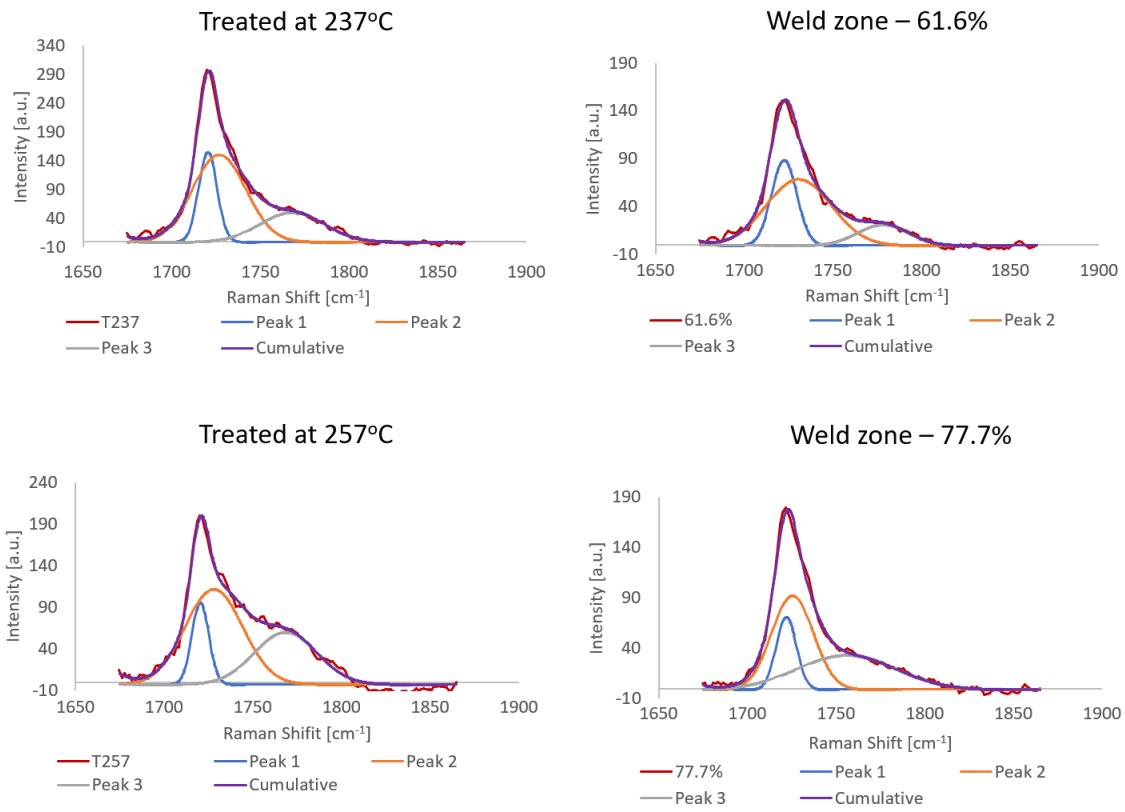


Figure 16 - Comparison between the deconvolutions of the spectrums in the PBT GF30 components and the weld zone in the A1 region.

For region B1 there is a slight change in the percentages, however the results are approximate, as shown in Figure 177. For the temperature of 237 ºC the spectrum with the most identical curve fitting and integrated intensity of the bands is 61.6% and for the temperature of 257 ºC the spectrum is in the percentage of 84.7% (Figure 177).

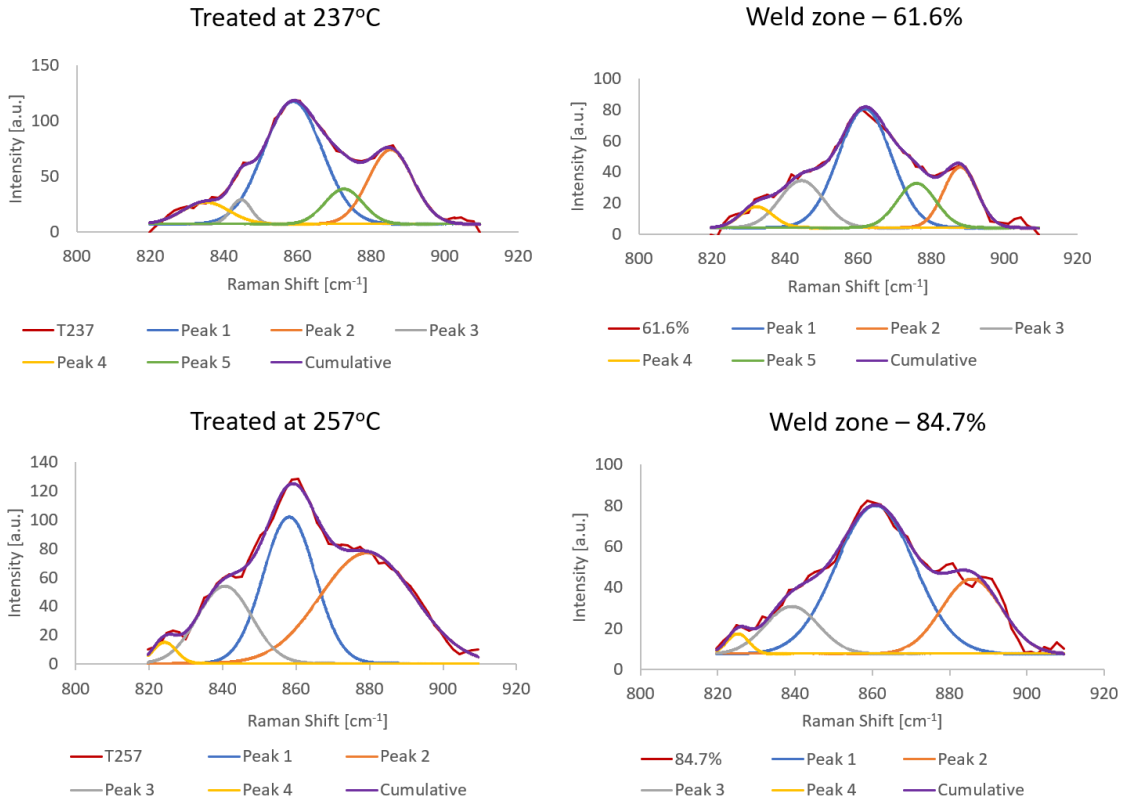


Figure 17 - Comparison between the deconvolutions of the spectrums in the PBT GF30 components and the weld zone in the B1 region.

Table 3 summarizes the results for the GF30 PBT composite gradient boundaries for both A1 and B1 regions.

Table 3 - Results of the layers boundaries at the weld area.

Regions	Substrate (PBT GF30 As received	Internal layer (PBT GF30 Treated at 225ºC	Middle layer (PBT GF30 Treated at 237ºC	External layer (PBT GF30 Treated at 257ºC
A1	Uncast material	61.6 %	15.4%	23%
B1	Uncast material	70%	23.1%	15.7%

5. Numerical results

For the validation of the numerical model, the welded zone layer divisions were simulated, with respect to the two regions characterized by Raman micro spectroscopy, as already presented in Table 3. The comparative results of the model with the experimental curves are shown in Figure 188.

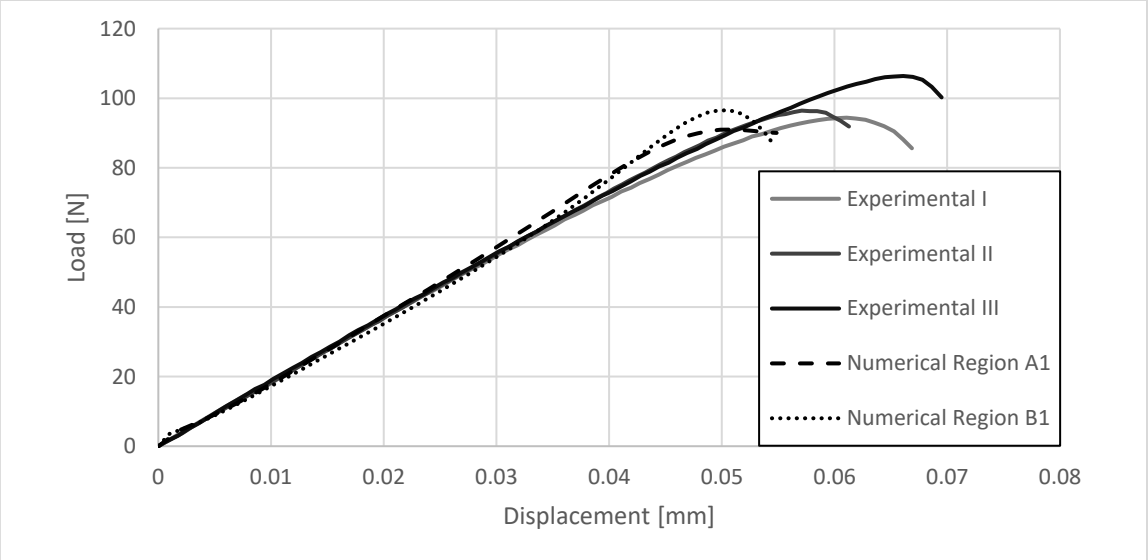


Figure 18 - Comparison of ductile damage numerical models between different layers and experimental results obtained by Silva et. al (2022).

The results point to a good degree of convergence, especially when comparing failure loads. The maximum relative error for this case was just 14.45 %.

When the displacement is analysed, there is a small divergence which can be explained by the presence of gaps and displacement of the elements in the tensile machine, since the joints are small with a small displacement of less than a tenth of a millimetre.

When comparing the fracture cross section of the experiment with the model fracture for the two modelled regions, a great degree of similarity is shown, as shown in Figure 199.

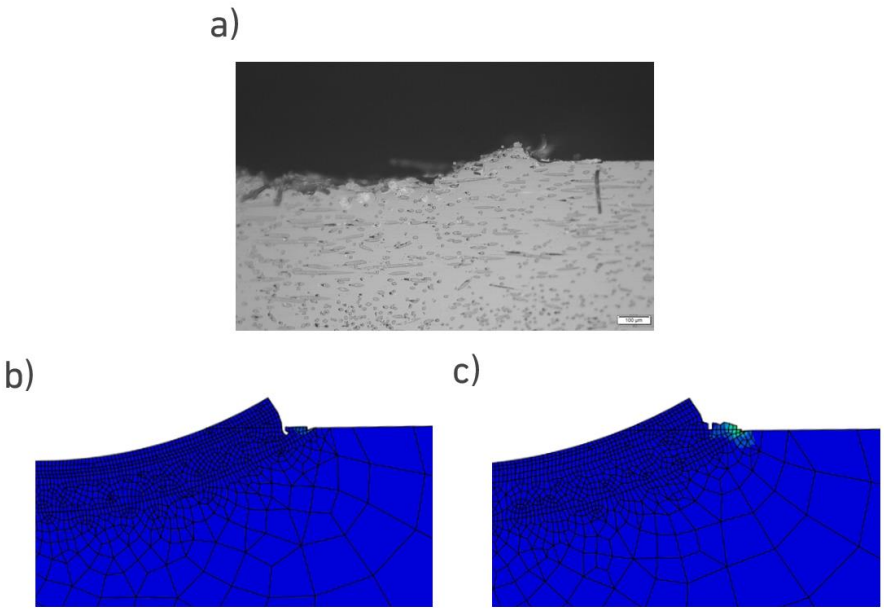


Figure 19 – Simulation of the fracture process on the weld region. a) Experimental, b) Numerical A1 and c) Numerical B1.

6. Conclusions

In the current research, the mechanical properties of different thermal conditions of PBT GF30 were correlated with its chemical properties through the use of an innovative Raman spectroscopy method. The properties for PBT GF30 were analysed for the as received state, different temperatures and compared with a welded zone. Key findings of this research are:

- It is observed that the temperature at which the PBT matrix has a direct influence on the interfacial bonding between the matrix and the glass fibres. With the

increase of the temperature, there is a higher adhesion between the fibres and the matrix.

- According to the Raman spectroscopy results for PBT GF30, it can be stated that the representative peaks are similar to those obtained for pure PBT (reference). There are only slight changes between the spectra, which may be due to the presence of glass fibres, potentially due to their fluorescence;
- Qualitatively analysing the temperature to which PBT GF30 was subjected, it can be concluded that with the increase in temperature new spectral features appear in the Raman spectrum probably due to the formation of new chemical bonds. This allowed to define distinct regions within the joint, which were converted into a gradient in the mechanical properties of the material.
- There is a convergence of results between the mechanical properties gradient, characterised by Raman, and the proposed numerical model.

References

1. Bahl, S., et al., *A systematic review on recent progress in advanced joining techniques of the lightweight materials.* AIMS Materials Science, 2021. **8**(1): p. 62-81.
2. Nirudhoddi, B.S., et al., *Journal of Advanced Joining Processes.*
3. Sivanur, K., K. Umananda, and D. Pai. *Advanced materials used in automotive industry-a review*. in *AIP Conference Proceedings*. 2021. AIP Publishing LLC.
4. Taub, A.I. and A.A. Luo, *Advanced lightweight materials and manufacturing processes for automotive applications.* Mrs Bulletin, 2015. **40**(12): p. 1045-1054.
5. Silva, L.R.R., et al., *Study of the optical, thermal, morphological and mechanical characteristics of a laser weldable fiber reinforced polymer*. Polymer Composites.
6. Silva, L.R., et al. *Experimental and Numerical Study for the Optimization of Process Parameters in Laser Welded and Adhesively Bonded PBT GF30 Fillet Joints*. in *International Conference on Industrial Applications of Adhesives*. 2024. Springer.